078
82383

GEND-INF-084

January 1988

cy 1

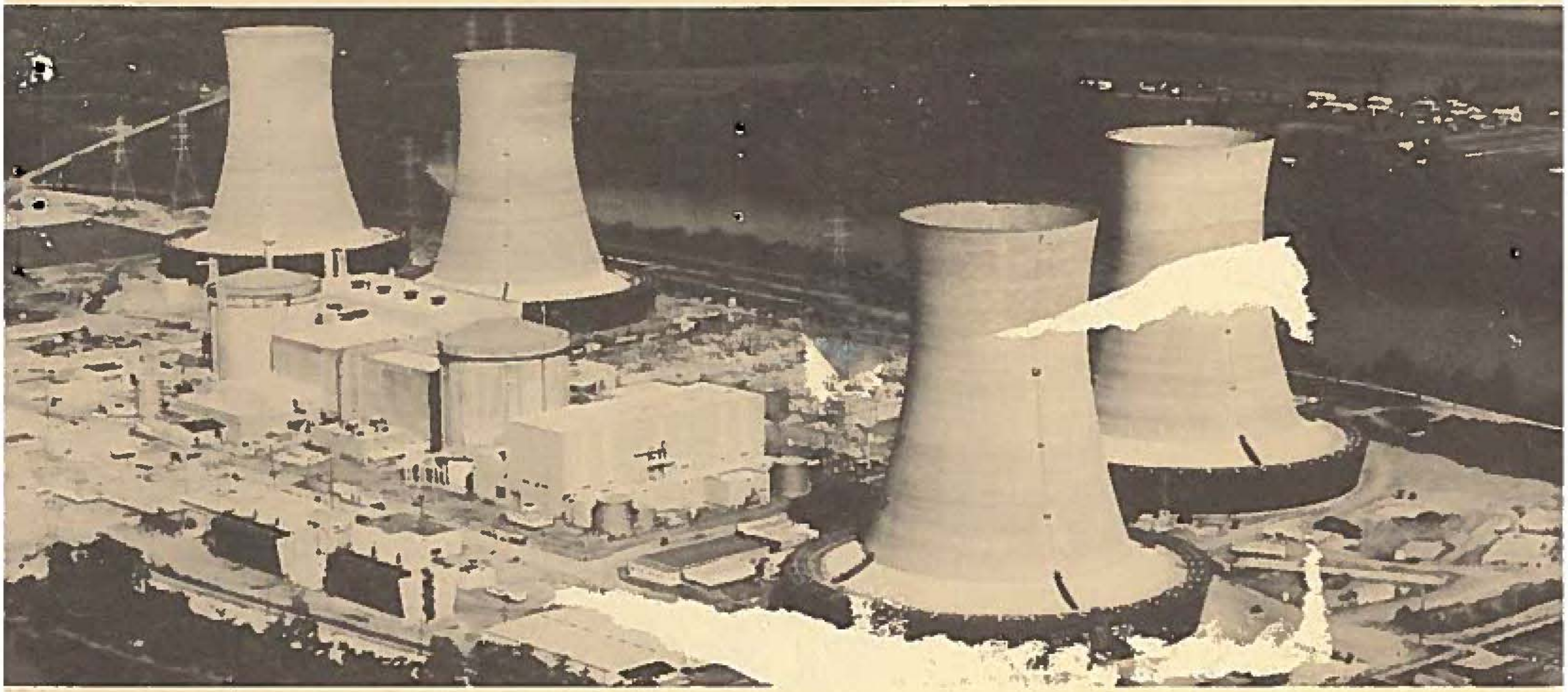

GEND

General Public Utilities • Electric Power Research Institute • U.S. Nuclear Regulatory Commission • U.S. Department of Energy

EXAMINATION OF DEBRIS FROM THE LOWER HEAD OF THE TMI-2 REACTOR

Charles S. Olsen
Douglas W. Akers
Richard K. McCardell

Prepared for the
U.S. Department of Energy
Three Mile Island Operations Office
Under Contract No. DE-AC07-76ID01570

DISCLAIMER

GEND-INF-084

EXAMINATION OF DEBRIS FROM THE LOWER HEAD OF THE TMI-2 REACTOR

Charles S. Olsen
Douglas W. Akers
Richard K. McCardell

Published January 1988

EG&G Idaho, Inc.
Idaho Falls, Idaho 83415

Prepared for the
U.S. Department of Energy
Idaho Operations Office
Under DOE Contract No. DE-AC07-76ID01570

ABSTRACT

Sixteen particles of prior-molten debris were removed from the lower reactor vessel head of the TMI-2 reactor through access ports around the periphery of the reactor vessel. Eight of these particles, which broke into eleven samples during shipping, were examined at the Idaho National Engineering Laboratory to obtain data on the physical properties, material structure, constituents, and radiochemical composition of the debris. In addition, portions of the same samples were sent to Argonne National Laboratory for further metallurgical examinations. The samples had dimensions up to 6.3 cm in diameter and weighed up to 550 g; they were generally homogeneous prior-molten material. Radiochemical data indicated varying retentions of fission products in the prior-molten material: Cs-137 (13%), I-129 (3%), Sb-125 (2.5%), and Ru-106 (6%). These amounts are low but at expected concentrations for prior molten core debris.

EXECUTIVE SUMMARY

Sixteen particles of debris were removed for examination from the surface of the debris bed located in the lower reactor vessel head of the TMI-2 reactor. The object of these examinations was to characterize the debris material in the lower reactor vessel head to better understand the physical and chemical state of the damaged TMI-2 reactor core and to support the defueling effort being performed by General Public Utilities. Eight of the particles of debris were shipped to the Idaho National Engineering Laboratory (INEL) for analysis. During shipping, some particles fractured, producing a total of 11 particles of debris from which samples were obtained for analysis. The particles ranged in weight from 0.4 to 553.9 g, with radiation levels up to 42 R/h gamma at 25 cm from the largest particle.

The matrix density of the material was measured by immersion density techniques for six particles of debris that weighed more than 15 g each. The density ranged from 6.57 to 8.25 g/cm^3, with an average value of 7.07 g/cm^3. The closed porosity in the particles was extensive, ranging from 8 to 30%, with an average of about 25%.

Two small areas of ceramic material containing only U and no Zr were found in the largest particle. Although the oxygen content of these areas was not measured, the adjoining material was identified as stoichiometric $(U,Zr)O_2$. The UO_2 appears to have been subjected to temperatures near the melting point; therefore, the minimum peak temperature reached by this particle was near 3100 K.

The lower plenum samples contained little bulk metallic material. However, many metallic inclusions were observed that were generally associated with dendritic structures in the grain boundaries. These inclusions were frequently found to be rich in nickel and often contained tin. In a few cases, the fission product ruthenium was also present; less frequently, silver was found in the inclusions, along with molybdenum and indium.

Elemental analyses were performed on samples from the lower vessel debris using inductively coupled plasma spectroscopy (ICP) to determine the composition of the particles and to provide elemental information for the radionuclide retention comparisons. The elemental data indicate that the composition of the debris is similar to what would be expected if the principal components of the original core were mixed, melted, and a fraction subsequently relocated to the lower plenum of the reactor. The average uranium content of the samples was 60 to 70%, with the balance being zirconium (10 to 15%), oxygen, and structural materials. The presence of molybdenum in the debris indicates that the Inconel-718 grid spacers were one of the sources of structural material in the lower vessel debris. No significant amounts of control rod materials (e.g., silver, indium, or cadmium) were measured in the debris.

Radiochemical analyses were performed for the principal gamma-ray emitters (Co-60, Ru-106, Sb-125, Cs-134, Cs-137, Ce-144, and Eu-154), fissile (U-235) and fertile (U-238) material content, I-129, and Sr-90. Tracers were used during the sample dissolutions to evaluate the chemical yields of Sr-90, I-129, and elemental tellurium during analysis.

The retention of fission products in the debris was determined by comparing the measured fission product concentrations with the predicted average quantities of fission products per gram of fuel, as calculated using the ORIGEN2 code. This comparison provides a relative indication of retention. The Ce-144 content, which is not expected to separate from the fuel by melting or vaporizing based on its known volatility, provides an indicator of the accuracy of the analysis (i.e., a measured Ce-144 retention of 100% indicates that the sample material comes from a region of of the core with burnup near the core average). Hence, comparisons with core average ORIGEN2 comparisons are appropriate. The fractional radionuclide retentions were calculated using the ORIGEN2-calculated radionuclide concentrations for the combined 1.98 and 2.64% enriched fuel assemblies (i.e., the central core region where most of the prior-molten fuel originated). The U-235 enrichment data indicate that little of the 2.96% enriched fuel was present, and consequently that those fuel assemblies did not participate in the melt that reached the lower vessel.

Table S-1 lists the average and range in percent of retained fission products for the six particles analyzed. These results are listed in order of increasing volatility, Ce-144 being the least, I-129 the most volatile. The averages indicate that the Ce-144 and Sr-90 are mostly retained in the fuel material. The wide ranges of retention for these radionuclides listed in Table S-1, however, are due principally to variations in the burnup of individual samples. The average Ce-144 retention (102%) indicates, however, that the average burnup of all samples is near the average of the interior core fuel assemblies. These data suggest that the average calculated retentions are good indications of actual fission product retention in the core materials analyzed.

The average retention listed for Eu-154 is probably not accurate (±50% uncertainty) because this radionuclide is produced by neutron activation of Eu-153, a fission product. Evaluations to be completed in 1988 will reduce the uncertainty in the Eu-154 predicted concentrations and will make the Eu-154 data a better indicator of the behavior of the europium radionuclides (i.e., burnup analyses are being performed to better define the production of Eu-154 as compared to Ce-144 and other low volatiles).

The Sb-125 and Ru-106 have substantially relocated out of the lower vessel debris samples. Other analyses indicate that these radionuclides may be retained as metallics in the core and may have become associated with localized accumulations of structural materials.

As expected, based on the relative volatility of this radionuclide, I-129 has a low average retention in the prior-molten material. However, retention of Cs-137 is significantly higher than I-129, and is substantially higher than predicted for prior-molten fuel. Autoradiographs of the debris show substantial quantities of radioactivity at grain boundaries and in voids in the prior-molten material. The autoradiographs indicate that the areas of high activity in the voids are spherical. Although some of this apparent activity is due to surface defects, Argonne-East has suggested that accumulations of activity are present and that some of the retained

TABLE S-1. AVERAGE RADIONUCLIDE RETENTION[a]
(in percent retained normalized to uranium content)

Radionuclide	Average	Range
Low volatile		
Ce-144	102	83-152
Medium volatile		
Sr-90	106	68-177
Eu-154	71	57-87
Ru-106	5.8	0-16
Sb-125	2.5[b]	0-15
High volatile		
Cs-137	12.8	0.38-35
I-129	2.8[c]	0-22

---

[a] Retention calculated using the ORIGEN-2 predicted concentrations for the average burnup of the combined 1.98 and 2.69% enriched fuel assemblies.

[b] Detection limit values have been included in the average. If excluded, the percent retention would increase to 5.8%.

[c] Detection limit values have been included in this average. If excluded the percent retention would increase to 3.2%.

activity may be volatile fission products (e.g., Cs-137) that were unable to diffuse out of the molten mass and were retained as surface deposited activity in pores in the debris material.

ACKNOWLEDGMENTS

Many people contributed to the sample acquisition and examination of the particles obtained from the lower reactor vessel. GPU and Bechtel personnel contributed substantially to the sample acquisition effort at TMI. The initial handling and mechanical properties tests at the Idaho National Engineering Laboratory were performed by S. K. McClaskey and G. A. Rigby at the hot cells located at the Test Reactor Area. The optical metallography was performed by M. L. Lindstrom and P. M. Stephen. S. T. Croney and A. W. Marley performed much of the radiochemical analysis work and L. A. Weinrich of the Radiochemistry unit performed the Sr-90 analyses. Y. D. Harker and P. R. Napper performed the fissile and fertile material measurements using the fast neutron flux unit at the Advanced Reactivity Measurement Facility. The scanning auger spectroscopy and microprobe analyses were performed at Argonne National Laboratory in Illinois by R. V. Strain, J. A. Sanecki, and L. A. Neimark. The elemental analyses using inductively coupled plasma spectroscopy were performed at Westinghouse Hanford by the Chemistry and Analysis group (J. J. McCown and staff).

CONTENTS

FIGURES

TABLES

EXAMINATION OF DEBRIS FROM THE LOWER HEAD OF THE TMI-2 REACTOR

1. INTRODUCTION

The Three Mile Island Unit 2 (TMI-2) pressurized water reactor (PWR) underwent a prolonged loss of coolant accident (LOCA) on March 28, 1979, that resulted in severe damage to the reactor core. As a consequence of the TMI-2 accident, numerous aspects of light water reactor (LWR) safety have been questioned, and the U.S. Nuclear Regulatory Commission (NRC) has embarked on a thorough review of reactor safety issues, particularly the causes and effects of severe core damage accidents. The nuclear community acknowledges the importance of examining TMI-2 in order to understand the nature of the core damage. Immediately after the accident, four organizations with interests in both plant recovery and acquisition of accident data formally agreed to cooperate in these areas. These organizations [General Public Utilities Nuclear Corporation (GPU Nuclear--owner/operator of TMI), Electric Power Research Institute (EPRI), the NRC, and the U.S. Department of Energy (DOE), collectively known as GEND] are presently involved in postaccident evaluations of TMI-2. The DOE is providing a portion of the funds for reactor recovery (in those areas where accident recovery knowledge will be of generic benefit to the LWR industry in the United States). In addition, DOE is funding acquisition and examination of samples obtained from the damaged reactor core.

The end-state configuration of the TMI-2 core just after the accident, as determined by closed circuit television (CCTV), mechanical probing, and core boring operations,[1] is illustrated in Figure 1. Current estimates indicate that approximately 25% of the original core mass formed an upper layer of debris supported by a hard crust. Below the upper debris bed are zones of prior-molten material and standing fuel rod segments that account for 20 and 42% of the core mass, respectively. Finally, it has been estimated that approximately 4.5 m^3 of core material (~16000 kg) flowed down onto the lower reactor vessel head. The CCTV examinations of the debris deposited on the lower reactor vessel head were used to estimate the volume of deposited material.[2]

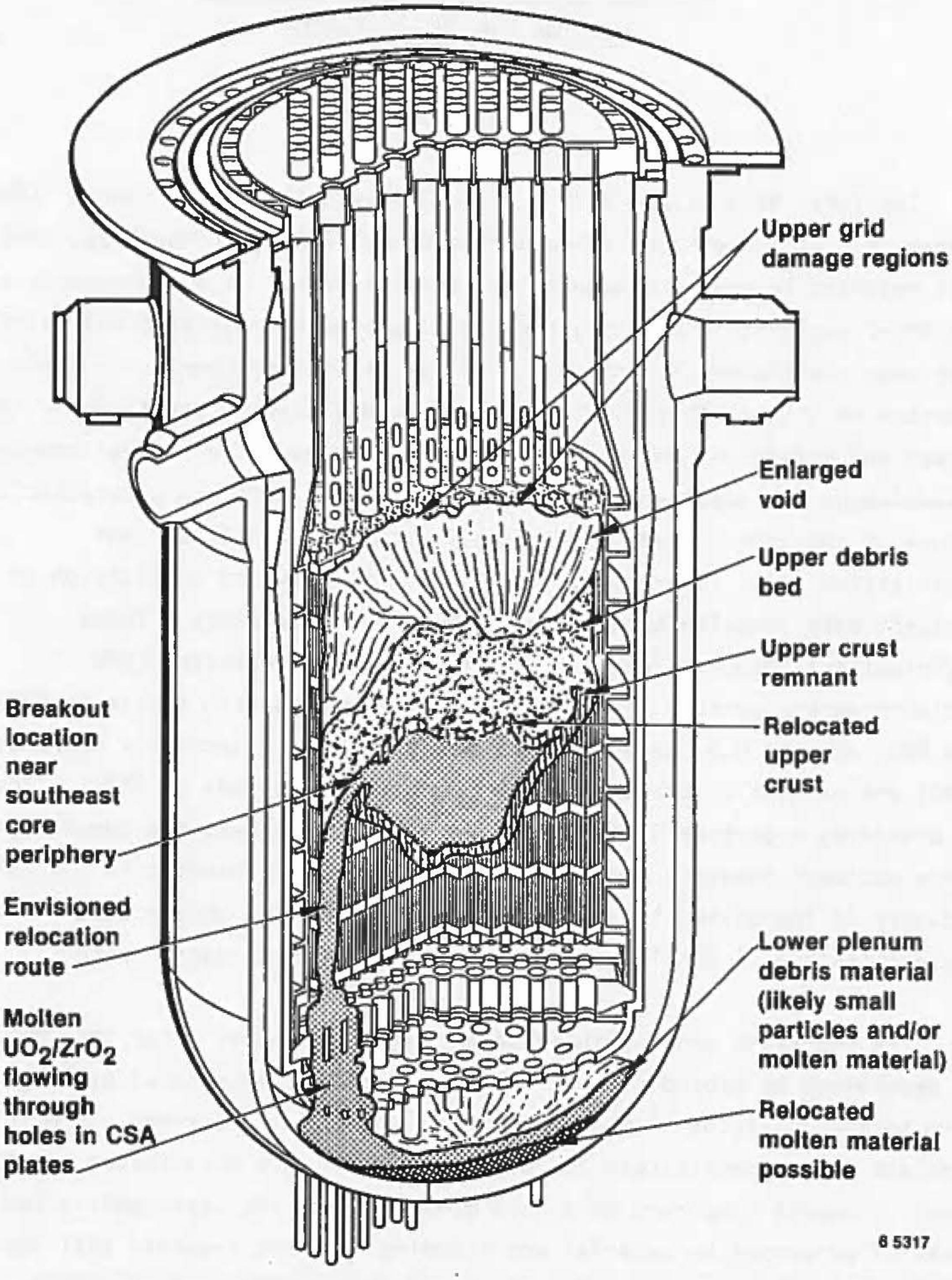

Figure 1. TMI-2 end-state core conditions.

During the week of July 21, 1985, 16 particles of debris from the lower reactor vessel head were obtained through the 25-cm annulus, between the thermal shield and the reactor vessel, that provides access from the top of the reactor vessel to the lower reactor vessel cavity. A jointed, long-handled tool (>4-m long) was used to grab the samples from the surface of the debris bed. All samples were removed from inspection ports Nos. 7 and 11 on the south and southwest sides of the core, respectively. The samples were removed from the surface of the debris pile near the edge of the core. Of the 16 particles removed from the core, 8 were transported to the Idaho National Engineering Laboratory (INEL) for analysis, with the remainder reserved for preliminary examinations at the mobile laboratory on the TMI site.

Upon receipt of the particles at the INEL in October 1985, an examination program was begun in which the particles were subjected to a series of physical, metallurgical, and radiochemical examinations. The physical characterization measurements consisted of both materials and mechanical property tests. The properties evaluated included porosity, dry weight, immersion density, and radiation field measurements. The mechanical property tests (e.g., drilling and cutting properties, and crushability) were performed to support the reactor defueling effort being performed by GPU Nuclear. The metallurgical examinations were performed to characterize the materials properties of the debris (e.g., pore distribution, and composition including oxygen content). Analyses were performed using optical metallography, scanning electron microscopy (SEM) with energy dispersive x-ray (EDX) analysis, Auger electron spectroscopy, electron microprobe analysis, and x-ray diffraction analysis. The radiochemical measurements were made to determine the chemical composition of the debris and to help define the extent of radionuclide retention in the debris. The radiochemical measurement techniques used consisted of gamma spectroscopy, beta spectroscopy, neutron activation analysis, liquid scintillation analysis, and delayed neutron counting.

The following sections discuss the examination plan, and results of the physical, metallurgical, chemical, and radiochemical analyses. The concluding sections are a discussion of the contributions of these results to understanding the TMI-2 accident, and a summary of the observations and conclusions.

2. EXAMINATION PLAN AND ANALYSIS METHODS

Acquisition and examination of the debris from the lower reactor vessel head is one of the tasks identified in the core examination plan,[3] which describes the technical/scientific data that should be acquired from examining the TMI-2 core. The general objectives of the TMI-2 accident evaluations are to understand

- The physical and chemical states of the TMI-2 core and related structures, and the external influences that affected the accident
- What happened during the accident, which includes developing a qualified data base and standard problem of the TMI-2 accident to benchmark severe accident analysis codes and methodologies
- The relationship between the phenomena and processes controlling the accident and the important severe accident/source term technical issues.

An additional objective is to obtain data to aid in defueling the reactor. From these general objectives, an examination plan was developed for the lower vessel debris to obtain data to address the following specific informational needs:

- Physical form of the debris (weight, density, shape, and morphology)
- Chemical form and composition of the particles of debris (fuel, cladding, control material, structural material, reaction products, etc.) and the peak temperatures to which those materials were exposed
- Amount and identity of radionuclides retained in the debris
- Mechanical crushing and cutting behavior for defueling concerns.

Table 1 lists the particles obtained from the lower reactor vessel and the type and number of analyses performed on each particle. The prefixes 7 and 11 identify the inspection port where the samples were obtained [i.e., the No. 7 inspection port (southern core quadrant) and the No. 11 inspection port (south western core quadrant), respectively]. The order in which the analyses were performed was dictated by the hot cell handling requirements. Most physical analyses were performed on the bulk particles before sectioning for the mechanical properties, metallurgical, and radiochemical analyses.

The analysis methods and procedures used for the lower vessel debris samples were, in most instances, standard laboratory techniques, with necessary modifications to adapt them to the physical characteristics of the samples and to remote analysis because of the high radiation levels.

The initial characterization following unloading of the particles included photography, weights, and immersion densities on all intact particles. The particles were then sectioned to provide samples for the metallurgical, radiochemical, and mechanical property tests. The mechanical property tests and the grinding and polishing of samples for the metallurgical analyses were performed in a hot cell. Particle cross sections were transported to the chemical laboratories where 20 to 100 mg samples were obtained from the interior of the samples at selected locations for the radionuclide and chemical analyses. These samples were dissolved using a pyrosulfate fusion technique in a closed system for measurement of the volatile constituents of the retained fission products. Iodine-129 and Sr-90 tracers were added to the intact sample before dissolution, and a tellurium tracer was added after the dissolution to determine losses of these radionuclides during the dissolution and subsequent separations. A brief description of the analysis methods used for the lower vessel debris samples is presented in Appendix A, and a more detailed discussion of these techniques is found in Reference 4.

TABLE 1. EXAMINATIONS PERFORMED ON THE DEBRIS FROM THE LOWER REACTOR VESSEL

	Particles Examined and Number of Analyses Performed										
Examinations	7-1	7-6	7-7	11-1	11-2	11-4	11-5	11-6	11-7	11-10	11-11
Physical											
Visual and photographic	1[a]	1	1	1	1	1	1	1	1	1	1
Weight	1	1	1	1	1	1	1	1	1	1	1
Immersion density	1			1	1	1	1	1	1		
Porosity	1			1	1	1	1		1		
Mechanical crushing[b]	1	1			1						
Drilling[b]					1						
Radiation field	1	1	1	1	1	1	1	1	1	1	1
Metallurgical											
Optical metallography	1			1	1	2	1	1	1		
SEM/EDX/WDX[c]	1			1	1	1	3	1	1		
Scanning auger spectroscopy (SAS)											
X-ray diffraction microprobe	1			1							
Chemical											
ICP[d]	5			4	6	7	9	3	3		
Radiochemical											
Gamma spectroscopy	5			4	6	7	9	3	3		
Fissile/fertile material	5			4	6	7	9	3	3		
I-129	5			4	6	7	9	3	3		

TABLE 1. (continued)

	Particles Examined and Number of Analyses Performed										
Examinations	7-1	7-6	7-7	11-1	11-2	11-4	11-5	11-6	11-7	11-10	11-11
Radiochemical (continued)											
Sr-90	5			4	6	7	9	3	3		
Tellurium	5			4	6	7	9	3	3		
Autoradiography					1	1	1	1	1		

---

a. Number of subsamples examined.

b. These tests were performed to support the defueling effort being performed by GPU Nuclear.

c. Scanning Electron Microscopy (SEM)/Energy Dispersive X-ray (EDX) or Wavelength Dispersive X-ray (WDX).

d. Inductively Coupled Plasma Spectroscopy

3. EXAMINATION RESULTS AND DISCUSSION

This section presents the results of the physical, metallurgical, chemical, and radionuclide analyses performed on the particles of debris obtained from the lower reactor vessel, and discusses these results as they relate to the TMI-2 accident. They are discussed in the order the analyses were performed; the physical analyses results (i.e., photovisual, weight, immersion density, sectioning and cutting, drilling, and compressive strength tests) are presented in the initial section. The results of the metallurgical analyses performed at the INEL and Argonne National Laboratory-East (ANL-E) are presented in Section 3.2. Sections 3.3 and 3.4 contain the results of the chemical and radionuclide analyses performed on the debris, respectively.

3.1 Physical Property Measurements

Measurements were performed to characterize the physical properties of the lower vessel debris. The following sections contain discussions of the principal physical properties measured. The density and porosity measurements are discussed in the first section (3.1.1.) followed by discussions of the visual inspection and sectioning (3.1.2.), the cutting and drilling property tests (3.1.3.), and, finally, the compressive strength measurements (3.1.4.).

Six particles were retrieved from Location 7; four were retained by GPU for examination, and two were shipped to the INEL. However, upon receipt at the INEL, five particles were found in the shipping container (Figure 2). Two particles were matched with those shipped by GPU, but three chips (probably broken from the large particle) were also present. Only one chip was large enough to identify as a sample.

Nine particles were removed from Location 11, and four of these were retained at TMI for examination. Like the shipment from Location 7, more particles were found in the shipping container upon receipt at the INEL (Figure 3) than were shipped. A total of seven large pieces (greater than 6 mm) and several very small fragments were found in the shipping

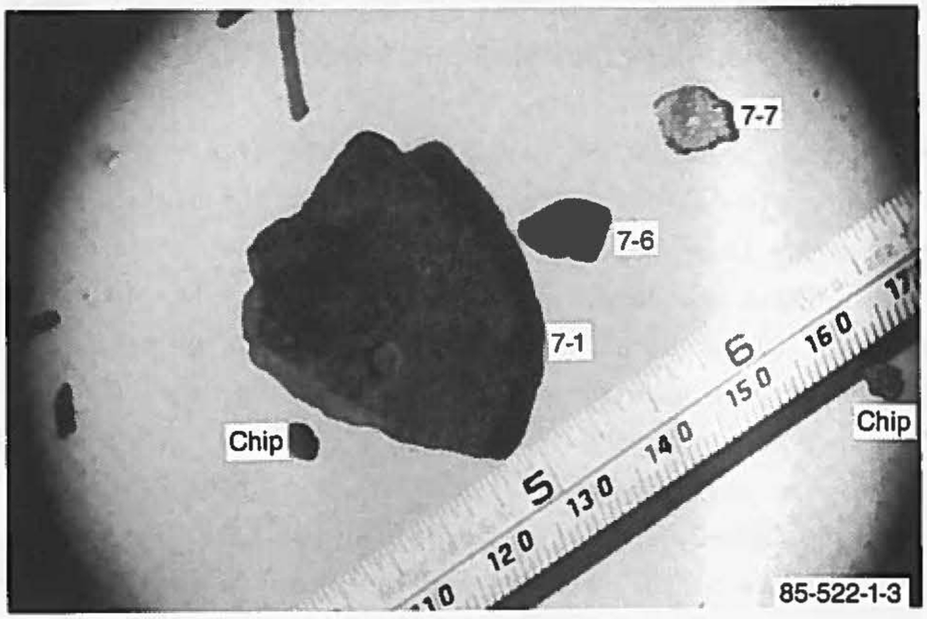

Figure 2. Particle samples and chips from TMI Location 7.

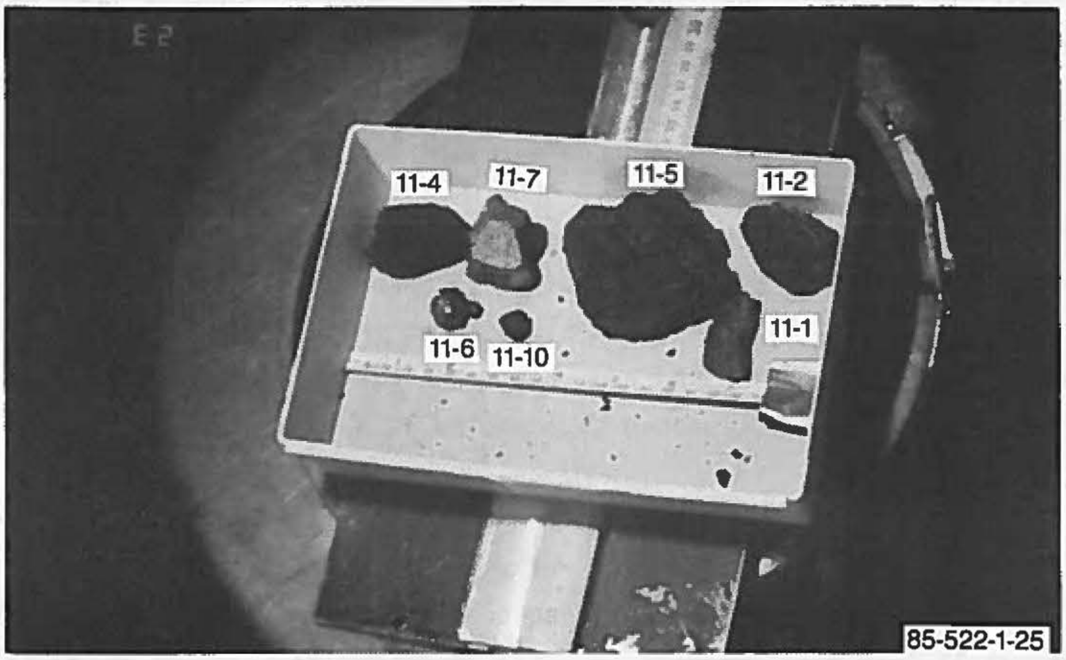

Figure 3. Particle samples and chips from TMI Location 11.

container. An attempt was made to match these particles to the GPU-provided descriptions as they were removed from the shipping container. Observations indicated that some samples had fractured into several pieces during shipping.

Radiation levels were measured for each identified particle and are listed in Table 2. These measurements ranged from 100 mR/h gamma to 7.5 R/h gamma. Although these measurements reflect some self-shielding by the particles themselves, the ratio of beta/gamma to gamma is about 10, which is expected of TMI-2 fuel cooled for about 6 years.

3.1.1 Density and Porosity Measurements

Density and porosity were measured for each particle in order to correlate density with composition, to provide data for analytical evaluations, and to estimate core mass at each location. The methods used are discussed in Appendix A. The density of the samples ranged from 6.57 to 8.25 g/cm^3 (Table 3). The total void fractions, as calculated from the data in Appendix B, are also included in the table. The void fractions ranged from 8% for Particle 11-7 to between 9 and 31% for the remaining particles. This substantial porosity is a significant contributor to the relatively low, measured density values of the samples, as compared with urania. The open porosity, which was 3% or less, is small compared with the total void fraction, which indicates that the pores are not interlinked. Metallography confirmed that the porosity was not interlinked, although some localized pore coalescence did occur.

Excluding Particle 11-7, which appears to be atypical, the average of the remaining matrix densities is 7.07 g/cm^3, with a variation (one standard deviation) of 0.57 g/cm^3. Correction for porosity yields an average density of 9.78 g/cm^3, with a standard deviation of 0.53 g/cm^3. Although the density of Particle 11-7 is within the range of the uncorrected densities, when the density value is corrected for porosity it is outside one standard deviation for the corrected density of the remaining particles.

TABLE 2. RADIATION LEVELS OF LOWER VESSEL SAMPLES

EG&G Sample Number	Beta/Gamma[a,b]	Gamma[b]	Distance from Sample (cm)
7-1	13 R/h	1.6 R/h	20
7-6	1.2 R/h	130 mR/h	20
7-7	800 mR/h	100 mR/h	20
11-1	12 R/h	1.2 R/h	20
11-2	26 R/h	3 R/h	20
11-4	25 R/h	2.9 R/h	20
11-5	>50 R/h (off scale)	7.5 R/h	20
	42 R/h[c]	5.5 R/h	29
11-6	4 R/h	500 mR/h	20
11-7	30 R/h	3.2 R/h	20
11-10	700 mR/h	100 mR/h	20
11-11	3.5 R/h	320 mR/h	20
11-12 (collected fines)	3.7 R/h	380 mR/h	20
Background Reading:	80 mR/h	50 mR/h	--

---

a. These readings are corrected for background radiation, which is normally insignificant.

b. The radiation readings were taken on November 6, 1985.

c. This reading for Particle 11-5 was made at 29 cm.

TABLE 3. DENSITIES OF LOWER VESSEL PARTICLES

Particle	Dry Weight (g)	Particle Density[a,b,c] (g/cm^3)	Void Fraction (%)	Open Porosity[d] (%)
7-1	50.1	6.57	27	0.00
7-6	1.0			
7-7	0.4			
11-1	39.7	8.25	23	2.04
11-2	123.9 123.9	6.98 6.75	30	2.75 2.66
11-4	107.1 107.1	6.94 6.94	31	3.14 2.53
11-5	553.9	6.60	27	1.99
11-6	12.9 12.9		25	
11-7	118.8 118.8	7.18 7.27	8	1.20 2.34
11-10	0.6			
11-11	5.5			
11-12	--	--		--

---

a. Envelope density = $W_d/(W_s - W_i)$*Rho.

b. Particle density = $W_d/(W_d - W_i)$*Rho.

c. Rho = Density of Water.

d. Open Porosity = $(W_s - W_d)/(W_s - W_i)$*100.

Where W_d = dry weight

W_s = saturated weight (dry weight with water in the surface porosity)

W_i = immersion weight (in water).

For comparison with the density of the lower plenum vessel samples, the density of elements and alloys found in the core region are listed in Table 4, as is the density of the oxides of these constituents. For a composition of 81% urania and 19% zirconia (oxidized zircaloy) typical for mixed fuel material (Table 4), the density would be 9.53 g/cm^3, compared to the average of 9.78 g/cm^3 for five of the six particles analyzed. The densities of these five particles compared to the theoretical density of urania and zirconia can be reconciled by void fraction and composition. However, the density of Particle 11-7 cannot be reconciled. The corrected density of this particle is 7.8 g/cm^3. The particle would have to contain about 45% urania and 55% zirconia, which is inconsistent with the elemental analysis results. The probable cause for this density variation is that some large pores were not visible in the cross section used for the porosity analysis.

3.1.2 Visual Examination And Sectioning

The discussion of the visual examination includes the visual observations of the external surface and of the cross sections of the particles.

Particle 7-1. The photograph of Particle 7-1 in Figure 4 shows that the sample was flat at one end and pointed at the opposite end. A reddish coating covered the top surface and a yellowish coating covered the sides. This sample was sectioned according to the diagram in Figure 5, without encapsulation in epoxy because epoxy makes the radiochemical analysis more difficult. Particle 7-1 was divided into five subsamples: one sample each for metallographic and radiochemical analysis, one sample for x-ray diffraction measurements, one sample for mechanical testing, and one sample for analysis by ANL-E. (Note that the X-ray diffraction analyses are not reported, as the technique was unable to provide useful data on the uranium chemical forms.)

TABLE 4. DENSITY OF CORE MATERIALS (g/cm^3)

Material	Alloy or Element	Oxide	Probable Chemical Species
Uranium	18.7	10.41	UO_2[a]
Zircaloy	6.55		
Zirconium	6.40	5.60	ZrO_2
Tin	7.28	6.446	SnO
Control Ag-In-Cd	9.91[b]		
Silver	10.5	--	
Indium	7.30	7.179	InO
Cadmium	8.642	8.15	CdO
Burnable Poison	3.84[b]		
Aluminum[c]	2.702	3.97	Al_2O_3
Boron Carbide	2.50	--	
304 Stainless Steel	8.02		
Iron[d]	7.86	5.7	FeO
		5.18	Fe_3O_4
		3.4-3.9	Fe_2O_3
Nickel[d]	8.90	7.45	NiO
Chromium[d]	7.20	5.21	Cr_2O_3
Inconel-718	8.21		
Niobium[e]	8.55	4.47	Nb_2O_5
		6.27	NbO
Molybdenum	10.2	6.47	MoO_2
Inconel X-750	8.25	4.50	MoO_3
Titanium	4.5	3.84	(Anatase)
Inconel 600	8.41		

---

a. Based on 95% of theoretical density.
b. Density is based on weighted average of elements.
c. Element is also present in alloys IN-718 and IN-X750.
d. Element is also present in alloys IN-718, IN-X750, and IN-600.
e. Element is also present in IN-X750.

Figure 4. Side and top view of Particle 7-1.

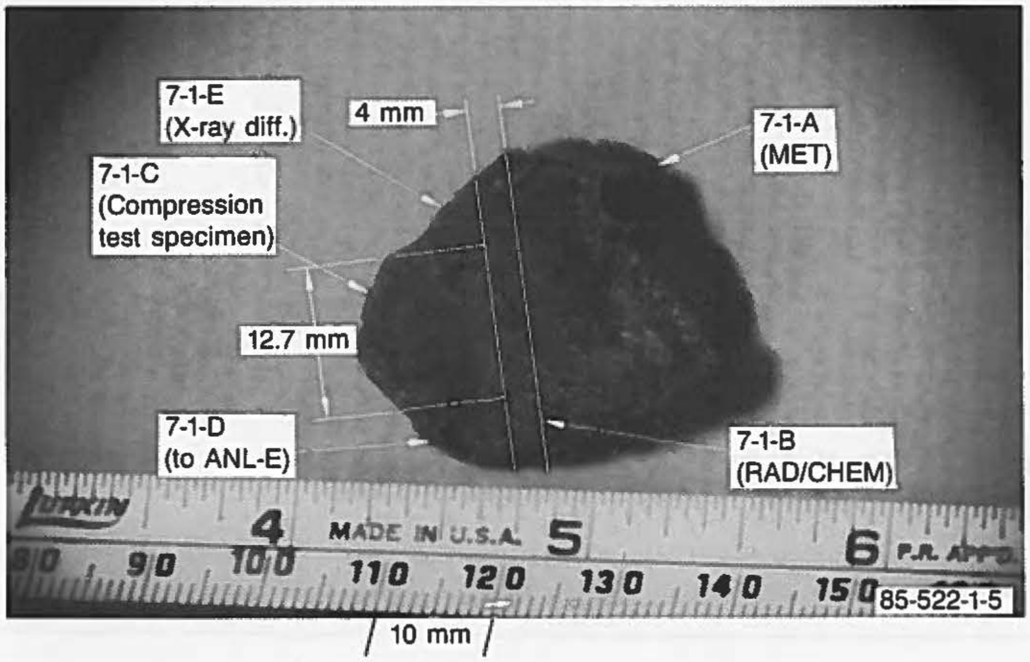

Figure 5. Sectioning diagram for Particle 7-1.

Figure 6 is an example of a cross section from Particle 7-1 that shows substantial porosity. The cross section reveals regions of either very large pores or fine pores, but not both, in the same region. The cross section shown in Figure 6 eventually broke in half during handling owing to a small crack in the sample. Such cracks were typical in other cross sections from Particle 7-1.

Particle 11-1. Two views of Particle 11-1 are shown in Figures 7 and 8. The side view in Figure 7 had a reddish-orange inclusion and a flat bottom, which is depicted in Figure 8. The sides of Particle 11-1 are nearly pointed at the top. The bottom had a yellowish surface deposit. The sectioning diagram for this sample is shown in Figure 9. Metallographic, radiochemical, and ANL-East samples were obtained. Particle 11-1 was not epoxied, and during the second cut the sample broke in half. The fractured surface, shown in Figure 10, has no surface coating and had metallic inclusions embedded in a ceramic matrix. A cross section from this particle is shown in Figure 11.

Particle 11-2. Three views of Particle 11-2 are shown in Figures 12 through 14. A triangular-shaped flat surface with an end converging to a point is shown in Figure 12. The particle had a reddish-orange color and contained numerous large pores. The base and one of the flat sides of this particle is shown in Figure 14, which revealed a blackish color with very large pores and some metallic inclusions. The sectioning diagram of Particle 11-2 is shown in Figure 15. Metallographic, radiochemical, and drilling test samples were obtained. A cut cross section of the metallographic specimen (Figure 16) has very large pores at the widest end, and fine pores at the end terminating at a point.

Particle 11-4. Two views of Particle 11-4 are shown in Figures 17 and 18. Figure 17 shows the relatively flat bottom, which was yellow, whereas Figure 18 reveals a pointed wedge shape. Particle 11-4 was sectioned according to the diagram in Figure 19. Two metallographic and two radiochemical samples were obtained from this sample. The samples were obtained so that analysis could be performed in two directions to evaluate possible gradients. A transverse cross section from this particle is shown

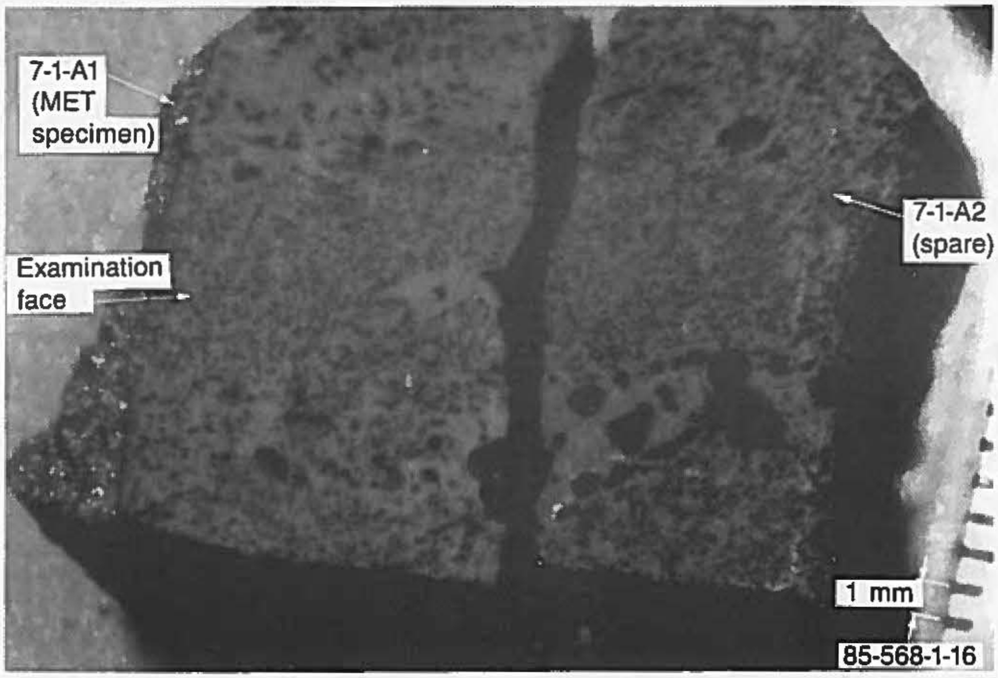

Figure 6. Cross section of metallographic sample from Particle 7-1.

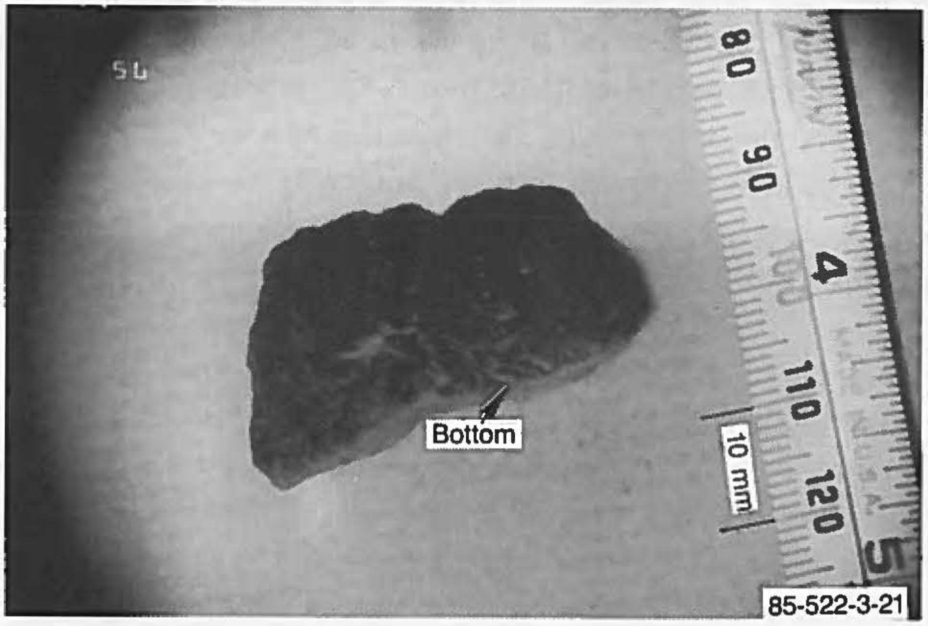

Figure 7. Side view of Particle 11-1.

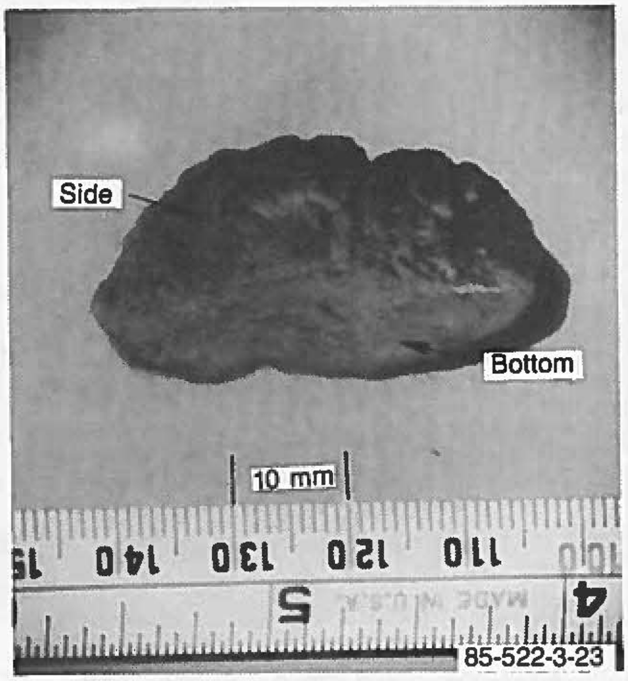

Figure 8. Bottom and side views of Particle 11-1.

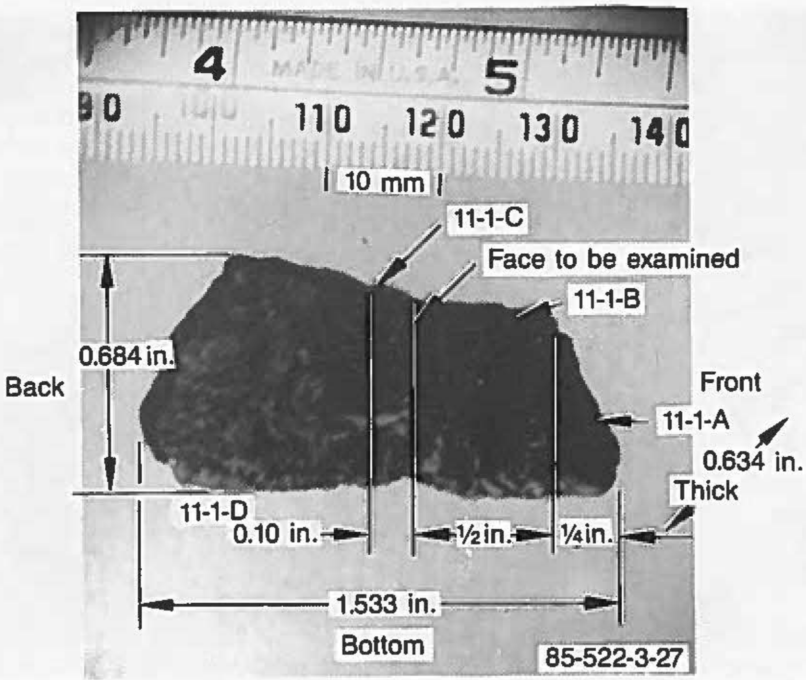

Figure 9. Sectioning diagram for Particle 11-1 (Argonne-East sample).

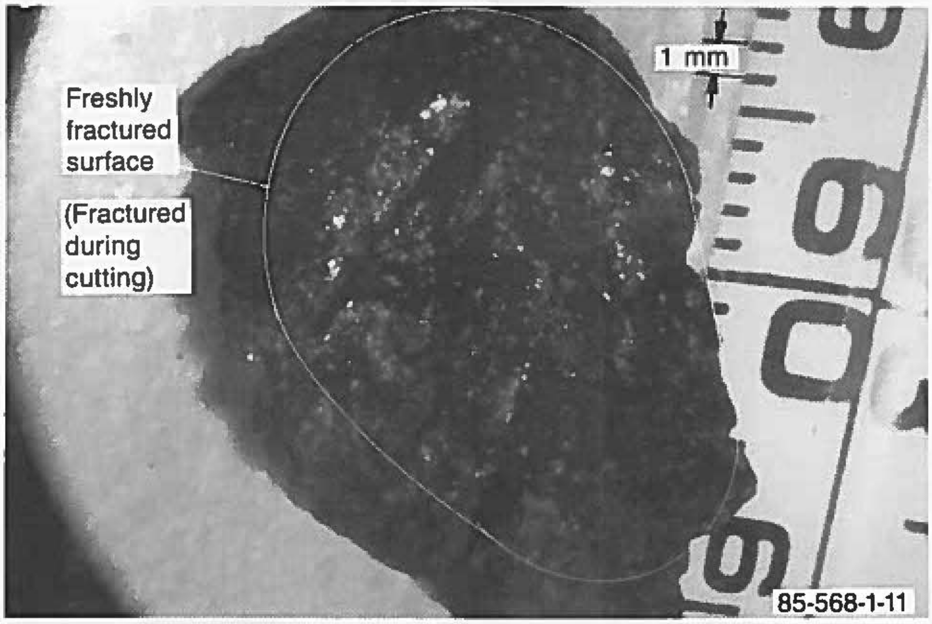

Figure 10. Fractured surface of sample from Particle 11-1.

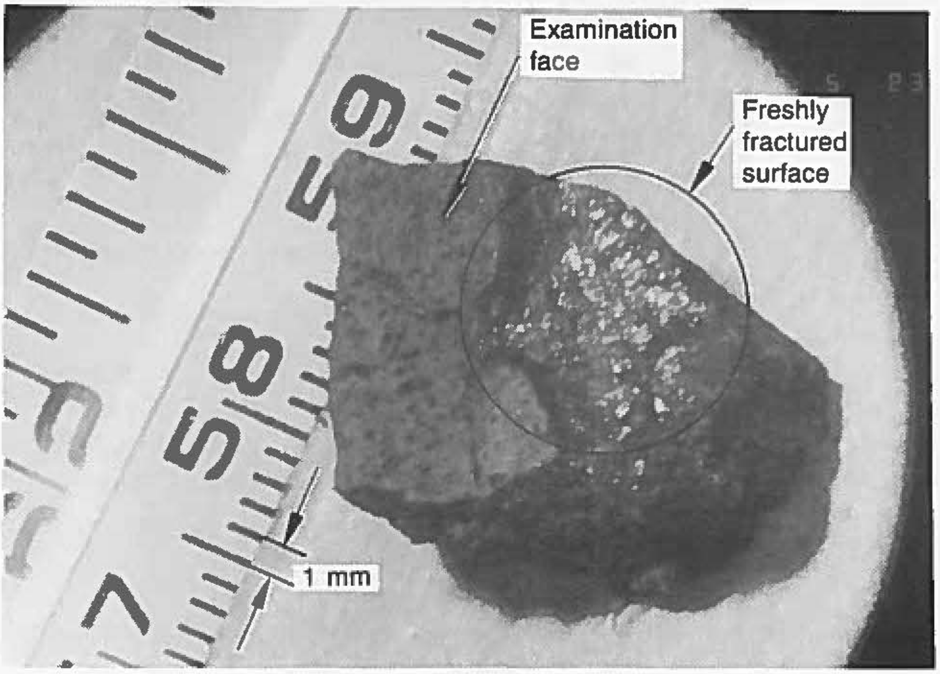

Figure 11. Cross section from Particle 11-1.

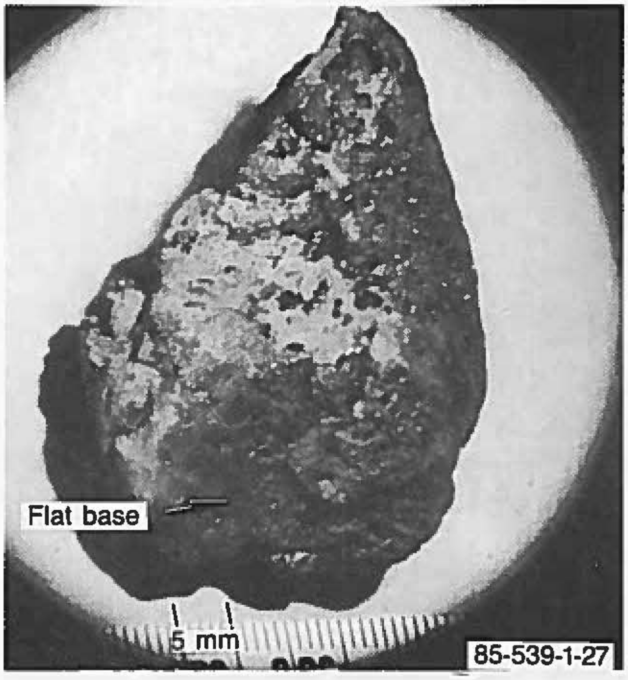

Figure 12. Bottom view of Particle 11-2.

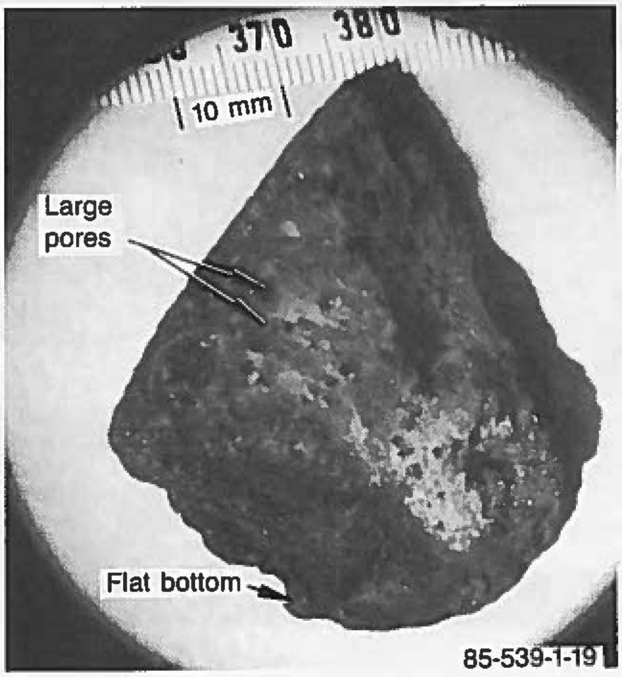

Figure 13. Side and top views of Particle 11-2 showing trapezoidal shape.

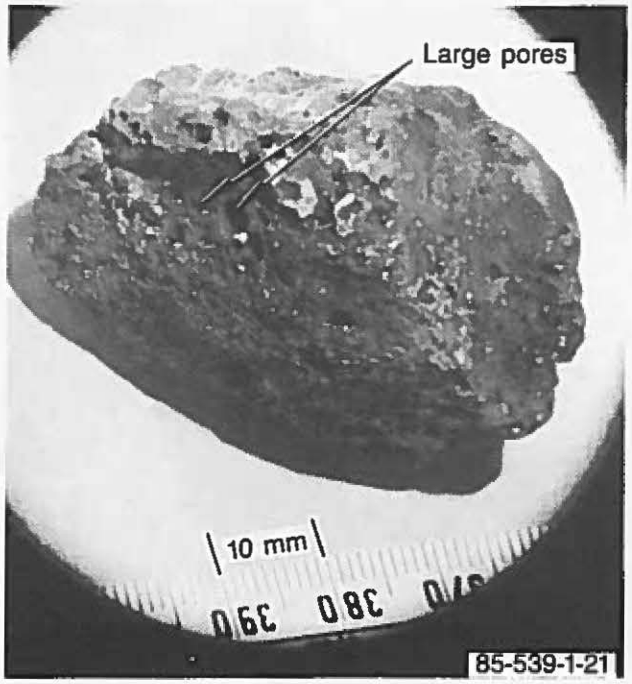

Figure 14. Side and bottom views of Particle 11-2.

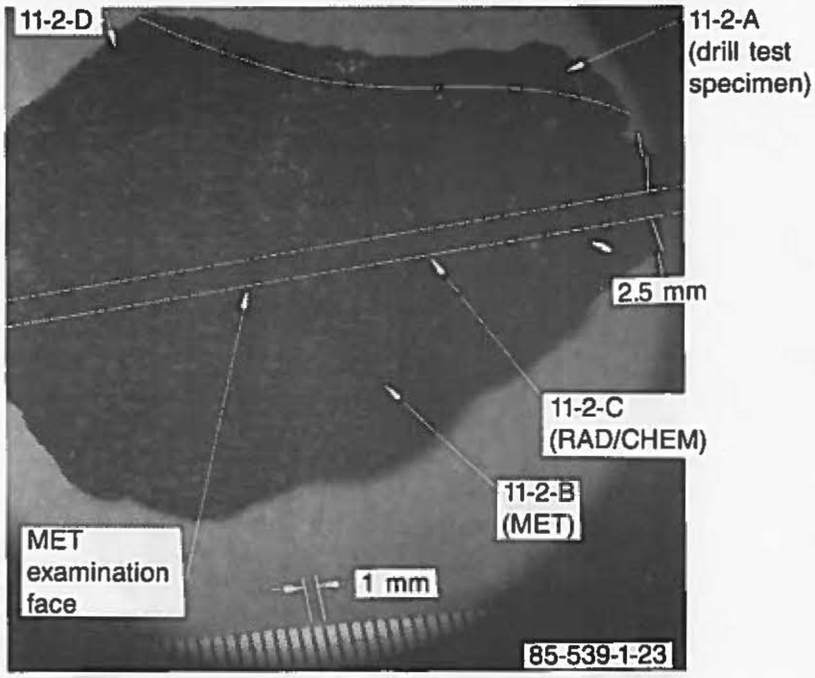

Figure 15. Sectioning diagram for Particle 11-2.

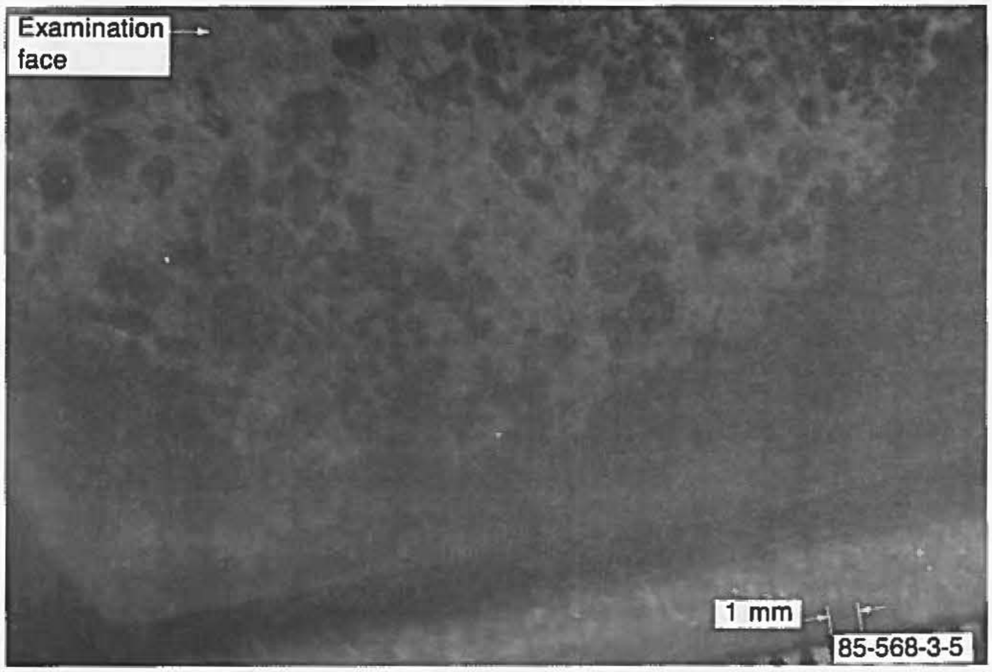

Figure 16. Cross section showing metallographic sample from Particle 11-2.

Figure 17. Bottom view of Particle 11-4.

Figure 18. Top view of Particle 11-4 showing pointed top.

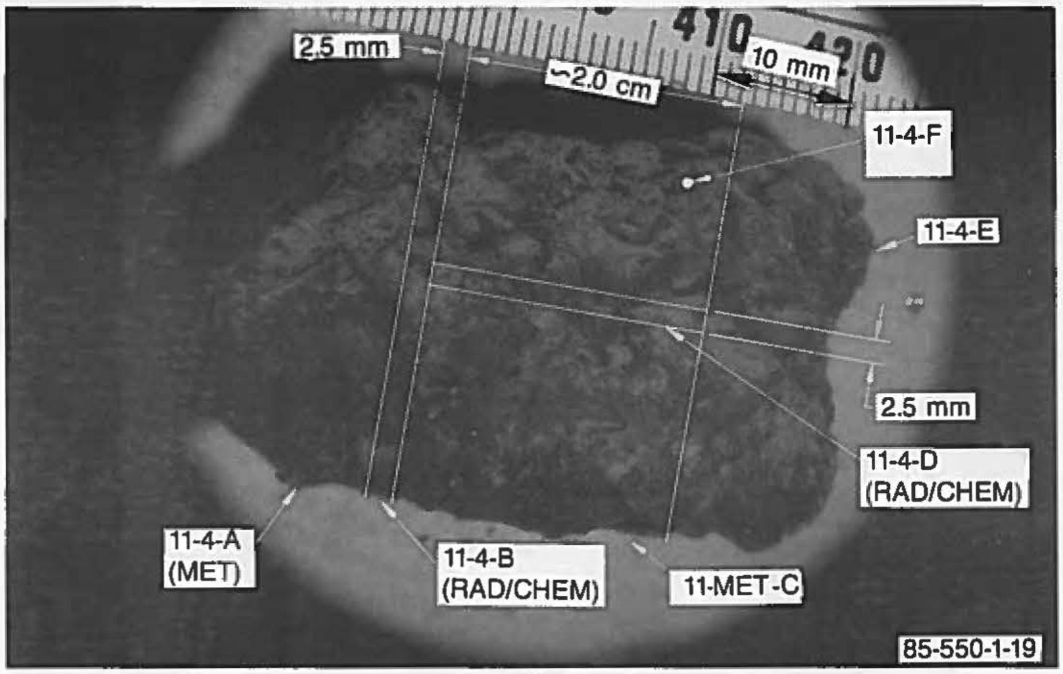

Figure 19. Sectioning diagram for Particle 11-4.

in Figure 20; a longitudinal section is shown in Figure 21. The transverse and longitudinal sections are similar to Particle 11-1. There are numerous large pores that appeared reddish at the bottom of the pore. The porosity distribution appears to be random.

Particle 11-5. Particle 11-5 had a flat surface similar to the other samples and was shaped like a rain drop in general appearance, except for the flat surface. Three views of Particle 11-5 are shown in Figures 22 through 24. Figure 22 shows a side of this particle that has a number of folds or fissures on the surface together with a number of large pores. Figure 23 is a view of another side of Particle 11-5, which is similar in appearance to that shown in Figure 22. From the surface appearance, a porosity-free slag appears to be embedded in a porous matrix. Another view (Figure 24) shows a porous matrix with only a few fissures. The sectioning diagram for this sample is shown in Figure 25. Radiochemical, metallographic, and compression test specimens were obtained from Particle 11-5. The metallographic specimen shown in Figure 26 contains a great deal of porosity and areas of only large pores with no fine pores.

Particle 11-6. A view of Particle 11-6 is shown in Figure 27. This particle appears as though fuel or a ceramic mixture may have frozen on a cooler zircaloy cladding ring that may have oxidized. The once-molten, pointed ceramic is the blackish material in Figure 27; the zircaloy ring looked like a yellow washer at the bottom of the photograph. However, a sectioned sample for a metallographic specimen (shown in Figure 28) was very uniform in structure and contained many fine pores. A radiochemical sample was obtained in addition to the metallographic sample.

Particle 11-7. Two views of Particle 11-7 are shown in Figures 29 and 30. Figure 29 shows flat bottom and side view of this particle. The backside has a depression or saddle as if the material contracted during solidification. The surface was yellowish-red in color. Figure 30 shows the flat bottom and front view of this particle. The front is a wedge-shaped particle. As with the other particles, this particle also has extensive large pores. The sectioning diagram of this particle is shown in

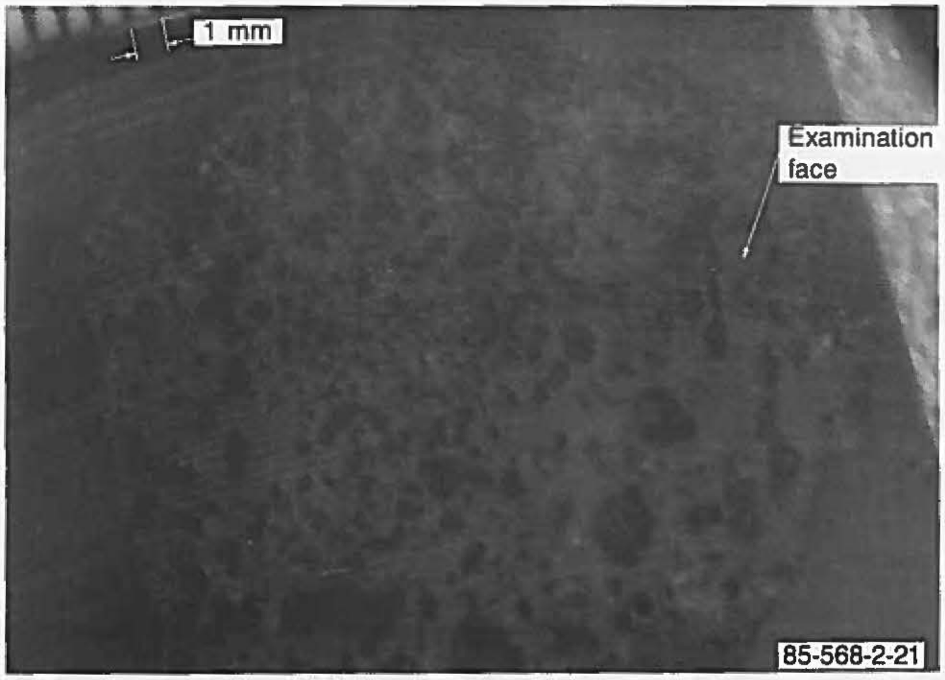

Figure 20. Transverse cross section showing metallographic sample from Particle 11-4.

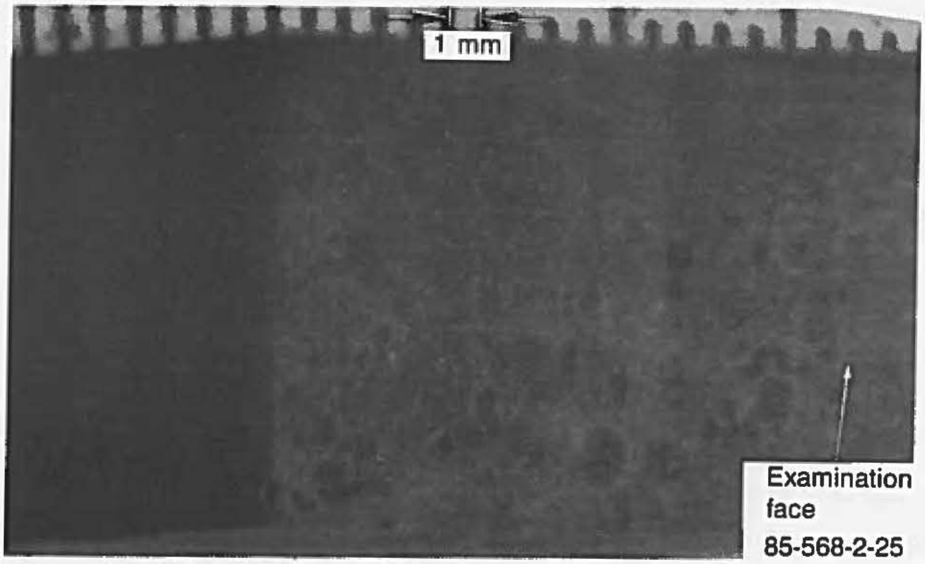

Figure 21. Longitudinal section showing metallographic sample from Particle 11-4.

Figure 22. Folds and fissures in side view of Particle 11-5.

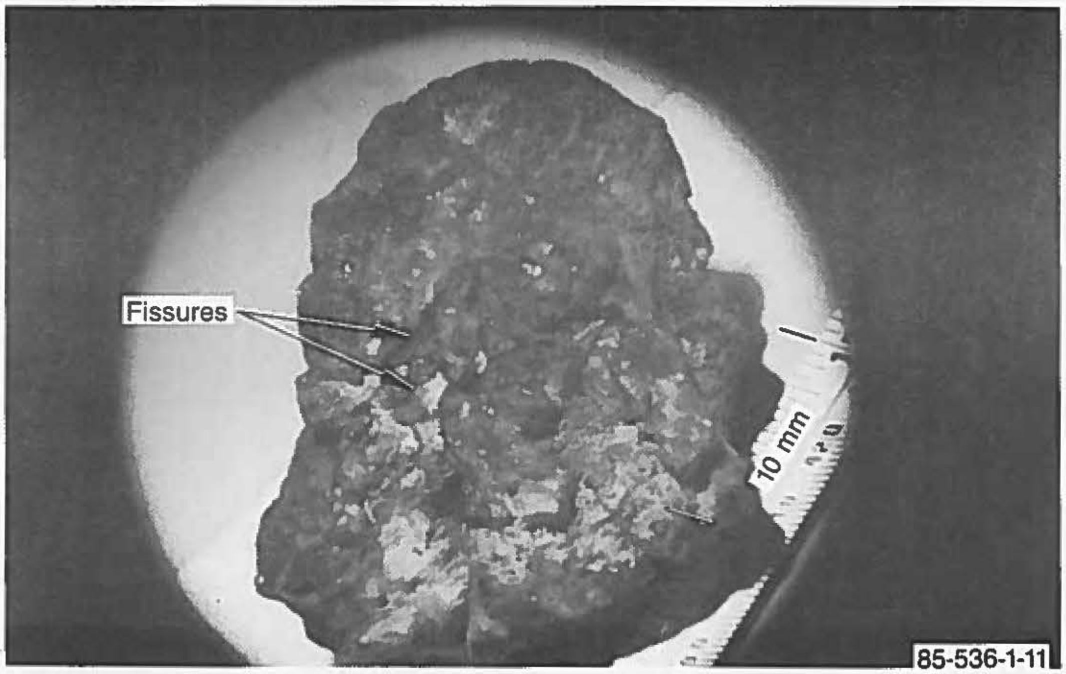

Figure 23. Fissures and porosity in side view of Particle 11-5.

Figure 24. Top view showing porosity in Particle 11-5.

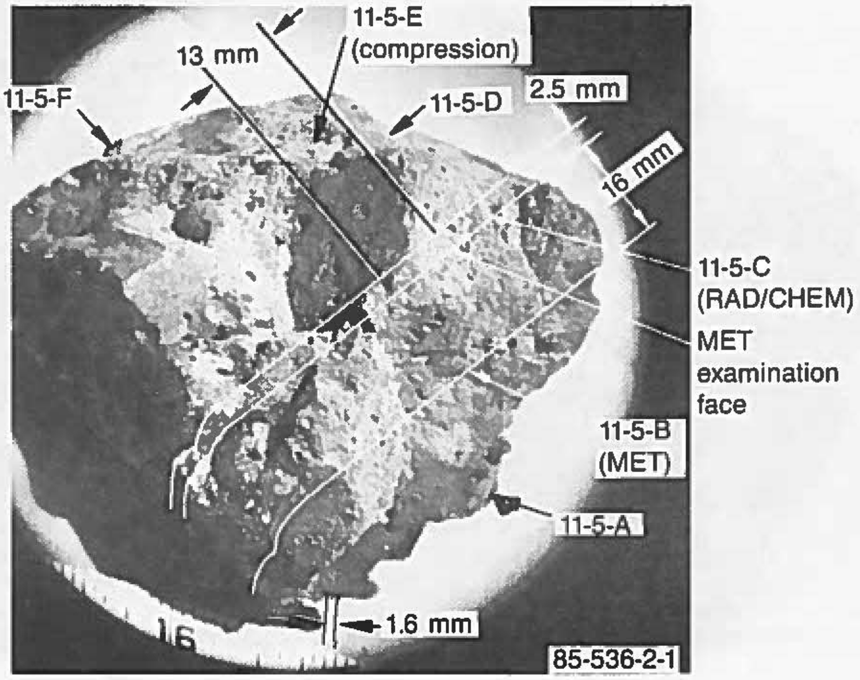

Figure 25. Sectioning diagram for Particle 11-5.

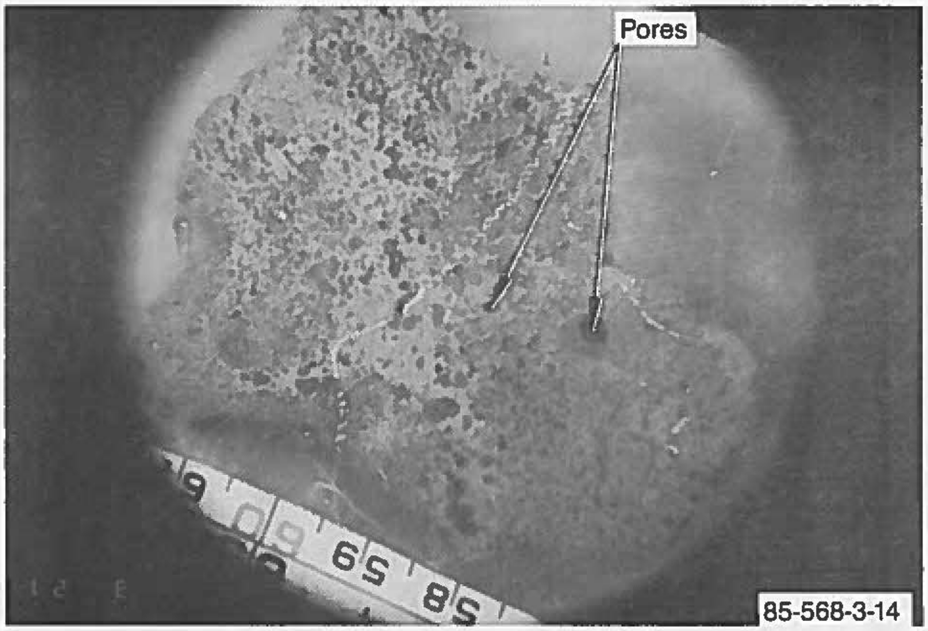

Figure 26. Cross section showing metallographic sample from Particle 11-5.

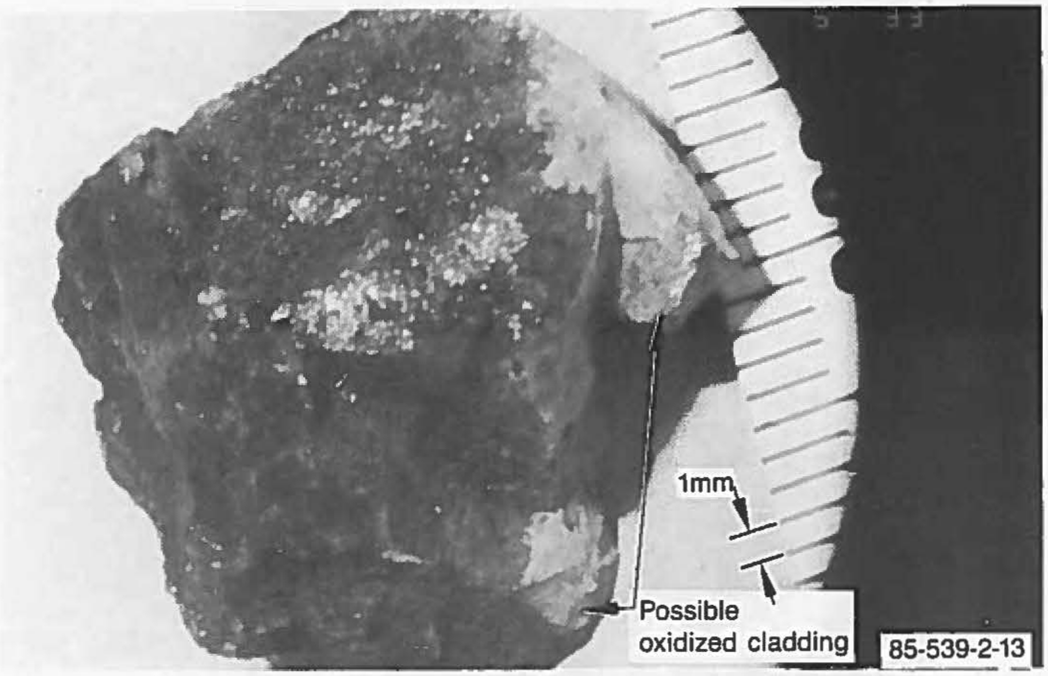

Figure 27. Top and side views of Particle 11-6 that resemble fuel rod segment.

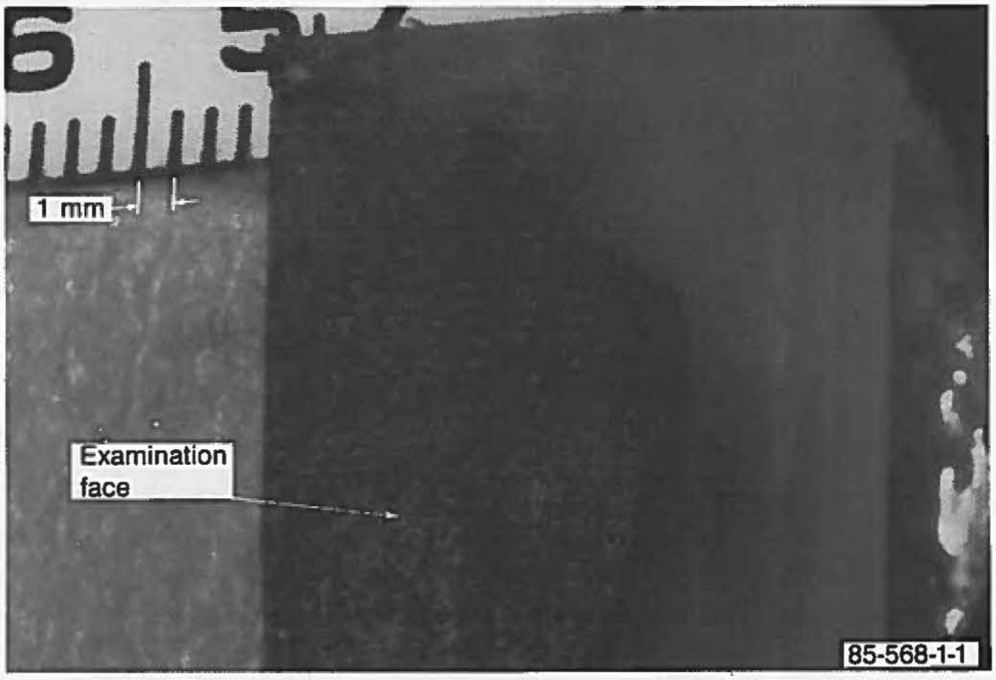

Figure 28. Cross section showing metallographic sample from Particle 11-6.

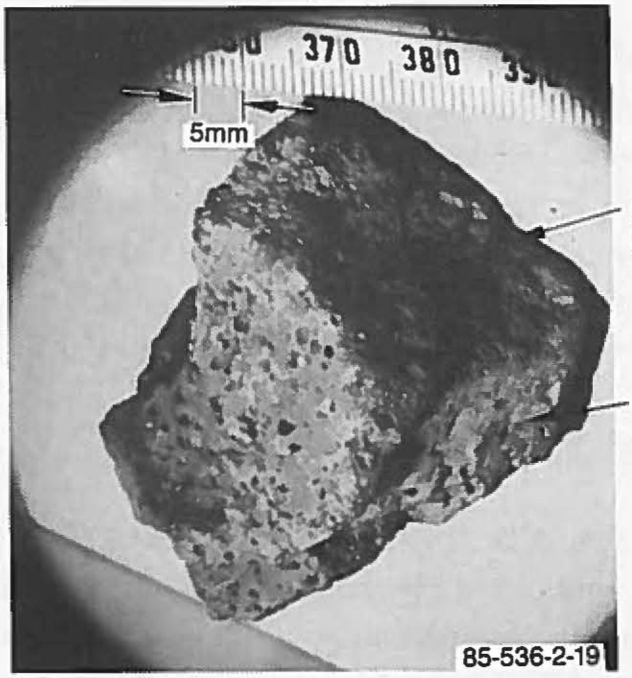

Figure 29. Bottom, back, and side views of Particle 11-7.

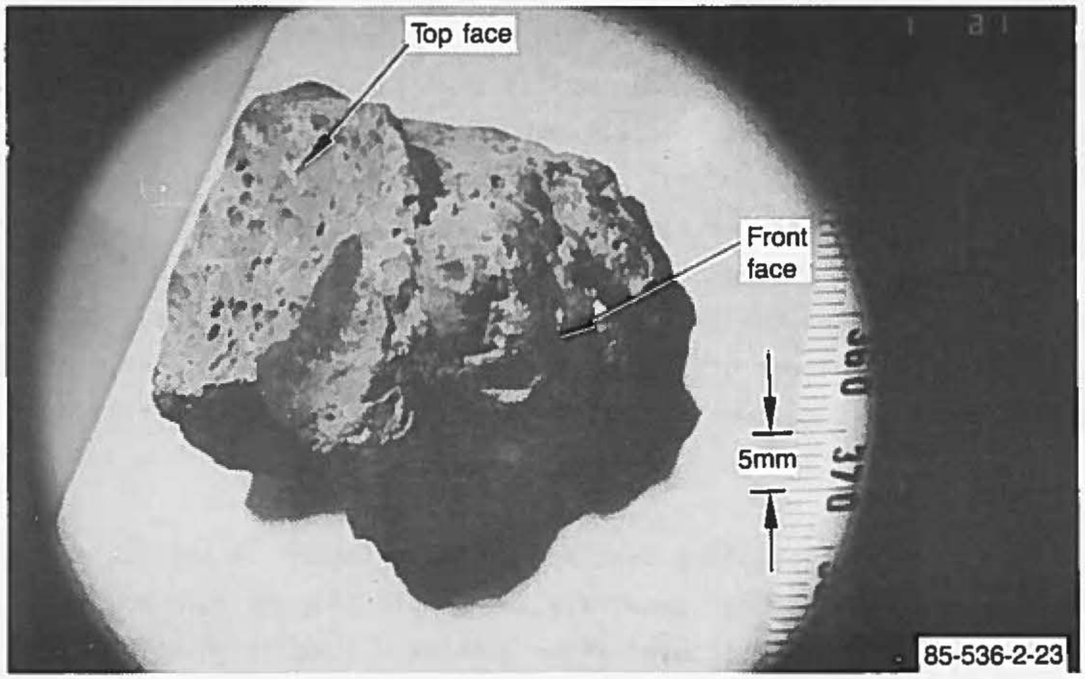

Figure 30. Bottom and front views of Particle 11-7.

Figure 31, which shows the top, side, and partial view of the front of this specimen. The top of this sample also has a saddle. Particle 11-7 was sectioned to obtain metallographic and radiochemical samples. The cut, metallographic section is shown in Figure 32. The saddle at the top is shown in the metallographic section that contains large pores. The metallographic section also shows areas of large pores with no fine pores, intermixed with other areas containing very fine pores.

3.1.3 Cutting and Drilling Tests

In order to provide data for TMI defueling activities, a series of cutting and drilling tests were conducted to provide drilling and cutting rate data using different cutting mediums. The cutting data were obtained during the sectioning of Particles 7-1 and 11-1. The time to cut through a sample was recorded and the area of the cut cross section was measured to calculate the cutting rate. An igneous rock was cut for comparison with the TMI particles. Particles 7-1 and 11-1 were not epoxied so the cutting results would not be compromised by the presence of epoxy. The results of the cutting evaluation are presented in Table 5. For the two TMI samples, the cutting rates were 245 and 285 mm^2/min for Particles 7-1 and 11-1, respectively, compared to 120 mm^2/min for the igneous rock. The cutting rates were twice as fast in TMI samples than in the igneous rock, probably because of the high degree of porosity in the TMI samples.

A section of Particle 11-2 was used for the drilling test. The drill bits were inserted in the chuck of a drill press (Figure 33). A load was placed on the arm of the drill press, which was magnified about 10 times by the mechanical leverage of the drill press. Three types of drill bits were used: a masonry tungsten-carbide bit, a cobalt-steel twist drill, and a diamond core drill.

Results of the drilling test are shown in Figure 34 and Table 6. The cobalt-steel drill did not penetrate the sample (Figure 35); however, slight penetration was achieved after putting a load of 38 kg on the drill bit. Penetration was achieved more by erosion than actual cutting. The carbide masonry bit did penetrate the sample, but the results were poor

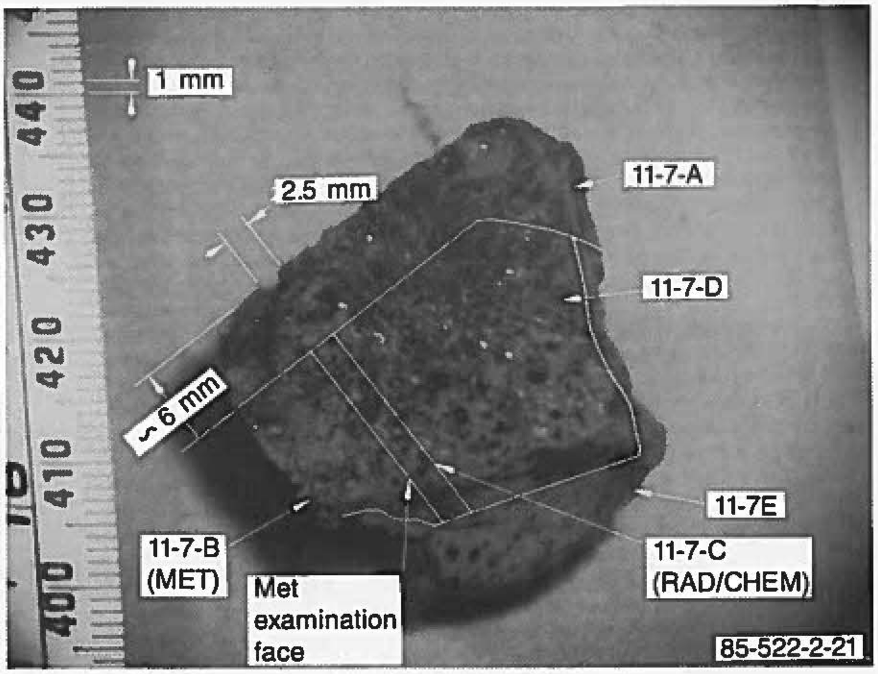

Figure 31. Sectioning diagram for Particle 11-7.

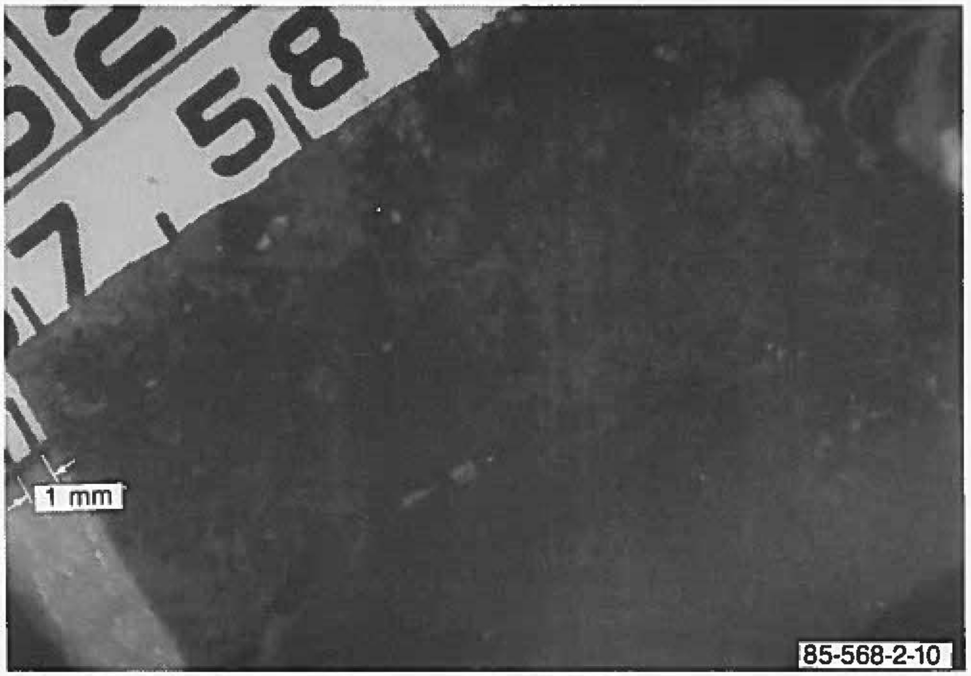

Figure 32. Cross section showing metallographic sample from Particle 11-7.

TABLE 5. DIAMOND CUTTING WHEEL EVALUATION

Particle	Particle Cross-Section (mm^2)	Cutting Time (s)	Cutting Rate (mm^2/min)
7-1	475	100	285
11-1	155	38	245
Lava Rock	300	150	120

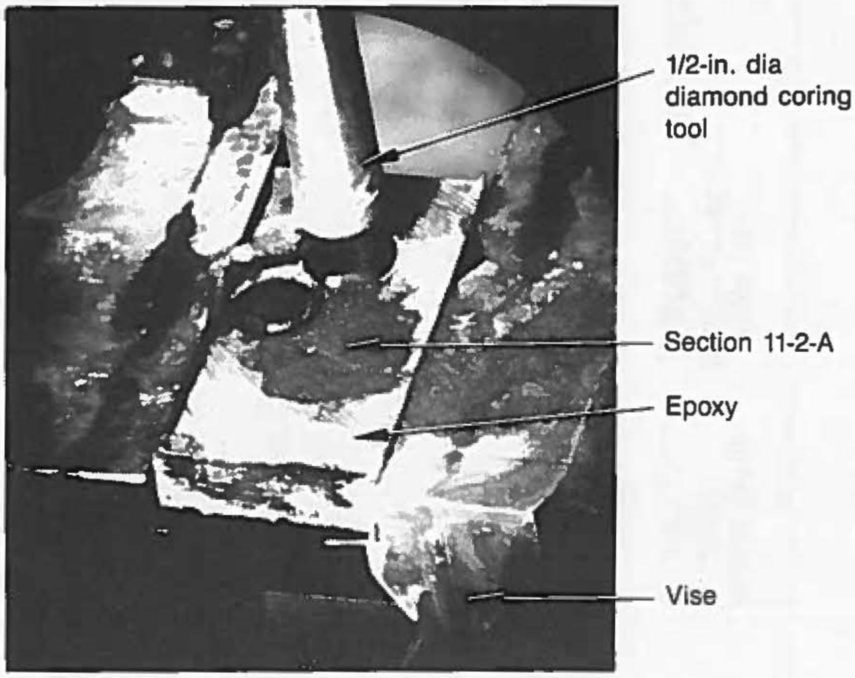

Figure 33. Drilling test set-up.

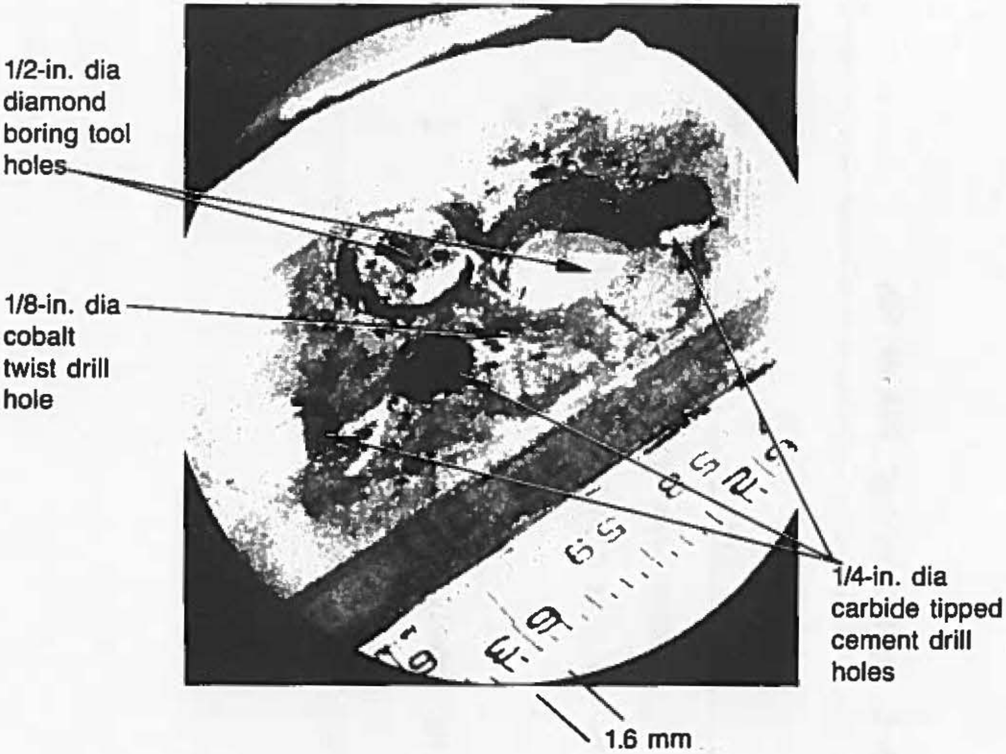

Figure 34. Drilling test specimen from Particle 11-2.

TABLE 6. DRILLING TOOL EVALUATION

Tool	Cut Number	Force (Kg)	Time (s)	Penetration Depth (mm)	Rate of Penetration (mm/min)	Tool Life
1/2 in. Diamond core drill	1	4	75	6.4	5.1	Excellent
1/4 in. Carbide-tipped masonry drill	1	4	30	0	0	--
	2	38	65	10.3	10.3	--
	3A	22	40	~3	~4.5	--
	3B	38	40	~7	11.0	Poor
1/8 in. Cobalt-steel twist drill	1	4	60	0	0	--
	2	22	60	0	0	--
	3	38	60	2.5	--	Failed

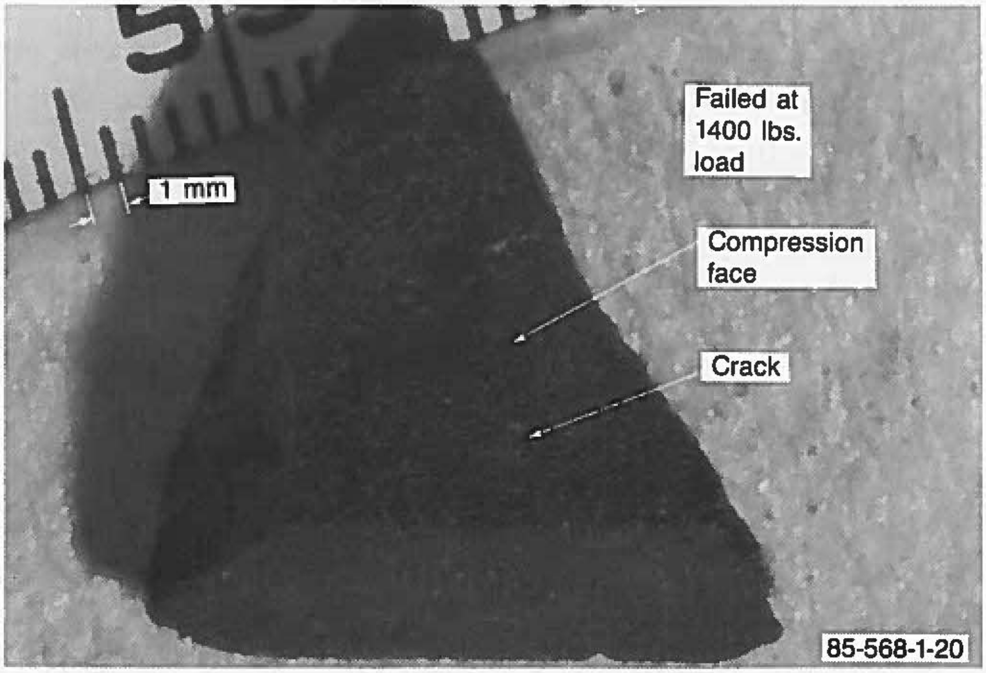

Figure 35. Compression specimen from Particle 7-1.

because of the excessive wear of the tungsten-carbide bit. The best results were achieved with the diamond bit, which produced the greatest penetration with the least wear on the bit. Penetration with the different bits is shown in Figure 34.

3.1.4 Compressive Strength Test

Compression samples were obtained using an unepoxied section from Particle 7-1 and an epoxied section from Particle 11-5 (Figure 36). The section from Particle 7-1 was very irregular in shape and had some cracks and fissures. Because of these cracks, another particle (7-6) was used, though it was irregularly shaped. The compression sample from Particle 11-5 (Figure 36) was cut to remove as much epoxy as possible and obtain a sample without any visual cracks (Figure 37). This sample was cut with the object of forming a rectangular section to acquire data on the relative compressive strength of the debris.

An Instron tensile test machine with a 8890-Nt load cell was used to make the compression-strength measurements. The load as a function of displacement is shown in Figure 38 for these three specimens. The compression specimens from Particle 7-1 and Particle 7-6 failed at 6230 Nt and 756 Nt, respectively; the sample from Particle 11-5 failed at 15,570 Nt. Because the latter sample was regularly shaped, a compressive strength of 111.4 MPa was calculated. Although there are some differences in sample areas, the cracks in Particle 7-1 undoubtedly lowered the failure load. For each of the samples, the samples failed in the direction parallel with the load. The crushed samples are shown in Figures 39 and 40 for the Particle 7-1 and 11-5 test specimens, respectively.

The compressive strength of 111.4 MPa represents material with about 30% porosity.[5] Projection of the 111.4 MPa to a material with 95% of theoretical density yields a compressive strength of 224.5 MPa. This projected value is substantially higher than the fracture strengths of 90 to 100 MPa reported for UO_2 in the literature[6,7]; however, the literature data were obtained by testing urania in tension rather than compression. Consequently, the measured value of 111.4 MPa for ceramic

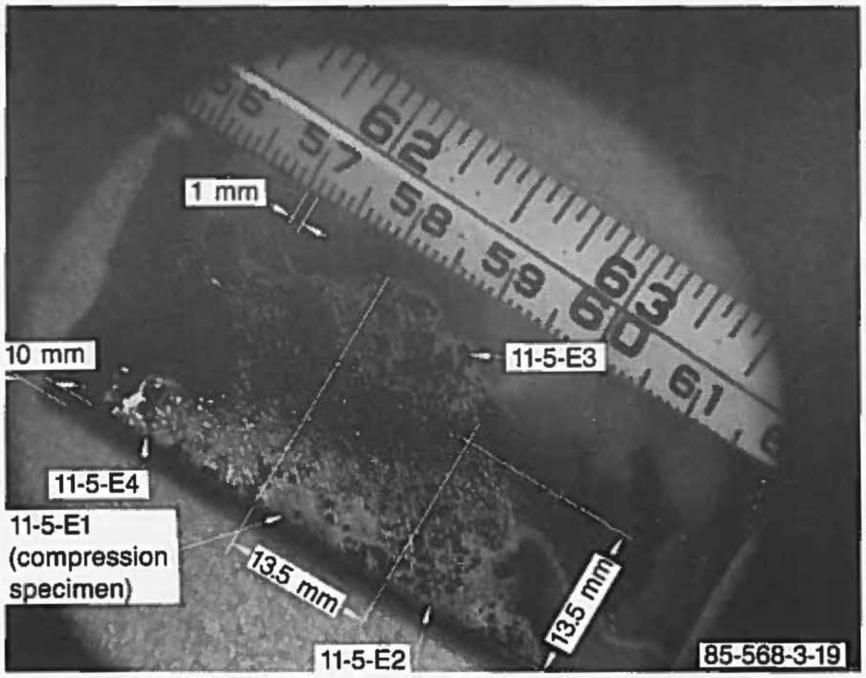

Figure 36. Sectioning diagram for compression test specimen from Section 11-5-E of Particle 11-5.

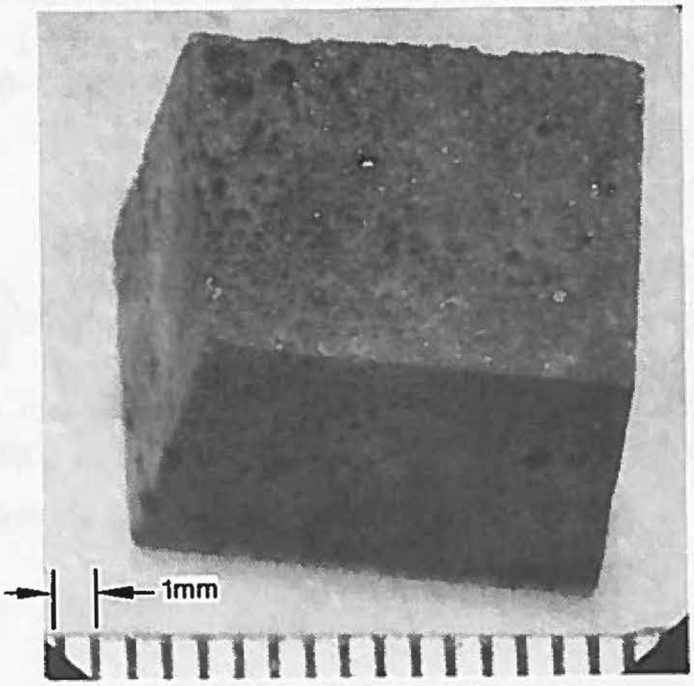

Figure 37. Compression specimen from Particle 11-5.

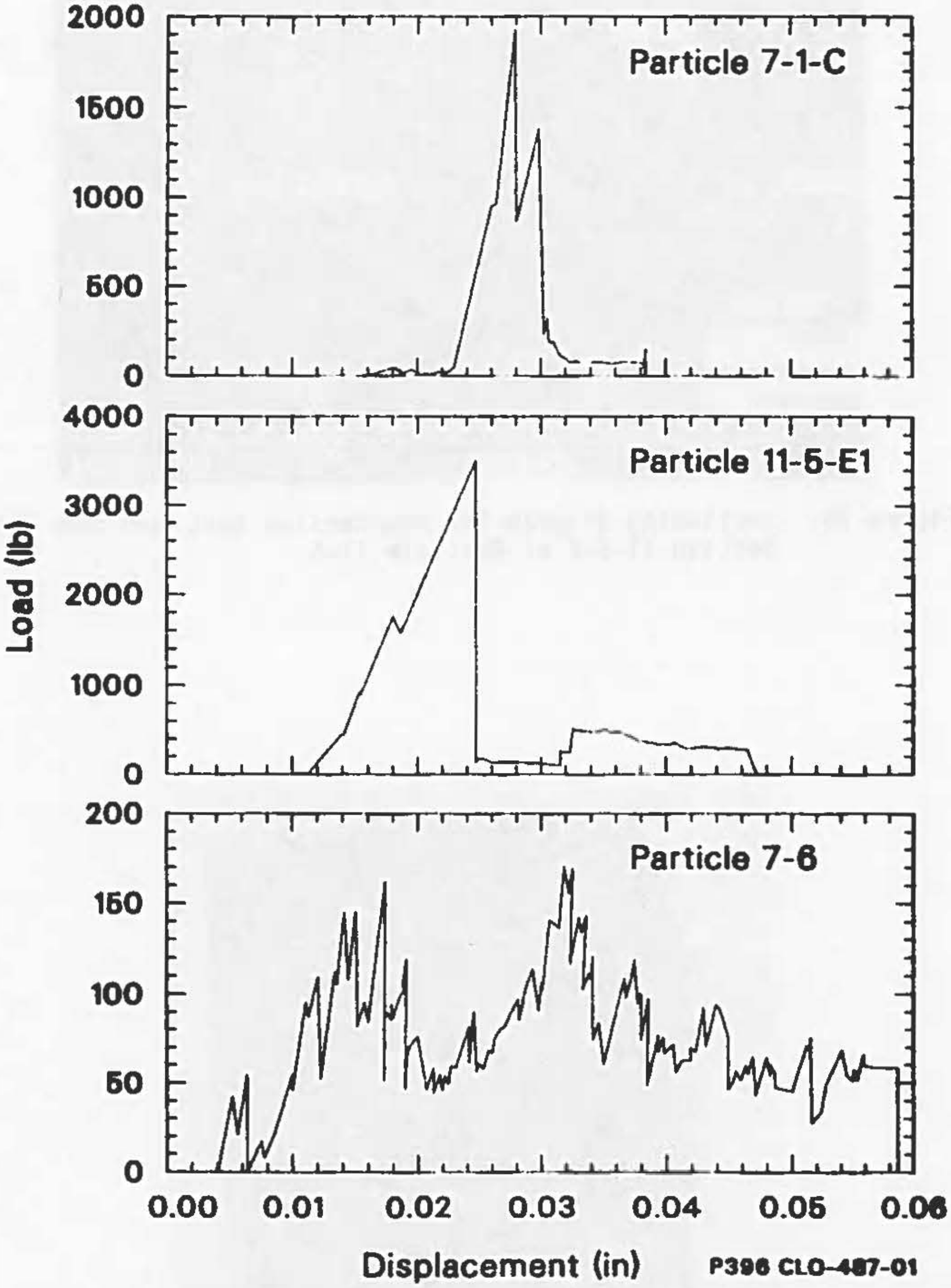

Figure 38. Load as a function of displacement for different compression specimens.

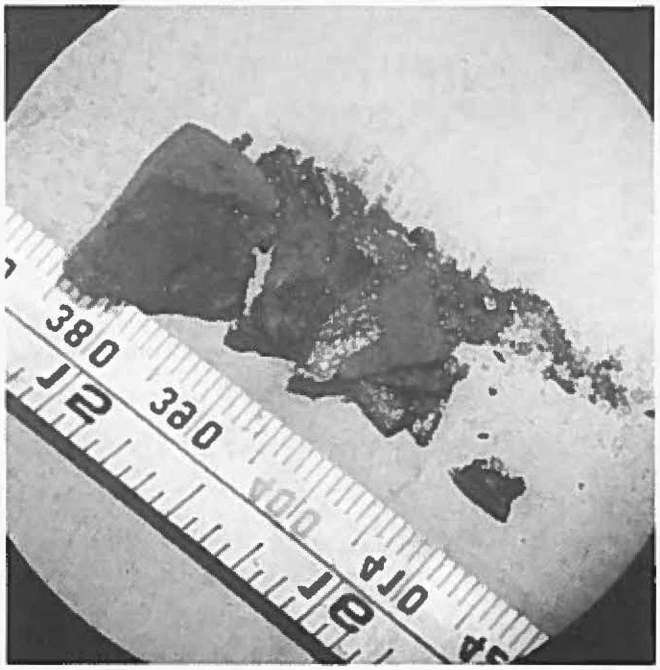

Failed at
1400 lb
load

Figure 39. Fractured remnants after compression testing specimen from Particle 7-1.

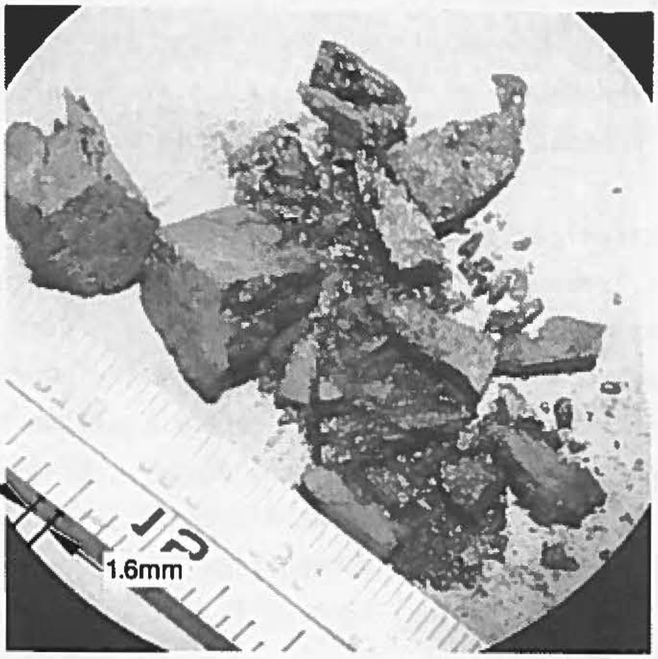

Failed at
3500 lb
load (15,570 Nt)
or Stress 110 MPa

Figure 40. Fractured remnants after compression testing specimen from Particle 11-5.

fuel material with 30% porosity is consistent with the literature, as ceramic materials are noted for higher strengths in compression than in tension.

3.2 Microstructural Characterization

From the general appearance of the metallographic sections, the lower plenum particles consisted of a continuous matrix of ceramic material that had void fractions between 8 and 31% (Figure 41). At a few locations, however, the porosity was as low as a few percent. In most of the particles, the material was essentially all ceramic, containing few metallic inclusions.

Energy-dispersive X-ray (EDX) analysis of all particles generally indicate that the matrix consisted primarily of uranium and zirconium (e.g., Figure 42). The electron microprobe data showed that, in addition to 66.9 wt% U and 15.6 wt% Zr, the matrix contained 0.9 wt% Fe, 0.4 wt% Cr, 0.3 wt% Si, and 0.1 wt% Ni. The undetected material (16.2 wt%) is assumed to be all oxygen. Assuming that all these elements were stoichiometric oxides, then the equivalent composition is 75.9 wt% UO_2, 21.1 wt% ZrO_2, 1.8 wt% FeO, 0.6 wt% Cr_2O_3, 0.7 wt% SiO_2, and 0.2 wt% NiO. The oxygen content has a high degree of uncertainty, as it is calculated based on measured elemental content and assumed chemical form.

In the largest particle extracted from the lower plenum (Particle 11-5), small areas were found where a second or intermediate phase surrounded the primary $(U,Zr)O_2$ grain (Figure 43). Electron microprobe analysis indicated that the composition of the intermediate phase was very similar to that of the matrix, except that the intermediate phase was slightly lower in Zr than the primary phase. The secondary phase may contain more undetected elements (low atomic number) than the primary phase, because the total percentage of elements detected was 97.8 wt%. For example, the Fe may be in the chemical form of Fe_3O_4, which would add more oxygen to the material.

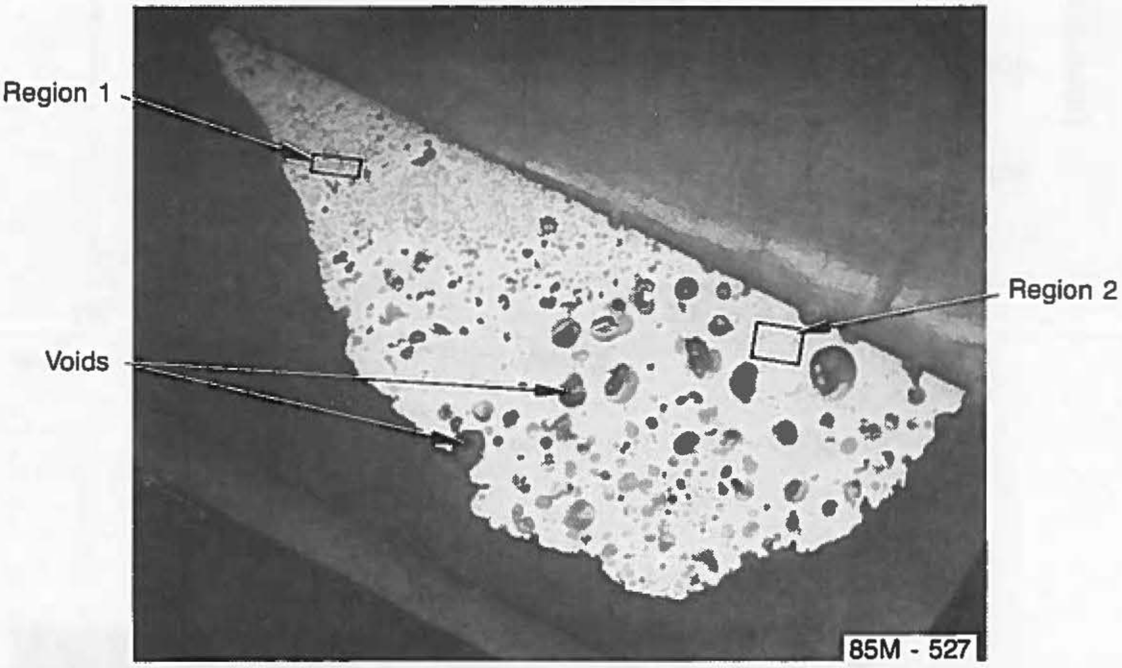

Figure 41. Cross section from Particle 11-2.

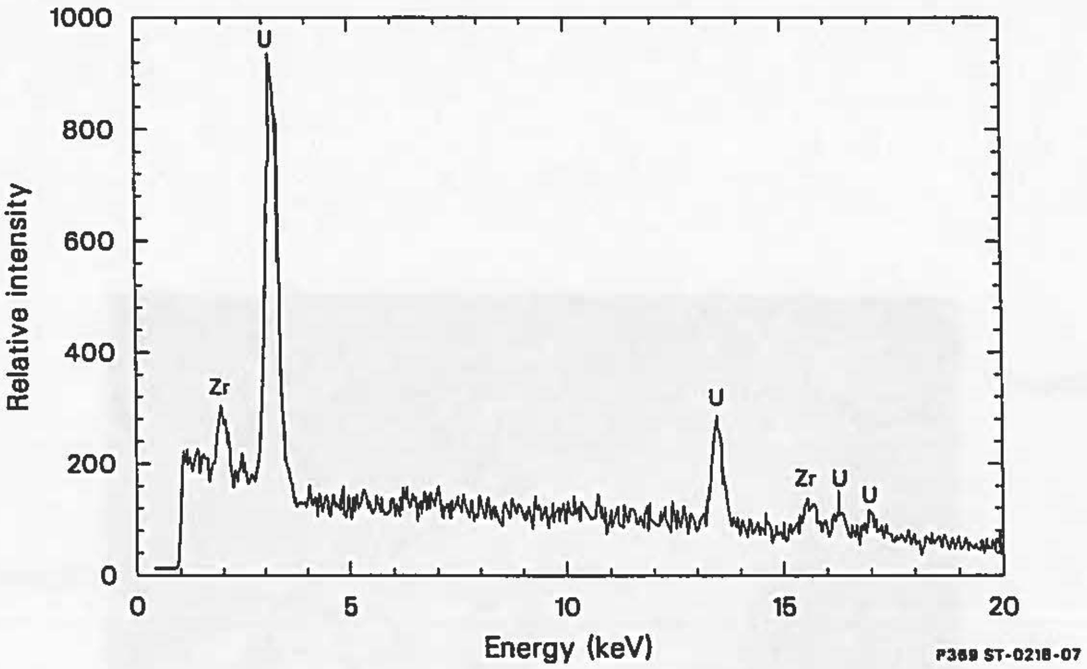

Figure 42. EDX spectra of material in matrix.

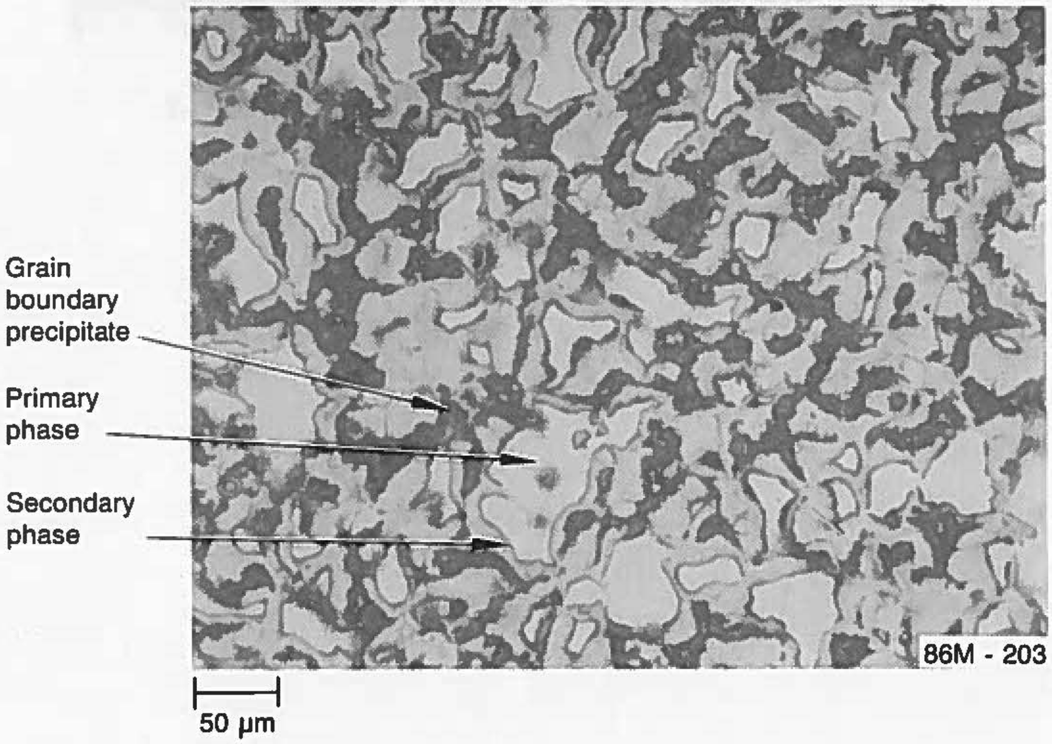

Figure 43. Primary and secondary phases in matrix.

The grain boundaries were generally found to be very broad and exhibited an eutectic structure, as shown in the SEM photographs (Figures 44 and 45). The dark phase in the grain boundaries of all of the samples examined contained Fe and Cr along with variable amounts of Al and Ni (Figure 46).

Electron microprobe data for the grain boundary phase (a ceramic), which contained Al and Ni, showed relatively high concentrations of Cr and Fe, and higher concentrations of Ni than in the matrix. As a ceramic, these constituents would be oxidized. A material balance was not achieved even assuming full oxidation of all constituents, probably because the electron microprobe was not capable of detecting Al. The light spots in the grain boundaries represent a high atomic number and are assumed to be UO_2. If the chemical form of the elements detected were oxides, and the undetected material was Al_2O_3, then a relatively high concentration of Al would have to be present. If the assumption is made that the U and Zr measured are components of the matrix rather than the grain boundary, the upper limit for the composition of the dark phase in the grain boundary would be 26.9 wt% FeO, 28.1 wt% Cr_2O_3, 38.7 wt% Al_2O_3, 4.8 wt% NiO, and 2.0 wt% SiO_2. This Al content was higher than what would be expected based on the Al_2O_3 content in the initial core composition relative to Fe and Cr. These data suggest the presence of other materials in the grain boundaries. Uranium and zirconium were detected but probably were measurable only because the beam extended beyond the grain boundary into the matrix.

An effort was made to locate and determine the composition of any metallic inclusions that were present in the pores (Figure 47). Two small particles, identified by EDX as silver, appeared to be spongy and porous at high magnifications on the SEM. The examination of several other voids indicated no metallic material. A small particle that was dissimilar to the sample matrix was found in a large crack. From EDX analysis, this particle was primarily Zr, but also contained Fe and Cr. It appeared to be fully oxidized (i.e., it did not appear metallic during optical microscopy).

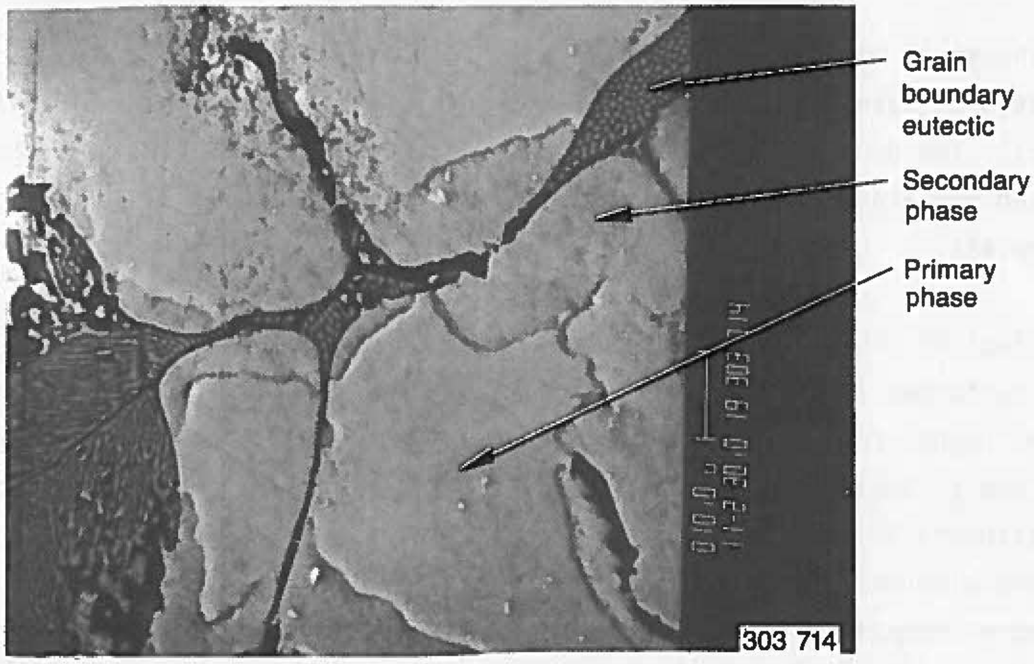

Figure 44. Eutectic structure in grain boundaries with primary secondary phases in matrix.

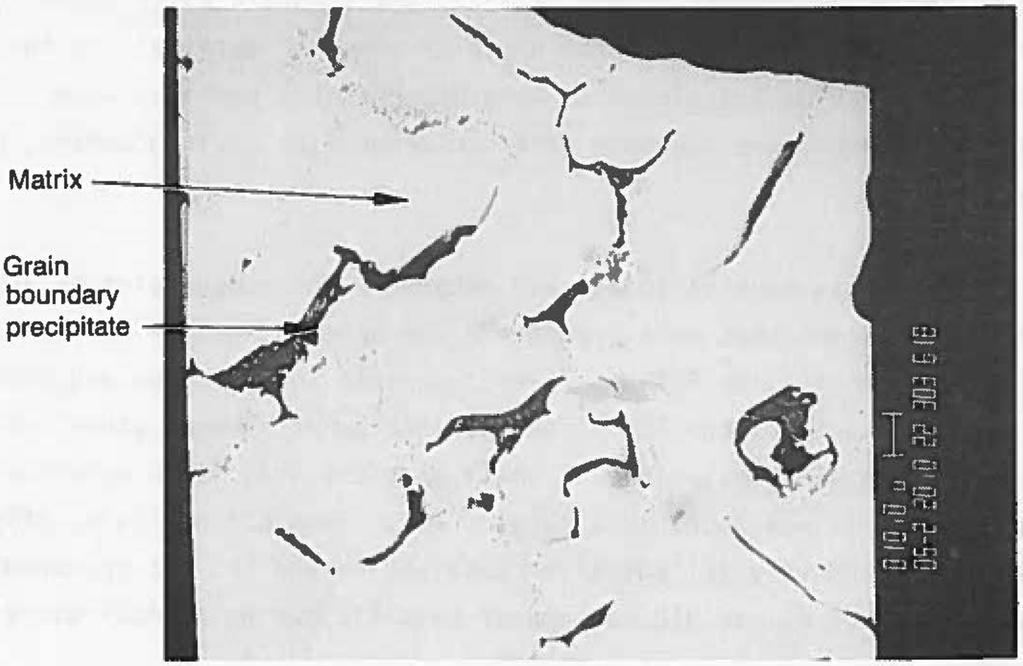

Figure 45. Backscattered electron image of grain boundary precipitates.

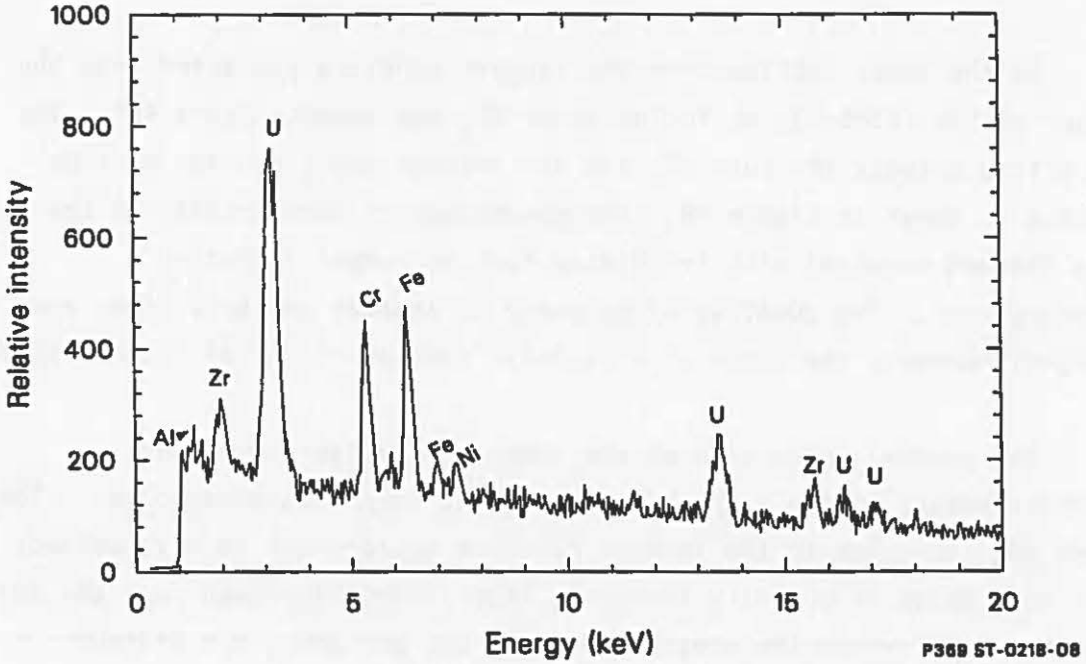

Figure 46. EDX spectra of material in grain boundaries.

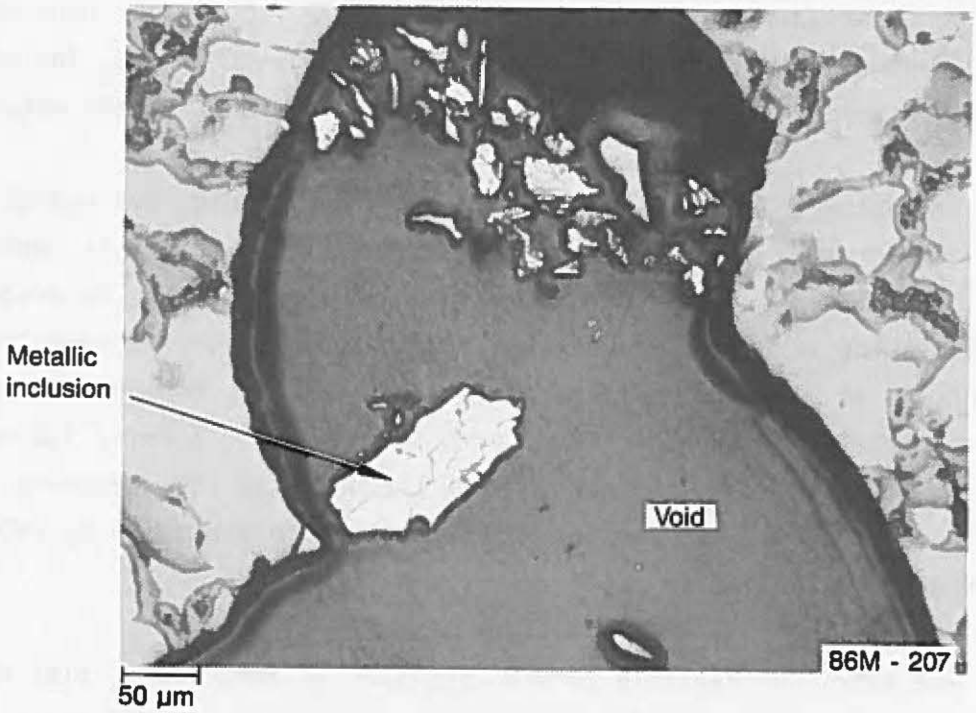

Figure 47. Metallic inclusion in void.

In the cross section from the largest particle extracted from the lower plenum (11-5-C), an inclusion of UO_2 was found (Figure 48). The interface between the pure UD_2 and the uranium and zirconium dioxide matrix is shown in Figure 49. The morphology of the porosity in the matrix has changed compared with irradiated fuel at normal operating temperatures. The quantity of porosity is greater and pore sizes are larger; however, the grain size is still similar to normal irradiated fuel.

The general appearance of the lower plenum debris and the microstructure of the samples indicate that they were once molten. The pure UO_2 inclusion in the largest particle appears not to have melted, but the change in porosity indicates that it may have been near the melting point. Considering the presence of only UO_2 and ZrO_2, the minimum melting temperature would be 2810 K at 65 mole% UO_2 (Figure 50).[4] However, about one percent each of iron and chromium oxides were found in solid solution with the uranium/zirconium mixed oxides and approximately 50 mole% of iron, chromium and nickel oxide were present in the grain boundaries. This composition suggests that the melting point of the grain boundary material could be lower than 2810 K. When iron is present, the melting point is lowered to values between 1573 and 1673 K, depending on the oxygen overpressure. However, the morphology of the UO_2 inclusion indicates temperatures higher than 2810 K for the bulk of the material.

The molten $(U,Zr)O_2$, at some point in time, would have had to come into contact with molten control rod and guide tube materials, which would have been either oxidized or become oxidized after mixing, to produce the quantities of structural constituents measurable in the prior-molten material. An alternative scenario is for the molten control rod and guide tube materials to have interacted with the zircaloy, forming low melting metallic mixtures before reacting with the UO_2, and then becoming oxidized by steam. Fe, Cr, and Ni cannot be oxidized to Fe_3O_4 CrO_2, and NiO by CO_2; steam is required.

The matrix of Particle 11-5-C consisted of large quantities of fuel (UO_2) and zircaloy. The Fe and Cr present in the grain boundaries were

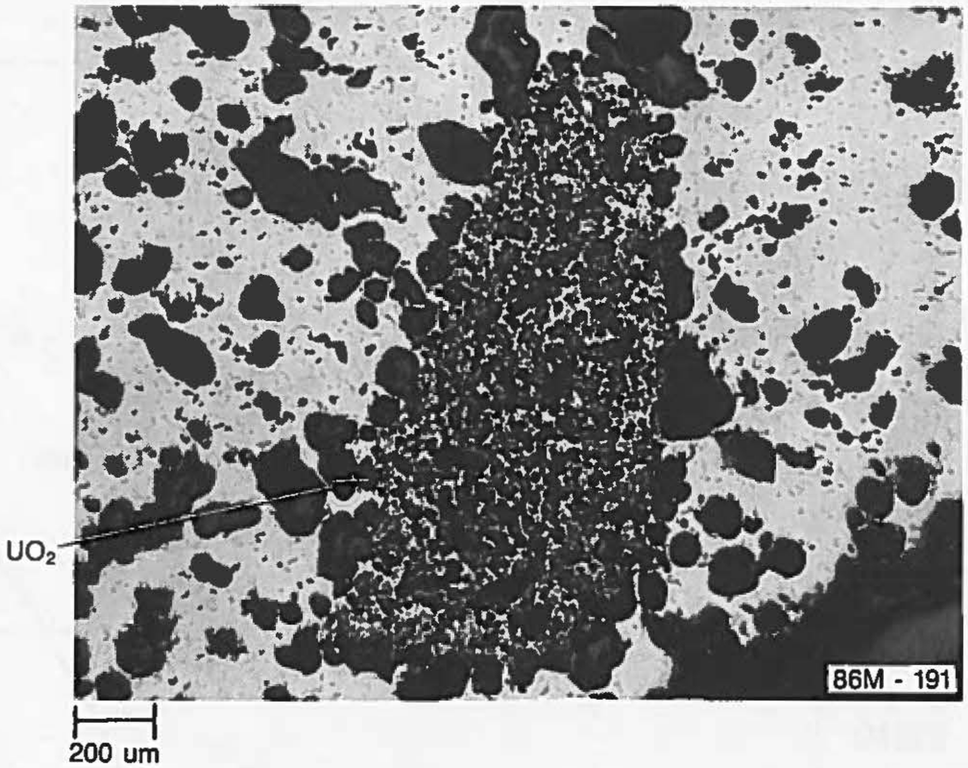

Figure 48. Ceramic inclusion in mixed-oxide matrix.

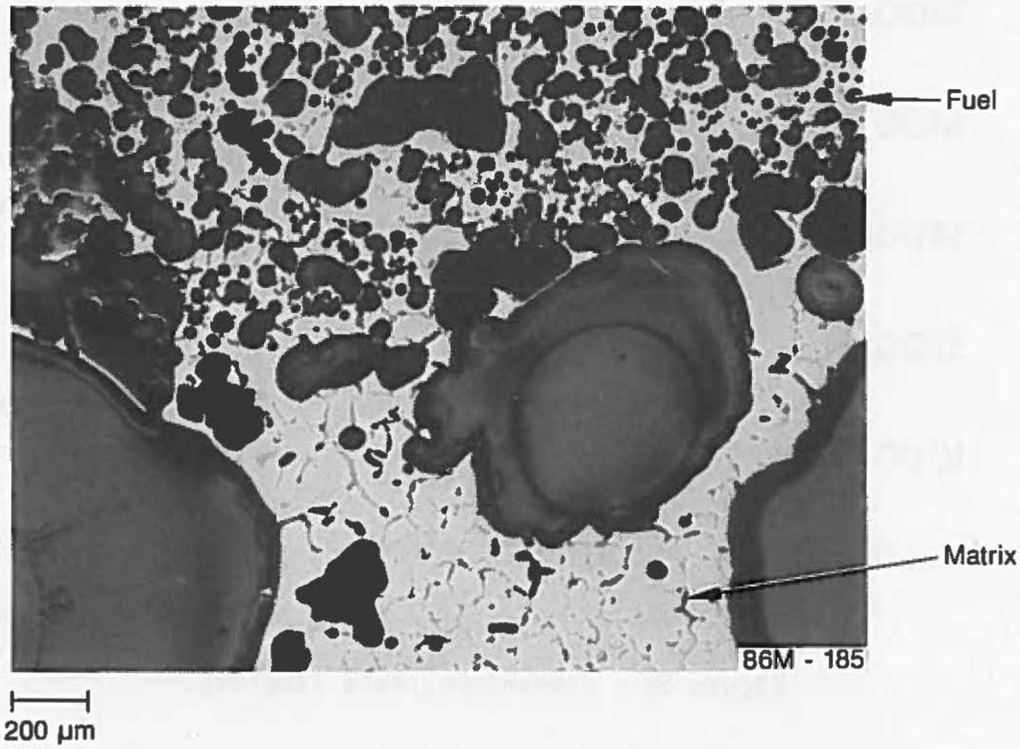

Figure 49. Pore structure of urania pellet.

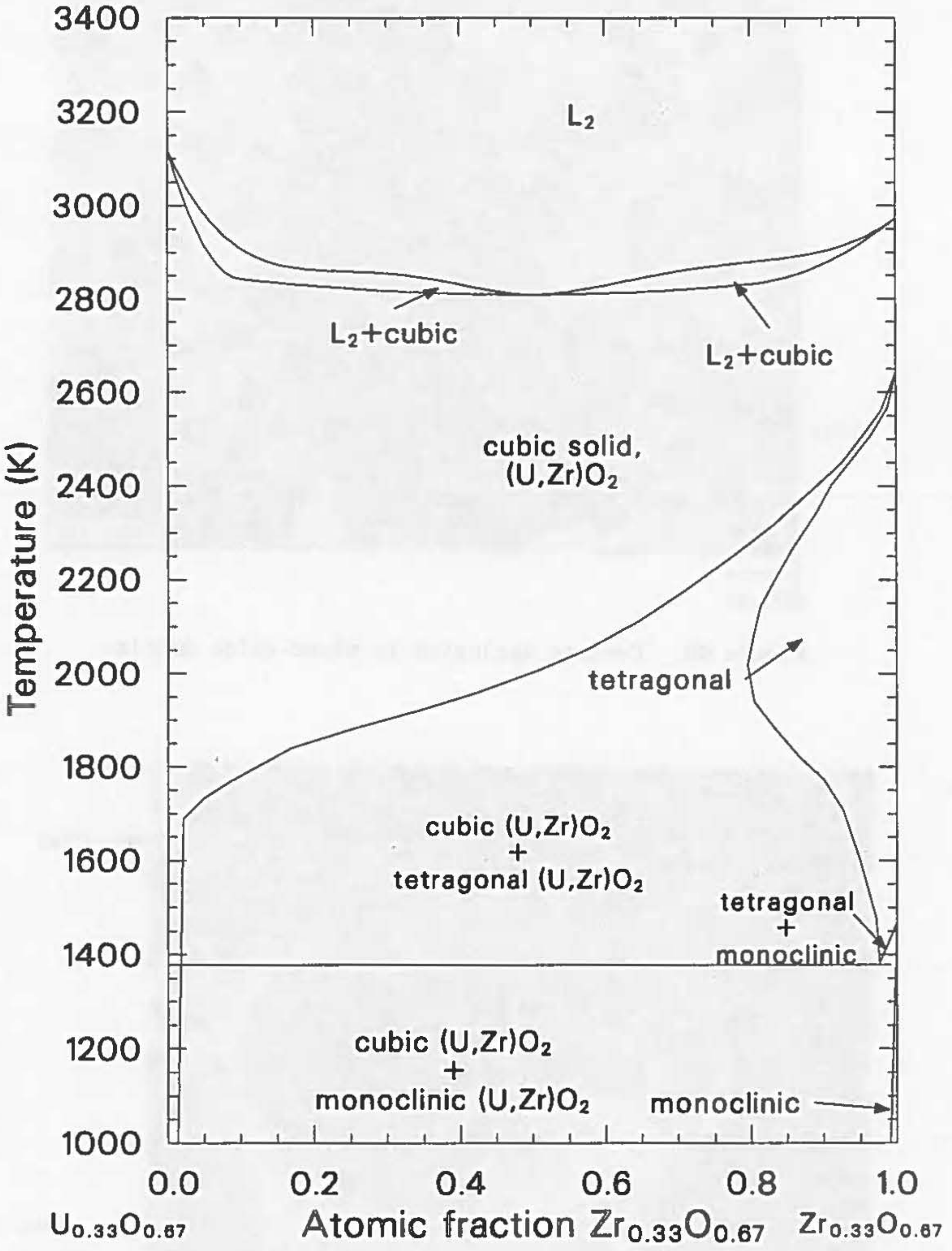

P300 SAP-1285-05

Figure 50. Zirconium-urania isopleth.

present as constituents from the stainless steel or Inconel. The relatively high concentrations of aluminum in the grain boundaries may have come from Al_2O_3 in the form of insulating pellets in thermocouple and instrument leads, and from the Al_2O_3/B_4C control rods.

The microstructures of the lower plenum particles indicate that the debris was cooled from a melt. The higher melting UO_2-ZrO_2 would solidify first; then the solution containing the lower melting structural material oxides (Fe, Cr, and Al) would solidify at the lower temperature.

3.3 Chemical Composition of the Lower Vessel Debris

Elemental analyses were performed on the dissolved lower vessel debris samples for 17 elements that constitute the principal components of the TMI-2 core. For comparison, Table 7[4,8] lists the composition of each of the core constituents. Table 8[4,8] lists the average core composition of the TMI-2 core, including the oxygen content of the uranium, but excluding oxygen that might be present owing to the oxidation of zircaloy and structural materials. After sectioning the particles, the particle cross sections were sampled to provide 20 to 100 mg samples for the chemical and radiochemical analyses. Figures 51 through 55 show the sampling locations for Particles 7-1-B, 11-2-C, 11-4-D, 11-5-C, and 11-6-B, respectively. Particles 11-1-A, 11-1-C, and 11-7-C were sampled only at the center and the edge of each particle. The results are listed in Appendix E. The sampling locations were chosen to characterize possible differences in chemical and radiochemical composition as a function of distance from the center of the particle. The elemental analysis results for the 37 samples obtained from the 7 particles (as identified in Table 1) are listed in Appendix E. These analyses were performed at the Hanford Engineering Development Laboratory (HEDL) on samples prepared at the INEL, using inductively coupled plasma (ICP) spectroscopy.[9]

Table 9 lists the average composition of each particle analyzed. These data are used to compare with the original composition and elemental distribution in the reactor core. Evaluation of the elemental analysis

TABLE 7. TMI-2 REACTOR CORE AND CONTROL ROD FUEL ASSEMBLY COMPOSITION

Material (Weight)	Element	Weight Percent	Material (Weight)	Element	Weight Percent
UO_2	U-235[a]	2.265	Inconel-718	Ni[a]	51.900
(94,029 kg)[8]	U-238[a]	85.882	(1,211 kg)	Cr[a]	19.000
(531.9 kg)[b]	O	11.853	(6.8 kg)[b]	Fe[a]	18.000
				Nb	5.553
Zircaloy-4	Zr[a]	97.907		Mo	3.000
(23,177 kg)[8]	Sn[a]	1.60		Ti	0.800
(125 kg)[b]	Fe[a]	0.225		Al[a]	0.600
	Cr[a]	0.125		Co	0.470
	O	0.095		Si[a]	0.200
	C	0.0120		Mn[a]	0.200
	N	0.0080		N	0.130
	Hf	0.0078		Cu[a]	0.100
	S	0.0035		C	0.040
	Al[a]	0.0024		S	0.007
	Ti	0.0020			
	V	0.0020	Ag-In-Cd	Ag[a]	80.0
	Mn[a]	0.0020	(2,749 kg)	In[a]	15.0
	Ni[a]	0.0020	(43.6 kg)[b]	Cd[a]	5.0
	Cu[a]	0.0020			
	W	0.0020	B_4C-Al_2O_3	Al[a]	34.33
	H	0.0013	(626 kg)	O	30.53
	Co	0.0010	(0 kg)[b]	B	27.50
	B[a]	0.000033		C	7.64
	Cd[a]	0.000025			
	U[a]	0.000020	Gd_2O_3-UO_2	Gd[a]	10.27
			(131.5 kg)	U	77.72
Type 304	Fe[a]	68.635	(0 kg)[b]	O	12.01
Stainless	Cr[a]	19.000			
Steel	Ni[a]	9.000			
(676 kg) and	Mn[a]	2.000			
Unidentified	Si[a]	1.000			
Stainless	N	0.130			
Steel	C	0.080			
(3,960 kg)	Co	0.080			
(16.8 kg)[b]	P	0.045			
	S	0.030			

---

a. Elements for which ICP analysis was performed.
b. Weight of material in a control rod fuel assembly.

TABLE 8. TMI-2 CORE COMPOSITION BY ELEMENTAL WEIGHT PERCENT

	Core Composition	
Element	Excluding Oxygen (wt%)	Including Oxygen[a] (wt%)
U	71.94	65.8
Zr	19.70	18.0
O	--	8.5
Fe	3.28	3.0
Ag	1.91	1.8
Cr	1.09	1.0
Ni	0.99	0.9
In	0.35	0.3
Sn	0.35	0.3
Al	0.19	0.2
B	0.15	0.1
Cd	0.12	0.1
Mn	0.10	0.08
Nb	0.05	0.04
Si	0.04	0.04
C	0.04	0.04
Mo	0.03	0.03
Gd	0.01	0.01
Ti	0.01	0.01
N	0.01	0.01
Co	0.01	0.01

---

a. Oxygen content of 11.8 wt% for the uranium (UO_2)is assumed.

Additional oxygen content may range from 4 to 7%, depending on the degree of oxidation of the zircaloy and structural materials.

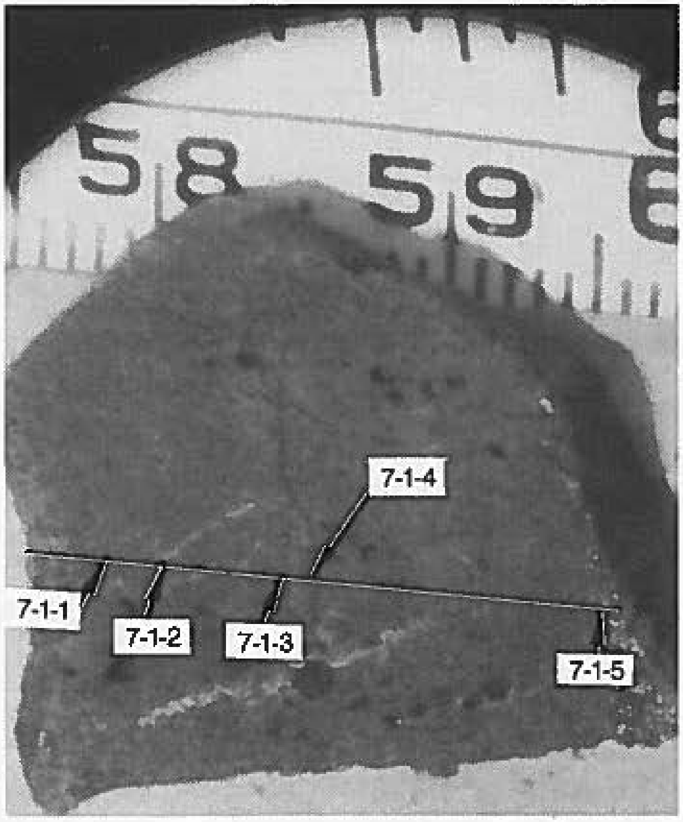

Figure 51. Sample locations for Particle 7-1-B.

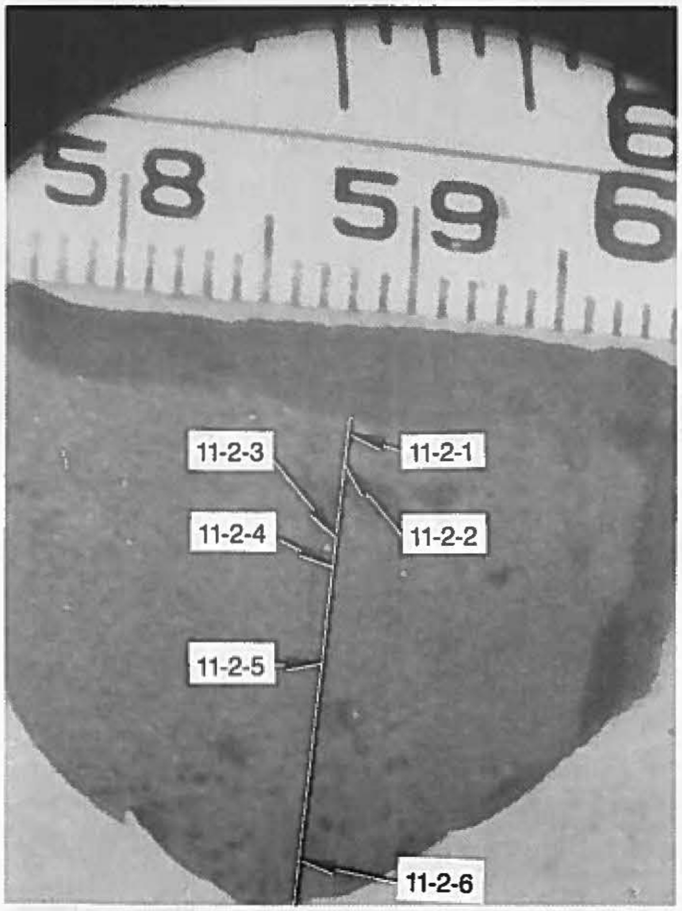

Figure 52. Sample locations for Particle 11-2-C.

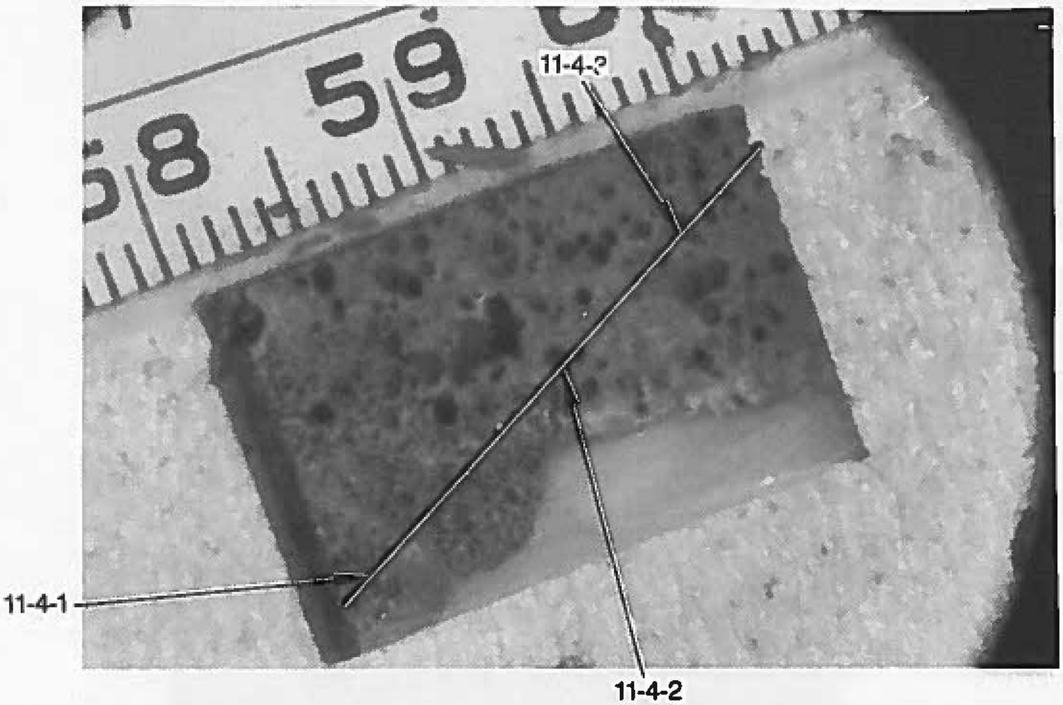

Figure 53. Sample locations for Particle 11-4-D.

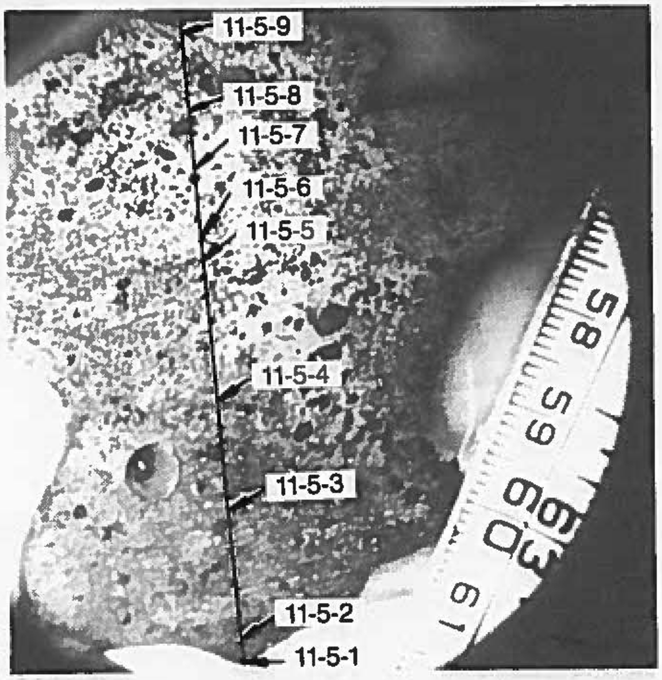

Figure 54. Sample locations for Particle 11-5-C.

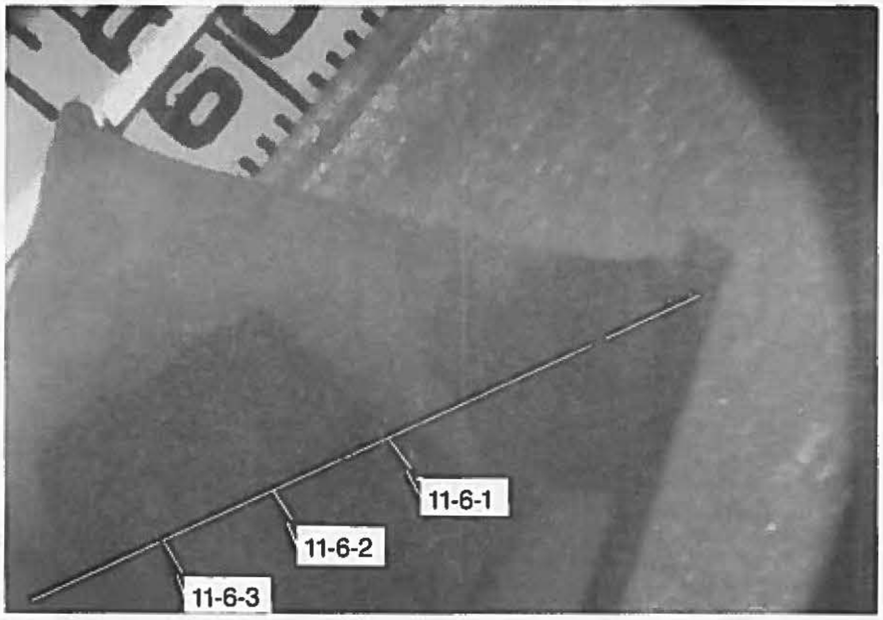

Figure 55. Sample locations for Particle 11-6-B.

TABLE 9. AVERAGE ELEMENTAL CONTENT OF THE LOWER VESSEL DEBRIS

	Average Elemental Concentration for Each Particle (wt%)								
Core Component/Element	7-1-B	11-1-A	11-1-C	11-2-C	11-4-B	11-4-D	11-5-C	11-6-B	11-7-C
Fuel									
U	6.53 E+1	6.68 E+1	6.42 E+1	6.32 E+1	6.51 E+1	6.56 E+1	6.40 E+1	6.95 E+1	6.23 E+1
Zr	1.20 E+1	1.28 E+1	1.30 E+1	1.29 E+1	1.50 E+1	1.21 E+1	1.22 E+1	1.17 E+1	1.26 E+1
Sn	--[a]	--[a]	--[a]	--[a]	--[a]	--[a]	--[a]	--[a]	--[a]
Control Rod									
Ag	2.2 E-1[b]	--[a]	--[a]	--[a]	--[a]	--[a]	--[a]	--[a]	--[a]
In	--[a]	--[a]	--[a]	--[a]	--[a]	--[a]	--[a]	--[a]	--[a]
Cd	--[a]	--[a]	--[a]	2.5 E-2[b]	--[a]	--[a]	--[a]	--[a]	6.5 E-2[b]
Burnable Poison Rod									
Al	--[c]	--[c]	--[c]	--[c]	--[c]	--[c]	--[c]	--[c]	--[c]
B	9.4 E-2	1.2 E-1	--[a]	7.1 E-2	6.6 E-2	1.2 E-1[b]	7.7 E-2	3.6 E-1[b]	9.6 E-2
Gd	--[a]	--[a]	--[a]	--[a]	--[a]	--[a]	--[a]	--[a]	--[a]
Structural Material									
Fe	2.4	1.88	2.28	2.48	2.90	3.70	2.04	1.83	2.41
Cr	9.5 E-1	5.9 E-1	6.0 E-1	7.9 E-1	9.9 E-1	9.6 E-1	6.5 E-1	5.8 E-1	6.1 E-1
Ni	--[a]	--[a]	2.4 E-1[b]	--[a]	2.6 E-1[b]	--[a]	2.0 E-1[b]	--[a]	2.4 E-1[b]
Mn	--[a]	8.7 E-2	--[a]	6.8 E-2[b]	8.5 E-2	8.9 E-2	6.5 E-2[b]	6.8 E-2	6.2 E-2[b]
Nb	--[a]	--[a]	--[a]	--[a]	--[a]	--[a]	--[a]	--[a]	--[a]
Si	--[c]	--[c]	--[c]	--[c]	--[c]	--[c]	--[c]	--[c]	--[c]

TABLE 9. (continued)

	Average Elemental Concentration for Each Particle (wt%)								
Core Component/Element	7-1-B	11-1-A	11-1-C	11-2-C	11-4-B	11-4-D	11-5-C	11-6-B	11-7-C
Structural Material									
Mo	1.4 E-1	1.9 E-1	1.2 E-1[b]	9.3 E-2[b]	1.3 E-1	2.1 E-1	1.1 E-1[b]	2.1 E-1[b]	1.2 E-1
Cu	4.6 E-1[b]	--[a]	--[a]	2.1 E-1[b]	--[a]	--[a]	--[a]	--[a]	--[a]
Total wt% of Sample	81	82	80	80	84	84	81	84	80

---

a. Below detectable concentrations.

b. Some elemental concentrations for this particle were below the detection limit. They have not been included in the listed value.

c. Results are not included as the samples were contaminated with these elements during dissolution or handling.

results is divided into characterization of the constituents of the four principal groups of materials present in the core: (a) uranium fuel and zircaloy cladding, (b) Ag-In-Cd control rod materials, (c) neutron poisons ($B_4C-Al_2O_3$ and $Gd_2O_3-UO_2$), and (d) structural materials (stainless steel and Inconel).

3.3.1 Uranium Fuel and Zircaloy Cladding

The average fuel material concentrations listed in Table 9 indicate a narrow range of U and Zr compositions for all particles. The lowest U concentration measured was 62.3 wt%; the highest was 72.2 wt%, with an average for all samples of 65.0 wt%. For Zr, the lowest concentration measured was 10.7 wt%; the highest was 15.6 wt%, with an average of 12.6 wt%. Tin, the other principal component of the cladding, was not measurable. These data indicate that the lower vessel debris is relatively homogeneous and that U and Zr are the two principal components of the debris.

The core average concentrations of U and Zr are expected to be about 65 and 18 wt%, respectively (Table 8) excluding oxidation of the zircaloy and structural materials. The average measured concentration for U is 65 wt%, which is approximately the expected concentration (65.8 wt%); however, the average measured Zr concentration is 12.5 wt%. This difference is probably due to the oxidation of the zircaloy cladding, which would reduce the total amount of Zr present relative to the U content. It should be noted that the uncertainty associated with this analysis is 10 to 15%.

Total oxygen content of the debris, assuming 65 wt% U and 18 wt% Zr and stoichiometric oxidation, would be 14 to 16 wt%. Consequently, if the total measured material contents listed in Table 9 (~79.8 to 84.5 wt% per sample) have oxygen added based on the actual composition of the samples and in the appropriate amounts to oxidize U, Zr, and some structural material, the data indicate that within the uncertainty of the measurements (~15%) all material in the samples has been accounted for by the ICP analysis.

A comparison of the average Zr/U ratio expected in the core (0.28) and the average measured ratio in the debris (0.19) would suggest that the Zr is not evenly in the debris and that there may be Zr accumulations; however, the effects of zircaloy oxidation make this uncertain.

3.3.2 Ag-In-Cd Control Rod Materials

Inspection of Table 9 indicates that the control rod materials were not measurable in the lower vessel debris, with the exception of Particle 7-1-B, where Ag was measurable at 0.22 wt% near the center of the particle. This is substantially less than the expected average concentration of Ag in the core (1.6 wt%). The ICP detection limit for Ag in these samples is 0.2 to 0.4 wt%, which suggests that Ag has not been evenly distributed in the core debris as compared to the core average distribution. No measurable amounts of Ag were found in the samples taken from the surface or near the surface of any particle, suggesting that surface deposition of control rod materials is also insignificant.

Cadmium was measurable at two locations in the lower vessel debris; near the center of Particle 11-2-C and near the surface of Particle 11-7-C. The measured concentrations of Cd are near the detection limit of the ICP analysis, and are substantially below the expected core average concentration of 0.1 wt%. The data suggest that Cd has been depleted below the core average concentration in this part of the reactor core.

Indium was not measurable in the lower vessel debris, however, the ICP detection limit for this element is 2 to 4 wt%, which is above the expected core average concentration.

3.3.3 Poison Materials

The neutron poisons present in the TMI-2 core consist of material from the two types of burnable poison rods and the substantial amounts of boron present in the reactor coolant. The two types of burnable poison rods are boron carbide/alumina rods, and gadolinia rods (10.3 kg Gd). Of the two possible poisons (B and Gd) in the TMI-2 reactor, only boron was found in measurable concentrations (0.07 to 0.36 wt%). Identifying the source of the boron, either from the coolant or poison rods, was not possible. The data do indicate, however, that the boron poison is deposited at a relatively constant concentration evenly through the interior of the particles.

3.3.4 Structural Material

The structural material concentrations listed in Table 9 indicate that substantial amounts of structural material have been retained in the prior-molten material. The structural material with the highest concentration is Fe. This element has relatively constant concentrations, ranging from 1.8 to 3.7 wt%. The expected concentration of Fe, if all in-core structural material were evenly incorporated into the core mass, would be 2.7 wt%. These data suggest that the expected amounts of Fe are retained in the prior-molten material. Also, there is no evidence of significant gradients within, or concentrations of Fe on, the surface of the particles, which suggests that the Fe was distributed in the particles when the debris was molten.

The average concentration of Cr in the core would be expected to be 0.9 wt%, if all core materials were evenly distributed in the mass. The lower vessel debris data indicate concentrations ranging from the 0.6 to 1.0 wt%, which indicates that Cr is present in the lower vessel debris in the expected concentrations. For most particles, there is no evidence of concentration gradients; however, for Particle 11-5-C, there is a generally consistent increase in the concentration of Cr of approximately a factor of four from sample locations 1 to 9. This increase in concentration may be related to the porosity of the debris.

The Ni concentrations measured in the lower vessel debris range from 0.2 to 0.26 wt% where this element was measurable (~50% of the samples, as shown in Table 9). However, the detection limit for this element is from 0.08 to 2.0 wt%, indicating that the measurable quantities are near the detection limit, which is near the expected average concentration in the core (0.8 wt%).

The concentration of manganese measurable at most sample locations ranged from 0.06 to 0.09 wt%. This compares with an expected average concentration of 0.08 wt%, suggesting similarity to those observed for Cr and Fe.

Molybdenum was measurable at most sample locations at concentrations higher than the expected core average concentration of 0.03 wt%. The measured concentrations range from 0.09 to 0.14 wt%, which suggests, as would be expected, that some of the structural material present in the lower vessel debris is Inconel 718 from the spacer grids, as there is no Mo present in 304 stainless steel. In a full-length fuel assembly, there is 15.1 kg of 304 stainless steel, mostly in the cladding of the control rods and 6.8 kg of Inconel. The measured concentration indicates that although there is more than expected amounts of Mo from the Inconel 718, there is probably a substantial fraction of 304 stainless steel also present.

Copper was measurable in samples from Particles 7-1-B and 11-2-C at concentrations ranging from 0.2 to 0.7 wt%; however, this element is a minor constituent of Inconel and makes up only about 0.001 wt% of the expected core mass. The presence of this element at the listed concentrations would suggest that this element is present as accumulations in the lower vessel.

3.4 Radiochemical Composition of the Lower Vessel Debris

Analyses to characterize the radiochemical composition of the lower vessel debris were performed at ANL-E and INEL. Results of the autoradiography analyses performed at ANL-E[9] are discussed first, as they provide the best initial indication of the gross distribution of radioactivity in the samples. These data are followed by results of the radiochemical analyses performed at INEL, and by a comparison of the measured fission product concentrations in the lower vessel debris with the expected concentrations for intact fuel as determined from ORIGEN2.[10]

3.4.1 Autoradiography Results

Figures 56 through 60 show SEM mosaic photographs and beta-gamma autoradiographs of Particles 11-2-B1, 11-4-C, 11-5-B1, 11-6-A, and 11-7-B1. The light areas in the autoradiographs indicate locations of higher activity. These autoradiographs were obtained by pressing a prepared plane surface of the sample against photographic film (KODAK high resolution, ESTAR thick-base safety film). A planar surface is necessary because surface irregularities can cause false indications of the presence of activity in the radiograph. The effect of surface irregularities on the distribution of activity in the autoradiographs is indicated by apparent regions of higher activity in hairline cracks that were generated during handling.

Examination of the autoradiographs indicates that there are apparent high levels of activity associated with the grain boundaries, particularly around some void regions, and with the voids themselves. Some indications of higher activity are due to surface irregularities. However, the apparent high activities at the grain boundaries and at the smaller voids would suggest that there is, in fact, substantial amounts of activity located at some grain boundaries and in some voids within the samples.

Personnel at ANL-E have suggested,[10,11] based on qualitative measurements, that the apparent activity at some of the grain bounddue to the presence of the activation product Co-60, which would be expected to be present in the grain boundaries as part of the dendritic structural material observed in the metallurgical examinations. It is important to note that the deposition of activity at the grain boundaries is not apparent throughout the particles and tends to be concentrated near some void regions.

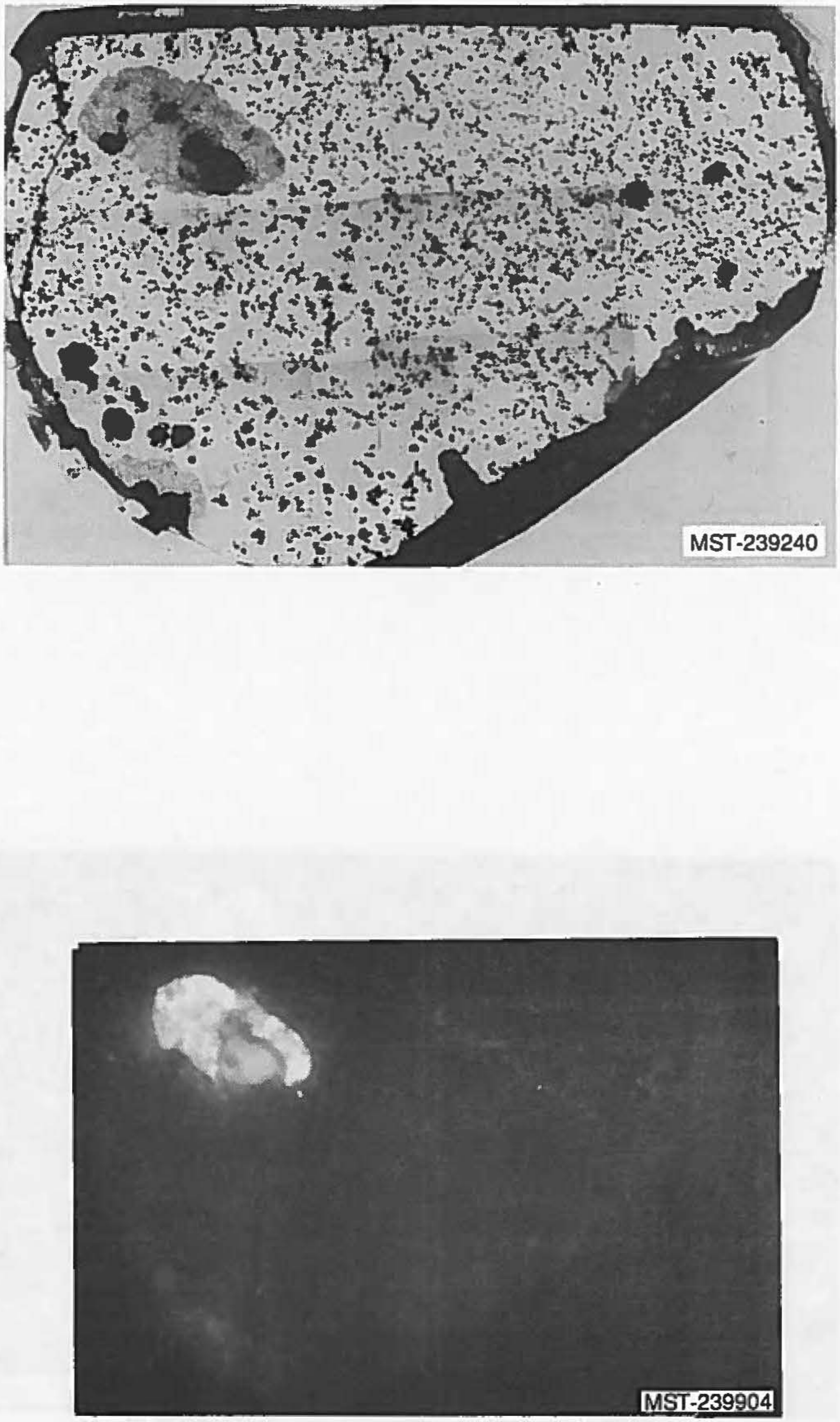

Figure 56. SEM mosaic photograph and autoradiograph for Particle 11-2-B.

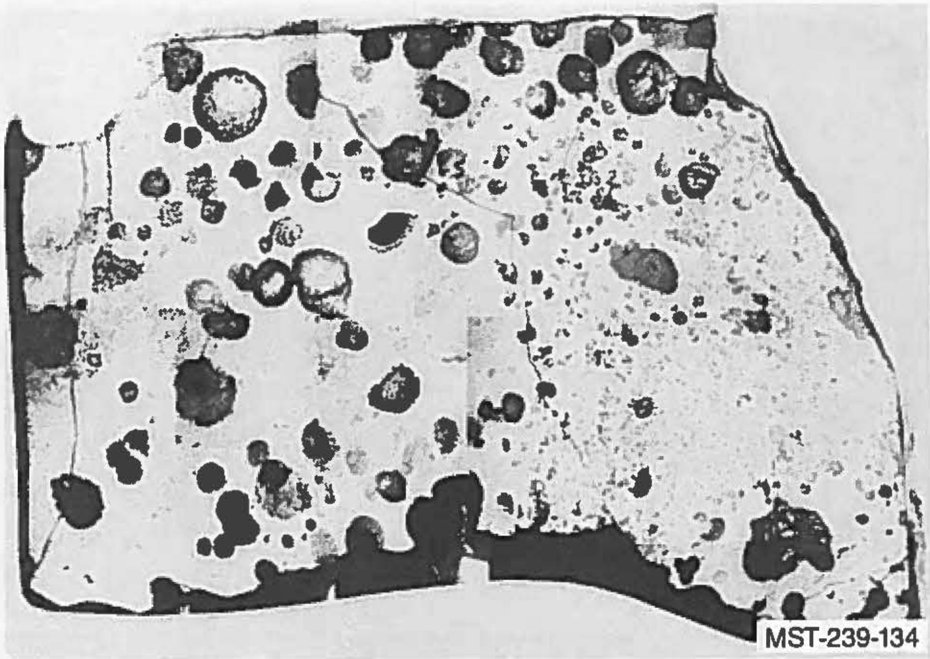

Figure 57. SEM mosaic photograph and autoradiograph for Particle 11-4-C.

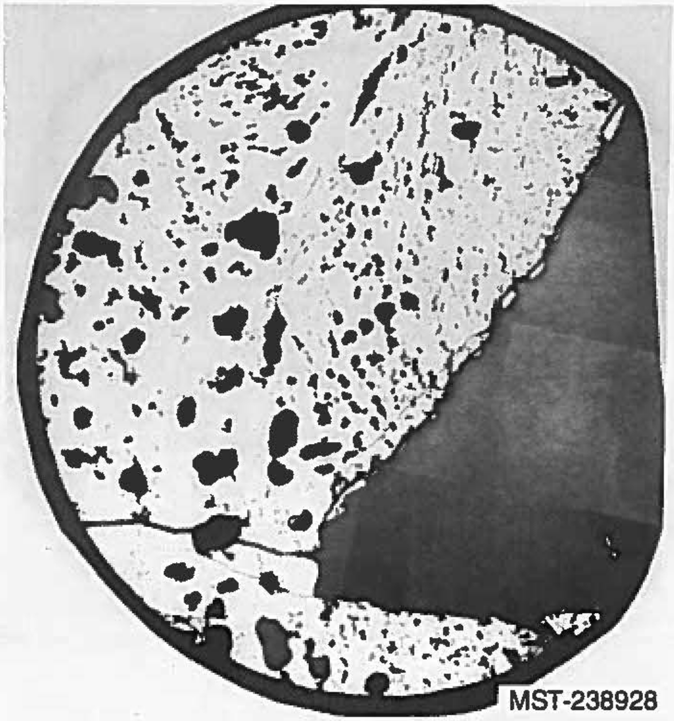

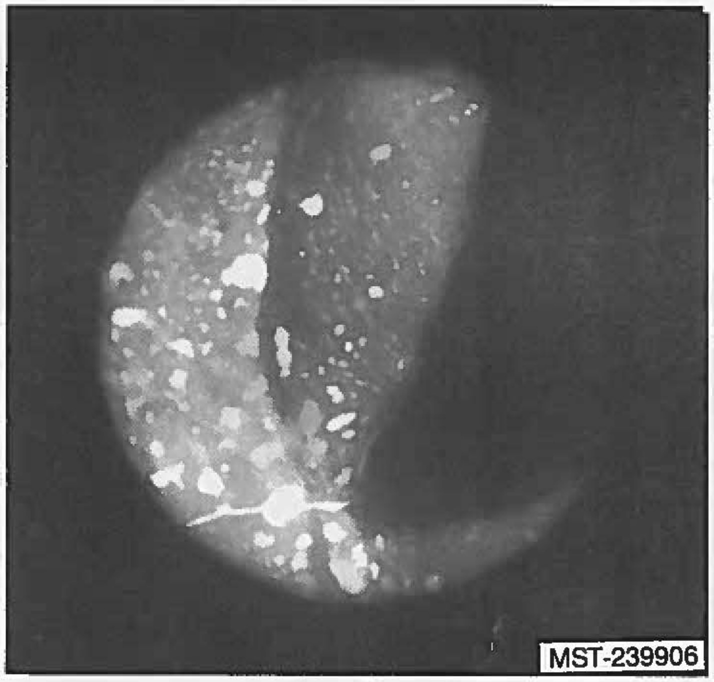

Figure 58. SEM mosaic photograph and autoradiograph for Particle 11-5-B-1.

Figure 59. SEM mosaic photograph and autoradiograph for Particle 11-6-A.

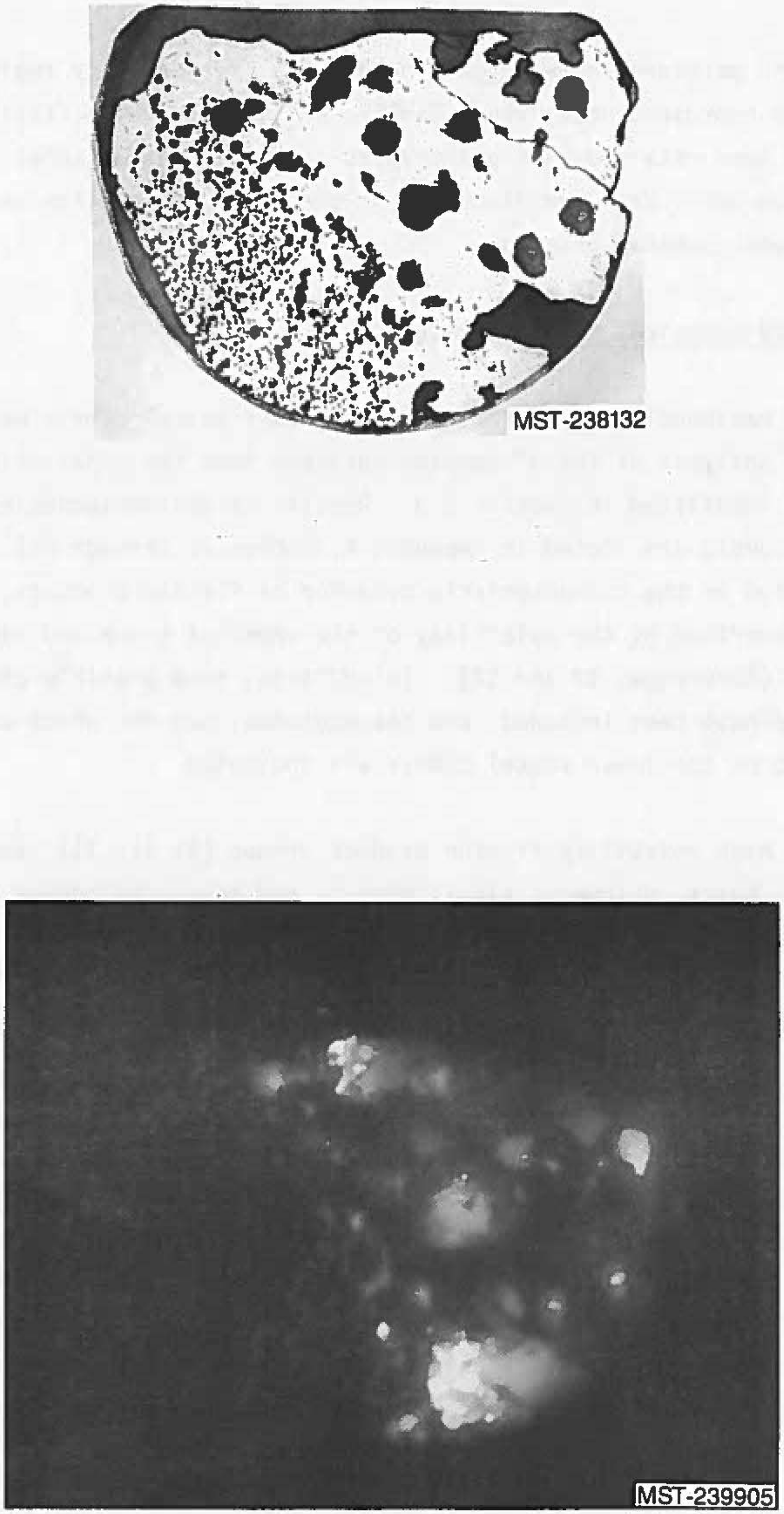

Figure 60. SEM mosaic photograph and autoradiograph for Particle 11-7-B-1.

ANL-E personnel have suggested that the high activity regions in the voids may represent areas where Cs-137, a highly volatile fission product, may have been retained as a gas trapped in the molten material. The autoradiographic data are discussed in the following section as they relate to the radiochemical results.

3.4.2 Radiochemical Analysis Results

The radionuclide composition of the lower vessel debris was determined from the analysis of the 37 samples obtained from the 9 particle cross sections identified in Section 3.3. Results of the radiochemical analysis of each sample are listed in Appendix F, Tables F1 through F11. To provide information on the characteristic behavior of fission products, they have been categorized by the volatility of the chemical group and element in Table 10 (References 13 and 14). In addition, some possible chemical compounds have been included, and the radionuclides for which analyses were performed on the lower vessel debris are indicated.

The high volatility fission product groups (I, II, III, and IV.a) are the noble gases, halogens, alkali metals, and heavy chalcogens. They are characterized by boiling points less than 1600 K for the elemental forms as well as for the listed oxide compounds. From this group, measurements were performed for I-129, Cs-137, and elemental tellurium.

The medium volatility fission products are characterized by boiling points less than 3100 K (UO_2 melting). These fission products are from the Group IV.b metals, alkaline earths, some of the rare earths, and actinides. Radionuclides from these groups for which measurements were made are Sb-125, Sr-90, Eu-154, and Ru-106. However, note that the volatility of these fission products strongly depends on the chemical form of the fission product. Ruthenium, boiling point = 4173 K, is included in the medium volatility group because it has two highly volatile oxides (i.e., RuO_2 and RuO_4), which either decompose or boil at less than 400 K.

TABLE 10. CORE MATERIAL VOLATILITY GROUPS

WASH-1400 Group Number	Chemical Group	Element	Boiling[a] Temperature (K)	Volatility	Possible Compounds	Boiling[a] Temperature (K)	Volatility	Analysis Performed
Fission Products								
I	Noble gases	Kr[b]	120	High		--	--	--
		Xe[b]	166	High		--	--	
II	Halogens	Br	332	High	CsBr	1573	High	
		I	458	High	CsI[b]	1553	High	X
					HI	238	High	
					I_2	457	High	
III	Alkali metals	Rb[b]	973	High	RbI	1573	High	
					Rb_2O	--	High	
					Rb_2O_2	1284	High	
		Cs[b]	963	High	CsI[b]	1553	High	X
					CsOH	~1350[c]	High	
					Cs_2O	--	High	
					Cs_2O_2	923	High	
					Cs_2UO_4[b]	--	--	
IV.a	Heavy chalcogens	Se[b]	958	High	SeO_3	453	High	
					SeO_2	--	--	
		Te[b]	1663	High	TeO_2	--	--	X
					Te_2O_2	--	--	
					silver-telluride	--	--	
					iron-telluride	--	--	
					zirconium telluride	--	--	
					tin-telluride	--	--	
					nickel telluride	--	--	
					chrome telluride	--	--	
Fission Products								
IV.b	Group VA metals	Sb[b]	1653	Medium	Sb_2O_3	1823	Medium	X

TABLE 10. (continued)

WASH-1400 Group Number	Chemical Group	Element	Boiling[a] Temperature (K)	Volatility	Possible Compounds	Boiling[a] Temperature (K)	Volatility	Analysis Performed
V	Alkaline earths	Sr	1639	Medium	SrO^b	~3100	Low	X
		Ba	1800	Medium	BaH_2	1673	Medium	
					BaO^b	~2273	Medium	
					BaO_2	1073	High	
					$Ba(OH)_2$	1053	High	
VI	Rare earths	Eu	--	Medium	$Eu_2O_3{}^b$	--	--	X
		Sm	2173	Medium	$Sm_2O_3{}^b$	--	--	
		Pm	3400	Low	$Pm_2O_3{}^b$	--	--	
	Actinides	Am	2873	Medium	$AmO_2{}^b$	--	--	
VI	Noble metals	Pd	2473	Low	PdO	--	--	
		Rh	6173 (est)	Low	RhO_2	--	--	X
					Rh_2O_3	--	--	
		Ru	4423	Low	RuO_2	--	X	
					RuO_4	125	High--	
		Mo	4780	Low	$MoO_2{}^b$			
					Mo_2O_3	--	--	
					MoO_3	--	--	
		Tc	--	Low		--	--	
VII	Rare earths	Y	3260	Low	$Y_2O_3{}^b$	--	--	
		La	3743	Low	LaO	--	Medium-High	
					$La_2O_3{}^b$	4473	Low	
		Ce	2690	Low	CeO_2	--	--	X
					$Ce_2O_3{}^b$	--	--	
		Pr	3400	Low	PrO_2	--	--	
					$Pr_2O_3{}^b$	--	--	
		Nd	3300	Low	Nd_2O_3	--	--	
	Actinides	Np	--	Low	$NpO_2{}^b$	--	--	
		Pu	3508	Low	$PuO_2{}^b$	--	Low	
		Cm	--	Low	$CmO_2{}^b$	--	--	

TABLE 10. (continued)

WASH-1400 Group Number	Chemical Group	Element	Boiling[a] Temperature (K)	Volatility	Possible Compounds	Boiling[a] Temperature (K)	Volatility	Analysis Performed
	Tetravalents	Zr[c]	>3173	Low	ZrO_2[b]	~5273	Low	
	Early transition	Nb	~3573	Low	NbO_2 Nb_2O_5	-- --	Low --	

---

a. Boiling temperature at 1 atm., data primarily from CRC Handbook of Chemistry and Physics, 56th Edition.

b. Probable chemical form of the fission product within the fuel.

c. Zirconium is both a fission product and a structural material.

The low volatility fission products include elements from the noble metals, the remaining rare earths and actinides, tetravalents, and early transition elements. Generally, the oxides of these elements have a low volatility; however, some (e.g., LaO or CeO) have lower boiling points than the elements. The only radionuclide from this group that was measurable during the lower vessel debris examination program was cerium/praseodymium. In addition, U-235 and U-238, which are also low volatile isotopes, were measured to evaluate uranium content and U-235 enrichment.

The evaluation of the radionuclide concentration data and the U-235/U-238 enrichment data is presented in Appendix F. The comparison of these analysis results with ORIGEN2 calculations are in Section 3.4.4. The discussion of the ORIGEN2 comparisons provides a more informative analysis of the results for the reader, although a discussion of the concentration data is also useful and is required for some data analyses.

3.4.3 Comparisons with ORIGEN2

The measured radionuclide concentrations of the lower vessel debris were compared with concentrations predicted by the ORIGEN2 code in order to assess retention of radionuclides in the fuel matrix and in the core. The ORIGEN2 analysis used for the TMI-2 core (Reference 14) divided the core into 1239 nodes, and calculations were performed for the full range of burnups for each of the three U-235 enrichments present (i.e., 1.98, 2.64, and 2.98%). The method used to estimate radionuclide retention is shown below:

$$\frac{\begin{array}{c}\text{Radionuclide}\\ \text{Concentration}\\ (\mu\text{Ci/g of sample})\end{array}}{\begin{array}{c}\text{Uranium content}\\ \text{(fractional content)}\end{array}} \times \frac{1}{\begin{array}{c}\text{ORIGEN2 predicted}\\ \text{radionuclide concentration}\\ (\mu\text{Ci/g uranium})\end{array}} = \begin{array}{c}\text{U-235 normalized}\\ \text{fission product}\\ \text{retention}\\ (\%)\end{array} \qquad (1)$$

Two different ORIGEN2-predicted concentrations have been used to calculate the retention of fission products in the prior-molten debris. The first, and most accurate method, is to compare the measured fission product concentrations with the average fission product content for the 1.98- and 2.64%-enrichment regions, as indicated in Appendix F. This method is expected to provide the best indicator of radionuclide retention, because the 2.96%-enriched fuel is located only in a single layer of fuel assemblies on the core periphery and, based on the enrichment analyses, only small amounts of this material (2 of 37 analyses with relatively large uncertainties) are present in the lower vessel debris.

The second method of calculating radionuclide retention is to compare the measured radionuclide concentrations with the ORIGEN2-predicted whole core average radionuclide concentrations. Although this method is inherently less accurate, the analysis is required for comparison with fission product retention analyses performed on other parts of the core.

The radionuclide concentrations used for these analyses are listed in Appendix F; the uranium content data are from the fissile/fertile material data listed in Appendix F, except where the delayed neutron data were unavailable or had large associated uncertainties. (In these cases, the elemental analysis results were used.) The ORIGEN2-predicted radionuclide concentrations for the whole core and the combined 1.98- and 2.64%-enriched assemblies are listed in Table 11.

The radionuclide retention comparisons with ORIGEN2 are listed in Tables 12, 13, and Appendix F, Tables F-12 through F-20. These data are discussed in sections evaluating the behavior of the low, medium, and high volatility radionuclides. Table 12 lists the average radionuclide retentions for the individual particles analyzed for both the combined 1.98 and 2.64% assembly concentrations and the whole core average concentrations (in parenthesis). These data were calculated by averaging the calculated retention data for each particle (a total of 37 samples listed in

TABLE 11. ORIGEN-2 CALCULATED RADIONUCLIDE CONCENTRATIONS

Radionuclide	Whole[a] Core Average (µCi/gm)	All 1.98% and 2.64% Fuel[a,b] (µCi/gm)	Ratio
^{90}Sr	7.74 E+3	8.33 E+3	1.08
^{106}Ru	3.57 E+2	4.13 E+2	1.16
^{125}Sb	2.73 E+2	3.08 E+2	1.13
^{129}I	2.80 E-3	3.11 E-3	1.11
^{137}Cs	8.90 E+3	9.68 E+3	1.09
^{144}Ce	5.69 E+2	6.17 E+2	1.08
^{154}Eu	6.60 E+1	8.00 E+1	1.21

---

a. Decay corrected to April 1, 1986.

b. Calculated using the listed core masses for each enrichment and the concentrations listed in References 7 and 8.

Enrichment	Mass
1.98%	26.23 tonnes
2.64%	28.58 tonnes
2.98%	28.11 tonnes

TABLE 12. AVERAGE RADIONUCLIDE RETENTION FOR THE COMBINED 1.98 AND 2.64% ASSEMBLIES

		Average Radionuclide Retention for Each Particle (%)[a]								
Radionuclide	Average Concentration[b]	7-1-B	11-1-A	11-1-C	11-2-C	11-4-B	11-4-0	11-5-C	11-6-B	11-7-C
^{90}Sr	7.74 E+3	93 (101)	93 (100)	93 (101)	126 (137)	131 (142)	119 (129)	90 (97)	171 (185)	142 (153)
^{106}Ru	3.57 E+2	6.4[c] (7.4)	3.5 (4.1)	6.0 (7.0)	5.3 (6.2)	7.9 (8.7)	5.7 (6.6)	7.1 (8.2)	--[d]	5.8 (6.7)
^{125}Sb	2.73 E+2	8.2[c] (9.3)	--[d]	4.5[c] (5.1)	3.0[c] (3.4)	8.8 (10)	6.2[c] (7.0)	4.3[c] (4.9)	--[d]	--[c]
^{129}I	2.81 E-3	4.4[c] (4.9)	1.1 (1.2)	0.47[c] (0.52)	2.5[c] (2.8)	11 (12)	0.90[c] (1.0)	0.99[c] (1.1)	2.3 (2.6)	1.3 (1.4)
^{137}Cs	8.9 E+3	20 (22)	10 (11)	6.6 (7.2)	10 (11)	19 (21)	16 (18)	7.0 (7.6)	14 (15)	15 (16)
^{144}Ce	5.69 E+2	111 (120)	90 (97)	106 (114)	103 (111)	111 (120)	109 (118)	93 (101)	93 (101)	105 (113)
^{154}Eu	6.6 E+1	71 (86)	66 (80)	74 (90)	66 (80)	68 (82)	68 (83)	77 (93)	75 (91)	69 (84)

---

a. Average retentions calculated normalized to uranium content for the ORIGEN-2 generated fission product concentrations for the combined 1.98 and 2.96% assemblies. The whole core average comparisons are listed in parentheses.

b. Core average concentrations (μCi/gm) decay corrected from data in Reference 7 for the combined 1.98 and 2.64% enrichments.

c. Analysis based on measurable results. Some radionuclide concentrations were below the detection limit.

d. No measurable results.

TABLE 13. RADIONUCLIDE RETENTION BY SEVERAL METHODS[a]

Radionuclide	Particle Average[b]	Sample Mean[c] (All Data)	Sample Mean[d] (Real Values)
^{90}Sr	117	106	106
^{106}Ru	5.9	5.8	6.2
^{125}Sb	5.8	2.5	6.7
^{129}I	2.8	2.8	3.2
^{137}Cs	13.1	12.8	12.8
^{144}Ce	102	102	102
^{154}Eu	70	71	71

---

a. The listed results are compared to the ORIGEN-2 generated concentrations for the combined 1.98 and 2.96% enriched fuel assemblies.

b. Average of particle analysis results in Table F-1.

c. Average of all analysis results in Tables F-12 to F-20 including zeroes. Analyses where no data were obtained are not included.

d. Average of all analysis results in Tables F-12 to F-20.

Appendix F, Tables F-12 through F-20). These data are listed in percent of the expected whole core average fission product concentrations; however, the discussions of retentions will be based on the more accurate ORIGEN2-predicted concentrations for the combined 1.98 and 2.64% assemblies. Conversion ratios for the data in Appendix F, Tables F-12 through F-20, are listed in Table 11.

Because of the difficulty in calculating average concentrations where some analyses are below the detection limit of the analyses, calculations were performed that both included and excluded measurement data where the concentrations were below the detection limit. These data provide bounds on the actual retentions of the fission products in the debris. For comparisons of the particle averages, all analyses (result includes zero for averaging) and all real values (excludes zero for averaging), are listed in Table 13. Results of the radionuclide retention data listed in Tables 12, 13, and Appendix F are discussed below in order of the relative volatility of the fission product (low, medium, and high).

3.4.4 Low Volatiles

The only low volatile radionuclide for which retentions can be calculated is Ce-144. The retention data in Appendix F indicate a range from 83 to 152% of the average retention (Table 12). This range is quite narrow for the range of possible concentrations of Ce-144, (a factor of 3.5) as calculated by ORIGEN2 for the TMI-2 core (see Reference 14). Inspection of the data in Appendix F indicates that Particles 7-1-B and 11-4-B are partially composed of material with greater than average burnup (>20%), as indicated by the cerium retention values. There are no analyses with retentions less than 20% below the average; however, Particles 11-1-A, 11-2-C, 11-5-C, and 11-6-B have some locations >10% below the average concentration. These data indicate that the bulk of the Ce-144 retentions fall within a narrow band, except in several particles where there are indications of high burnup material.

Inspection of Table 12 indicates a variation of less than 15% for the particle-averaged Ce-144 retentions, which is within the uncertainty of the analysis method. These data indicate that the retention of Ce-144 in the lower vessel debris is relatively consistent with the uranium content (i.e., the Ce-144-to-uranium ratio is relatively constant). Inspection of Table 13 further emphasizes the consistency of the retention data for this radionuclide. Table 13 indicates that the average Ce-144 retentions are very close (<2% deviation) from the average ORIGEN2-calculated retentions for the 1.98- and 2.64%-enriched assemblies. The results are similar for all three calculational methods used and suggest that the fission product production in the lower vessel debris is very close to the core average burnup for the interior core fuel assemblies. This is a fortuitous result, as burnup can range over a factor of two for the two fuel assembly enrichments, with corresponding changes in fission product production (Reference 10). These data, however, tend to support the conclusion arrived at from the enrichment data that the lower vessel debris is a generally homogeneous mixture of the 1.98 and 2.64% fuel assemblies with an average burnup. As a result, in the discussions of fission product retention, the Ce-144 retention data were used as relative indicators of burnup for the samples.

As noted above, some particles contain zones of high cerium concentration, or variations in enrichment within the same particle (Appendix Table F2). The data suggest that these particles are likely to represent interaction zones between the 1.98 and 2.64% assemblies. Particles that exhibit this behavior are 7-1-B, 11-4-B, and 11-7-C. In these particles, there are consistent changes in enrichment from one side of the particle to the other. There are also similar changes in burnup, as indicated by the gradients in cerium retentions. These data are discussed further as to the interaction zone effects on the retentions of other radionuclides.

For Particle 7-1-B, the Ce-144 data are not comparable with the enrichment analyses (i.e., the concentration of cerium does not always increase with increasing enrichment). At similar neutron fluxes, it is expected that the Ce-144 content for the 1.98%-enriched assemblies would be less than the content for an adjacent location in a 2.64%-enriched assembly. However, there are core locations where the 1.98%-enriched assembly has a higher burnup than an adjacent 2.64%-enriched assembly, and consequently, potentially higher fission product concentration. This results from the 1.98% assembly being nearer the center of the core (greater total neutron flux).

3.4.5 Medium Volatiles

Results of the radionuclide retention analyses for the medium volatile radionuclides (i.e, Sr-90, Eu-154, Ru-106, and Sb-125) indicate a substantially different behavior than that observed for Ce-144. The Sr-90 and Eu-154 are the most similar in behavior to the Ce-144, but exhibit substantial differences in both retention and behavior. Examination of Appendix F, Tables F-12 through F-20 indicate that the normalized retentions for Sr-90 and Eu-154 range from 68 to 177% and 57 to 88%, respectively.

The range of retentions for Sr-90 is substantially larger (a factor of 2.6) than that observed for the Eu-154 (1.5). The high Sr-90 retentions are constant (i.e., adjoining sample locations have similarly high retentions), which indicates that there are zones of high Sr-90 retention. Particles exhibiting greater than average Sr-90 retentions are 7-1-B, 11-2-C, 11-4-B, and 11-4-D.

In Particle 7-1-B (Appendix F, Table F-12), sample locations 1 and 2 have Sr-90 retentions greater than 130%. These retentions are consistent with the Ce-144 retentions for sample location 1, but not for sample location 2. At sample location 1, the Sr-90 retention is 135%; the Ce-144 retention is 149%. These data are within the uncertainty of the analysis methods used (∿15%) and indicate that the retention for Sr-90 is similar to what would be expected from the quantity of Ce-144 present. However, for sample location 2, the Sr-90 retention is 152%; the Ce-144 retention is 115%. These data are outside the uncertainty of the analysis and suggest that there is a probable relocation of Sr-90, and that this sample location is enhanced in Sr-90. Relocation of the Sr-90 at sample location 2 may have resulted from the fact that this sample appears to be at the interaction zone between two assemblies [i.e., the adjoining sample location (No. 3) is substantially different in both Ce-144 (97%) and Sr-90 (67%) content], suggesting that two different fuel assemblies interacted to form this particle, although the enrichments are similar at both sample locations.

For Particle 11-2-C (Appendix F, Table F-13), most of the higher-than-average Sr-90 retentions are generally similar to the Ce-144 retentions, except location 2 where the Sr-9D retention is 192%; the Ce-144 retention is 93%. These data suggest that the concentration of Sr-90 has been enhanced at this location above what would be expected for the measured Ce-144 retention. This sample location appears to be an isolated instance of high Sr-90 retention. However, the enrichment data indicate again that this may be an interaction zone, because location 2 has an enrichment of 2.6%, whereas the surrounding locations (1 and 3) have enrichments of 2.2 and 2.4%. These data again indicate a correlation between interaction zones and the possible relocation of Sr-90.

In Particles 11-4-B and 11-4-D, the higher-than-average Sr-90 retentions generally correspond to higher-than-average Ce-144 retentions, which indicates that the retentions are consistent with the burnup of the sample.

The average Sr-90 retentions for the individual particles (Table 12) and for the average of all samples (Table 13) are consistent with the average retention of about 106%. These data indicate that although there is some relocation of Sr-90, as indicated above, there is substantially complete retention of all Sr-90 in the debris, and that this retention is similar to the average Ce-144 retention (102%).

For Eu-154, the retentions are generally consistent with the Ce-144 data (i.e., the Ce-144/Eu-154 ratio for most samples is relatively constant). However, the average retentions indicated for Eu-154 are approximately 70%, whereas the Ce-144 retentions average 102%. This would suggest that the Eu-154 was not affected by melting, similar to Ce-144; however, there is an indicated average loss of about 30% of the expected inventory. The most likely reason for the difference between the Eu-154 and Ce-144 retentions is the mode of production for Eu-154. This radionuclide is produced by neutron activation of the fission product Eu-153 (a stable fission product) rather than the beta decay of Sm-154, which is stable. This mode of production for Eu-154 introduces a substantial uncertainty (>30%) into the ORIGEN2-calculated concentrations, because production and, consequently, the fission product concentrations in the intact fuel become quite dependent on the spectrum of the neutron flux at that specific location in the core. Additional measurements to be completed in 1988 will better define the production of Eu-154 as a function of burnup, which will be used to adjust the inventory of the europium radionuclides in the reactor core. Observations that can be made from the Eu-154 data are that the Eu-154 does appear to stay with the fuel and there is no probable, significant release of this radionuclide from the prior-molten fuel.

The Sb-125 and Ru-106 retentions in Appendix F, Tables F-10 through F-18, indicate a substantial release of both radionuclides. In many cases, the retained concentration of the fission product Sb-125 was below the detection limit for the analysis method. The Ru-106 retentions range from below the detection limit to 16% retention, with an average retention for all real data of 6.2%. The Sb-125 data range from the detection limit to 15% retention. The average retention is within the range between 2.5% (zeros included) and 6.7% (all real values). The most nearly correct retention is probably nearer the 6.7% value, if the actual Sb-125 concentrations are near the detection limit for the analysis (i.e., <9.0 μCi/g).

The retention results for Sb-125 and Ru-106 indicate no correlations between Sb-125 and Ru-106 and any other radionuclides, including each other. The higher concentrations for both radionuclides are not at similar locations. These data indicate substantial release of both radionuclides with no known retention mechanisms that can be deduced from the available data. However, the metallurgical analysis results and the analyses performed on the upper core debris (Reference 4) indicate that both radionuclides may become associated with metallic components in the molten material and tend to concentrate in metallic nodules. These data would suggest that the Ru-106 and Sb-125 content of the lower vessel debris has relocated to a different portion of the core (either in the core proper or in the lower plenum) and has perhaps become associated with metallic structural components (i.e., possibly control rod materials, as most other structural material is present at expected concentrations, as indicated in Section 3.3.4).

3.4.6 High Volatiles

The retention results (Appendix F, Tables F-12 through F-20, and Tables 12 and 13) for the high volatile radionuclides, Cs-137 and I-129, indicate that substantial percentages of both radionuclides have not been retained in the debris. The Cs-137 retentions range from 0.38 to 35.5%, with an average retention of approximately 13% (Appendix F). The higher-than-average Cs-137 retentions generally correspond with locations of higher burnup (i.e., greater-than-average Ce-144 retentions), which suggests that Cs-137 retention in the lower vessel debris is independent of burnup (i.e., of the quantity of Cs-137 produced in the intact fuel, a relatively constant fraction is retained through the melting process). Particles that have Cs-137 retentions substantially greater than the average are 7-1-B, 11-4-B, and 11-4-D. These particles all have correspondingly higher-than-average Ce-144 retentions, suggesting that the high Cs-137 retentions are due to increased burnup.

Lower-than-average Cs-137 retentions were observed only in Particle 11-5-C at sample locations 1 to 4. The Ce-144 retentions are at or below the average retention, indicating less-than-expected production; however, the retentions are substantially less than expected, indicating that more than the average amount of Cs-137 had been removed from these sample locations. Possible explanations for this behavior are that this particle may have been exposed to higher temperatures longer than the other particles, or particles with low retentions have greater surface-to-volume ratios, allowing more release.

It has been suggested that the high activity levels observed in the voids in the autoradiographs (Figures 56 to 60) are composed principally of Cs-137, which volatilized and deposited on the surface of the voids (Reference 9). Examination of the sampling diagram for Particle 11-5-C (Figure 54) supports this hypothesis, as the higher Cs-137 concentrations were measured in the porous region of sample locations 5 to 9, whereas the lower portion of the particle is visibly less porous and contains substantially lower Cs-137 retentions. Unfortunately, there are no other examples of this behavior in this group of particles.

The retention of I-129 ranged from 0.11 to 22%, with an average retention between 2.8 and 3.2%. The I-129 follows a very similar behavior to that observed for the Cs-137. The concentrations of the I-129 increase at corresponding locations of higher burnup (Ce-144 concentration) and appear to be substantially affected by the porosity of the debris, as indicated for Cs-137. Figure 61 shows a plot of the Cs-137 and I-129 data for Particle 11-5-B. The Ce-144 data indicate that the particle has a lower average burnup at the bottom end of the particle (sample locations 1 to 4) and a slightly higher burnup (10 to 15%) near the top end of the particle. These corresponding retentions are not consistent for all samples. Further examinations are being performed that may help to define the retention mechanisms for these radionuclides.

3.4.7 Tellurium Analysis Results

Tellurium analyses were performed on individual samples from Particle 11-1-A and 11-5-C, using methods that concentrate the tellurium content of sample. Specific samples analyzed are identified in Appendix E. All results were below the detection limit of the analysis method (at about 1 ppm). The expected core average concentration of fission product tellurium is 36 ppm.

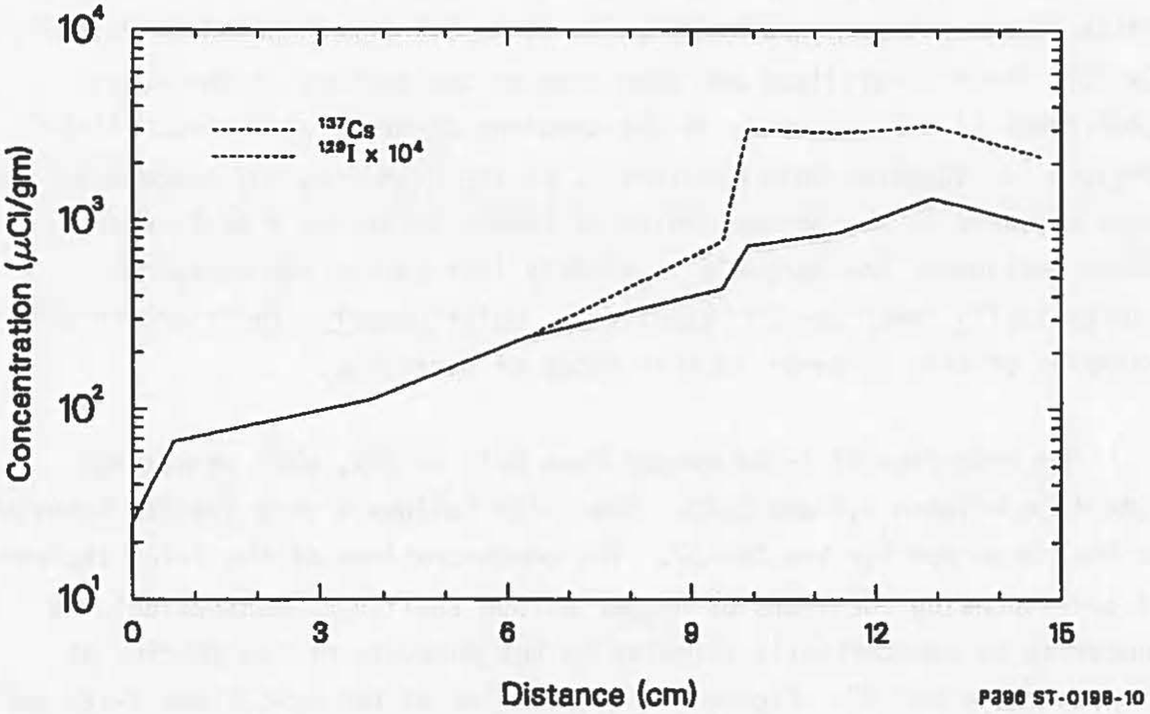

Figure 61. Cs-137 and I-129 concentrations for Particle 11-5-C.

4. CONTRIBUTIONS TO UNDERSTANDING THE TMI-2 ACCIDENT

The contributions of the lower vessel debris examinations to understanding the TMI-2 accident scenario, current condition of the core, and radionuclide retention/release from the core are discussed in this section. A brief summary of the known end-state of the core is presented, followed by sections describing (a) the temperature estimates and fuel behavior, (b) evaluation of the composition of the lower vessel debris, and (c) radionuclide retention and behavior.

4.1 End-State Core Configuration

The reactor defueling observations made over the past several years and the recent inspection of the lower core regions during the core boring operations have provided sufficient data to estimate the end-state core configuration (Reference 1) with reasonable certainty. These data show four distinct regions within the core and the lower plenum region below the core. Figure 62 (Reference 2) shows a cross section of the end-state core configuration through the K row of assemblies; Figure 63 shows a contour map of the lower plenum that has been constructed from available video surveys and sampling of the core. Described below is the end-state condition of the core and the lower plenum region.

4.1.1 Upper Core Void

A cavity existed at the top of the original core region with a volume of approximately 9.2 m^3. The cavity volume represents approximately 26% of the original core volume and extends nearly across the full diameter of the upper core region. The average depth of the cavity is approximately 1.5 m; in places the depth approaches 2 m. Standing fuel rod assemblies remained on the core periphery, with none of the 177 original assemblies appearing to be totally intact. About 42 fuel assemblies have full-length rods intact.

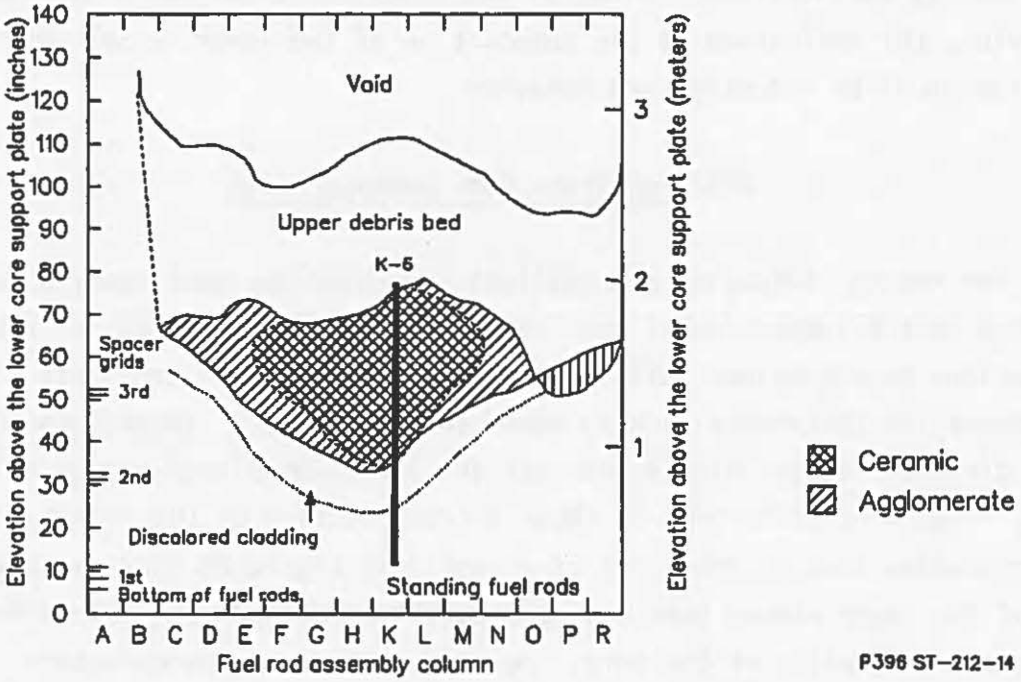

Figure 62. The end-state core configuration through the K row of the assemblies.

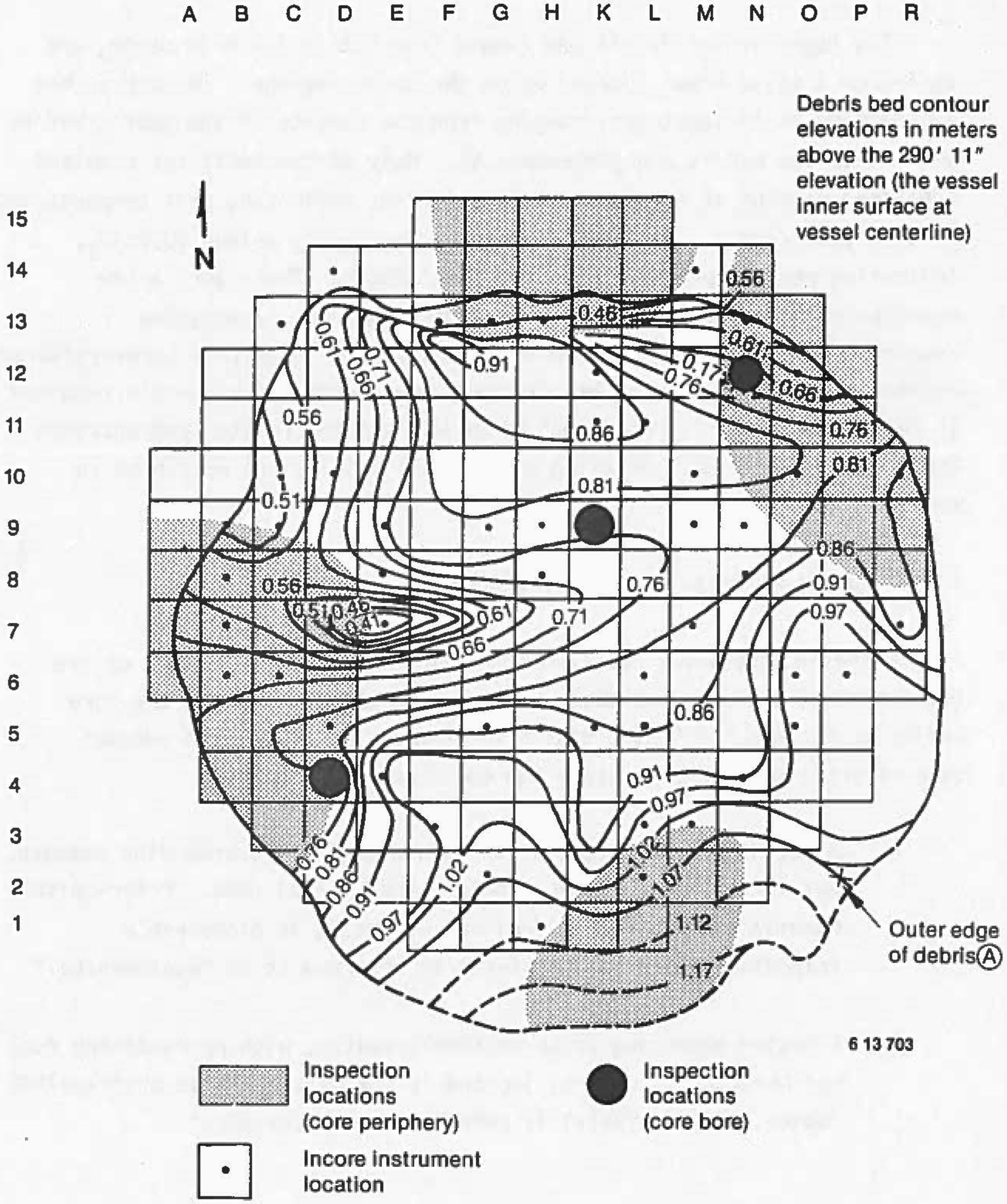

Figure 63. Lower plenum debris bed surface configuration.

4.1.2 Upper Vessel Debris Bed

The upper vessel debris bed ranged from 0.6 to 1.0 m in depth, and rested on a solid crust located below the core midplane. The debris bed was sampled at 11 locations, ranging from the surface of the debris bed to 94 cm into the debris bed (Reference 4). Many of the particles examined contained regions of previously liquid U-Zr-O, indicating peak temperatures greater than 2200 K. Of these, some were previously molten $(U,Zr)O_2$, indicating peak temperatures greater than 2800 K. There were a few examples of prior-molten material of almost pure UO_2, indicating temperatures up to 3100 K. However, based on the relatively unrestructured appearance observed of much of the fuel, considerable fuel debris remained at fairly low temperatures (<2000 K) or was exposed to high temperatures for only a short time. Detailed examination results are presented in Reference 4.

4.1.3 Molten Material in the Lower Core

A region containing prior-molten core material in a portion of the lower half of the core was observed in videos obtained during the core boring operations.[15,16] Two distinct regions containing prior-molten core material were observed from the core bore examinations:

1. A region of relocated, prior-molten material surrounding damaged, but intact, fuel pellets and/or partial fuel rods. Prior-molten material in which some fuel rod structure is discernible (cladding and/or fuel pellets) is referred to as "agglomerate."

2. A region appearing to be uniformly molten, with no remaining fuel rod structures evident, located in the center of the prior-molten region. This material is referred to as "ceramic."

4.1.4 Standing Fuel Rod Stubs

Standing fuel rod stubs extend from the bottom of the core to the interface with the solid, prior-molten region. Figure 62 shows the projected interface between the molten region and the rod stubs. The crust-like material forming the bottom of the molten core region is funnel-shaped, with the lowest point (approximately 0.5 m above the bottom of the fuel rods) near the center of the core. Near the core periphery, the elevation of the crust surface was found to be between 1 and 1.25 m from the bottom of the core.

4.1.5 Reactor Vessel Lower Plenum

Visual inspection of the lower plenum indicates that a substantial amount of prior-molten core material now rests on the reactor vessel lower head. Debris located on the head has a wide range of sizes, ranging from solid, irregularly shaped pieces >15-cm across to relatively fine, gravel-like particles. From Figure 63, it is estimated that the lower vessel debris bed contains about 15,000 kg of material.[17] The probable primary release path for the prior-molten material from the the reactor vessel to the lower plenum may be near the P-6 and R-7 core locations (the east side of the core), although there is evidence of release paths at other core locations. The lower vessel debris samples were obtained from the south and southwest quadrants of the reactor.

Estimates have been made for the volumes and masses of the various core regions using the core cross sections in Reference 1, estimated densities of the degraded core material, and known densities of the intact fuel rods. These estimates are summarized in Table 14.

The density of the consolidated (molten) core material is not known precisely; however, it is assumed to be identical to the lower plenum particles. Based on the estimated mass remaining in the core region, approximately 15,000 kg of core material are estimated to be in the lower plenum region.

TABLE 14. ESTIMATED END-STATE CORE VOLUMES AND MASSES

Estimated Volume Region	Estimated Volume (m^3)	Estimated Mass (uncertainty) (kg)
Original core	33.5	126,500 (1000)
Upper core void	9.2	-- --
Upper core debris	6.7	23,700 (1200)
Molten zone	3.5	25,600 (6600)
Standing rods	14.1	47,000 (3800)
Lower plenum debris	4.5	15,000 (5000)

4.2 Impact of Metallurgical Results on Understanding the Accident

The metallurgical analysis of 11 particle samples from the lower plenum region provide information in several areas that relate to the accident scenario. Estimates were made of core peak temperatures achieved during the accident, some indication of the temperature history was obtained, information on the chemical interactions of the fuel rod material with other core materials on a microscopic scale was obtained, and details of the relocation phenomenon were investigated. This section relates results of the metallurgical examinations to the end-state core condition described in Section 4.1. The discussion is presented in two sections: "Temperature Estimates" and "Fuel Behavior."

4.2.1 Temperature Estimates

The peak temperature or temperature range achieved during the transient was determined by detailed analysis of the microstructure and elemental composition of the rocks. Seven of the eleven particles that were examined showed evidence of higher temperatures than the other four. Depending on the mechanism of the interaction of the fuel rod materials with other core components, the lower plenum material could have attained temperatures of at least 2810 K. This temperature is the minimum solidus temperature for the uranium dioxide-zirconium dioxide isopleth. The presence of unmelted uranium dioxide fragments in Particle 11-5 indicates that the temperature of this particle would have to be less than 3100 K, the melting point of uranium dioxide. However, the presence of the iron and chromium oxides in the grain boundaries suggests that eutectic liquids could have been present to temperatures as low as 1573 to 1673 K on cooldown. The matrix material consisting primarily of uranium/zirconium oxide would solidify first and the remaining material consisting of the iron/chromium oxide eutectic would solidify last.

Temperature estimates may be complicated if the interaction begins with molten metallic control rod materials interacting with the fuel rod cladding and fuel, and then this mixture becomes oxidized, generating a liquid ceramic mixture. The melting point of a metallic mixture would be lower than the melting point of a mixture of the corresponding oxides, and if the temperature of the mixture was above the melting point of the oxides, the oxidation of the metallic mixture could take place without showing any evidence of concentration gradients, whereas oxidation in the solid state would proceed more slowly and concentration gradients would be more likely, which would be the case for solid-state oxidation.

4.2.2 Fuel Behavior

The lower plenum particles exhibited layers with different amounts of porosity, where bands of large and small pores were formed. The bonding between these bands was very intimate and solid. The layered structure of these particles suggests a prolonged candling sequence during the TMI-2 accident, where droplets of liquefied core materials had sufficient time to relocate down fuel rod exteriors, chemically react, solidify, and oxidize before other droplets arrived. Consequently, the melt process during the high-temperature portion of the TMI-2 accident should not be viewed as a single core-wide event, but rather as a complex sequence of interrelated and possibly intermittent melting and freezing phenomena.

4.3 Evaluation of Lower Vessel Debris Elemental Composition

Knowing the elemental composition of the lower vessel debris provides information that will be used to understand the behavior of the prior-molten fuel material and its interaction with structural materials. Also, the elemental data are used to provide information to assist in the analysis of the fission product behavior data.

The elemental composition of the lower vessel debris is quite consistent and indicates a relatively homogeneous material. Uranium and Zr, the most common of the elements present in the debris, have elemental concentrations in the lower vessel debris samples that are quite similar, 60 to 70% and 10 to 15%, respectively. This is the range of concentrations expected if the fuel, cladding, and in-core structural materials were melted, stoichiometrically oxidized, and mixed. These data suggest that the lower vessel debris samples analyzed were relatively evenly mixed and transported to the lower reactor reactor vessel without significant ablation of the structural materials in the flow pathway. This result is substantiated by the structural material results (i.e., Fe, Cr, Ni, and Mn), which are nearly the same as the expected core average concentrations of these elements.

The control rod materials (Ag-In-Cd) are significant fractions of the original core mass [i.e., Ag (1.6 wt%), In (0.3 wt%), and Cd (0.1 wt%)]. These elements were essentially not measurable in the lower vessel debris except at three isolated sample locations at concentrations near the detection limit for the analysis, which is substantially below the expected core average concentrations. These data suggest that the lower vessel debris was substantially depleted in control rod materials. Possible explanations for this depletion are that these relatively volatile core constituents either volatilized and were transported out of the fuel mass, or the control rod materials may have possibly relocated to the lower reactor vessel head. Some examination results indicate that there may be a layer of nonfuel material located on the lower reactor vessel head.[1]

4.3.1 Fission Product Retention in the Lower Plenum Debris

Fission product retention in the lower vessel debris is substantial for many of the low and medium volatile radionuclides. Table 13 lists the average radionuclide retentions for all sample analyses (37) and for the particle-averaged retentions (Table 12). The particle-averaged retentions are presented because they provide a better indication of the range of the bulk of the data, and they substantially reduce the impact of the variations in burnup. Note that the Ru-106 and Sb-125 data are affected by the inclusion of zeros in the calculation of the averages, and they tend to provide low estimates of retention. Averages that do not include the detection limit data are listed in Table 13 and provide an upper bound to the results.

The first contribution of the radionuclide retention data to the understanding of the accident is that the lower vessel debris appears to be substantially composed of a combination of the 1.98- and 2.64%-enriched assemblies. The enrichment data indicate that some of the particles appear to be at interaction zones between assemblies. There are particles where one edge is composed of 2.64%-enriched material, whereas the opposite edge is composed of 1.98%-enriched material. In addition, there are some particles (e.g., 11-1-C) that appear to be composed of material from a single enrichment zone. These data suggest that the lower vessel debris is a relatively chemically homogeneous mass of fuel and structural materials, which on the isotopic basis is principally composed of unhomogeneously mixed 1.98 and 2.64% fuel assemblies.

The average Ce-144 data in Table 15 indicate almost complete retention of this radionuclide in the debris. The high and low retentions indicated in the range appear to be due principally to greater- and lower-than-average burnup samples; however, the averaged data indicates that these are relatively isolated instances. If complete Ce-144 retention is assumed, then this radionuclide may be used as an indicator of the burnup and used to evaluate variations in the retentions of other radionuclides on the basis of the burnup of the material.

The medium volatile data indicate a wide range of retentions, with the Sr-90 and Eu-154 being most significantly retained. The average data in Table 13 indicates that all of the Sr-90 is retained; however, this radionuclide exhibits quite high concentrations in some samples, which do not appear to be burnup-related variations. Typically, these samples are from particles that exhibit variations in enrichment, which suggests that there are interaction zones between assemblies. At these interaction zones, there may be a relocation of Sr-90.

The Eu-154 indicates retentions in most samples with a similar range to that observed for Ce-144, except that the average retentions are substantially (30%) lower. This is most likely from the fact that this radionuclide is produced by neutron capture of Eu-153, and, therefore, the production of Eu-154 is highly dependent on the neutron flux spectrum at the core location where the material originated; consequently, the

TABLE 15. AVERAGE RADIONUCLIOE RETENTIONS[a]
(in percent retention normalized to uranium content)

Radionuclide	Average	Range
Low volatile		
Ce-144	102 (102)[b]	83-152 (90-111)
Medium volatile		
Sr-90	106 (117)	68-177 (90-171)
Eu-154[c]	71 (70)	57-87 (66-77)
Ru-106	5.8 (5.9)	0-16 (3.5-7.5)
Sb-125	2.5[d] (5.8)	0-15 (0-8.2)
High volatile		
Cs-137	12.8 (13.1)	0.38-35 (6.6-20)
I-129	2.8 (2.8)	0-22 (0.47-117)

---

a. Retentions calculated using the ORIGEN-2 predicted concentrations for the combined 1.98- and 2.96%-enriched fuel assemblies.

b. Average of particle concentrations from Tables 12 and 13.

c. Produced by neutron capture of a fission product.

d. Values below the detection limit are not include in this analysis.

uncertainty in this analysis is approximately 50%, and the retentions for this radionuclide are probably not as low as indicated.

The Ru-106 and Sb-125 retentions indicate substantial relocation of both fission products. Metallurgical and upper vessel debris examinations indicate that these radionuclides become associated with other metallics and are retained as metallic nodules or layers in the core. Therefore, the Sb-125 and Ru-106 originally present in the fuel, of which the lower vessel debris is composed, has relocated and may be in the core or possibly on the reactor vessel head. Initial indications from the core bore examinations indicate that significant quantities of these radionuclides may be present in the metallics within the resolidified mass at the bottom of the loose debris bed.

The high volatile radionuclides, Cs-137 and I-129, have been substantially released from the debris and much of the inventory of these radionuclides has relocated from the fuel material. It is surprising that the amount of residual Cs-137 present in the prior-molten debris ranged up to 35%, with an average retention of about 13%. These data suggest a mechanism that retains Cs-137 within the prior-molten material. The autoradiographs indicate high concentrations of radioactivity on the surfaces of the core voids. It has been suggested that the retention mechanism for the higher-than-expected concentrations of Cs-137 is that this radionuclide has volatilized and deposited on the surfaces of voids in the particles during cooling.[12]

5. CONCLUSIONS/OBSERVATIONS

Principal observations and conclusions that have been obtained from examining the lower vessel debris include results of the physical, metallurgical, chemical, and radiochemical analyses and correlation of these results with the known information on the core condition. The principal observations and conclusions include the following:

- The lower plenum debris is a mixture consisting of uranium and zirconium mixed oxides in the matrix
- Interaction zones were present around a number of pores that contained iron and chromium mixed oxides in the grain boundaries, with some varying amounts of nickel and aluminum
- Metallic inclusions were present in the fuel matrix, as well as in the voids
- Some metallic inclusions in pores were silver, whereas others in the matrix were nickel with dissolved amounts of silver, tin, or, in some cases, ruthenium
- The density of the lower plenum debris varied from 6.57 to 8.25 g/cm^3, which can be accounted for by the measured porosity of the samples and a mixture of approximately 80% UO_2 and 20% ZrO_2
- The material could be readily cut by diamond tipped media, and, because of the extensive porosity, it could be cut faster than similar but less porous material
- The compressive strength for the crushing samples was 111.4 MPa
- The U-Zr composition of the lower vessel debris is similar to the concentrations that would be expected if all core constituents were evenly mixed

- The maximum temperature of the lower debris exceeded 2810 K

- Based on the elemental analyses results, the debris, $(U, Zr)O_2$, is generally stoichiometric with respect to oxygen

- Boron appears to be evenly deposited throughout the particles at concentrations that are consistent with the amount of boron found in the reactor coolant

- Almost no control rod material is measurable in the sample material, suggesting that this material may have accumulated at other core locations, possibly up in the core or on the reactor vessel lower head

- Structural material (Fe, Cr, Ni, and Mn) content is near the core average and is evenly distributed in the prior-molten material

- There are indications of Cr concentrations in areas of high porosity (e.g., Particle 11-5-C), which suggests that this structural material component is affected by the melting of the core

- There are indications of accumulations of copper in the debris, which comes from the structural materials.

- The enrichment data indicate that the debris is composed principally of 1.98- and 2.64%-enriched assemblies, and that little or none of the 2.96%-assembly material is contained in the particles examined

- There is evidence in the enrichment data that some of the particles examined are composed of the interaction zone between two assemblies of different enrichment

- The Ce-144 retention in the lower vessel debris indicates almost complete retention of this radionuclide in the debris

- The Sr-90 data indicate almost complete retention of this radionuclide in the debris; however, there are some indications that this radionuclide may be mobile in the interaction zone between assemblies

- The Eu-154 data indicate a low average retention, of about 70% (This estimate has a relatively high uncertainty, as this radionuclide is produced from neutron capture of another fission product, and may not be a highly accurate indication of the retention of Eu-154.)

- The Sb-125 and Ru-106 have been substantially removed from the lower vessel debris, but are not found in substantial concentrations outside the reactor vessel (other data indicate that this material may be present in metallic nodules in the reactor vessel).

- Both Cs-137 and I-129 have been released, mostly from the prior-molten material; however, the average Cs-137 retention (11%) is substantially higher than the I-129 average retention of 2.8%.

6. REFERENCES

1. E. L. Tolman et al., TMI-2 Accident Scenario Update, EGG-TMI-7489, December 1986.
2. J. Adams and R. Smith, Lower Plenum Video Data Survey, EGG-TMI-7429 July 1987.
3. M. L. Russell et al., TMI-2 Accident Evaluation Program Sample Acquisition and Examination Plan for FY 1987 and Beyond, EGG-TMI-7521, February 1987.
4. O. W. Akers et al., TMI-2 Core Debris Grab Samples--Examination and Analysis, GEND-075, September 1986.
5. D. L. Hagerman et al., MATPRO Version 11 (Rev. 2) A Handbook of Materials Properties for Use in the Analysis of Light Water Reactor Fuel Rod Behavior, NUREG/CR 0479, August 1981.
6. J. T. A. Roberts and Y. Ueda, "Influence of Porosity on Deformation and Fracture of UO_2," Journal of the American Ceramic Society, 55, 3, 1972, pp. 117-124.
7. R. F. Cannon, J. T. A. Roberts, R. J. Beals, "Deformation of UO_2 at High Temperatures," Journal of the American Ceramic Society, 54. 1971, pp. 105-112.
8. Babcock and Wilcox letter of October 1, 1981, from D. L. Husser to L. C. Rogers, "Request for Assembly Weight--Material Type Breakdown." FRD & P-82-249.
9. J. J. McCown, Letter, "Elemental Analysis Results," Westinghouse Hanford, May 1986.
10. R. V. Strain et al., Results of Micro-Examination of Samples from the TMI-2 Lower Plenum, Argonne National laboratory (to be published).
11. R. V. Strain to Distribution, letter, "Review of Results of Autoradiography from TMI-2 Lower Plenum Samples," July 2, 1986.
12. N. Rasmussen et al., Reactor Safety Study--An Assessment of Accident Risk in U.S. Commercial Nuclear Power Plants, WASH-1400, NUREG-75/014, October 1975.
13. J. M. Broughton, private communication, EG&G Idaho, Inc., May 1985.
14. B. G. Schnitshler and J. B. Briggs, TMI-2 Isotopic Inventory Calculations, EGG-PBS-6798, August 1985.
15. E. L. Tolman et al., TMI-2 Core Bore Acquisition Summary Report, EGG-TMI-7385, September 1986.

16. G. Worku, "Conditions in the Reactor Vessel Lower Head," *TMI-2 Technical Bulletin 87-11*, May 18, 1987.

17. E. L. Tolman and N. Nishio, *Fission Product and core material mass Balance*, to be published.

APPENDIX A

EXAMINATION TECHNIQUES

APPENDIX A

EXAMINATION TECHNIQUES

This appendix presents a brief overview of techniques used during examination of the TMI-2 lower vessel debris samples, including physical, metallurgical, chemical, and radiochemical examinations.

PHYSICAL EXAMINATIONS

Visual/Photographic

A visual examination of each sample was made, using a scale to record the appearance and size of each sample. A 35-mm single lens reflex (SLR) camera body was attached to a Kollmorgen periscope at the camera port. A data back as part of the camera door was used to record a number on the negative, in conjunction with a photo log to track each photograph taken. A scale was placed along the side of each sample to determine the magnification of the photograph. In some cases, the samples were rotated to obtain a view at different orientations.

Mass

The mass of each sample was determined with an electronic top loader balance with a capacity of 3000 g and a resolution of 0.01 g.

Immersion Density

The matrix density and open porosity were determined using an immersion technique. This technique uses the dry mass and the mass of the immersed sample to determine the matrix density (matrix density can be determined within ±0.05 g/cm^3). After the sample is immersed, it is placed on a saturated towel to remove only the excess water on the surface, and then weighed again. The saturated weight, immersed weight, and dry weight are used to calculate open porosity (as discussed in the text). Because vacuum impregnation was not used to force water into the smaller pores, the open porosity measurements reflect only large pore sizes.

Radiation Field

The radiation level of each particle was measured by placing the sample near a port of the hot cell and measuring the beta/gamma and gamma radiation levels at 20 cm. In one case, because of the high radiation levels, the measurement had to be performed 25 cm from the sample.

Metallurgical Examinations

Optical Metallography

The optical metallography technique involved viewing highly polished particles using a light microscope at magnifications up to about 500X. In addition, the particles often were treated with etchants to highlight grain boundaries and second phases.

Small samples less than 19-mm dia were mounted in 31.8 mm-brass mounts. A brass holder (Figure A-1) was used to hold the sample in a lead/bismuth alloy. The alloy is melted (melting point 123.9°C) in a metal beaker and then poured into a preheated brass mount. The sample is placed in the mount with the surface to be examined facing up. If the sample floats, it is held down so the examination surface is even with the lead/bismuth surface. If the sample does not float, then spacers may be required between the sample and the bottom of the well to support the sample at the lead bismuth surface.

For large samples that do not fit into the brass mount, the samples are placed in a 12.7-cm-dia aluminum ring set in a groove in an aluminum plate (Figure A-2). The sample is placed on the plate with the examination face facing toward the plate. After epoxy is poured around the sample, the mount with the sample is inserted in a vacuum chamber to vacuum impregnate the sample with epoxy. The epoxy is allowed to cure for 24 h.

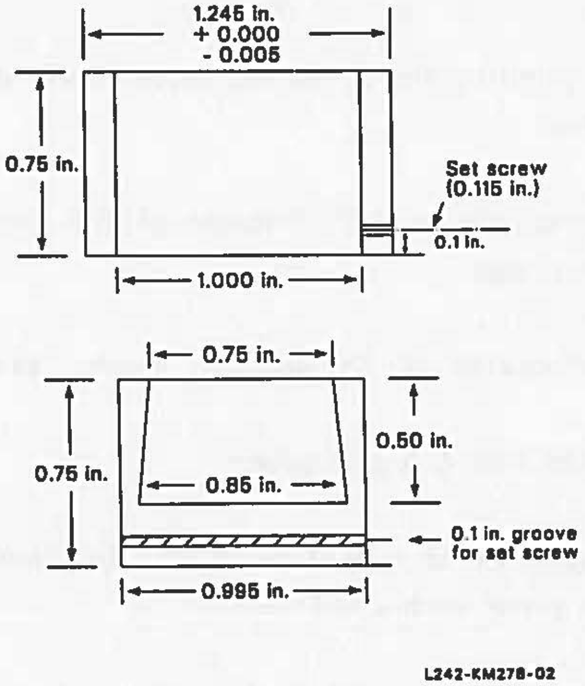

Figure A-1. Schematic drawing of 1-1/4 in. metallographic mount.

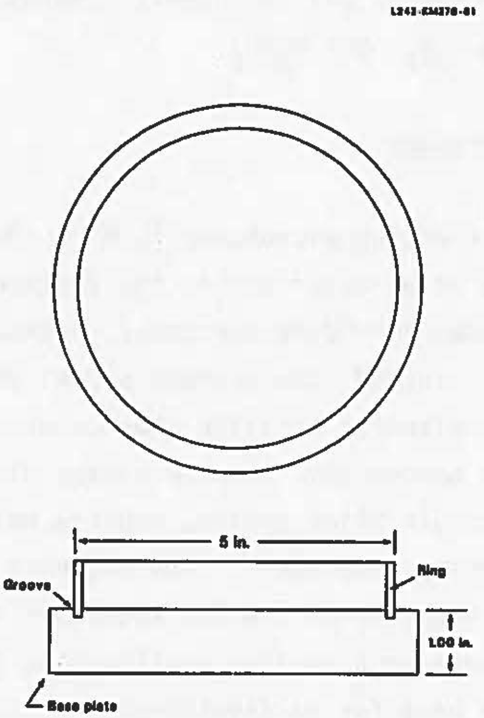

Figure A-2. Schematic drawing of 5 in. metallographic mount.

The following grinding and polishing sequence was used for the TMI-2 core debris particles:

1. Course grind with water-lubricated silicon carbide 120 grit paper with a whirlamat
2. Medium grind with 240 and 400 grit paper. Wash between grit sizes
3. Final grind with 600 grit paper
4. Initial polish with 6 μm diamond grit in mineral oil-type fluid on a hard paper with a whirlamat
5. Final polish with 3 μm diamond grit in mineral oil on a short nap nylon cloth.

In general, a swab-etching was used, with the etching time varying, depending on whether a heavy or light etch was appropriate. The following fuel etchant was used because all the debris samples were ceramic and contained urania: 85% H_2O_2, 15% H_2SO_4.

Scanning Electron Microscopy

For the scanning electron microscopy (SEM) technique, a finely focused electron beam is swept in a raster across the surface of a sample. The types of signals included secondary electrons, backscattered electrons, and characteristic x-rays. In SEM, the primary signal of interest is the variation in secondary electron emission that occurs as a result of the differences in surface topography. The secondary electrons are collected by a scintillator-photomultiplier system, and the resultant signal is displayed on a cathode-ray tube (CRT). The scanning electron beam is synchronized with the scanning of the CRT such that images can be presented on a storage oscilloscope or a monitor oscilloscope for photographing. This procedure is also used for backscattered electron images. These electrons have a higher energy than secondary electrons, resulting in greater escape depths. The primary advantage of backscattered electron images is that they differentiate between elements of low and high atomic numbers by the brightness displayed on the screen.

If areas in the large (12.7-cm-diameter) samples need to be examined by SEM or Auger methods, small circular samples are obtained by core drilling. A 12.7-mm-OD diamond-tipped core bore is inserted in the chuck of a drill press. As the sample is drilled, the circular core bore is fed inside the core drill, after which it is mounted in a brass mount described above.

Energy-Dispersive X-Ray Spectroscopy

Energy-dispersive x-ray spectroscopy (EDS) analysis is performed by measuring characteristic detectable x-rays from elements above atomic number 10 that are excited by a scanning electron beam. The beam is typically 1 µm in diameter, but scattering produces x-rays over a region up to 10 times wider. A SEM/EDS system is very convenient for fast area surveys of elemental content and spectral uniformity, and produces superb images and photographic records. Other advantages are the low beam energy and relatively low operating vacuum, both of which limit absorption of deposited molecules. However, the usefulness of this instrument is reduced by its susceptibility to background radiation, its inability to detect oxygen and carbon, and its inability to provide binding energy information.

The limit of detection for most elements on the SEM/EDX and Auger electron spectrometer is between 0.5 and 5 wt% under ideal conditions; however, radioactivity affects the signal-to-noise ratio for both analysis methods, particularly for the SEM. Therefore, elements that exist in the sample with concentrations of less than 1 to 2 wt% may not be detected by SEM analysis.

Scanning Auger Spectroscopy (SAS)

This instrument rasters an electron beam over a sample region, ionizing surface atoms, and generating characteristic x-rays and secondary electrons in the process. Rather than recording the x-rays, auger spectroscopy collects and analyses the energy from the emitted auger electrons of elements above atomic number 2. The double-focusing electron optics and tight energy resolution essentially eliminate interference from background radiation. Moreover, the detected secondary electrons are able to escape only the outermost atomic or molecular layers, so depth resolution is extremely fine. Most SAS systems incorporate inert gas ion sputter-etching for both specimen cleaning and depth profiling; the positive ion flux counterbalances charging by incident electrons. The elemental detection threshold is typically 0.1 at%, which is comparable to EDS. The SAS spatial resolution is equal to the beam diameter, which varies between 0.1 to 20 μm, depending upon the particular model.

Chemical Examinations

Inductively Coupled Plasma Spectrometry

Dissolved solid samples are nebulized and pulse-injected into an inductively (radio frequency) heated plasma, causing all elements present to emit characteristic light wavelengths. The light is separated on a diffraction-grating monochromator, and the wavelength intensities are sequentially measured by a photomultiplier tube. [As such, inductively coupled plasma (ICP) spectrometry is a refinement of atomic emission spectroscopy.] This technique generally is free of elemental interferences, is highly accurate, and has a detection threshold of approximately 0.001 at% (10 ppm).

Radiochemical Examinations

Gamma Spectroscopy

The initial radiochemical analysis performed was gamma spectroscopy. This technique is based on gamma-ray emissions that produce a spectrum specific to individual radionuclide species. The spectra were analyzed by a computerized gamma spectroscopy system using DEC PDP-15 and PDP-11/44 computers with a GAUSS VI analysis program.[a] This program (a) identifies the radionuclides associated with the gamma-ray energy peaks, and (b) determines their emission rates corrected for detector efficiency, random pulse summing, and decay during the count. The values were converted to disintegration rates by dividing them by the gamma-ray emission probability. The equipment used was fabricated at EG&G Idaho and calibrated using standards of the National Bureau of Standards.

Dissolved portions of samples were diluted and analyzed in 60-mL bottles at calibrated distances with a computerized Ge(Li) gamma spectroscopy system. They were analyzed as point source geometries at distances ranging up to 195 cm from the detector. The mass of each portion analyzed was less than or equal to 100 mg, to keep the specific radionuclide concentration low and to minimize the effects of mass attenuation. The effects of mass attenuation were evaluated and corrected. The uncertainty of the gamma spectroscopy analysis method is less than 10%, with the exception of those radionuclides whose concentrations were determined using low-energy gamma rays (^{152}Eu and ^{125}Sb). The uncertainty associated with these radionuclides is approximately 30%.

Neutron Activation/Delayed Neutron Analysis

The fissile/fertile material content was measured by neutron activation/delayed neutron analysis at the Coupled Fast Reactivity Measurement Facility (CFRMF). The total fissile/fertile material content was measured by remotely exposing individual 1 x 5-cm-long cylinders containing sample material to a fast spectrum neutron flux in the central region of the CFRMF core. The cylinder was removed after a 1-min exposure; the delayed neutrons were measured after about 40 s, using a He-3 detector in a hydrogen moderator.

---

[a] J. E. Klein, M. H. Putnam, R. H. Helmer, GAUSS VI, A Computer Program for the Automatic Analysis of Gamma Rays from Germanium Spectrometers, ANRC-13, June 1973.

The fissile material content was determined by exposing the cylinder to a thermal spectrum neutron flux, causing only the U-235 and Pu-239 within the material to fission and emit delayed neutrons. It was assumed that the quantity of Pu-239 was insignificant (<2 wt% based on theoretical predictions). However, a bias between 5% and 8% may have resulted. The fertile material contents were determined by subtracting the measured fissile material content (U-235 and Pu-239) from the total fissile/fertile material content using appropriate calibrations. Calibration measurements were made using both mass and various enrichment standards (depleted U, natural U, 4.3% enriched U, and 93% enriched U).

I-129, Sr-90, and Tellurium Analyses

Analyses for Sr-90 and I-129 were performed on the dissolved sample material. After an organic separation, the volatile sample fraction was analyzed via neutron activation with a subsequent gamma spectroscopy analysis. The I-129 present in the dissolved material was activated to I-130, a gamma-ray-emitting radionuclide. The sample material then was analyzed via gamma spectrometry, and the I-129 concentration calculated from the measured I-130.

The Sr-90 analysis was performed on the nonvolatile sample fractions by precipitating the Sr carrier and Sr-90 from the other radionuclides, followed by beta analysis performed in a liquid scintillation counter (Packard Tricarb 3385).

There is a total uncertainty associated with the Sr-90 and Te analyses of 10 to 15%. Uncertainties associated with these analyses result from the sample dissolution and individual analytical techniques. The uncertainty associated with the dissolution is due to potential material losses on glassware surfaces and the occasional presence of small (<10%) amounts of insoluble material after the dissolution. However, for some samples, the uncertainties are 30 to 50% owing to uncertainties in sample weight for small (<10 mg) portions and losses during dissolution, as determined by comparing the fissile/fertile and chemical analysis results.

APPENDIX B

PORE SIZE DISTRIBUTIONS

APPENDIX B

PORE SIZE DISTRIBUTIONS

Mount 7-1-A
Void

Photograph-85m-546 Magnification 50X Total area: 496760		Photograph-85m-547 Magnification 50X Total area: 496100		Photograph 85-548 Magnification 50X Total area: 496810	
Number of Points	Size (mm)	Number of Points	Size (mm)	Number of Points	Size (mm)
188	0	114	0	250	0
177	1	152	2	241	1
108	1	89	2	222	2
127	3	85	3	194	3
106	4	70	4	177	4
89	5	49	5	121	5
67	6	44	6	87	6
55	7	38	7	66	7
51	8	34	8	60	8
44	9	29	9	59	9
42	10	33	10	52	10
40	11	20	11	49	11
38	12	18	12	45	12
32	13	17	13	42	13
29	14	15	14	41	14
25	15	15	15	37	15
25	16	15	16	36	16
21	17	13	17	36	17
21	18	12	18	34	18
21	19	12	19	32	19
15	22	11	20	31	20
14	23	10	21	29	21
12	24	9	22	27	22
11	25	9	23	27	23
8	30	8	24	27	24
7	35	8	25	26	25
6	40	8	30	22	30
6	45	6	35	21	35
5	50	6	40	17	40
5	55	4	45	14	45

Mount 7-1-A (continued)
Void

Photograph-85m-546
Magnification 50X
Total area: 496760

Number of Points	Size (mm)
4	60
4	70
3	80
3	90
3	100
3	120
2	130
2	140
1	150
1	500
0	510

Photograph-85m-547
Magnification 50X
Total area: 496100

Number of Points	Size (mm)
4	50
4	55
4	60
2	70
1	80
0	90

Photograph 85-548
Magnification 50X
Total area: 496810

Number of Points	Size (mm)
11	50
10	55
10	60
8	70
6	80
4	90
2	100
1	110
1	260
0	270

Mount 7-1-A (continued)
Void

Photograph-85m-549
Magnification 50X
Total area: 492320

Number of Points	Size (mm)
167	0
161	1
149	2
136	3
127	4
107	5
97	6
91	7
78	8
76	9
71	10
68	11
67	12
65	13
63	14
62	15
59	16
56	17
54	18
52	19
50	20
48	21
46	22
46	23
46	24
44	25
38	30
31	35
20	40
17	45
14	50
11	55
10	60
6	70
4	80

Photograph-85m-550
Magnification 50X
Total area: 492310

Number of Points	Size (mm)
148	0
139	1
130	2
118	3
105	4
99	5
91	6
82	7
80	8
77	9
72	10
66	11
63	12
63	13
62	14
59	15
57	16
57	17
56	18
55	19
51	20
49	21
48	22
45	23
45	24
42	25
40	30
36	35
27	40
19	45
17	50
11	55
10	60
8	70
5	80

Photograph 85m-552
Magnification 50X
Total area: 496130

Number of Points	Size (mm)
299	0
287	1
277	2
244	3
202	4
170	5
126	6
101	7
88	8
84	9
67	10
59	11
55	12
49	13
39	14
33	15
30	16
28	17
24	18
22	19
21	20
18	21
17	22
15	23
13	24
10	25
3	30
2	35
1	40
1	500
0	510

Mount 7-1-A (continued)
Void

Photograph-85m-549
Magnification 50X
Total area: 492320

Number of Points	Size (mm)
2	90
0	100

Photograph-85m-550
Magnification 50X
Total area: 492310

Number of Points	Size (mm)
3	90
1	100
0	110

Photograph 85m-552
Magnification 50X
Total area: 496130

Number of Points	Size (mm)

Mount 7-1-A (continued)
Void

Photograph-85m-553
Magnification 50X
Total area: 497080

Number of Points	Size (mm)
263	0
262	1
228	2
193	3
170	4
149	5
125	6
107	7
94	8
78	9
69	10
58	11
56	12
51	13
41	14
36	15
34	16
31	17
29	18
28	19
27	20
25	21
24	22
23	23
23	24
22	25
17	30
15	35
12	40
11	45
10	50
10	55
9	60
8	70
6	80

Photograph-85m-554
Magnification 50X
Total area: 496960

Number of Points	Size (mm)
122	0
115	1
104	2
91	3
71	4
63	5
53	6
47	7
42	8
38	9
34	10
33	11
30	12
29	13
28	14
27	15
27	16
23	17
23	18
23	19
23	22
22	24
21	25
19	30
18	35
17	40
15	45
15	50
12	55
10	60
6	70
6	80
6	90
6	100
5	110

Photograph 86m-98
Magnification 50X
Total area: 548170

Number of Points	Size (mm)
178	0
173	1
154	2
135	3
111	4
101	5
86	6
73	7
66	8
57	9
48	10
44	11
42	12
38	13
32	14
30	15
28	16
28	17
28	18
26	19
24	20
22	22
20	24
19	26
19	28
19	30
19	32
17	34
17	36
17	38
17	40
16	45
15	50
14	55
14	60

Mount 7-1-A (continued)
Void

Photograph-85m-553
Magnification 50X
Total area: 497080

Number of Points	Size (mm)
6	90
4	100
4	110
3	120
2	130
2	140
1	150
1	350
1	360

Photograph-85m-554
Magnification 50X
Total area: 496960

Number of Points	Size (mm)
4	120
3	130
2	140
2	170
1	180
1	190
0	200

Photograph 86m-98
Magnification 50X
Total area: 548170

Number of Points	Size (mm)
12	70
11	75
9	80
8	85
7	90
6	95
4	100
4	110
1	120
1	140
0	150

Mount 7-1-A (continued)
Void

Photograph-86m-46
Magnification 50X
Total area: 508220

Number of Points	Size (mm)
	0
359	1
328	2
304	3
245	4
214	5
182	6
114	7
94	8
83	9
61	10
57	11
50	12
44	13
42	14
42	15
37	16
32	17
31	18
29	19
27	20
24	22
23	24
22	26
21	28
19	30
13	35
12	40
12	45
10	50
9	55
8	60
6	65
6	70
6	75

Photograph-85m-48
Magnification 50X
Total area: 504560

Number of Points	Size (mm)
168	0
159	1
150	2
131	3
116	4
108	5
100	6
92	7
83	8
79	9
73	10
70	11
67	12
65	13
65	14
64	15
64	16
61	17
60	18
60	19
58	20
56	22
53	24
52	26
49	28
48	30
45	35
44	40
39	45
35	50
32	55
29	60
24	65
24	70
22	75

Photograph 86m-77
Magnification 50X
Total area: 504810

Number of Points	Size (mm)
393	0
385	1
360	2
307	3
269	4
236	5
204	6
172	7
138	8
114	9
101	10
90	11
82	12
76	13
68	14
63	15
59	16
56	17
48	18
42	19
39	20
33	21
32	22
30	23
25	24
25	25
25	26
19	27
19	28
16	29
16	30
11	32
10	34
9	36
8	38

Mount 7-1-A (continued)
Void

Photograph-86m-46
Magnification 50X
Total area: 508220

Number of Points	Size (mm)
5	80
5	85
5	90
4	95
4	100
3	110
2	120
2	130
1	140
1	170
0	180

Photograph-85m-48
Magnification 50X
Total area: 504560

Number of Points	Size (mm)
19	80
15	85
13	90
12	95
11	100
8	110
7	120
7	130
5	140
3	150
0	160

Photograph 86m-77
Magnification 50X
Total area: 504810

Number of Points	Size (mm)
7	40
4	45
3	50
3	55
3	60
2	65
2	175
1	180

Mount 7-1-A (continued)
Void

Photograph-86m-79
Magnification 50X
Total area: 505150

Number of Points	Size (mm)
462	0
424	1
379	2
307	3
278	4
239	5
192	6
152	7
129	8
115	9
88	10
80	11
73	12
66	13
60	14
46	15
42	16
38	17
34	18
34	19
32	20
29	22
24	24
22	26
20	28
20	30
19	32
18	34
17	36
17	38
17	40
16	45
15	50
13	55
11	60

Mount 7-1-A (continued)
Void

Photograph-86m-79
Magnification 50X
Total area: 505150

Number of Points	Size (mm)
7	65
6	70
5	75
4	80
4	85
4	90
3	95
3	100
3	110
3	130
2	140
2	150
1	160
1	220
0	230

Mount 11-1-B
Void

Photograph-85m-558
Magnification 50X
Total area: 493420

Number of Points	Size (mm)
155	0
149	1
142	2
128	3
117	4
102	5
92	6
88	7
85	8
81	9
77	10
75	11
70	12
66	13
64	14
58	15
57	16
56	17
52	18
51	19
49	20
45	21
44	22
42	23
38	24
36	25
32	30
30	35
25	40
22	45
18	50
13	55
9	60
7	65
7	70

Photograph-85m-559
Magnification 50X
Total area: 492870

Number of Points	Size (mm)
129	0
124	1
123	2
112	3
103	4
93	5
88	6
80	7
77	8
70	9
67	10
65	11
61	12
59	13
55	14
52	15
51	16
50	17
48	18
46	19
46	20
42	21
42	22
39	23
37	24
36	25
35	30
29	35
27	40
24	45
20	50
18	55
15	60
13	65
11	70

Photograph 85m-560
Magnification 50X
Total area: 491930

Number of Points	Size (mm)
184	0
176	1
159	2
143	3
125	4
107	5
93	6
82	7
71	8
71	9
60	10
60	11
56	12
52	13
49	14
47	15
42	16
39	17
39	18
34	19
34	20
34	21
32	22
32	23
31	24
30	25
26	30
23	35
21	40
20	45
20	50
18	55
16	60
13	70
8	80

Mount 11-1-B (continued)
Void

Photograph-85m-558
Magnification 50X
Total area: 493420

Number of Points	Size (mm)
7	80
6	85
6	90
5	95
4	100
3	110
2	120
2	130
1	140
0	150

Photograph-85m-559
Magnification 50X
Total area: 492870

Number of Points	Size (mm)
10	75
6	80
5	85
3	90
2	95
1	100
1	110
1	140
0	145

Photograph 85m-560
Magnification 50X
Total area: 491930

Number of Points	Size (mm)
8	90
8	100
7	110
3	120
3	130
2	140
1	170
0	180

Mount 11-1-B (continued)
Void

Photograph-85m-561
Magnification 50X
Total area: 496350

Number of Points	Size (mm)
184	0
157	1
147	2
114	3
108	4
90	5
85	6
79	7
75	8
70	9
61	10
57	11
53	12
51	13
48	14
46	15
42	16
39	17
38	18
35	19
33	20
33	21
30	22
28	23
26	24
24	25
18	30
13	35
10	40
8	45
5	50
5	55
4	60
3	70
3	95

Photograph-85m-562
Magnification 50X
Total area: 493660

Number of Points	Size (mm)
173	0
169	1
152	2
143	3
131	4
113	5
104	6
103	7
103	8
95	9
86	10
78	11
60	12
55	13
55	14
55	15
48	16
46	17
41	18
39	19
39	20
32	21
30	22
30	23
30	24
27	25
16	30
10	35
7	40
4	45
4	90
2	95
1	140
1	340
0	345

Photograph 85m-563
Magnification 50X
Total area: 493250

Number of Points	Size (mm)
138	0
130	1
119	2
112	3
103	4
87	5
80	6
67	7
57	8
52	9
44	10
38	11
33	12
28	13
28	14
22	15
18	16
14	17
10	18
9	19
9	20
9	21
9	24
8	25
4	30
4	35
2	40

Mount 11-1-B (continued)
Void

Photograph-85m-561
Magnification 50X
Total area: 496350

Number of Points	Size (mm)
2	100
2	190
1	200
1	270
0	275

Photograph-85m-562
Magnification 50X
Total area: 493660

Number of Points	Size (mm)

Photograph 85m-563
Magnification 50X
Total area: 493250

Number of Points	Size (mm)

Mount 11-1-B (continued)
Void

Photograph-86m-122
Magnification 50X
Total area: 459530

Number of Points	Size (mm)
199	0
196	1
185	2
169	3
151	4
138	5
130	6
119	7
110	8
105	9
96	10
93	11
81	12
77	13
72	14
65	15
64	16
62	17
59	18
51	19
51	20
49	21
44	22
43	23
41	24
38	26
34	28
26	30
26	32
24	34
19	36
19	38
16	40
12	42
10	44

Photograph 86m-222
Magnification 50X
Total area: 515370

Number of Points	Size (mm)
207	0
196	1
186	2
166	3
148	4
135	5
122	6
108	7
100	8
95	9
91	10
86	11
79	12
75	14
74	14
72	15
71	16
69	17
65	18
63	19
60	20
60	21
59	22
59	23
56	24
54	25
54	26
50	28
46	30
43	32
39	34
39	36
37	38
34	40
32	45

Mount 11-1-B (continued)
Void

Photograph-86m-122 Magnification 50X Total area: 459530		Photograph 86m-222 Magnification 50X Total area: 515370	
Number of Points	Size (mm)	Number of Points	Size (mm)
8	46	27	50
7	48	23	55
6	50	19	60
5	55	15	65
4	60	12	70
4	65	9	75
4	70	8	80
4	75	6	85
3	80	5	90
3	90	3	95
2	95	3	100
2	100	2	105
2	110	1	110
2	200	1	115
0	210	0	120

Mount 11-4-A
Void

Photograph-86m-210 Magnification 200X Total area: 515360		Photograph-86m-216 Magnification 200X Total area: 514720		Photograph 86m-217 Magnification 50X Total area: 459990	
Number of Points	Size (mm)	Number of Points	Size (mm)	Number of Points	Size (mm)
137	0	70	0	202	0
135	1	65	1	193	1
127	2	61	2	173	2
112	3	56	3	148	3
91	4	47	4	124	4
82	5	42	5	104	5
74	6	38	6	90	6
67	7	38	7	80	7
62	8	36	8	70	8
59	9	34	9	64	89
56	10	31	10	54	10
55	11	26	11	47	11
52	12	25	12	41	12
50	13	22	13	36	13
49	14	21	14	33	14
47	15	21	15	27	15
40	16	20	16	24	16
38	17	20	17	22	17
37	18	19	18	20	18
36	19	18	19	19	19
30	20	16	20	18	20
28	21	15	21	16	22
28	22	15	22	15	24
26	23	15	23	13	26
25	24	13	24	13	28
24	25	12	25	10	30
24	26	10	28	9	32
23	27	30	30	9	34
20	28	8	32	6	36
20	30	7	34	4	38
17	31	7	38	4	40
17	33	6	40	3	45
15	34	4	45	3	50
14	35	4	50	1	55
12	40	4	60	1	100

Mount 11-4-A (continued)
Void

Photograph-86m-210
Magnification 200X
Total area: 515360

Number of Points	Size (mm)
9	45
9	50
8	55
8	60
7	65
4	70
3	75
3	80
2	85
2	90
1	95
1	135
0	140

Photograph-86m-216
Magnification 200X
Total area: 514720

Number of Points	Size (mm)
3	65
3	70
2	75
2	115
1	120
0	125

Photograph 86m-217
Magnification 50X
Total area: 459990

Number of Points	Size (mm)
0	110

Mount 11-4-A (continued)
Void

Photograph 86M-219
Magnification 50X
Total area: 456040

Number of Points	Size (mm)
214	0
203	1
185	2
145	3
118	4
99	5
79	6
61	7
52	8
49	9
40	10
38	11
33	12
32	13
30	14
28	15
28	16
28	17
27	18
27	19
24	20
22	22
20	24
17	26
15	28
12	30
11	2
11	36
9	38
8	40
6	45
5	55
4	60
3	65
3	70

Mount 11-4-A (continued)
Void

Photograph 86M-219
Magnification 50X
Total area: 456040

Number of Points	Size (mm)
3	75
3	80
2	100
1	110

Mount 11-4-A (continued)
Void

Photograph-85m-536
Magnification 200X
Total area: 500970

Number of Points	Size (mm)
210	0
194	1
173	2
134	3
106	4
80	5
63	6
50	7
45	8
44	9
40	10
35	11
35	12
32	13
30	14
26	15
23	16
22	17
21	18
20	19
18	20
14	25
11	30
10	35
6	40
6	45
6	50
5	60
1	70
1	90
0	100

Photograph-85m-540
Magnification 50X
Total area: 502820

Number of Points	Size (mm)
199	0
196	1
172	2
142	3
132	4
117	5
110	6
98	7
91	8
87	9
82	10
77	11
73	12
72	13
70	14
68	15
67	16
66	17
64	18
61	19
60	20
59	21
58	22
55	23
54	24
54	25
45	30
40	35
34	40
27	45
23	50
20	55
18	60
12	70
8	80

Photograph-85m-217
Magnification 50X
Total area: 501990

Number of Points	Size (mm)
213	0
203	1
182	2
163	3
144	4
128	5
116	6
106	7
98	8
95	9
88	10
87	11
85	12
82	13
79	14
73	15
70	16
69	17
64	18
63	19
56	20
54	21
54	22
54	23
53	24
52	25
45	30
39	35
34	40
29	45
25	50
18	55
18	60
13	70
10	80

Mount 11-4-A (continued)
Void

Photograph-85m-536 Magnification 200X Total area: 500970		Photograph-85m-540 Magnification 50X Total area: 502820		Photograph-85m-217 Magnification 50X Total area: 501990	
Number of Points	Size (mm)	Number of Points	Size (mm)	Number of Points	Size (mm)
		6	90	8	90
		3	100	4	100
		3	110	3	110
		3	140	2	120
		2	150	1	130
		2	170	1	150
		1	180	0	160
		1	210		
		0	220		

Mount 11-4-A (continued)
Void

Photograph-85m-543
Magnification 50X
Total area: 511810

Number of Points	Size (mm)
307	0
283	1
256	2
235	3
197	4
174	5
153	6
133	7
116	8
109	9
92	10
81	11
76	12
73	13
63	14
57	15
55	16
50	17
49	18
43	19
40	20
39	21
36	22
36	23
33	24
31	25
26	30
19	35
13	40
5	45
3	50
2	55
2	360
1	370
1	560

Photograph-85m-544
Magnification 50X
Total area: 514870

Number of Points	Size (mm)
252	0
235	1
219	2
183	3
151	4
134	5
108	6
89	7
78	8
71	9
61	10
56	11
48	12
46	13
40	14
37	15
36	16
35	17
29	18
27	19
27	20
27	21
24	22
20	23
17	24
15	25
13	30
7	35
5	40
3	45
2	50
2	400
1	420
1	560
0	570

Photograph-85m-545
Magnification 50X
Total area: 518680

Number of Points	Size (mm)
242	0
233	1
213	2
179	3
158	4
123	5
97	6
77	7
65	8
54	9
45	10
40	11
33	12
28	13
20	14
18	15
16	16
16	17
15	18
10	19
10	20
9	21
9	22
9	23
9	24
9	25
6	30
5	35
5	40
5	45
5	50
5	60
4	70
4	80
3	90

Mount 11-4-A (continued)
Void

Photograph-85m-543
Magnification 50X
Total area: 511810

Number of Points	Size (mm)
0	570

Photograph-85m-544
Magnification 50X
Total area: 514870

Number of Points	Size (mm)
3	100

Photograph-85m-545
Magnification 50X
Total area: 518680

Number of Points	Size (mm)
3	130
3	170
2	180
2	190
1	200
0	210

Mount 11-4-A (continued)
Void

Photograph-86m-175
Magnification 200X
Total area: 515620

Number of Points	Size (mm)
166	0
156	1
142	2
119	3
101	4
84	5
69	6
60	7
52	8
48	9
38	10
34	11
32	12
28	13
26	14
25	15
23	16
23	17
22	18
21	19
19	20
17	22
15	24
13	26
11	28
10	30
6	35
5	40
4	45
3	50
3	55
2	60
2	65
2	70
1	75

Photograph-86m-160
Magnification 50X
Total area: 455780

Number of Points	Size (mm)
448	0
429	1
409	2
340	3
294	4
244	5
200	6
168	7
127	8
107	9
88	10
79	11
72	12
67	13
59	14
50	15
40	16
35	17
32	18
23	19
20	20
17	21
15	22
15	23
15	24
13	26
13	28
11	30
10	32
9	34
8	36
7	38
7	40
6	45
4	50

Mount 11-4-A (continued)
Void

Photograph-86m-175
Magnification 200X
Total area: 515620

Number of Points	Size (mm)
1	110
0	115

Photograph-86m-160
Magnification 50X
Total area: 455780

Number of Points	Size (mm)
3	55
3	60
3	95
2	100
2	110
1	120
1	135
0	140

Mount 11-5-B
Void

Photograph-86m-186
Magnification 100X
Total area: 515260

Number of Points	Size (mm)
238	0
233	1
223	2
211	3
202	4
197	5
180	6
168	7
157	8
151	9
141	10
134	11
122	12
118	13
108	14
101	15
93	16
90	17
87	18
83	19
77	20
73	21
73	22
72	23
71	24
69	25
53	30
44	35
37	40
28	45
23	50
20	55
17	60
13	65
10	70

Photograph-86m-196
Magnification 50X
Total area: 455410

Number of Points	Size (mm)
138	0
131	1
117	2
97	3
81	4
57	5
45	6
37	7
30	8
27	9
22	10
20	11
20	12
20	13
20	14
17	15
14	16
14	17
14	18
13	19
13	20
10	22
10	24
9	26
8	28
8	30
8	32
8	34
8	60
7	65
6	70
6	80
5	85
5	95
4	100

Photograph-86m-198
Magnification 50X
Total area: 454770

Number of Points	Size (mm)
225	0
211	1
197	2
168	3
140	4
115	5
92	6
82	7
68	8
60	9
50	10
48	11
43	12
37	13
33	14
32	15
31	16
28	17
25	18
20	19
20	20
17	22
15	24
13	26
10	28
9	30
9	32
8	34
6	36
5	38
5	40
4	45
4	50
4	60
2	65

Mount 11-5-B (continued)
Void

Photograph-86m-186
Magnification 100X
Total area: 515260

Number of Points	Size (mm)
7	75
6	80
6	85
5	90
4	95
4	100
4	110
1	120
1	130
1	140
0	150

Photograph-86m-196
Magnification 50X
Total area: 455410

Number of Points	Size (mm)
4	110
3	120
2	130
2	140
2	160
1	170
1	300
0	310

Photograph-86m-198
Magnification 50X
Total area: 454770

Number of Points	Size (mm)
2	70
2	80
1	85

Mount 11-5-B (continued)
Void

Photograph-86m-208
Magnification 200X
Total area: 515090

Number of Points	Size (mm)
270	0
260	1
246	2
235	3
210	4
197	5
176	6
164	7
153	8
145	9
139	10
135	11
120	12
115	13
104	14
95	15
86	16
85	17
81	18
76	19
73	20
69	21
66	22
62	23
61	24
58	26
45	28
42	30
39	32
34	35
28	40
22	45
18	50
18	55

Mount 11-5-B (continued)
Void

Photograph-86m-208
Magnification 200X
Total area: 515090

Number of Points	Size (mm)
15	60
11	65
10	70
10	75
9	80
8	90
5	100
4	110
2	120
1	130
1	170
0	175

Mount 11-6-A
Void

Photograph-85m-564
Magnification 100X
Total area: 501570

Number of Points	Size (mm)
108	0
102	1
90	2
75	3
71	4
63	5
60	6
57	7
52	8
49	9
42	10
42	11
38	12
37	13
37	14
36	15
36	16
33	17
32	18
32	19
32	20
31	25
26	30
23	35
21	40
19	45
17	50
14	60
13	70
11	80
7	90
6	100
3	110
3	120
1	130
0	140

Photograph-86m-565
Magnification 100X
Total area: 501650

Number of Points	Size (mm)
181	0
176	1
167	2
154	3
143	4
123	5
117	6
99	7
80	8
77	9
70	10
67	11
64	12
55	13
50	14
48	15
45	16
42	17
37	18
36	19
35	20
29	25
24	30
20	35
16	40
15	45
15	50
12	60
8	70
6	80
5	90
4	100
4	110
3	120
2	130
1	140
0	150

Photograph-85m-568
Magnification 50X
Total area: 496860

Number of Points	Size (mm)
231	0
218	1
208	2
199	3
187	4
176	5
164	6
155	7
148	8
140	9
125	10
121	11
117	12
114	13
110	14
102	15
98	16
90	17
81	18
80	19
76	20
68	21
63	22
62	23
58	24
56	25
42	30
25	35
20	40
14	45
7	50
6	55
6	60
3	70
2	80
0	90

Mount 11-6-A (continued)
Void

Photograph-85m-569
Magnification 50X
Total area: 496910

Number of Points	Size (mm)
209	0
200	1
178	2
151	3
130	4
118	5
104	6
98	7
93	8
87	9
83	10
80	11
77	12
77	13
74	14
70	15
68	16
67	17
64	18
61	19
60	20
57	21
53	22
52	23
49	24
44	25
31	30
26	35
19	40
15	45
10	50
9	55
6	60
3	70
2	80

Photograph-85m-570
Magnification 50X
Total area: 496930

Number of Points	Size (mm)
212	0
203	1
197	2
190	3
183	4
173	5
164	6
161	7
150	8
141	9
133	10
125	11
116	12
105	13
99	14
92	15
89	16
79	17
70	18
64	19
61	20
57	21
53	22
52	23
46	24
41	25
25	30
17	35
14	40
10	45
10	50
9	55
7	60
5	70
3	80

Photograph-85m-571
Magnification 50X
Total area: 496290

Number of Points	Size (mm)
133	0
127	1
121	2
116	3
107	4
101	5
94	6
90	7
83	8
81	9
76	10
74	11
72	12
67	13
59	14
56	15
52	16
49	17
47	18
44	19
42	20
38	21
37	22
35	23
31	24
30	25
25	30
21	35
15	40
13	45
13	50
9	55
8	60
5	70
5	80

Mount 11-6-A (continued)
Void

Photograph-85m-569
Magnification 50X
Total area: 496910

Number of Points	Size (mm)
0	90

Photograph-85m-570
Magnification 50X
Total area: 496930

Number of Points	Size (mm)
2	90
1	100
1	260
0	270

Photograph-85m-571
Magnification 50X
Total area: 496290

Number of Points	Size (mm)
4	90
4	100
2	110
2	120
2	140
1	150
1	240
0	250

Mount 11-6-A (continued)
Void

Photograph-85m-572
Magnification 50X
Total area: 496150

Number of Points	Size (mm)
167	0
156	1
149	2
132	3
121	4
107	5
99	6
89	7
81	8
78	9
76	10
74	11
71	12
67	13
62	14
61	15
59	16
55	17
50	18
48	19
47	20
45	21
41	22
40	23
38	24
36	25
33	30
29	35
21	40
17	45
15	50
13	55
9	60
7	70
5	80

Photograph-86m-104
Magnification 50X
Total area: 489330

Number of Points	Size (mm)
261	0
231	1
190	2
154	3
123	4
107	5
95	6
80	7
73	8
68	9
61	10
61	11
59	12
57	13
53	14
52	15
51	16
48	17
48	18
47	19
46	20
46	21
45	22
45	23
44	24
43	25
38	28
33	31
33	33
29	35
26	40
21	45
18	50
13	55
10	60

Photograph-86m-106
Magnification 50X
Total area: 483880

Number of Points	Size (mm)
261	0
216	1
192	2
156	3
125	4
102	5
92	6
88	7
78	8
73	9
68	10
65	11
61	12
61	13
60	14
58	15
54	16
54	17
53	18
49	19
47	20
46	21
46	22
44	23
43	24
42	26
39	28
39	30
35	32
32	34
31	36
30	38
26	40
19	45
17	50

Mount 11-6-A (continued)
Void

Photograph-85m-572
Magnification 50X
Total area: 496150

Number of Points	Size (mm)
5	90
3	100
3	110
2	120
1	130
1	190
0	200
1	210
0	220

Photograph-86m-104
Magnification 50X
Total area: 489330

Number of Points	Size (mm)
8	65
7	70
7	75
7	80
7	85
4	90
4	95
2	100
2	110
2	120
1	130
1	140
1	180
0	190

Photograph-86m-106
Magnification 50X
Total area: 483880

Number of Points	Size (mm)
13	55
11	60
9	65
8	70
6	75
5	80
4	85
3	90
3	95
3	100
2	105
1	110
1	130
0	135

Mount 11-6-A (continued)
Void

Photograph-86m-114
Magnification 50X
Total area: 484170

Number of Points	Size (mm)
243	0
223	1
212	2
166	3
142	4
122	5
107	6
101	7
98	8
94	9
81	10
76	11
68	12
58	13
54	14
45	15
43	16
40	17
39	18
36	19
32	20
29	21
27	22
27	23
26	24
25	26
23	28
22	30
24	32
23	34
21	36
21	38
17	40
16	42
15	44

Photograph-86m-116
Magnification 50X
Total area: 484130

Number of Points	Size (mm)
197	0
176	1
167	2
145	3
129	4
124	5
116	6
111	8
110	9
108	10
93	11
91	12
91	13
88	14
84	15
79	16
78	17
77	18
75	19
71	20
68	21
68	22
68	24
66	26
61	28
60	30
56	32
53	34
49	36
46	38
45	40
39	42
32	44
27	46
26	48

Mount 11-6-A (continued)
Void

Photograph-86m-114
Magnification 50X
Total area: 484170

Number of Points	Size (mm)
14	46
13	48
13	50
11	55
11	60
11	65
11	70
11	75
9	80
5	85
4	90
4	95
2	100
1	110
1	130
0	140

Photograph-86m-116
Magnification 50X
Total area: 484130

Number of Points	Size (mm)
24	50
19	55
14	60
12	65
12	70
10	75
7	80
4	85
3	90
2	95
2	100
2	110
2	130
1	140
0	150

Mount 11-7-8
Void

Photograph-86m-227
Magnification 100X
Total area: 518620

Number of Points	Size (mm)
148	0
144	1
138	2
129	3
111	4
102	5
93	6
87	7
61	8
59	9
56	10
51	11
47	12
43	13
40	14
36	15
36	16
33	17
31	18
30	19
29	20
29	21
28	28
27	23
26	24
25	27
23	29
22	31
19	35
16	40
14	45
12	50
8	55
8	60
7	65
6	70

Photograph-86m-229
Magnification 50X
Total area: 518620

Number of Points	Size (mm)
197	0
188	1
160	2
117	3
96	4
83	5
73	6
59	7
45	8
42	9
36	10
27	11
22	12
19	13
14	14
13	15
12	16
10	17
9	18
6	19
4	20
3	21
3	22
3	23
3	25
2	26
2	40
0	41

Mount 11-7-B (continued)
Void

Photograph-86m-227
Magnification 100X
Total area: 518620

Number of Points	Size (mm)
4	75
4	85
3	90
2	95
1	100
0	105

Photograph-86m-229
Magnification 50X
Total area: 518620

Number of Points	Size (mm)

Mount 11-4-A
Metallic Inclusions

Photograph-85m-210
Magnification 200X
Total area: 515380

Number of Points	Size (mm)
22	0
19	1
19	2
18	3
15	4
14	5
13	6
12	7
11	8
8	9
8	10
7	11
6	12
6	13
6	15
5	16
5	18
4	19
3	20
3	25
2	26
2	29
1	30
1	48
0	49

Photograph-86m-216
Magnification 200X
Total area: 515280

Number of Points	Size (mm)
28	0
25	1
22	2
16	3
14	4
11	5
8	6
4	7
4	8
3	9
2	10
2	11
1	12
1	13
0	14

Photograph-86m-256
Magnification 200X
Total area: 515340

Number of Points	Size (mm)
34	
33	1
32	2
26	3
23	4
20	5
17	6
14	7
12	8
12	9
10	10
8	11
8	12
3	13
2	14
1	15
1	22
0	23

Mount 11-4-C
Metallic Inclusions

Photograph-86m-175
Magnification 200X
Total area: 515620

Number of Points	Size (mm)
18	
16	1
15	2
14	3
14	4
14	5
13	6
11	7
10	8
10	9
10	10
10	11
10	12
8	13
7	14
6	15
6	16
6	17
5	18
5	22
4	23
3	24
3	27
2	28
2	30
1	31
1	34
0	35

Mount 11-7-B
Metallic Inclusions

Photograph-86m-229
Magnification 50X
Total area: 515380

Number of Points	Size (mm)
30	0
27	1
27	2
20	3
15	4
10	5
5	6
3	7
1	8
0	9

APPENDIX C

METALLOGRAPHIC EXAMINATION RESULTS FROM THE LOWER VESSEL DEBRIS SAMPLES

APPENDIX C

METALLOGRAPHIC EXAMINATION RESULTS FROM THE LOWER VESSEL DEBRIS SAMPLES

Metallographic sections were obtained from each of the particles described in the body of the text. Each metallographic section is described below.

Particle 7-1. The polished section from this particle is shown in Figure C-1. A large void was present near one end, around which an interaction zone was present and contains porosity-free material. However, the matrix contained many fine pores, which are shown in Figure C-2. Fourteen measurements of the porosity were obtained for different areas of the sample; the large void was excluded from these measurements. The void fraction varied from 5.4 to 56.5%, with an average of 27%. The pores were irregularly shaped, perhaps formed from some pore coalescence. Some of these pores had interaction zones around them similar to the large pore in this sample.

The interaction zone around the large pore is shown in Figure C-3. There was no porosity in the interaction zone but there was a second phase, as evidenced by the delineation of the grain boundaries in this unetched sample. The details of this interaction zone are shown in Figure C-4. The second phase is a grain boundary precipitate that formed the broad grain boundaries.

Particle 11-1. The metallographic section is shown in Figure C-5. A large void is present near the side facing the orientation marker, around which is an interaction zone containing apparently porosity-free material. At one point, a metallic inclusion was imbedded in this large pore, but it came out during ultrasonic cleaning. The interaction zone around the large void is shown in Figure C-6. The structure of this interaction zone is very similar to the one in Figure C-3, although porosity is evident at higher magnifications. There are a few elongated pores, with the long axis of the pore oriented in the circumferential direction around the void. Other pores, not as large as this one, also had similar interaction zones.

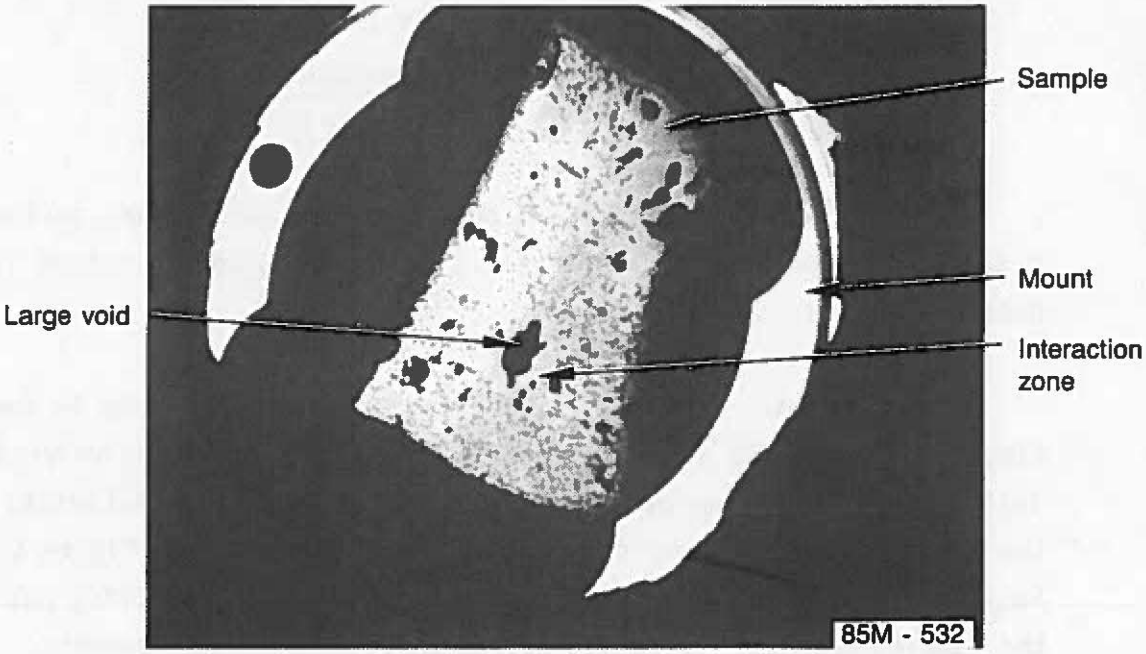

Figure C-1. Cross section from Particle 7-1.

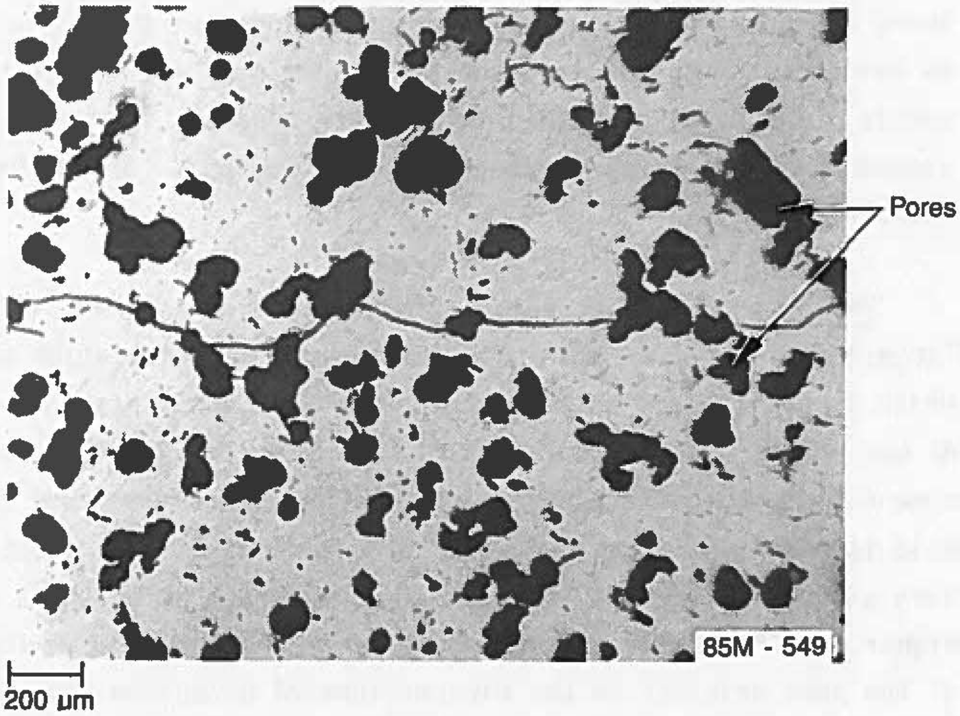

Figure C-2. Pore structure in Particle 7-1.

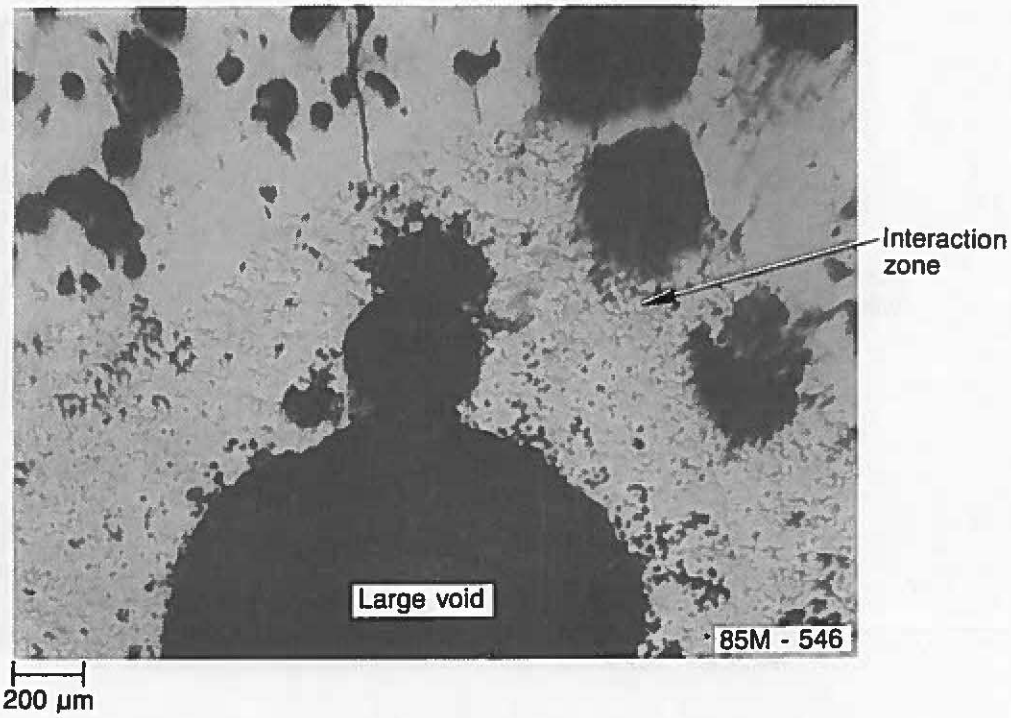

Figure C-3. Large void and surrounding interaction zone.

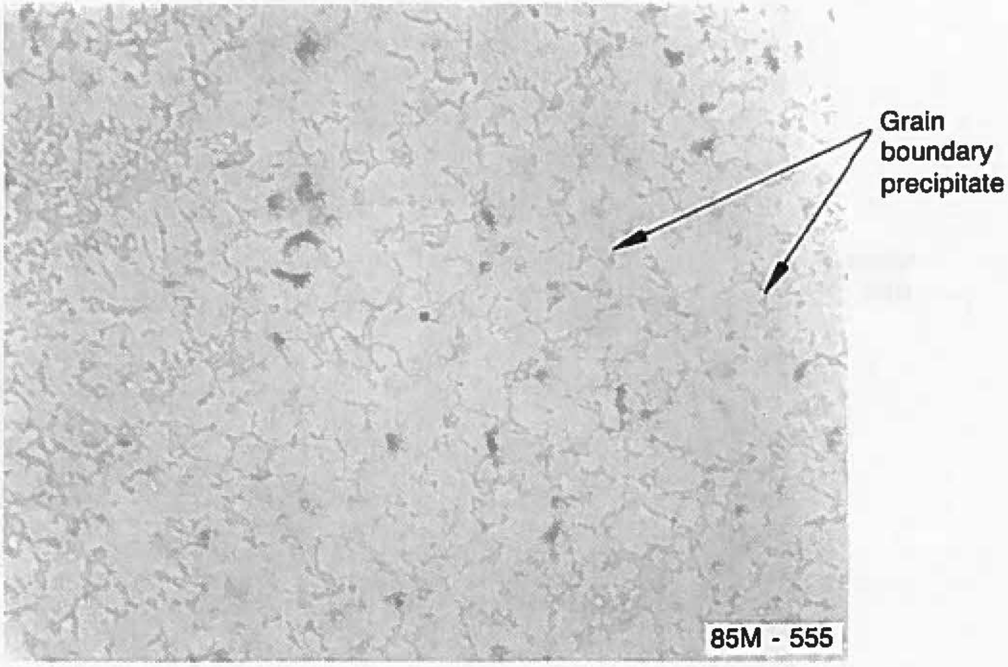

Figure C-4. Grain boundary precipitates in interaction zone.

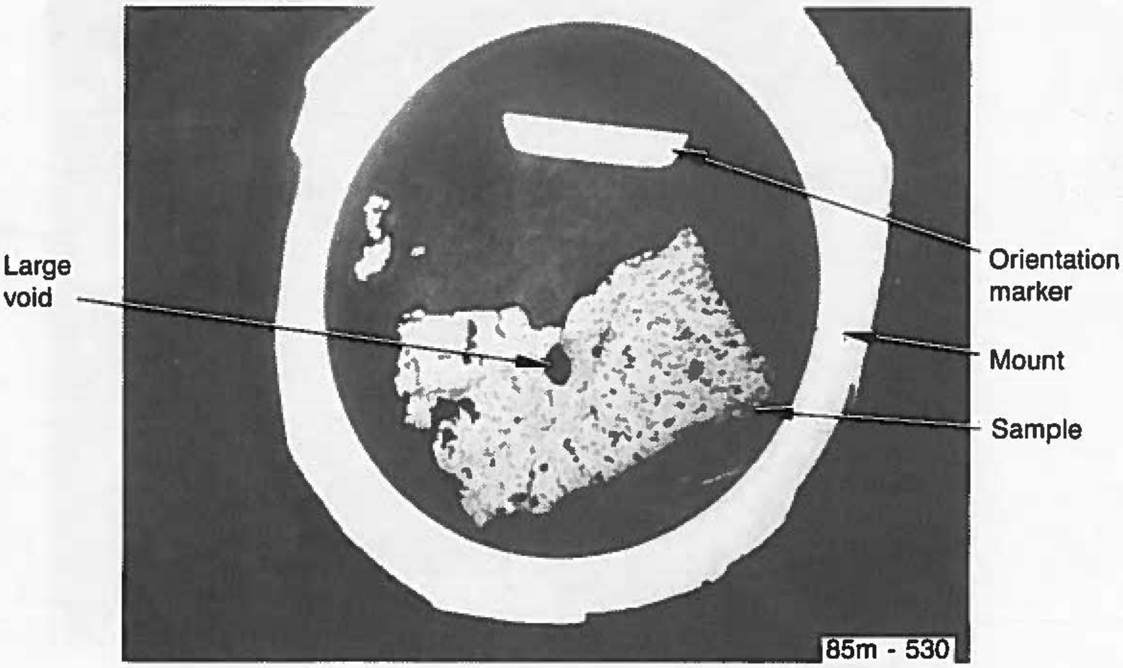

Figure C-5. Cross section from Particle 11-1.

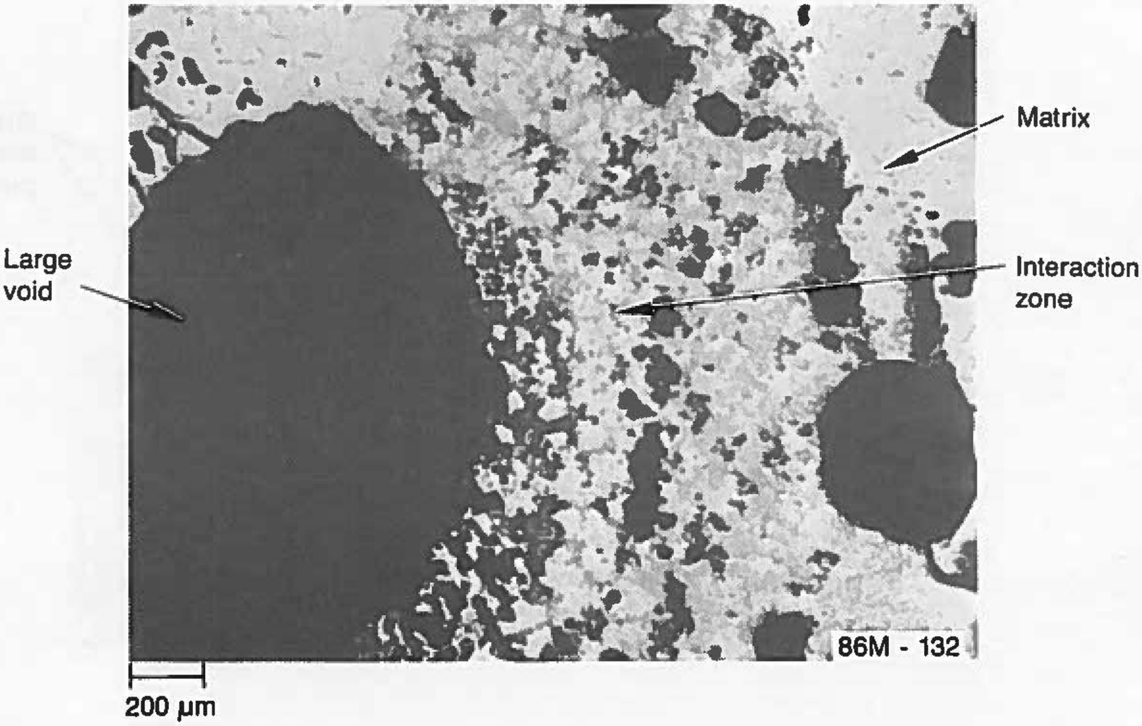

Figure C-6. Interaction zone surrounding large void in Particle 11-1.

Another example of an interaction zone surrounding a void is shown in Figure C-7. In this case, the void is very small, about 150 μm dia. The interaction zone consisted of grain boundary precipitates, the same as other voids.

The structure of the matrix consisted of small voids, as shown in Figure C-8. These voids again are irregular in shape representing some coalescence of spherical voids. Excluding the large void, the average pore fraction of the small voids was 23% (varying from 2.7 to 30.3%).

The structure of the grain boundaries in the interaction zone is shown in Figure C-9. Precipitates are clearly shown in the grain boundaries, along with debris in the voids. Energy dispersive x-ray (EDX) analysis shows that the elements in the grain boundaries were principally iron, chromium, and aluminum or nickel. The latter two elements varied substantially from sample to sample. The debris in the pores is not a result of sawing, grinding, or polishing. The entrapment of debris from these operations is very unlikely, considering the washing and ultrasonic cleaning between each operation. Even a metallic inclusion was removed after ultrasonic cleaning.

Particle 11-2. The polished metallographic section is shown in Figure C-10. Fine porosity is located at the pointed end of the sample (Region 1); large pores with almost no fine porosity were located at the wide end of the sample (Region 2). The measured pore fraction was 30%. The typical structure of Region 1 is shown in Figure C-11. The porosity is small, and in this unetched sample, the grain boundaries were not resolved. However, upon etching this sample, the grain boundaries revealed "dark" and "mottled" areas in the grain boundaries. The "dark" phase in the grain boundaries was composed of iron, chromium, nickel, and aluminum. However, the aluminum content appeared to be lower than that in some other samples. The "mottled" areas were similar in composition to that of the dark areas.

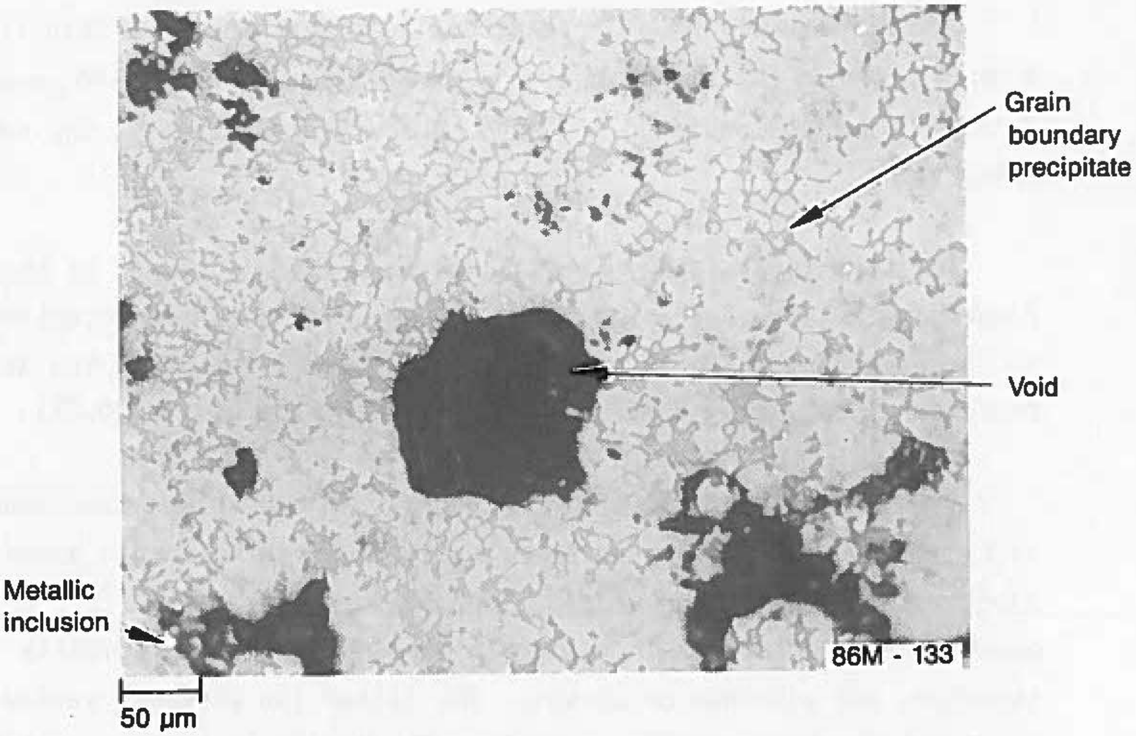

Figure C-7. Interaction zone around small void.

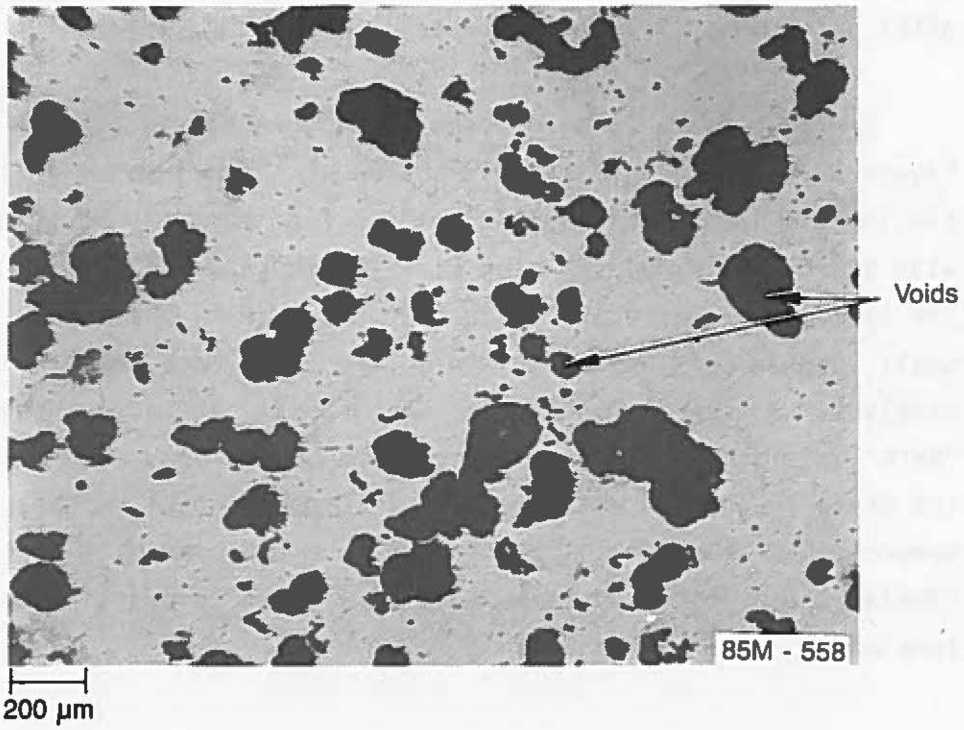

Figure C-8. Pore structure in matrix.

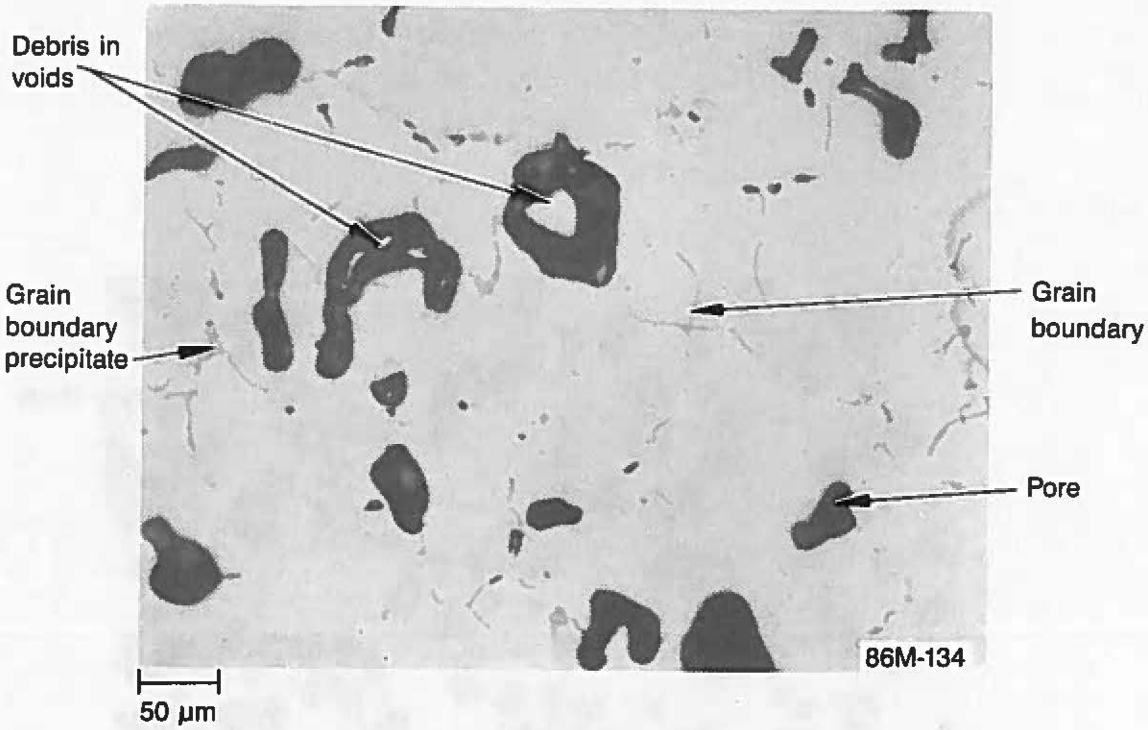

Figure C-9. Grain boundary precipitates and debris in pores in interaction zone.

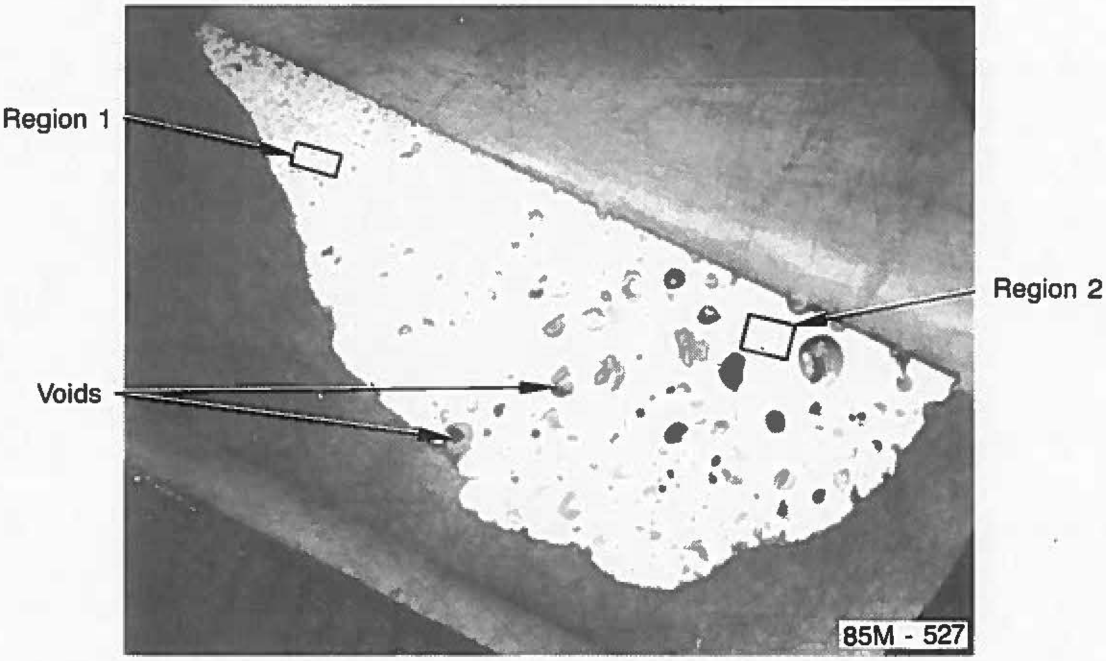

Figure C-10. Cross section from Particle 11-2.

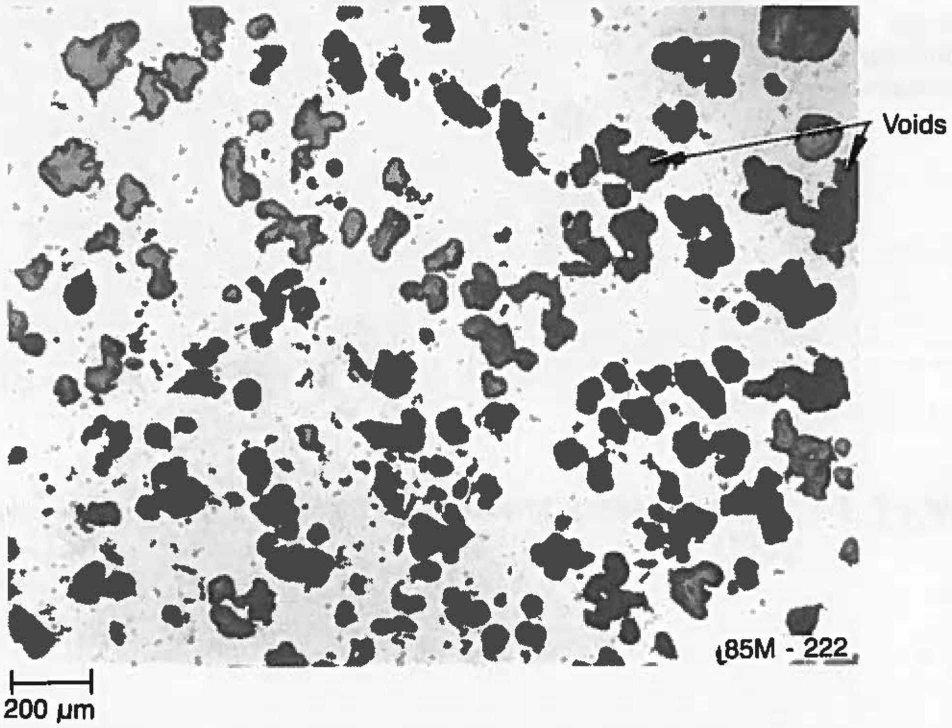

Figure C-11. Pore structure in Particle 11-2.

Metallic inclusions and grain boundary precipitates in Region 1 are shown in Figure C-12. The metallic inclusions were predominantly associated with interaction zones around pores. The EDX analysis of one of the larger metallic inclusions adjacent to a void shows that it was primarily composed of nickel and ruthenium. A light phase in the inclusion, as revealed by the scanning electron microscope (SEM), was very high in ruthenium content. The darker phase in the inclusion was considerably higher in nickel, but EDX analysis still indicates that a significant amount of ruthenium was present.

The typical structure in Region 2 is shown in Figure C-13. This area contained some very fine pores, and the surrounding area around the pores had a mottled structure. This mottled structure appeared to be similar to the grain boundary precipitates found in Region 1.

Particle 11-4. The polished section taken from the longitudinal direction (Section 11-4-C) is shown in Figure C-14. This section contained a number of large voids distributed uniformly across the section, but some fine porosity is located at the sample edge opposite the orientation indicator. The typical structure of this section is shown in Figure C-15. This view shows a few large pores and many small pores. The pore fraction in this sample varied from 8.1 to 80.4%, with an average of 31%. The wide variation in porosity is a result of the variation in large and small pores in this section.

At high magnifications, metallic inclusions in the matrix and inside the pores were resolved. The volume fraction of the metallic inclusions was about 0.8%. This section had more metallic inclusions than Particles 7-1, 11-1, or 11-2. Metallic inclusions in the matrix and grain boundary precipitates are shown in Figure C-16. Debris in the pores, which also included some metallics, is shown in Figure C-17. This debris is similar to the pore debris found in Particle 11-1. A photograph of the pore debris obtained from the SEM is shown in Figure C-18. The EDX analysis shows that the metallic inclusion was silver. A high magnification of a metallic

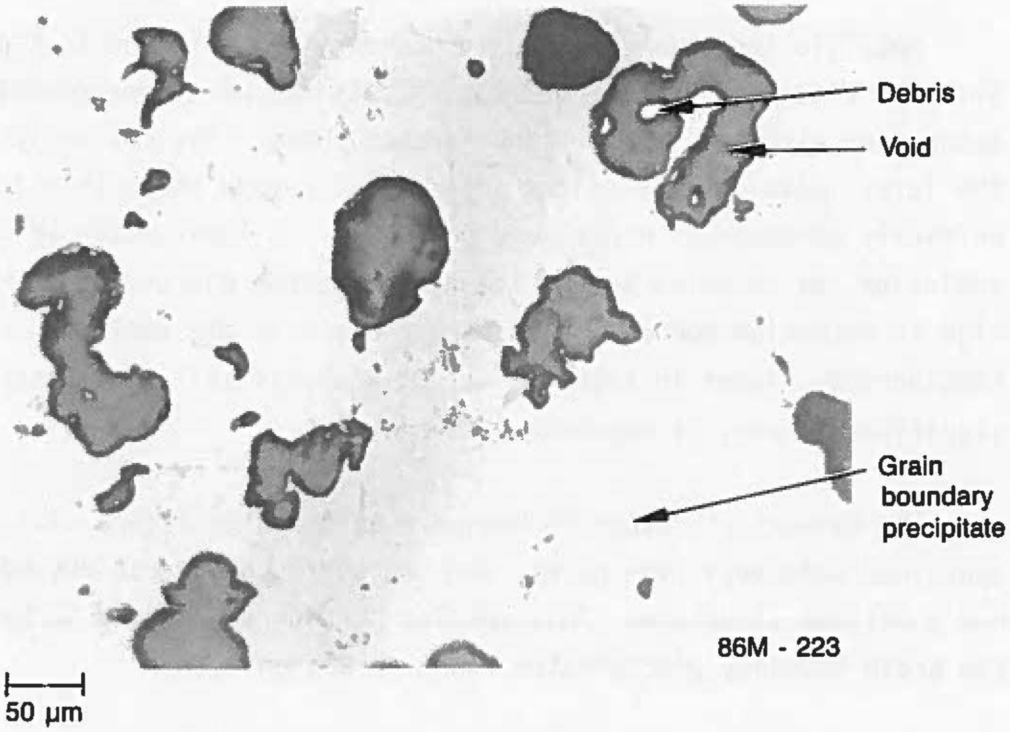

Figure C-12. Microstructure of Region 1.

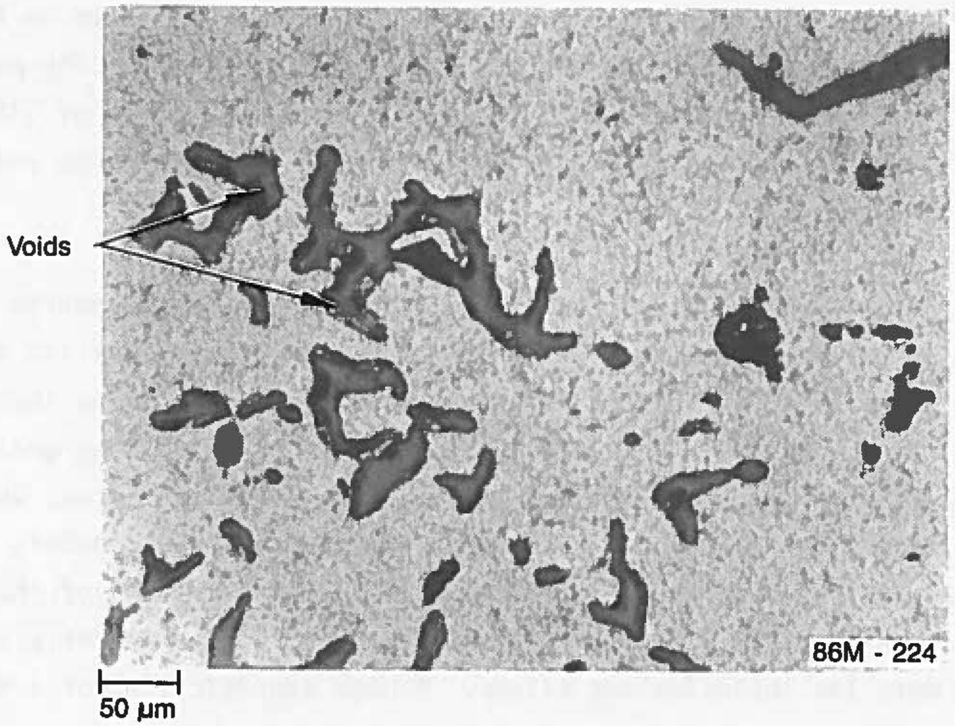

Figure C-13. Typical microstructure of Region 2.

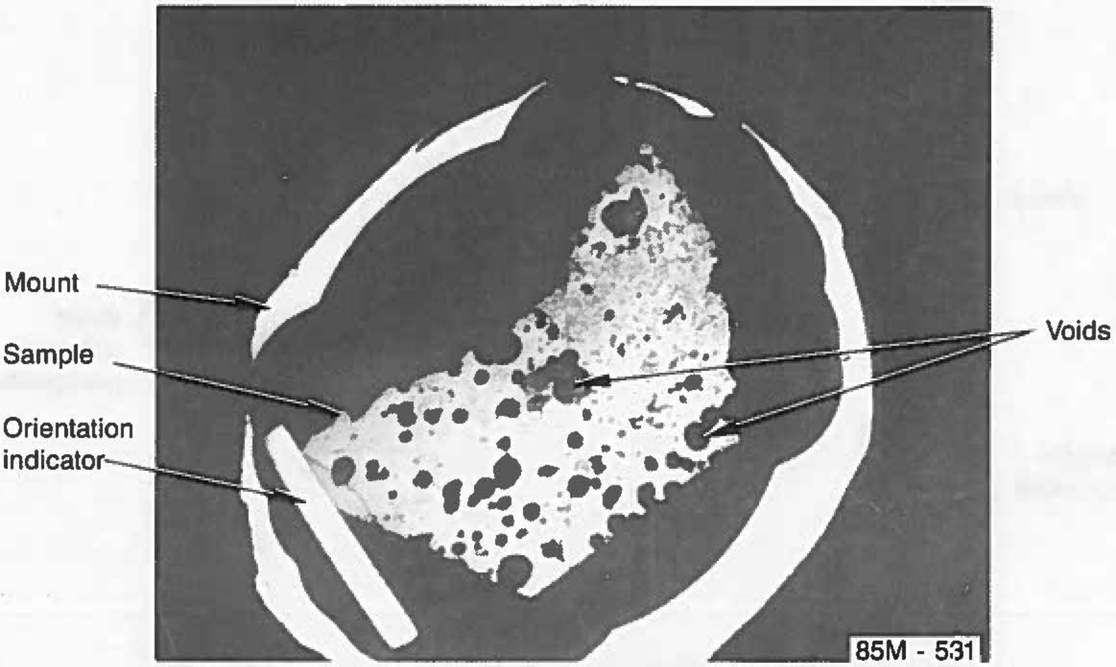

Figure C-14. Longitudinal cross section from Particle 11-4.

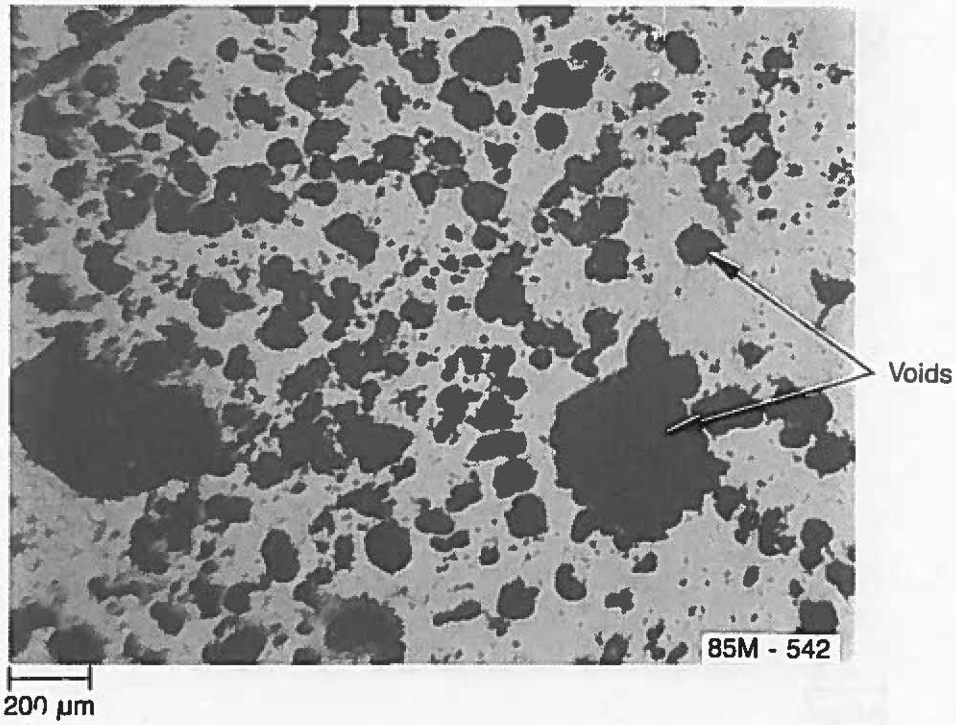

Figure C-15. Pore size distribution.

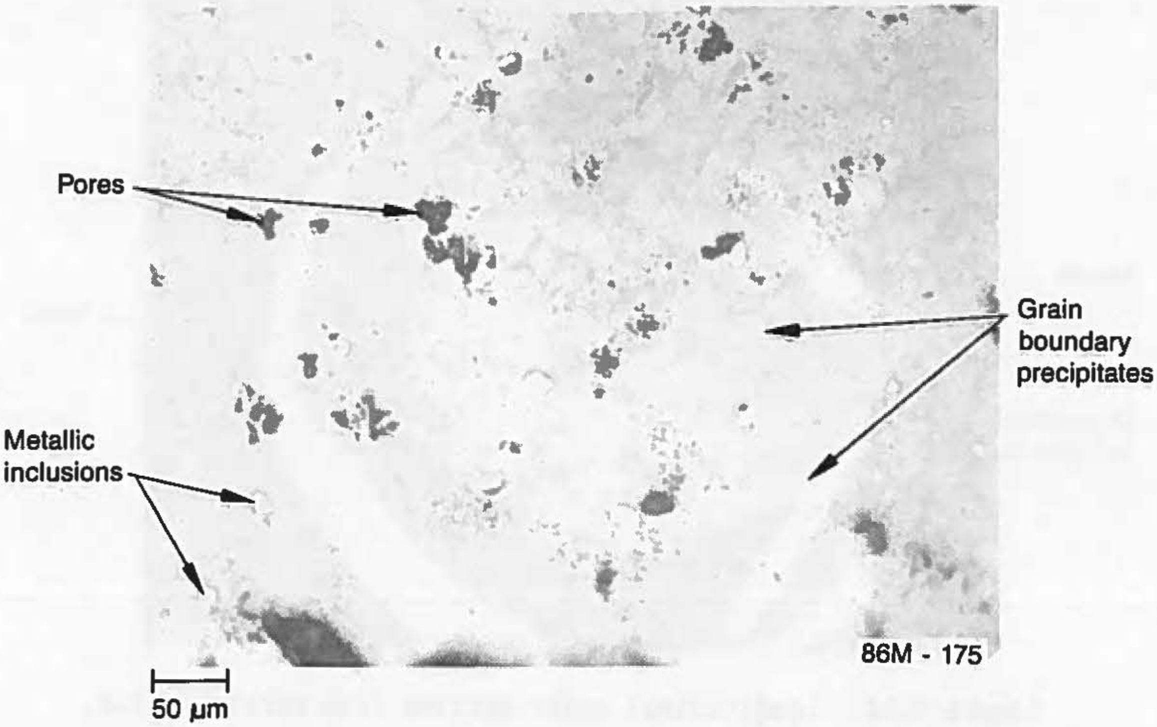

Figure C-16. Grain boundary precipitates and metallic inclusions.

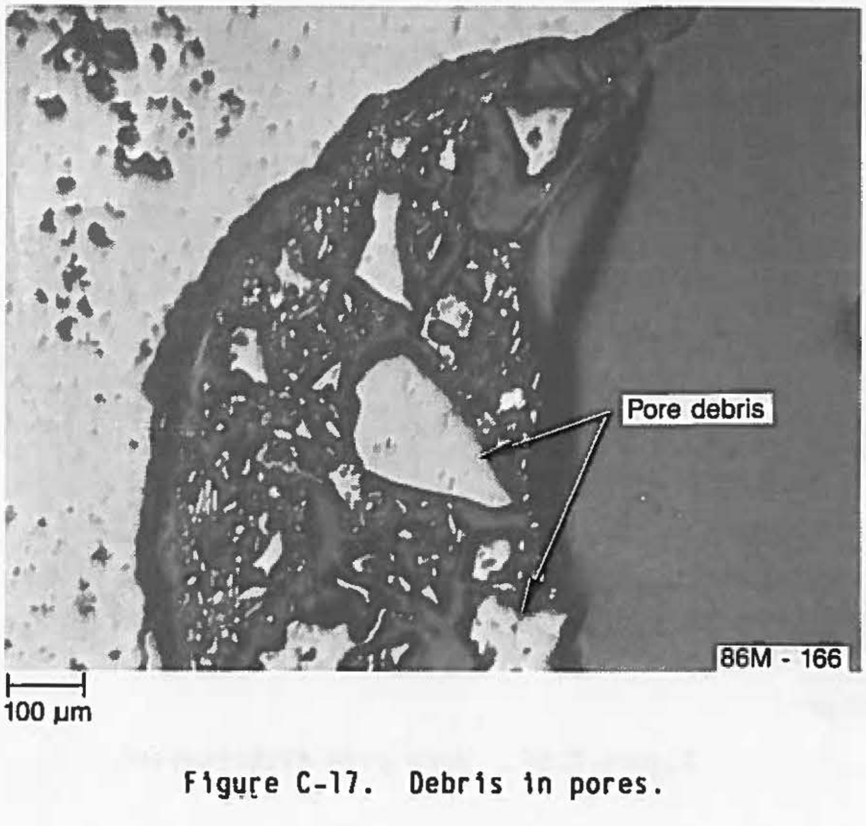

Figure C-17. Debris in pores.

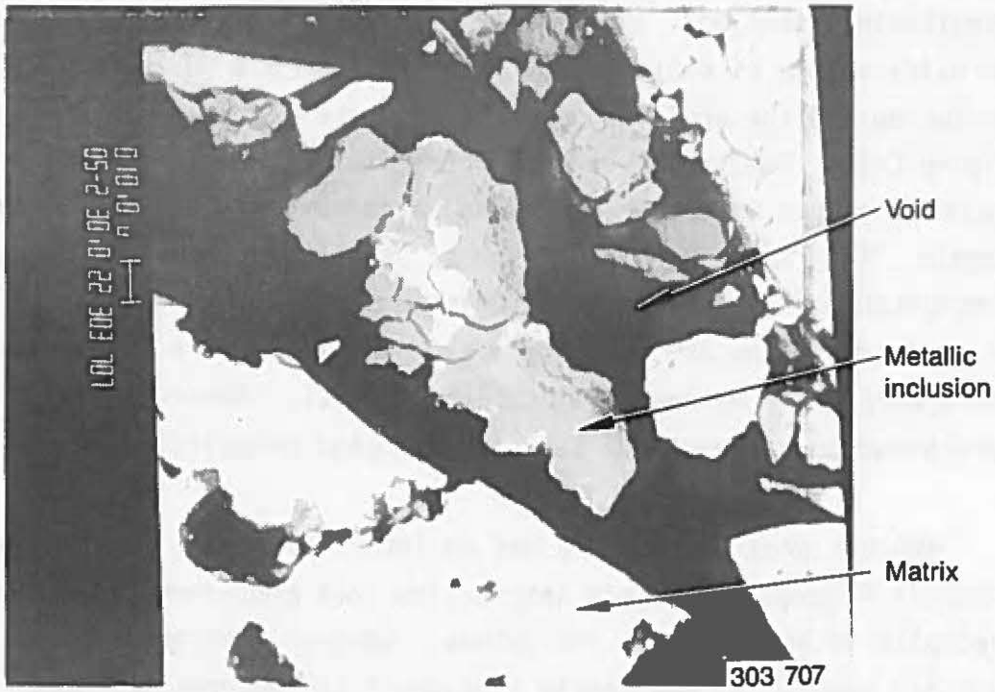

Figure C-18. Metallic inclusion in pore.

inclusion in the matrix is shown in Figure C-19. This figure also shows grain boundary precipitates that are the eutectic structure of the iron and chromium oxides.

The polished section taken from the transverse direction (Section 11-4-A) is shown in Figure C-20. Although this sample contained some large voids, the voids were not as numerous as those in the longitudinal section. The smaller number of voids resulted in an average porosity volume of only 9%, which varied from 0.8 to 13.6%. A metallic inclusion and the grain boundary precipitates near a void are shown in Figure C-21. The grain boundary precipitates are the mixture of iron and chromium oxides with some nickel and aluminum, which varied from sample to sample. This structure is similar to others where the grain boundary precipitates are part of the interaction zone around voids. In some areas, in addition to the grain boundary precipitates, there were areas where there were grain boundary voids (Figure C-22). These grain boundary voids were broad and appeared to be interconnected porosity.

Another area where there was an interaction zone surrounding a pore is shown in Figure C-23. This interaction zone contained grain boundary precipitates and metallic inclusions. However, the metallic inclusions were not present in the matrix outside of the interaction zone. The volume of the metallic inclusions varied from 0.1 to 0.4%.

Particle 11-5. The polished metallographic section is shown in Figure C-24. The porosity varied substantially in this section from areas of only large pores to areas of only small pores. The average void fraction in this sample was 27%, which varied from 6.8 to 34.7%.

At the V-notch and near the center of the sample, an inclusion containing very fine pores compared with the matrix was present. An example of an inclusion is shown in Figure C-25. The EDX analysis shows that this inclusion contained only uranium and no zirconium. From this composition, the inclusion is apparently an undissolved urania fuel pellet. The zirconium concentration decreased with distance into the uranium-rich inclusion. The interface between the urania inclusion and the

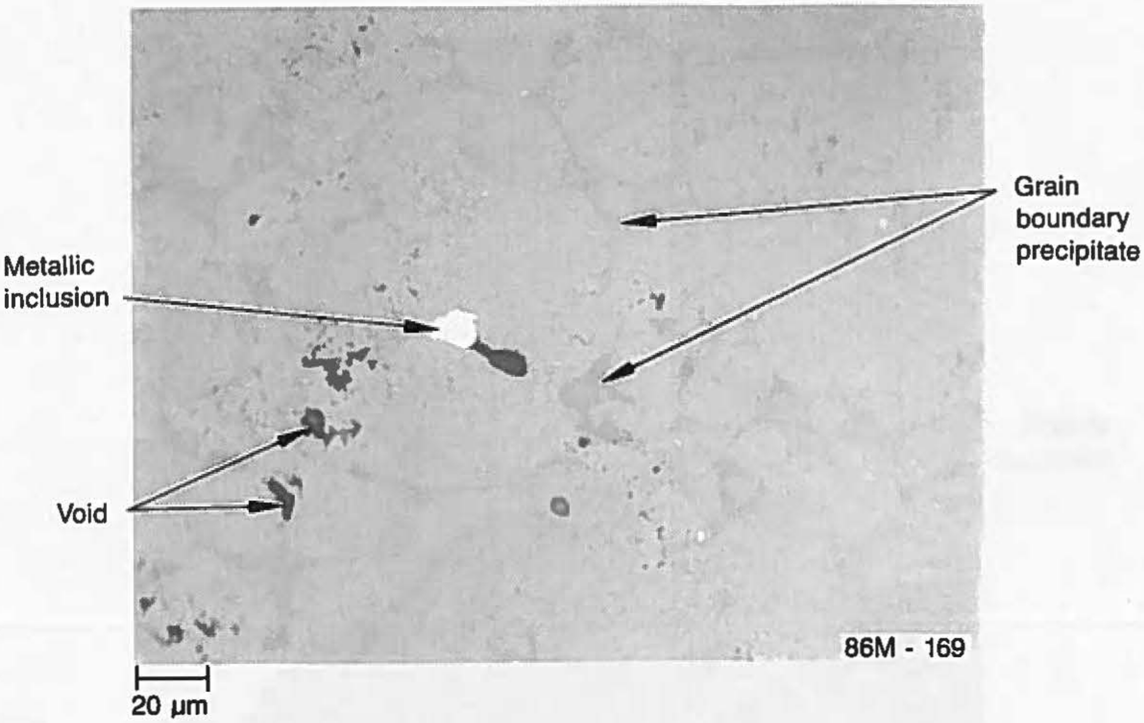

Figure C-19. Metallic inclusion and grain boundary precipitates around void.

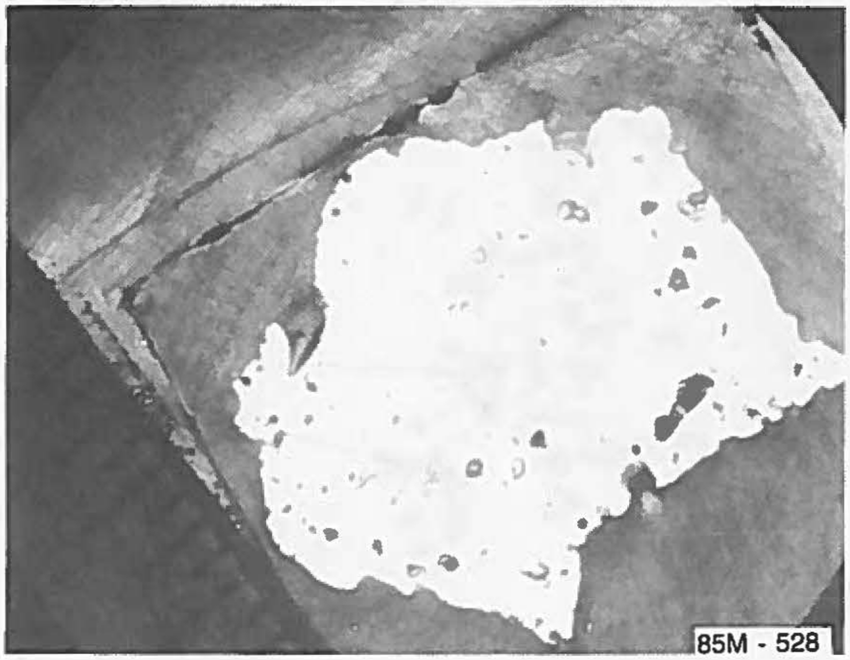

Figure C-20. Transverse section from Particle 11-4.

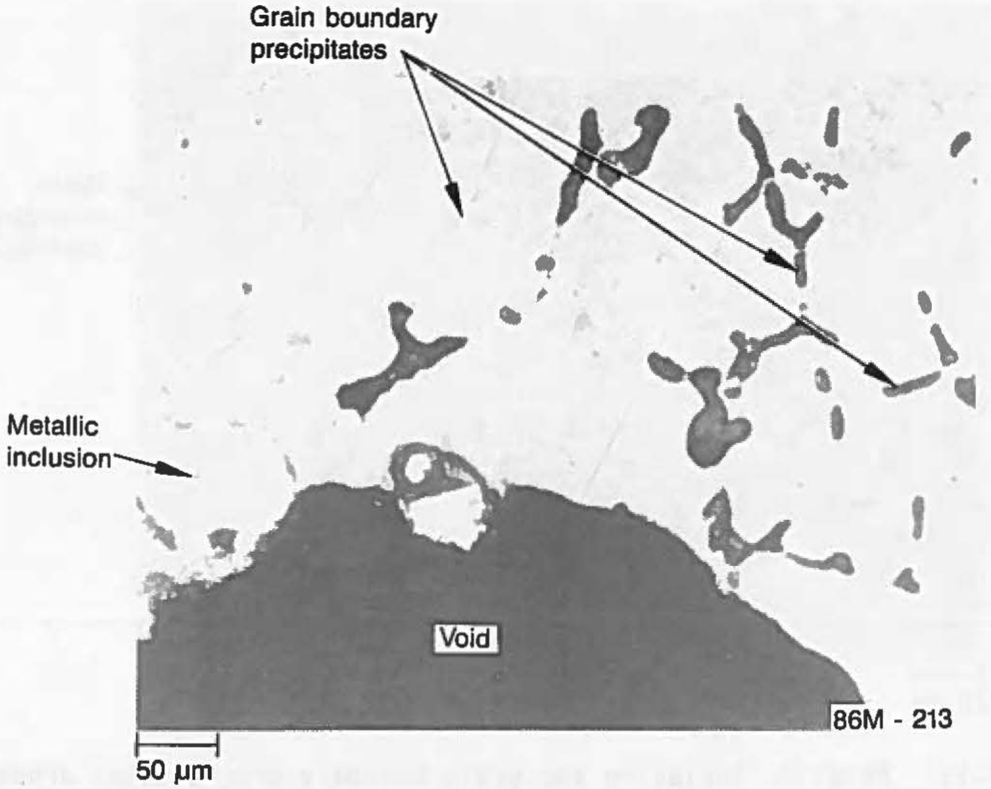

Figure C-21. Metallic inclusion and grain boundary precipitates around void in transverse section.

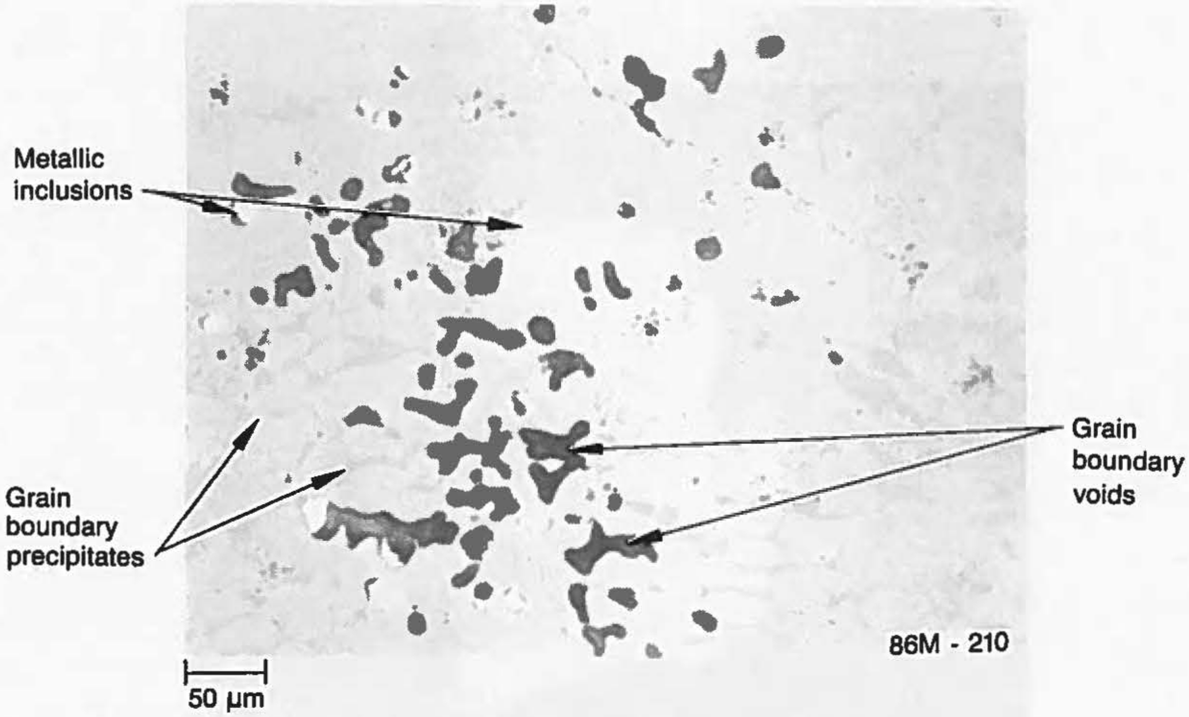

Figure C-22. Grain boundary voids and metallic inclusions.

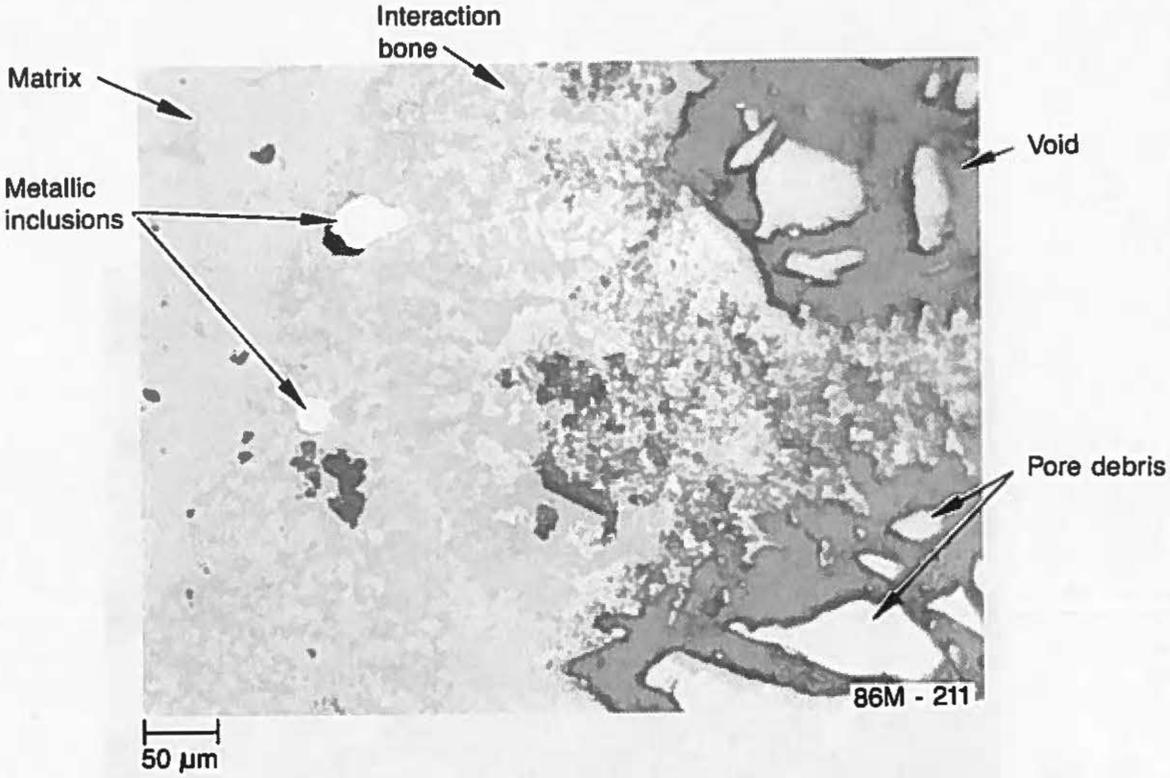

Figure C-23. Interaction zone around void.

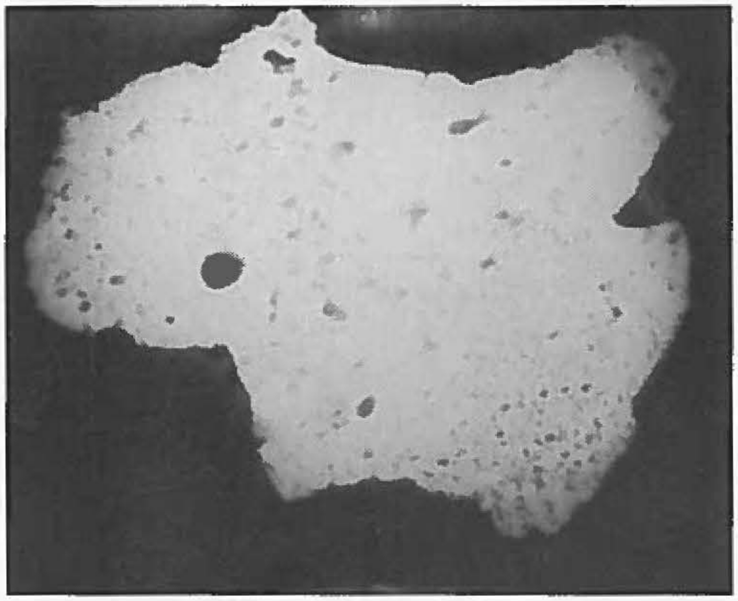

Figure C-24. Cross section from Particle 11-5.

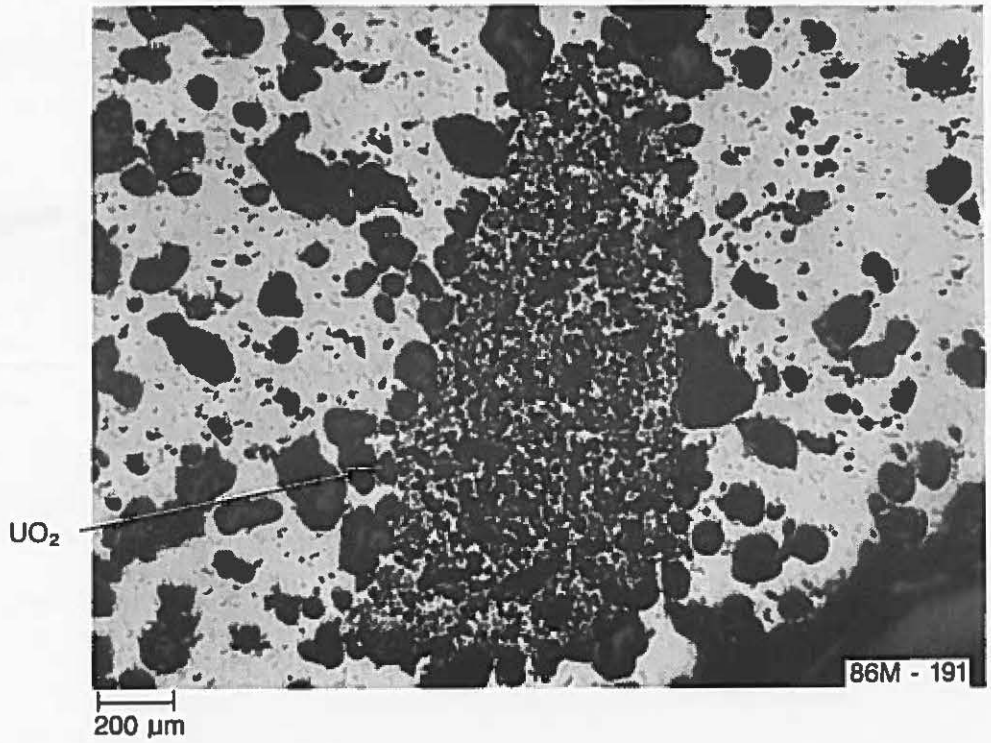

Figure C-25. Urania inclusion in mixed-oxide matrix.

matrix is shown in Figure C-26. A large pore is shown in the matrix compared with many small pores in the urania inclusion. The details of the urania structure is shown in Figure C-27. The grains have not grown very much, but the pores are extremely large for irradiated fuel. Some pore coalescence may have occurred to achieve pores of this size.

Another area contained a region of very large pores separated by a region of fine pores. The structure at the interface is shown in Figure C-28. In the area of small pores, a few large pores were present; in the area of large pores, only a few small pores were present.

A metallic inclusion in a pore and grain boundary precipitates around that pore are shown in Figure C-29. The metallic inclusion had a substructure that was revealed without etching. The EDX analysis of similar metallic debris in pores shows that the only detectable element in these inclusions was silver.

An unusual grain structure was found in this sample in which a second phase appeared to encompass the primary grain (Figure C-30). The primary phase appeared as a light-gray phase; the secondary phase appeared as a darker-gray phase. The grain boundary precipitate was darker than either of the other two phases. Analysis of the primary phase (light-gray phase) using EDX indicates that only uranium and zirconium were present in detectable amounts. Quantitative measurements using wavelength dispersive x-rays (WDX) show the matrix was composed of 66.9 wt% U, 15.6 wt% Zr, 0.9 wt% Fe, 0.4 wt% Cr, 0.3 wt% Si, 0.1 wt% Ni, and 15.8 wt% for other elements. A material balance was achieved if the chemical form of these elements was assumed to be oxides. The EDX analysis results from the secondary phase adjacent to the primary grain structure also show that only uranium and zirconium were present, just as the case for the primary phase. Quantitative WDX measurements indicate that the secondary phase was slightly lower in zirconium than the primary phase. A high magnification SEM photograph Figure C-31 shows details of these two phases.

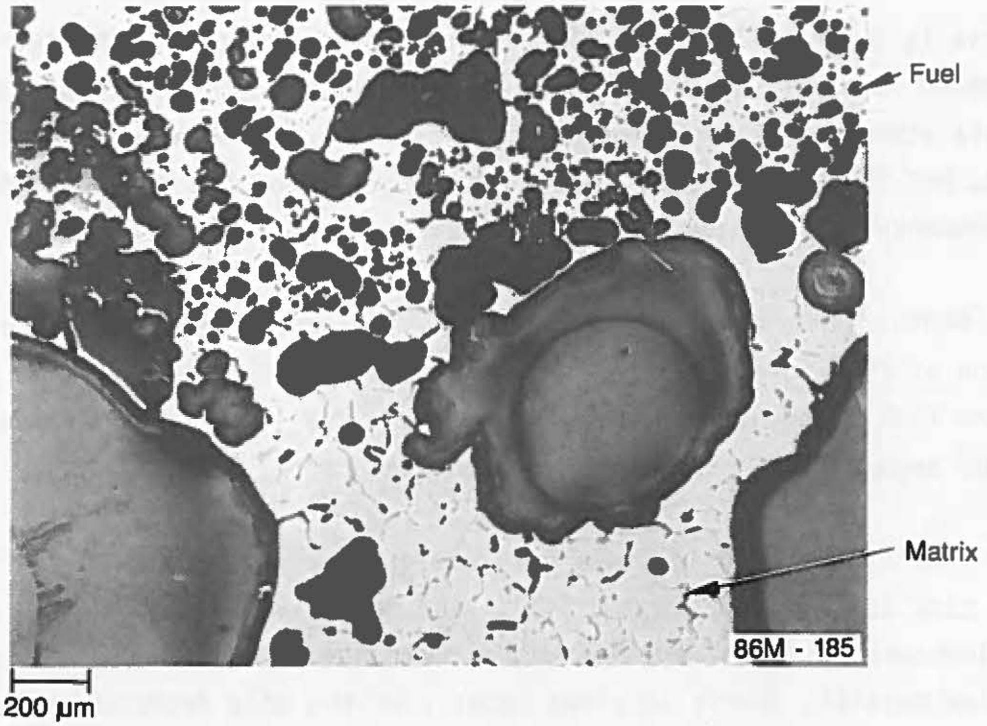

Figure C-26. Pore structure of urania pellet.

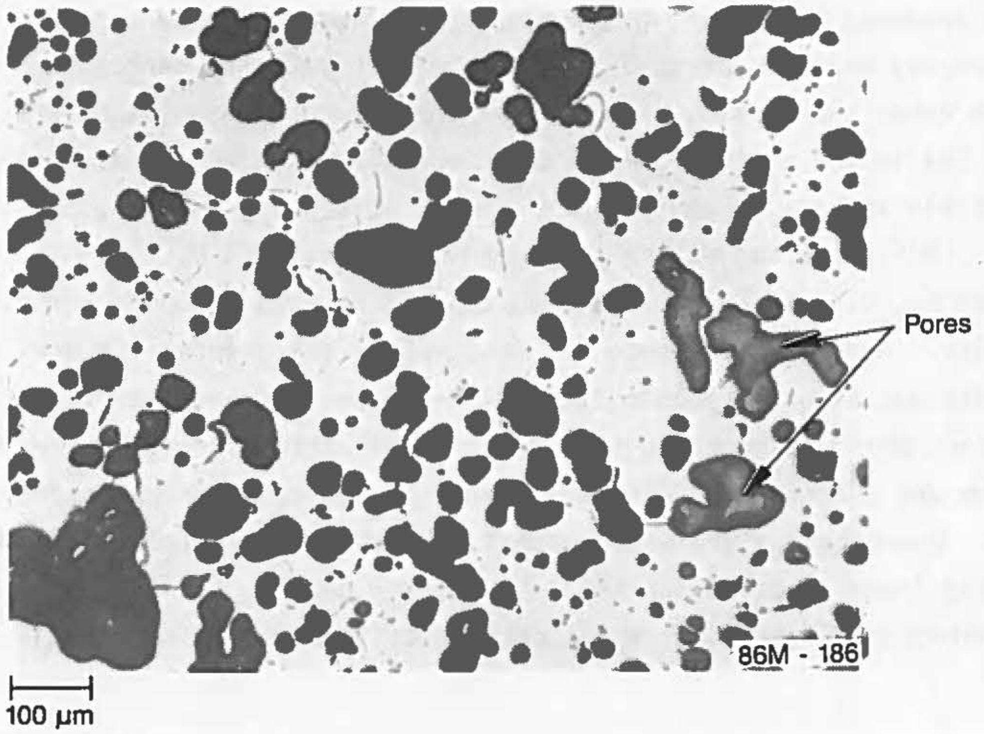

Figure C-27. Fuel/matrix interface.

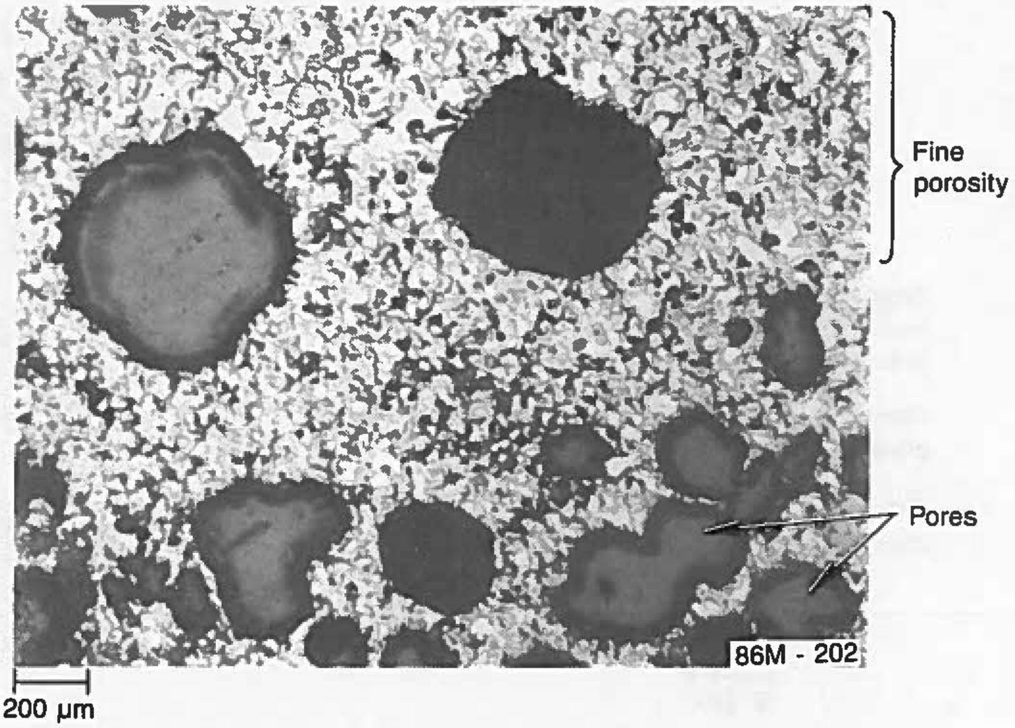

Figure C-28. Pore structure at interface between regions of large and small pores.

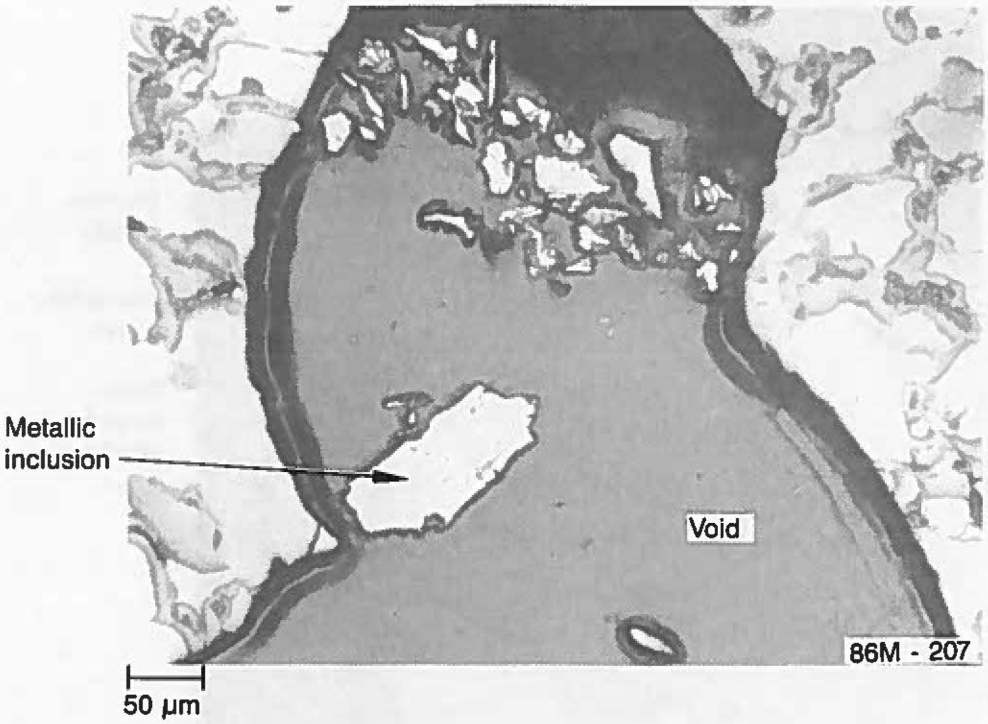

Figure C-29. Metallic inclusion in void.

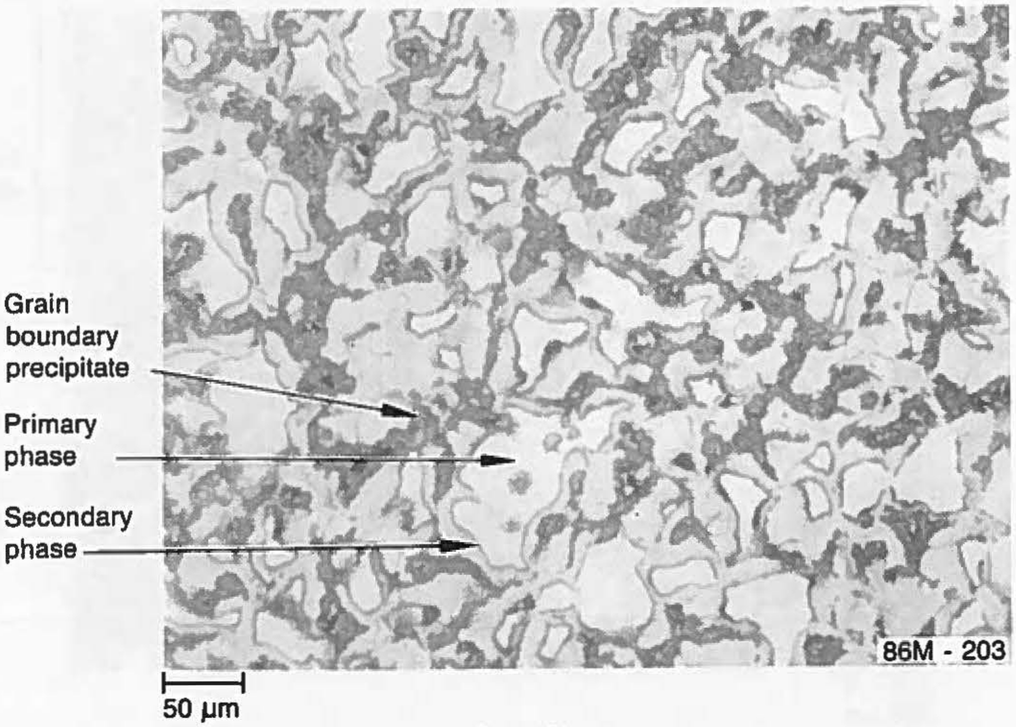

Figure C-30. Primary and secondary phases in matrix.

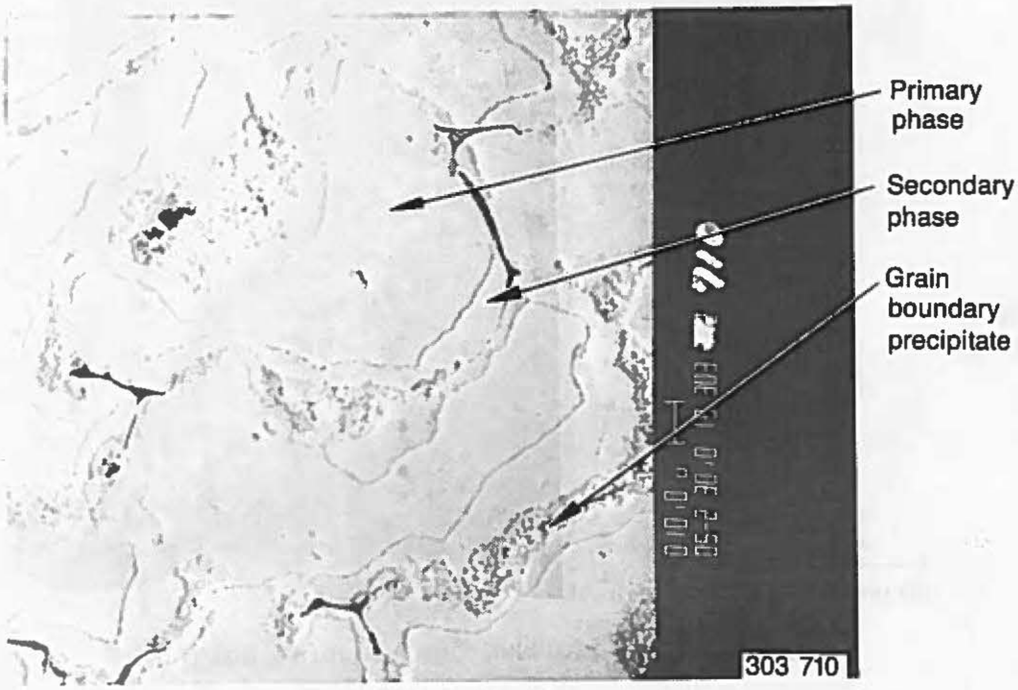

Figure C-31. Backscattered electron image of primary and secondary phases.

The grain boundary precipitates are shown in detail in Figure C-32. The precipitates are a eutectic structure (almost dendritic), which consists of the lower melting point oxides of iron and chromium. These precipitates are also shown in Figure C-33 in very broad grain boundaries.

Particle 11-6. The polished metallographic section of this sample is shown in Figure C-34. It first appeared that this particle might have been the remains of a fuel rod with molten material in the center of the zircaloy cladding. From the metallographic section, small pores were distributed uniformly across the section. The pore fraction from 10 measurements varied from 16.8 to 35.3%, with an average of 25%. From the narrow range of these measurements, a uniform pore distribution is indicated. The typical structure in Region 1 is shown in Figure C-35. This area contains the grain boundary precipitates, like the other samples. After etching, the microstructure was similar to that of Particle 11-5 in which primary grains are surrounded by a secondary phase. However, the amount of the secondary phase was not as much as that of Particle 11-5. The EDX analysis of the primary and secondary phases indicate that the zirconium content is lower in the secondary phase than in the primary phase, which is similar to that of Particle 11-5.

The microstructure of Region 2 is shown in Figure C-36. The grain structure is revealed without etching because of the grain boundary precipitates. The pores are very small and uniformly distributed. A higher magnification of this structure is shown in Figure C-37. The pores are slightly larger than the grains. The grain boundary precipitates are quite evident at this magnification. The details of the grain boundary precipitates and a metallic inclusion at a void is shown in Figure C-38. The grain boundaries are dark and appear to have a mottled appearance at this magnification.

An example of an interaction zone around a void is shown in Figure C-39. Although there are a few other voids in this interaction zone, the nucleus of this zone appears to be centered at a void containing

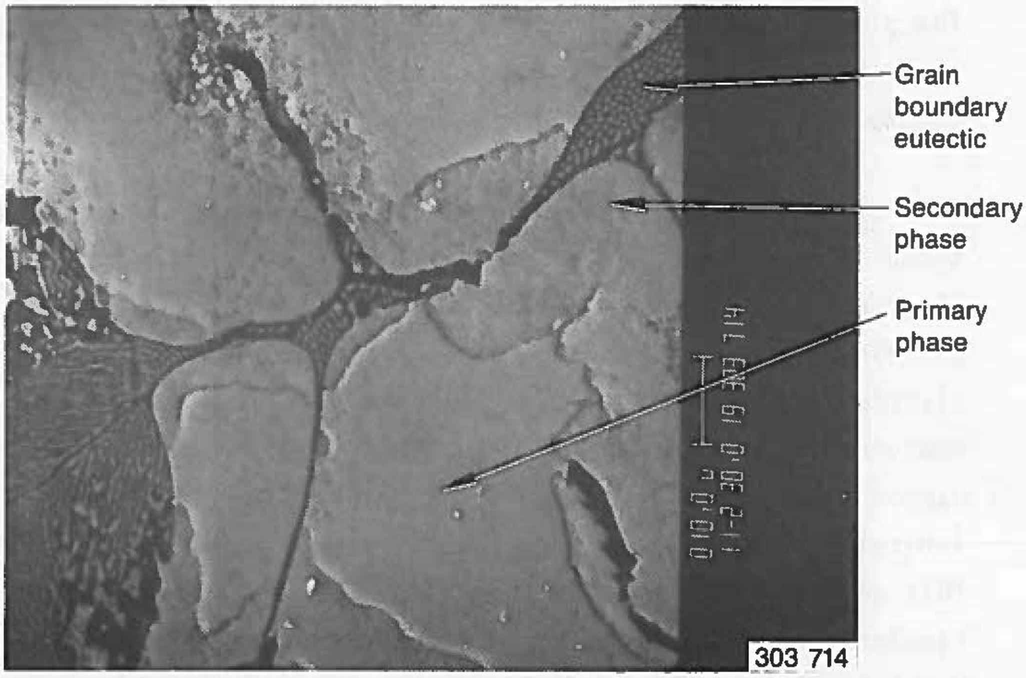

Figure C-32. Eutectic structure in grain boundaries with primary and secondary phases in matrix.

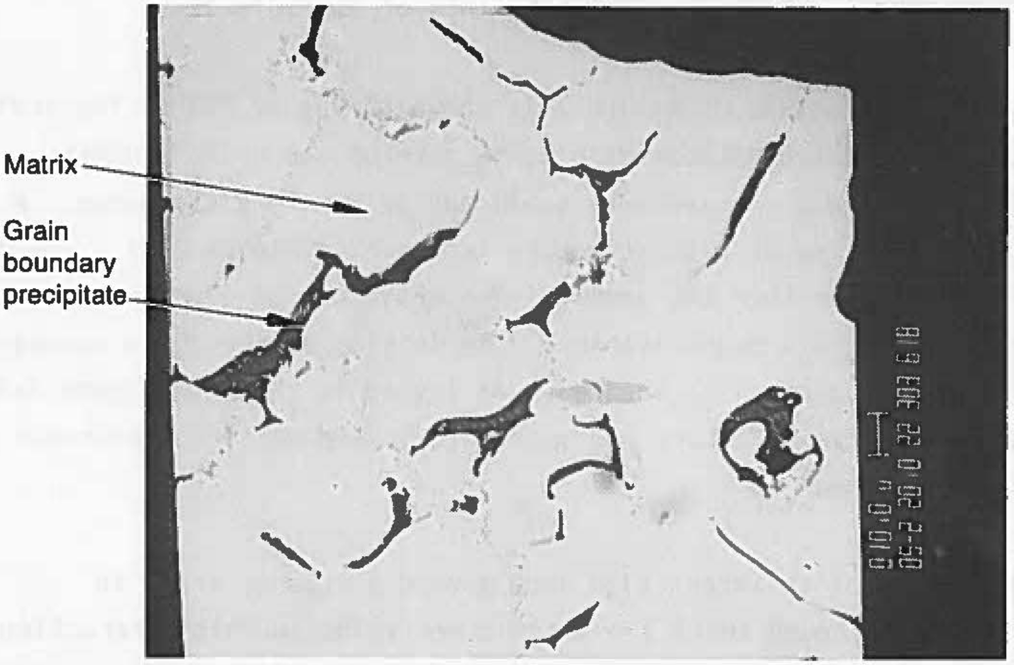

Figure C-33. Backscattered electron image of grain boundary precipitates.

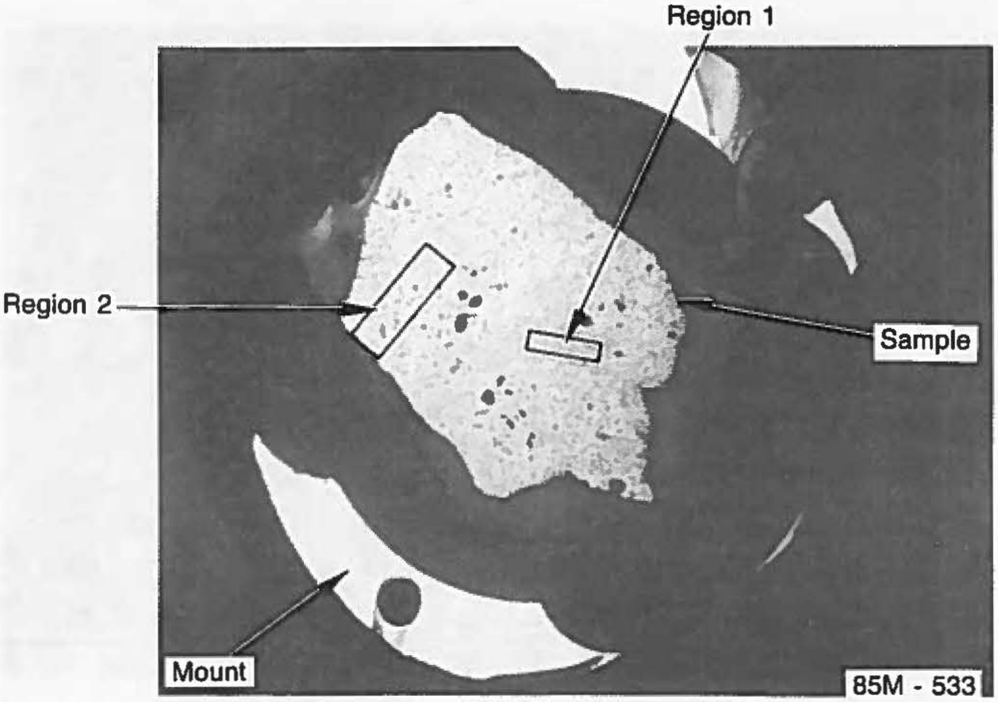

Figure C-34. Cross section from Particle 11-6.

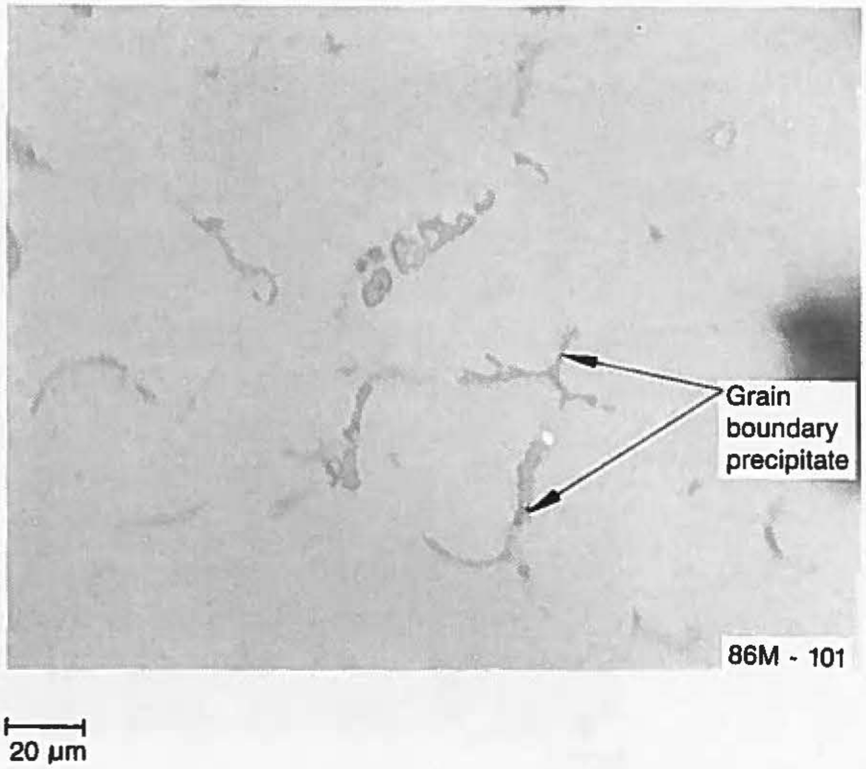

Figure C-35. Typical structure of Region 1.

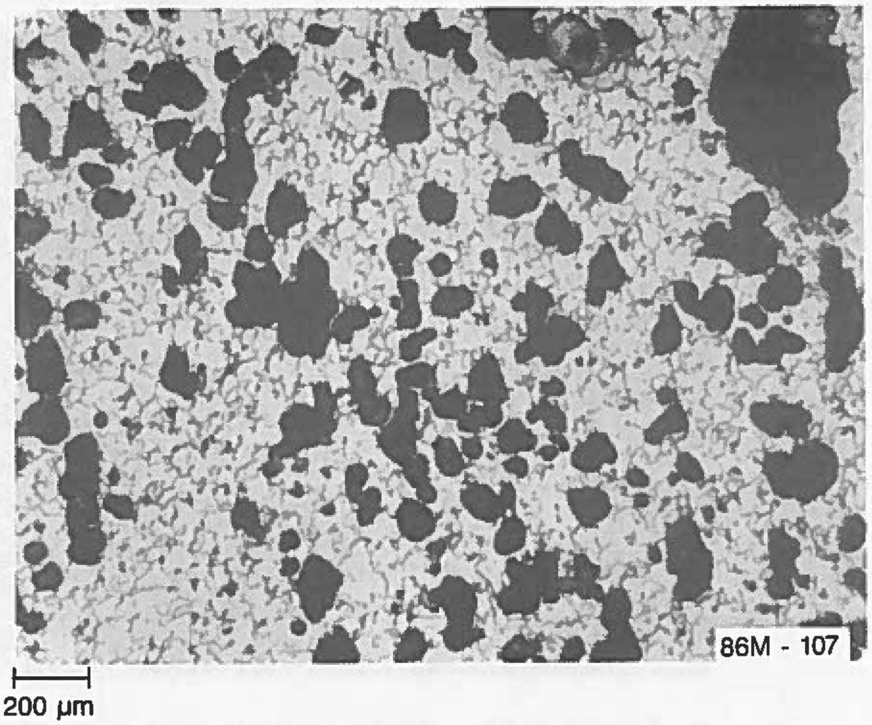

Figure C-36. Typical microstructure of Region 2.

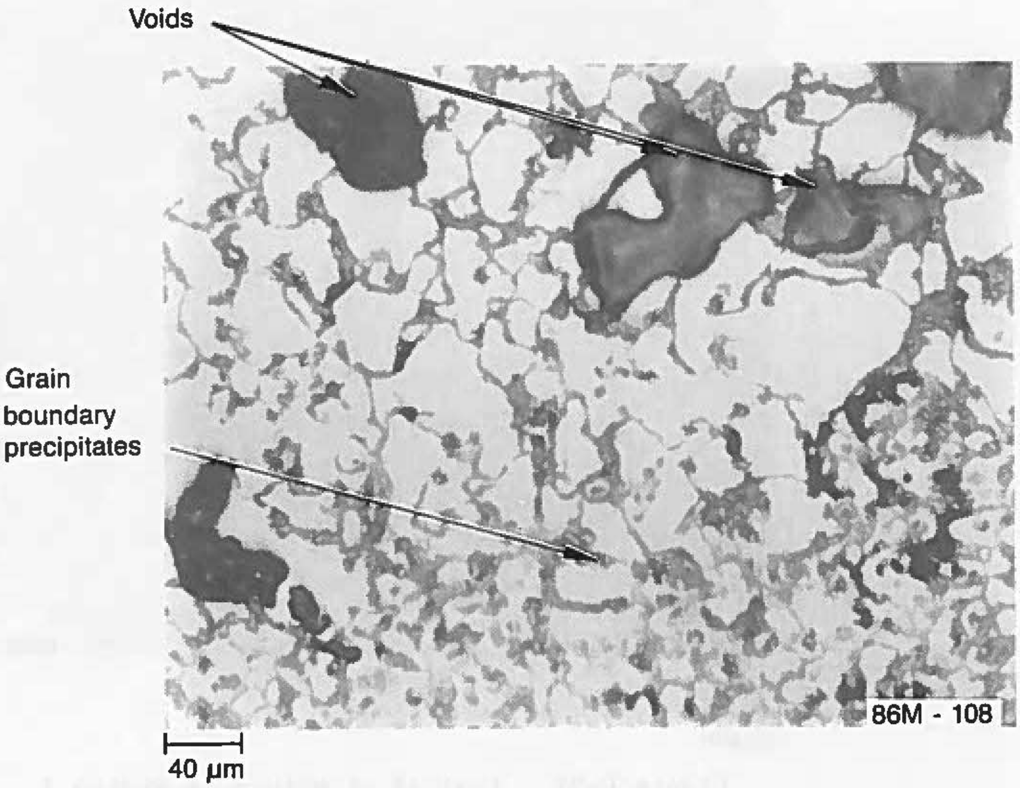

Figure C-37. Interaction zone containing grain boundary precipitates.

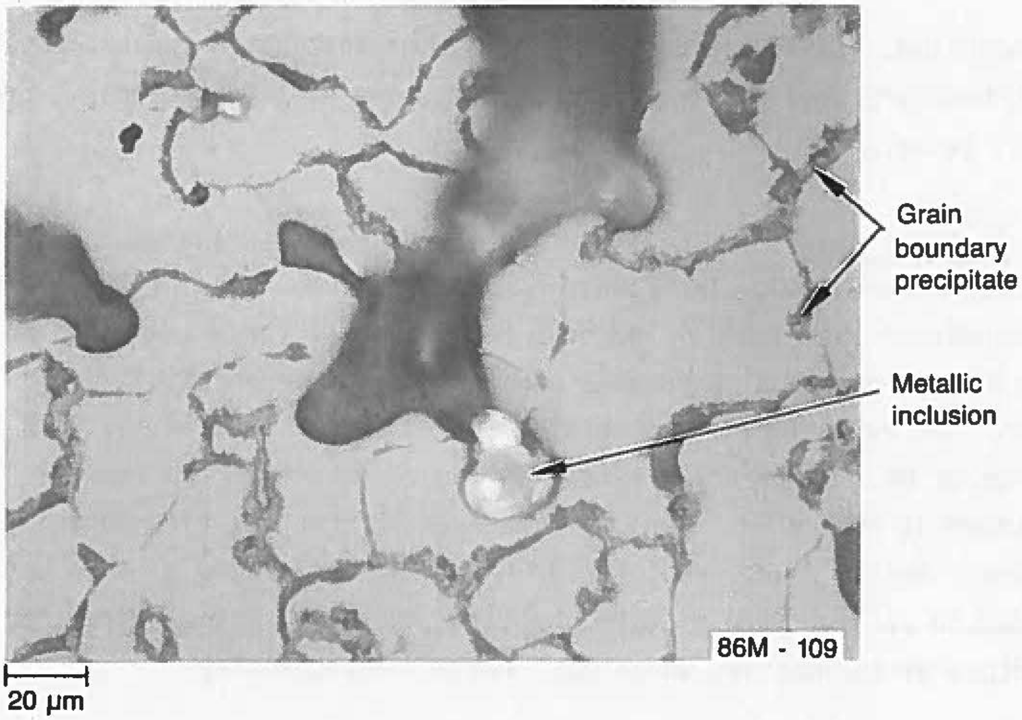

Figure C-38. Detailed microstructure of grain boundary precipitates.

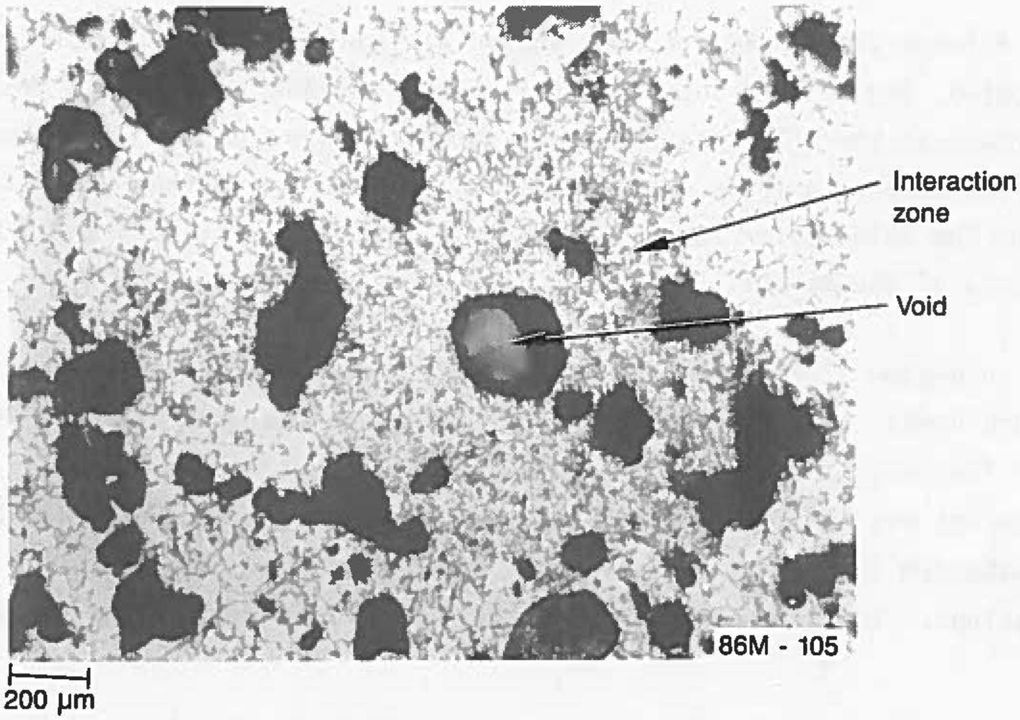

Figure C-39. Example of interaction zone around void.

an inclusion. This zone is similar to other interaction zones containing grain boundary precipitates that are a mixture of iron, chromium, and nickel oxides.

Particle 11-7. The polished section of the metallographic sample is shown in Figure C-40. The sample consisted of two types of structures. In the middle of the sample is an area consisting of large voids and no fine porosity; at each end is an area consisting of fine porosity, but no large voids. The porosity in this section varied from 2.1 to 14.4%, with an average of 8%. Three areas were examined to determine the typical structure in each area. Region 1 was examined for the fine porosity present. Region 2 was examined for the structure around a large void located in an area free of fine porosity. Region 3 was examined for the structure of the matrix, which was free of fine porosity.

The fine porosity in Region 1 is shown in Figure C-41. The matrix material appears very dark; the details of the matrix are shown in Figure C-42 in which the ceramic grains are surrounded with metallic precipitates in the grain boundaries.

A large void in Region 2 is shown in Figure C-43. The pore is elongated, and an interaction zone is present around this void. The interface at the interaction zone is shown in Figure C-44. The matrix material appears uniform in composition with only a few small pores. Inside the interaction zone, islands of a second material appear to float in a sea of the matrix.

In Region 3, metallic inclusions were present in the matrix (Figure C-45). Metallic inclusions similar to these were examined with EDX. The results show that the primary constituent of the metallic inclusions was nickel with small amounts of tin and iron. Trace quantities of ruthenium and tellurium were found in some of these metallic inclusions. The volume fraction of the metallic inclusions was about 0.1%.

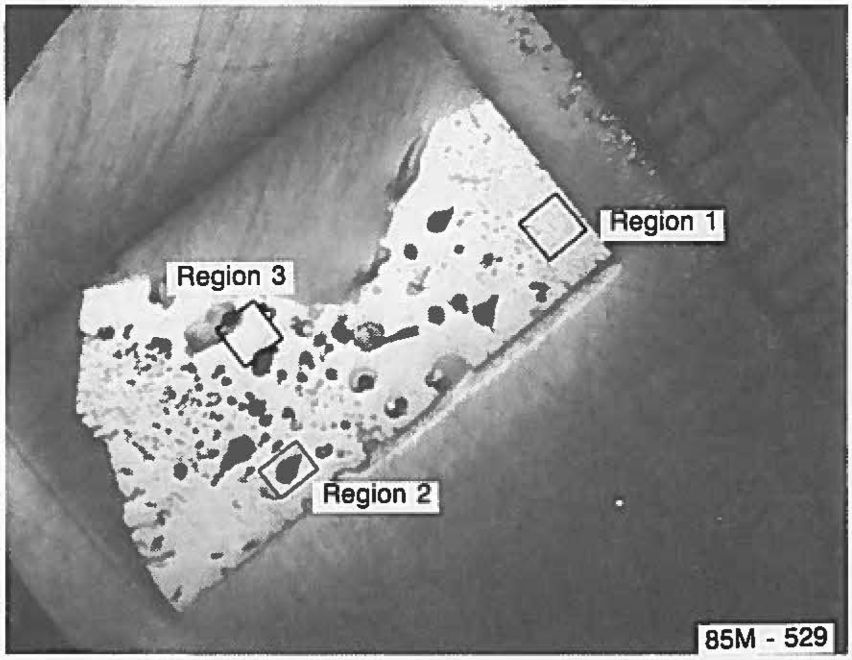

Figure C-40. Cross section from Particle 11-7.

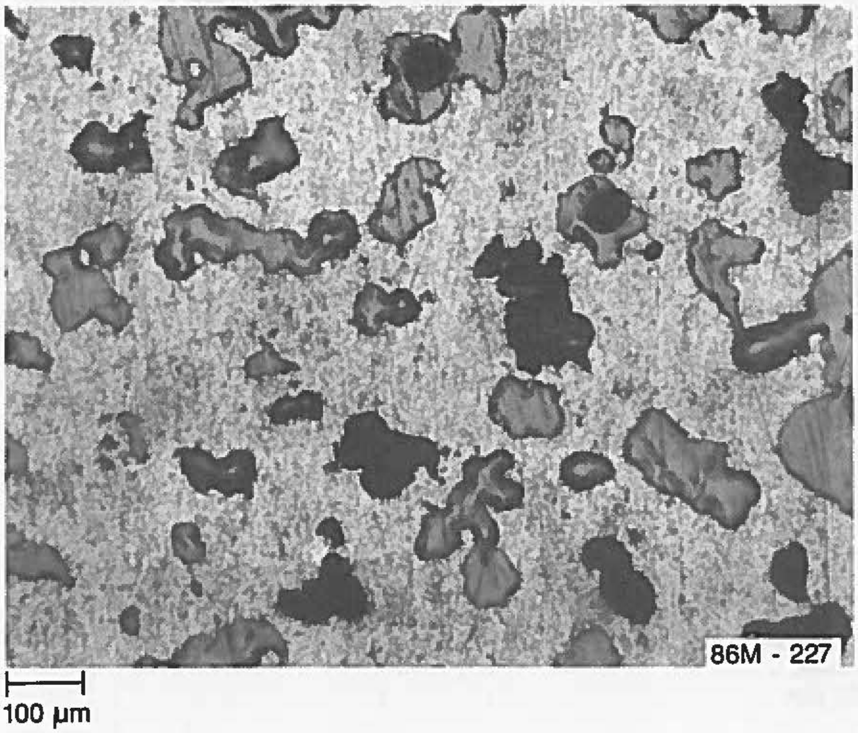

Figure C-41. Fine porosity in Region 1.

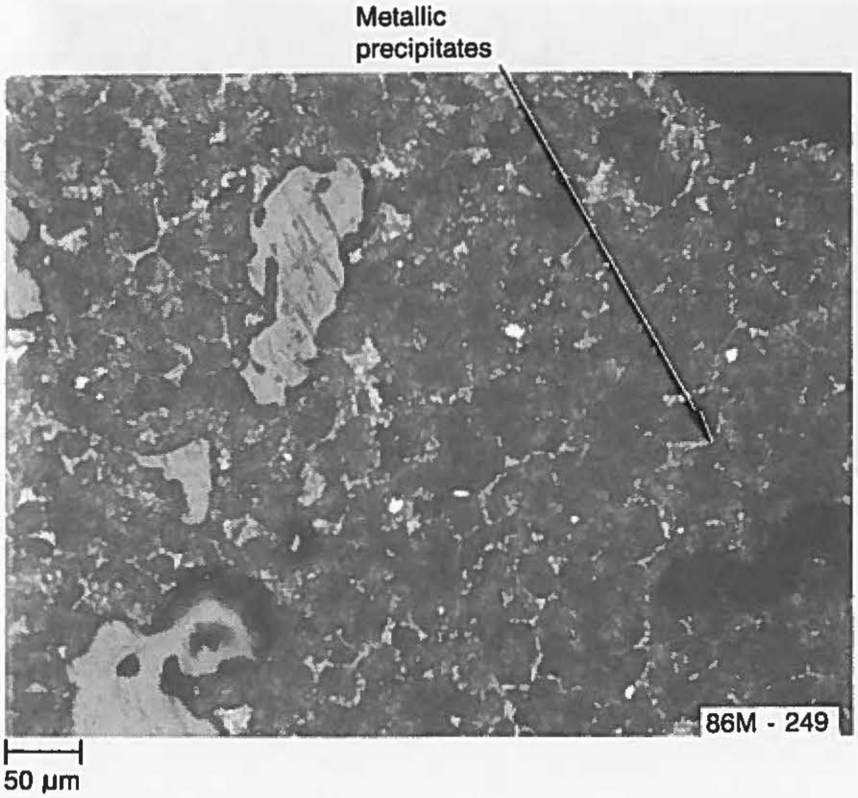

Figure C-42. Metallic precipitates in grain boundaries in Region 1.

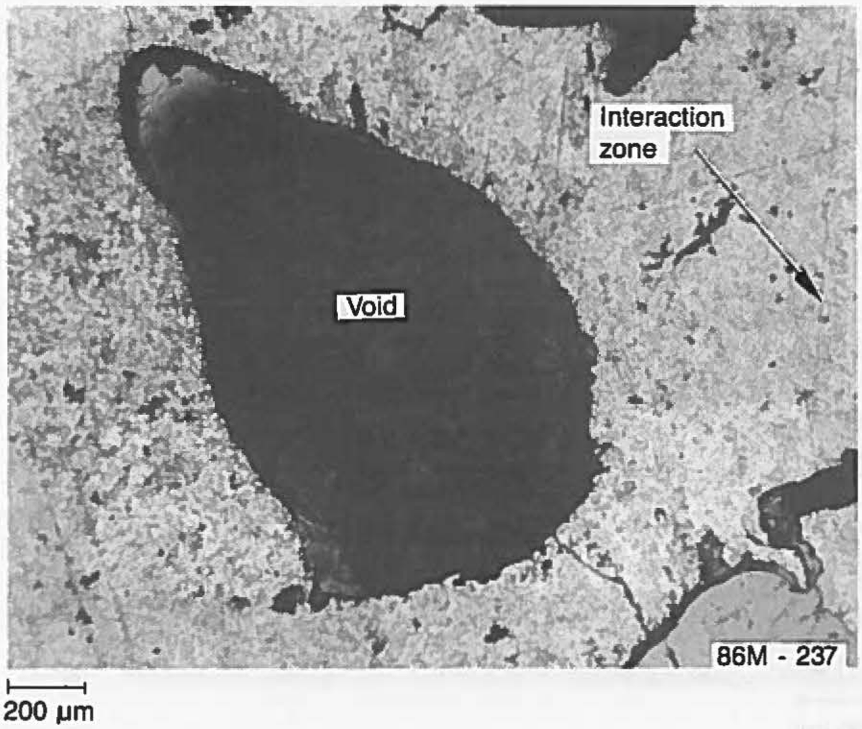

Figure C-43. Interaction zone around void in Region 2.

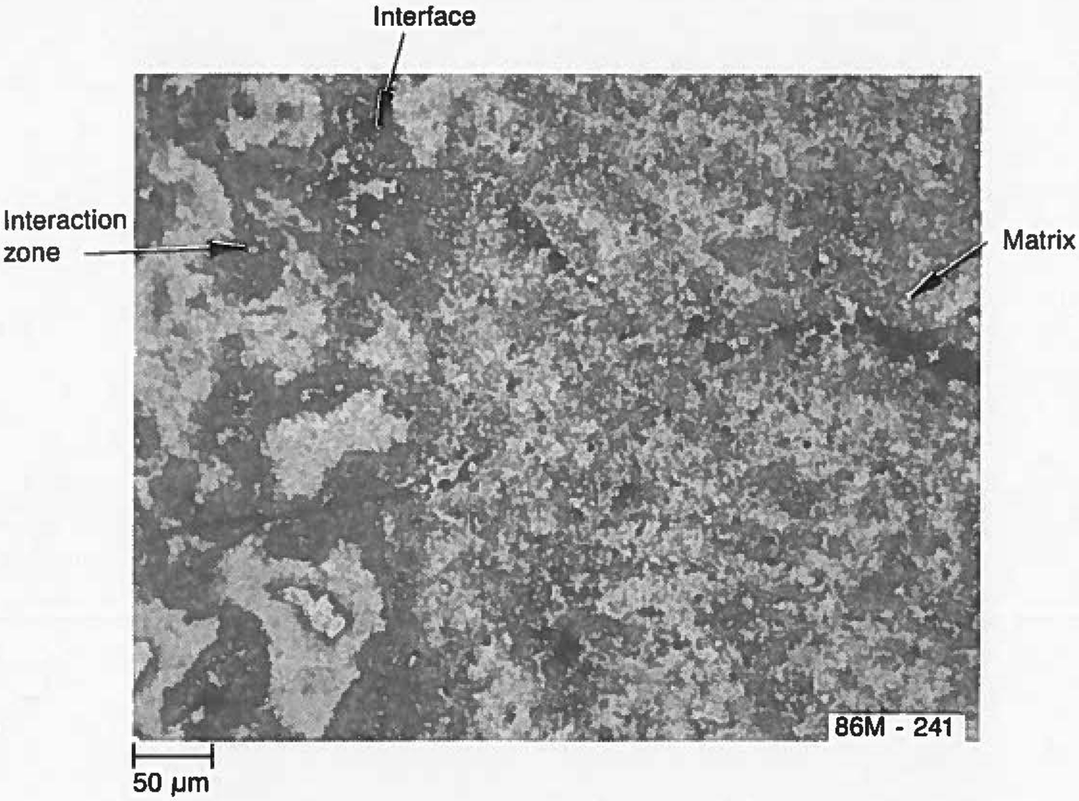

Figure C-44. Two-phase structure in interaction zone.

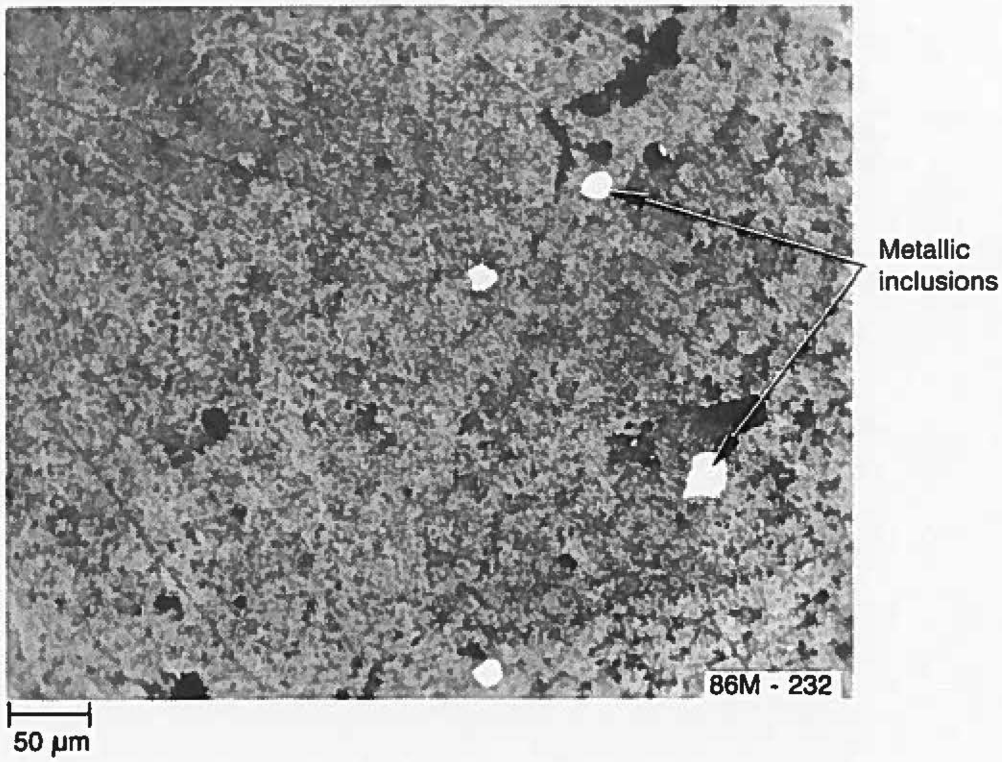

Figure C-45. Metallic inclusions in Region 3.

APPENDIX D

ARGONNE SAMPLE ACQUISITION

APPENDIX D

ARGONNE SAMPLE ACQUISITION

As part of the effort to involve other facilities in the examination of samples from the TMI-2 reactor, samples were obtained for Argonne National Laboratory (ANL) to perform elemental analysis using the scanning electron microscope (SEM) with energy dispersive x-ray (EDX) capabilities, Auger spectroscopy, and wavelength dispersive x-ray (WDX) spectroscopy using an electron microbe. The U.S. Nuclear Regulatory Commission (NRC) provided funding for these examinations, and ANL has prepared a separate report of their examination results. A brief description of the samples obtained for ANL is presented here in order to complement the metallographic results and assimilate the elemental analysis results with the metallographic results.

Eight metallographic samples were shipped to ANL representing the seven particles obtained from TMI-2 reactor. Four of these were the same mounts used at the Idaho National Engineering Laboratory (INEL). Because the elemental analysis was not planned to be performed at the INEL, these samples were sent to ANL for this analysis so that the results could be incorporated with the metallography results. Photographs of the four Particles, 7-1-A, 11-1-B, 11-4-C, and 11-6-A shipped directly to ANL, are shown, respectively, in Figures D-1, D-2, D-3, and D-4. These samples were mounted in a lead/bismuth alloy contained in a brass holder in order to reduce the organic contamination for faster outgassing on the Auger and SEM, minimizing interference from organic contamination during Auger analysis, and reducing the radiation levels. However, some organics were introduced into the samples because two of the samples had to be cast into epoxy for sectioning before mounting.

The remaining four samples examined at the INEL were cast in epoxy contained in a 5-in. ring because of the size of these samples. The large sections were used in order to ensure that all the specific features could be detected, and any gradients present would be measured. However, ANL required small samples for their analysis. From the results of the metallography, locations in the large sections were identified for unique

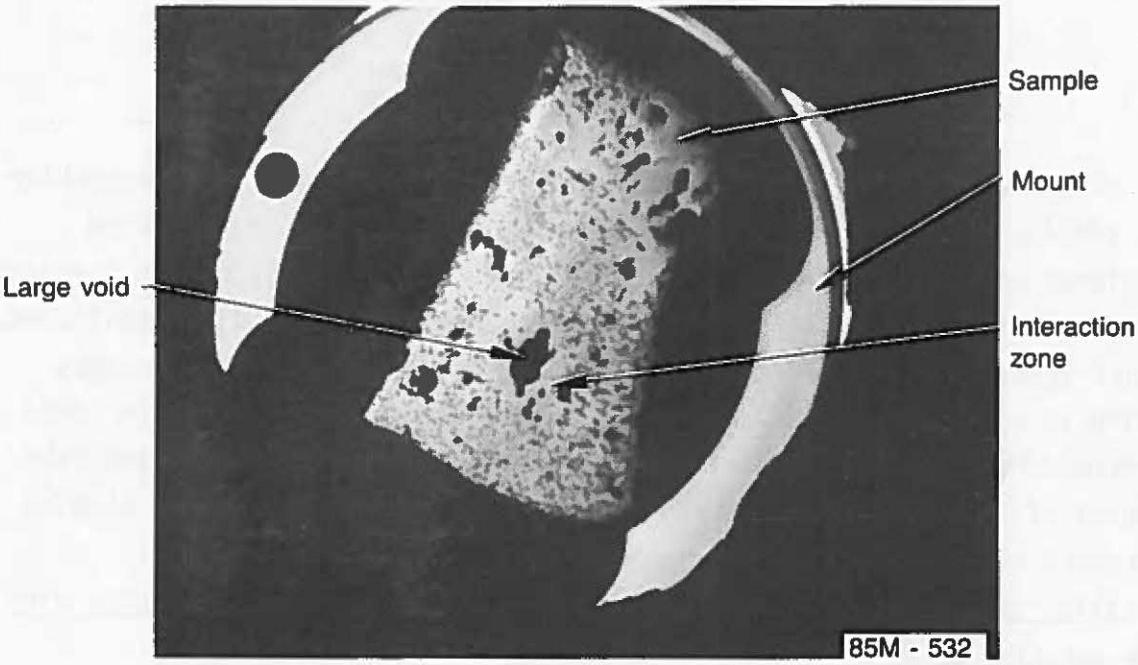

Figure D-1. Cross section from Particle 7-1.

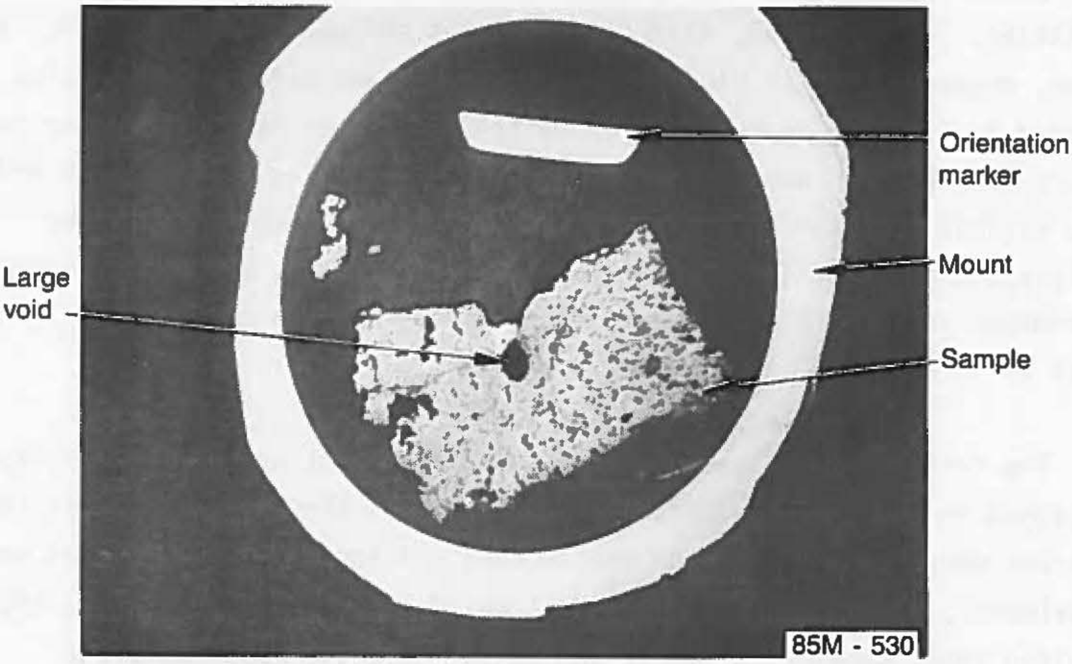

Figure D-2. Cross section from Particle 11-1.

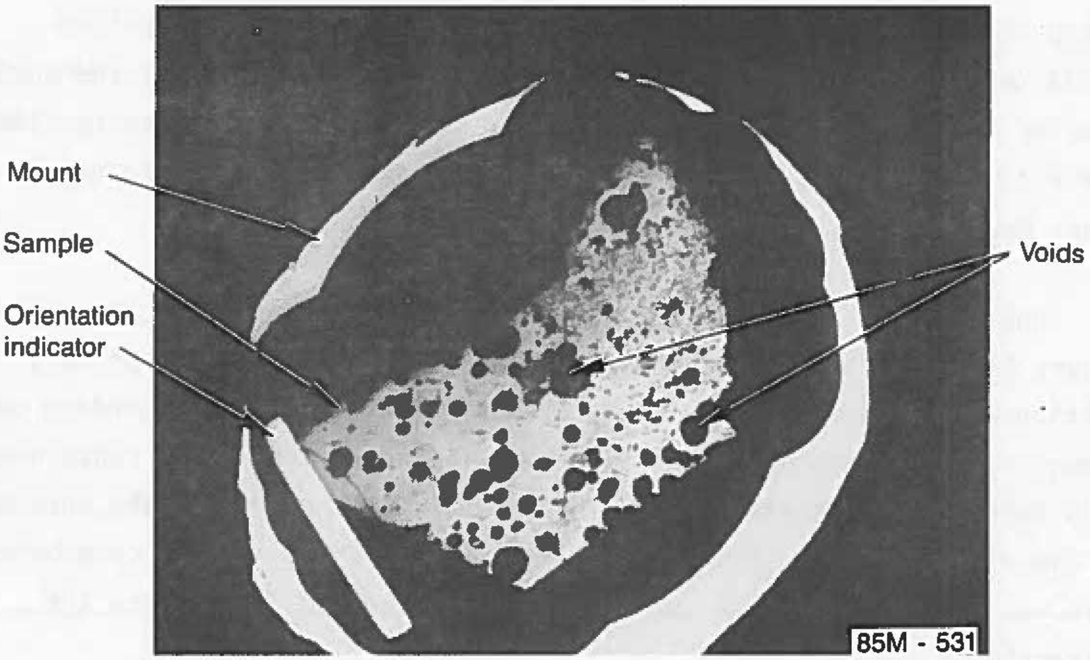

Figure D-3. Transverse cross section from Particle 11-4.

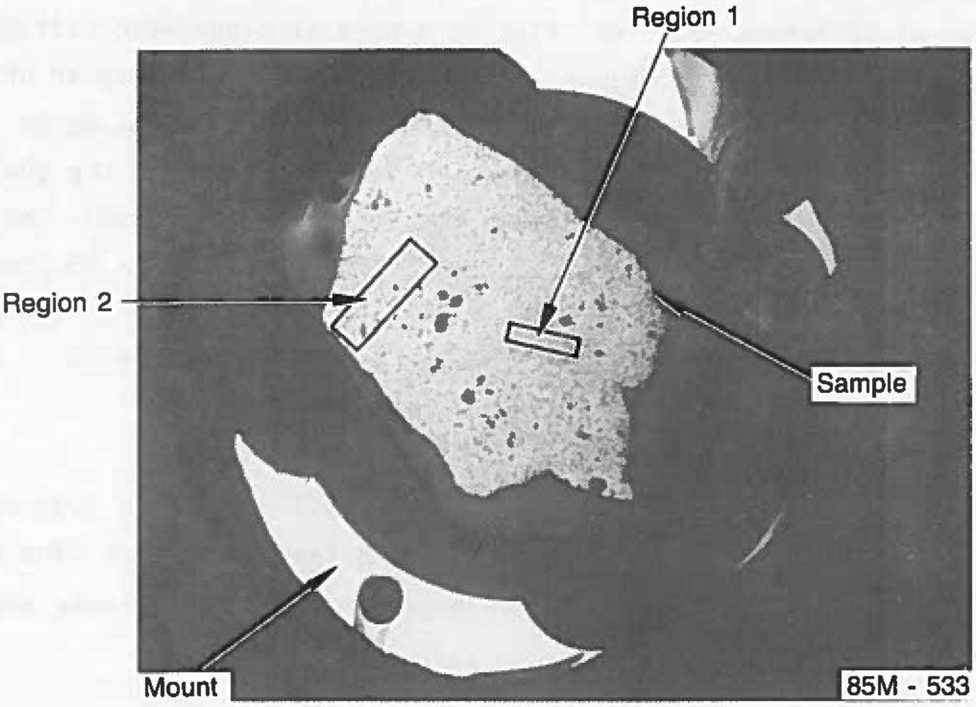

Figure D-4. Cross section from Particle 11-6.

features, and core drill samples were obtained from each identified location. A 0.5-in. OD diamond core drill was used to extract the small samples from each metallographic section. After each core-bore specimen was extracted, it was remounted in the lead/bismuth alloy contained in a brass mount.

One core-bore specimen was extracted from Section 11-2-B, as shown in Figure D-5. For this ANL sample, material at the pointed end of this section was obtained for the fine porosity at the tip. Also pending on the diameter of the core bore, some of the material from the area containing only large pores was extracted. This area is on the edge of the core bore at the wide end. The structures of the large section and the core bore were not identical because the core bore had been polished since the extraction.

Also, only one core bore was extracted from Section 11-4-A, as shown in Figure D-6. This area contained some large voids with interaction zones around the void. Some metallic inclusions were also present.

Because Section 11-5-B was the largest section examined and exhibited a number of different features, five core-bore sections were extracted from this section, as shown in Figure D-7. Core Bore B1 contained an urania inclusion; Core Bore B2 contained metallic inclusions in the pores. Core Bore B3 had porosity free zones and an unusual structure in the grain boundaries. Core Bore B4 was suppose to contain another urania inclusion and some metallic inclusions, but none was found. Core Bore B5 contained fine pores at the edge and a region of large pores adjacent to the area of fine porosity. As Figure D-7 shows, samples were obtained from representative areas of this section.

The unique features of Section 11-7-B were incorporated into one core bore, shown in Figure D-8. This section contained an area of fine porosity at the edge and an adjoining area of large pores. Both of these areas were extracted in one core bore.

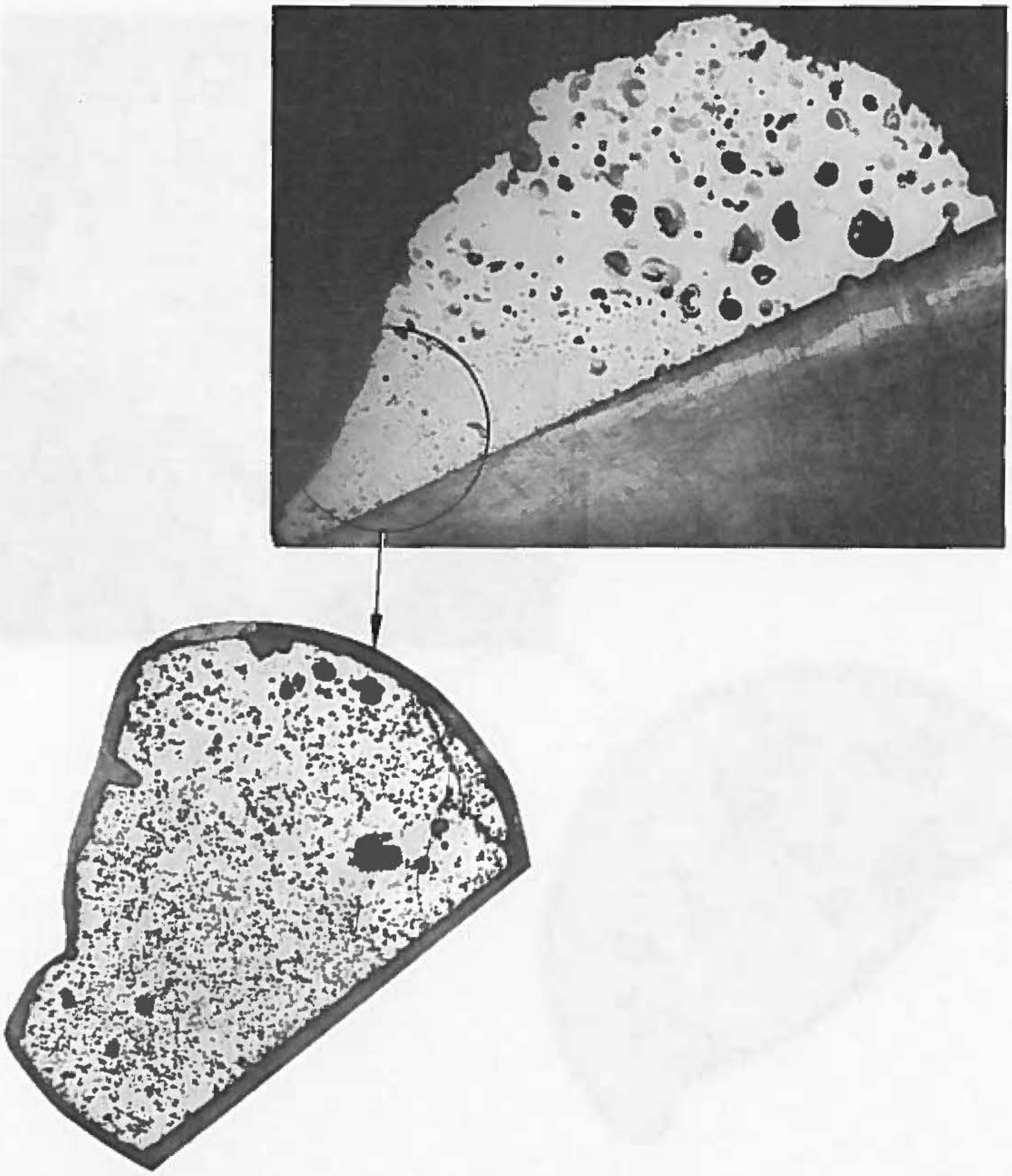

Figure D-5. Core bore location and sample from metallographic section from Particle 11-2.

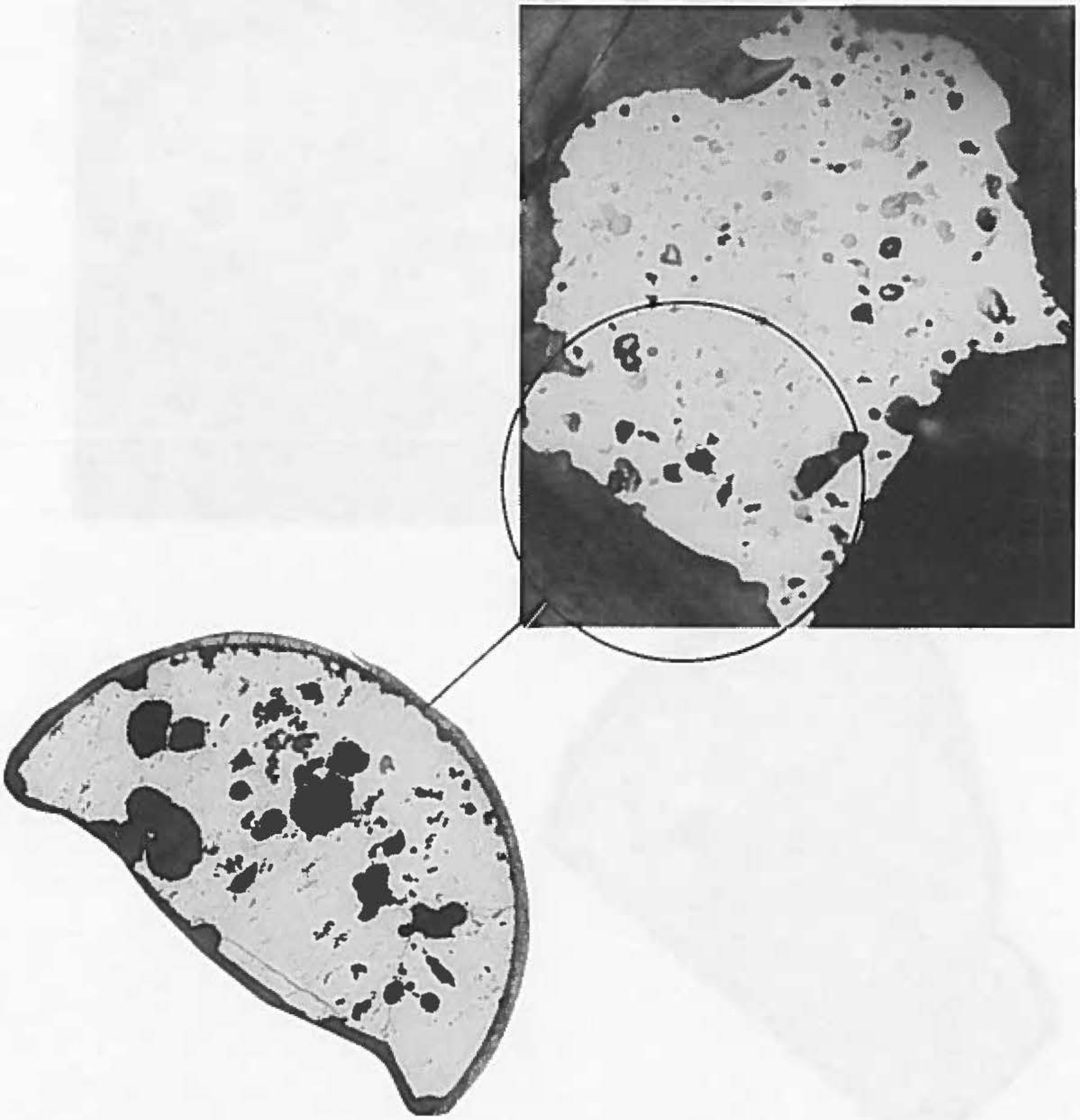

Figure D-6. Core bore location and sample from transverse section from Particle 11-4.

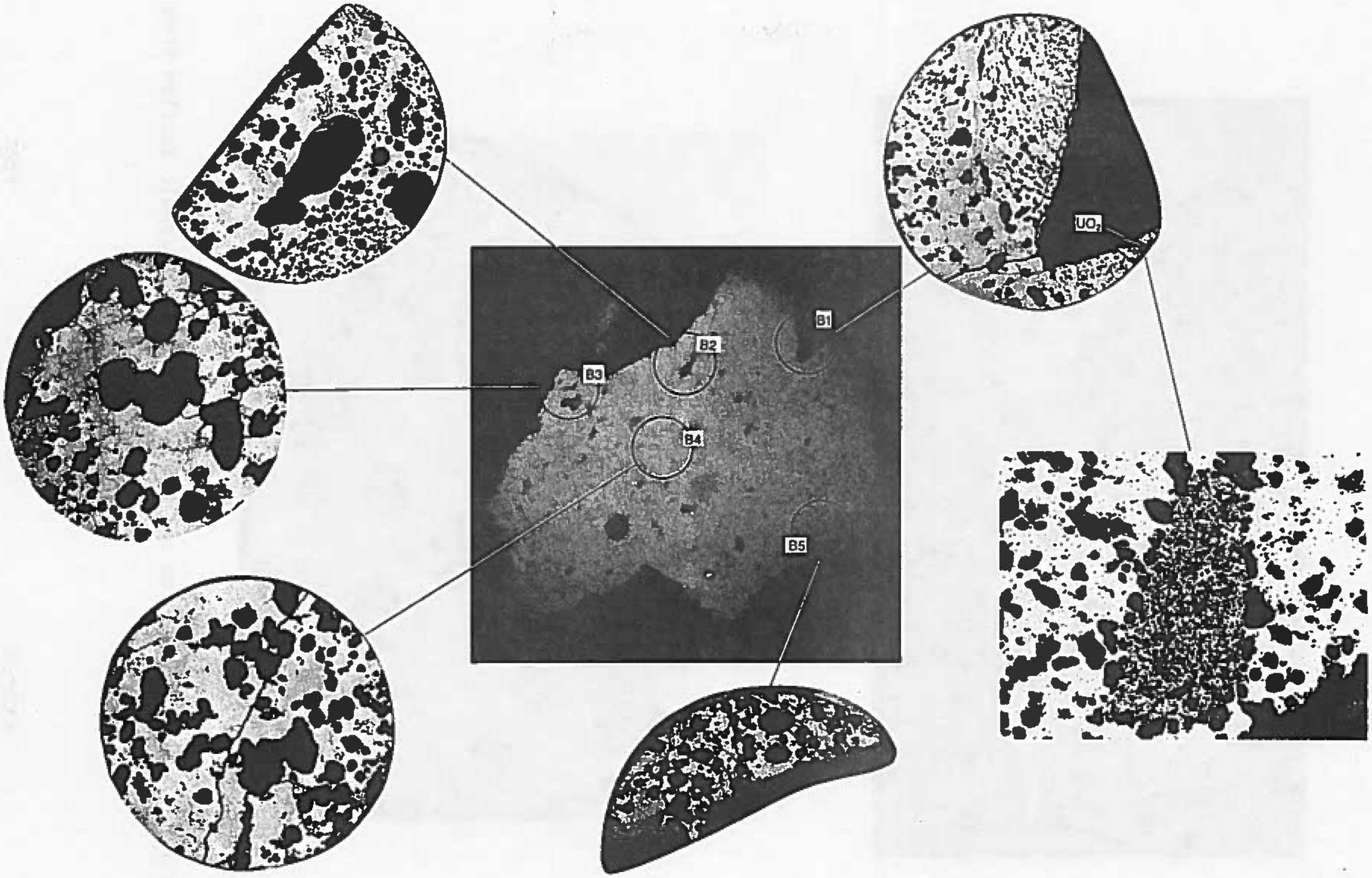

Figure D-7. Core bore locations and samples from metallographic section from Particle 11-5.

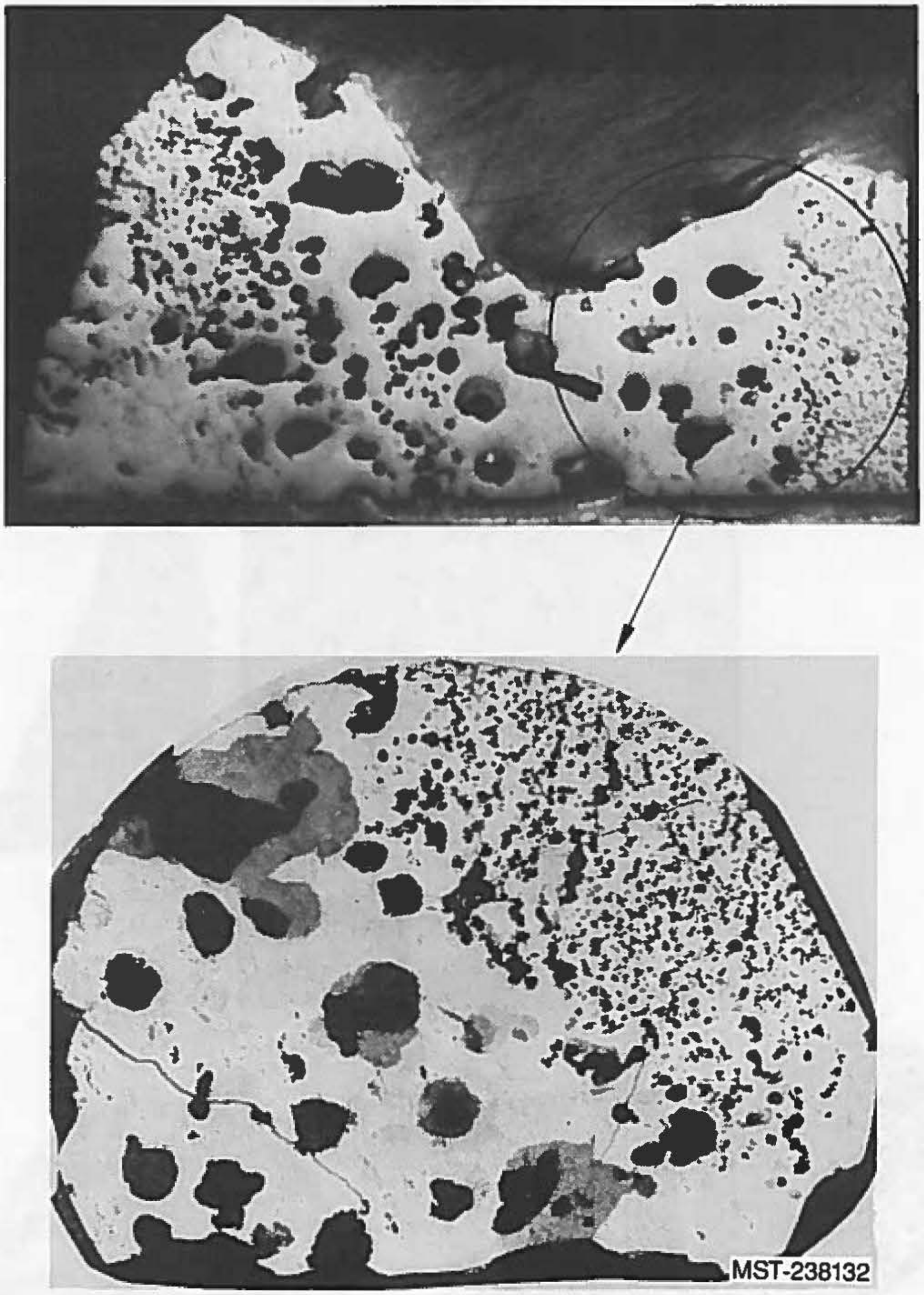

Figure D-8. Core bore location and sample from metallographic section from Particle 11-7.

Two additional samples shipped to ANL were unmounted, allowing the examination of surface deposits: Particle 7-1-D, which had some yellowish and reddish surface coatings, and a section from Particle 11-1 (11-1-D1) was obtained, which had a yellowish flat surface. This sample also had a fractured surface that could be used for comparison with surface deposits.

APPENDIX E

ELEMENTAL ANALYSIS RESULTS

APPENDIX E

ELEMENTAL ANALYSIS RESULTS

This appendix presents results of the elemental analyses performed on lower vessel debris samples, using inductively coupled plasma (ICP) spectroscopy. The analysis was performed on the nonvolatile, dissolved liquid portions of the samples. The results are given in weight percent.

There appears to be a consistent low bias of 5 to 10% in the ICP results, as compared to the fertile material analyses performed by EG&G Idaho, which are consistent with the expected composition of the samples. The uncertainty quoted for the ICP analysis results by the Hanford Engineering Development Laboratory (HEDL) is 10%; therefore, the actual total uncertainty is approximately 20%. The probable cause for the reduced elemental content is plate-out on the shipping containers in which the samples were sent to HEDL, and possible losses during dissolution.

TABLE E-1. ELEMENTAL CONTENT OF THE CORE DEBRIS SAMPLES FROM THE LOWER VESSEL (BULK PARTICLE 11-1-C)

	Samples	
Element	400[a] (26.42 mg)	401[a] (39.51 mg)
Ag	<3.4 E-1	<2.3 E-1
Al	--[b]	--[b]
B	<6.8 E-2	<4.6 E-2
Cd	<4.8 E-2	<3.2 E-2
Cr	1.16	4.6 E-2
Cu	<3.4 E-1	<2.3 E-1
Fe	3.00	1.55
Gd	<1.2	<6.8 E-1
In	<6.8	<4.56
Mn	<1.0 E-1	<6.8 E-2
Mo	<1.7 E-1	1.2 E-1
Nb	<6.8 E-1	<4.6 E-1
Ni	<2.0 E-1	<1.4 E-1
Si	2.00[b]	1.47[b]
Sn	<1.02	<6.8 E-1
U	6.36 E+1	6.47 E+1
Zr	1.38 E+1	1.22 E+1

---

a. Samples 400 and 401 were obtained from pieces of Particle 11-1-C, which fractured during handling.

b. Contamination occurred during analysis.

TABLE E-2. ELEMENTAL CONTENT OF THE CORE DEBRIS SAMPLES FROM THE LOWER VESSEL (BULK PARTICLE 11-4-D)

Element	Location Number 1 403 (21.43 mg)	2 402 (33.96 mg)	3 404 (41.13 mg)
Ag	<4.2 E-1	<2.7 E-1	<2.2 E-1
Al	--[a]	--[a]	--[a]
B	1.2 E-1	<5.3 E-2	<4.4 E-2
Cd	<5.9 E-2	<3.7 E-2	<3.1 E-2
Cr	8.5 E-1	9.5 E-1	1.07
Cu	<4.2 E-1	<2.7 E-1	<2.2 E-1
Fe	4.23	3.41	3.46
Gd	<1.26	<8.0 E-1	<6.6 E-1
In	<8.40	<5.30	<4.38
Mn	<1.3 E-1	9.0 E-2	8.9 E-2
Mo	2.7 E-1	2.0 E-1	1.5 E-1
Nb	<8.4 E-1	<5.3 E-1	<4.4 E-1
Ni	<2.5 E-1	<1.6 E-1	<1.3 E-1
Si	2.28[a]	1.78[a]	1.23[a]
Sn	<1.26	8.0 E-1	<6.6 E-1
U	6.55 E+1	6.71 E+1	6.43 E+1
Zr	1.20 E+1	1.25 E+1	1.19 E+1

---

a. Contamination occurred during analysis.

TABLE E-3. ELEMENTAL CONTENT OF THE CORE DEBRIS SAMPLES FROM THE LOWER VESSEL (BULK PARTICLE 11-6-B)

	Location Number		
Element	1 405 (25.19 mg)	2 406 (29.40 mg)	3 407 (72.36 mg)
Ag	<3.6 E-1	<3.1 E-1	<1.2 E-1
Al	--[a]	--[a]	--[a]
B	6.4 E-1	7.1 E-2	<4.9 E-2
Cd	<5.0 E-2	<4.3 E-2	<1.7 E-2
Cr	6.4 E-1	5.8 E-1	5.2 E-1
Cu	<3.6 E-1	<3.1 E-1	<1.2 E-1
Fe	1.97	2.29	1.24
Gd	<1.07	<9.2 E-1	<3.7 E-1
In	<7.15	<6.12	<2.49
Mn	<1.1 E-1	9.6 E-2	4.1 E-2
Mo	<1.8 E-1	2.1 E-1	<6.2 E-2
Nb	<7.1 E-1	<6.1 E-1	<2.5 E-1
Ni	<2.1 E-1	<1.8 E-1	<7.5 E-2
Si	49.78[a]	1.86[a]	7.2 E-1[a]
Sn	<1.07	<9.2 E-1	<3.7 B-1
U	6.84 E+1	7.22 E+1	6.78 E+1
Zr	1.07 E+1	1.15 E+1	1.28 E+1

---

a. Contamination occurred during analysis.

TABLE E-4. ELEMENTAL CONTENT OF THE CORE DEBRIS SAMPLES FROM THE LOWER VESSEL (BULK PARTICLE 7-1-B)

	Location Number				
Element	1 410 (86.46 mg)	2 409 (28.78 mg)	3 412 (40.87 mg)	4 411 (65.94 mg)	5 408 (16.47 mg)
Ag	--[a]	<3.1 E-1	2.2 E-1	<1.4 E-1	--[a]
Al	--[a,b]	--[b]	--[b]	--[b]	--[a,b]
B	--[a]	1.4 E-1	7.9 E-2	6.3 E-2	--[a]
Cd	--[a]	<4.4 E-2	<3.1 E-2	<1.9 E-2	--[a]
Cr	--[a]	1.83	5.7 E-1	4.4 E-1	--[a]
Cu	--[a]	<3.1 E-1	2.2 E-1	6.9 E-1	--[a]
Fe	--[a]	4.07	1.78	1.35	--[a]
Gd	--[a]	<9.4 E-1	<6.6 E-1	<4.1 E-1	--[a]
In	--[a]	<6.25	<4.40	<2.73	--[a]
Mn	--[a]	<9.4 E-2	<6.6 E-2	5.1 E-2	--[a]
Mo	--[a]	2.0 E-1	1.3 E-1	1.0 E-1	--[a]
Nb	--[a]	<6.3 E-1	<4.4 E-1	<2.7 E-1	--[a]
Ni	--[a]	<1.9 E-1	<1.3 E-1	<8.2 E-2	--[a]
Si	--[a]	1.71[b]	1.41[b]	1.11[b]	--[a]
Sn	--[a]	<9.4 E-1	<6.6 E-1	<4.1 E-1	--[a]
U	--[a]	6.38 E+1	6.56 E+1	6.64 E+1	--[a]
Zr	--[a]	1.29 E+1	1.19 E+1	1.13 E+1	--[a]

---

a. Data unused owing to loss of sample material.

b. Contamination occurred during analysis.

TABLE E-5. ELEMENTAL CONTENT OF THE CORE DEBRIS SAMPLES FROM THE LOWER VESSEL (BULK PARTICLE 11-4-B)

	Location Number			
Element	1 413 (48.01 mg)	2 414 (38.83 mg)	3 415 (78.61 mg)	4 416 (64.60 mg)
Ag	--[a]	<2.3 E-1	<1.1 E-1	<1.4 E-1
Al	--[a,b]	--[b]	--[b]	--[b]
B	--[a]	8.8 E-2	5.0 E-2	5.9 E-2
Cd	--[a]	<3.2 E-2	<1.6 E-2	<2.0 E-2
Cr	--[a]	1.00	1.07	8.9 E-1
Cu	--[a]	<2.3 E-1	<1.1 E-1	<1.4 E-1
Fe	--[a]	3.21	2.87	2.61
Gd	--[a]	<7.0 E-1	<3.4 E-1	<4.2 E-1
In	--[a]	<4.64	<2.29	<2.79
Mn	--[a]	9.7 E-2	8.5 E-2	7.2 E-2
Mo	--[a]	2.1 E-1	6.3 E-2	1.2 E-1
Nb	--[a]	<4.6 E-1	<2.3 E-1	<2.8 E-1
Ni	--[a]	<1.4 E-1	3.6 E-1	1.6 E-1
Si	--[a]	1.55[b]	9.2 E-1[b]	1.07[b]
Sn	--[a]	<7.0 E-1	<3.4 E-1	<4.2 E-1
U	--[a]	6.54 E+1	6.41 E+1	6.59 E+1
Zr	--[a]	1.56 E+1	1.48 E+1	1.45 E+1

---

a. Data unused owing to loss of sample material.

b. Contamination occurred during analysis.

TABLE E-6. ELEMENTAL CONTENT OF THE CORE DEBRIS SAMPLES FOR THE LOWER VESSEL (BULK PARTICLE 11-7-C)

	Location Number		
	1	2	3
	419[a,b]	418[b]	417[b]
Element	(22.29 mg)	(27.85 mg)	(116.26 mg)
Ag	<4.0 E-1	<3.2 E-1	<7.7 E-2
Al	--[c]	--[c]	--[c]
B	8.9 E-2	1.6 E-1	3.9 E-2
Cd	6.5 E-2	<4.5 E-2	<1.1 E-2
Cr	7.8 E-2	7.8 E-1	9.8 E-1
Cu	<4.0 E-1	<3.2 E-1	<7.7 E-2
Fe	2.72	2.71	1.80
Gd	<1.21	<9.7 E-1	<2.3 E-1
In	<8.08	<6.46	<1.55
Mn	<1.2 E-1	<9.7 E-2	6.2 E-2
Mo	<2.0 E-1	1.7 E-1	6.5 E-2
Nb	<8.1 E-1	<6.5 E-1	<1.5 E-1
Ni	<2.4 E-1	<1.9 E-1	2.4 E-1
Si	1.74[c]	1.61[c]	5.4 E-1[c]
Sn	<1.21	<9.7 E-1	<2.3 E-1
U	5.90 E+1	6.61 E+1	6.19 E+1
Zr	1.18 E+1	1.21 E+1	1.39 E+1

---

a. Analysis results indicate a possible loss of sample material.

b. Samples 417 and 419 were obtained from the edges of the particle, and Sample 418 was obtained from near the center.

c. Contamination occurred during analysis.

TABLE E-7. ELEMENTAL CONTENT OF THE CORE DEBRIS SAMPLES FROM THE LOWER VESSEL (BULK PARTICLE 11-2-C)

	Location Number					
Element	1 422 (34.61 mg)	2 424 (21.88 mg)	3 423 (64.74 mg)	4 421 (116.19 mg)	5 425 (67.15 mg)	6 420 (52.13 mg)
Ag	<2.6 E-1	<4.1 E-1	<1.9 E-1	<7.7 E-2	<1.3 E-1	--[a]
Al	--[b]	--[b]	--[b]	--[b]	--[b]	--[a,b]
B	6.8 E-2	<8.2 E-2	8.3 E-2	5.9 E-2	7.5 E-2	--[a]
Cd	<3.6 E-2	<5.8 E-2	<2.7 E-2	<1.1 E-2	2.5 E-2	--[a]
Cr	7.7 E-1	9.8 E-1	6.5 E-1	8.7 E-1	6.7 E-1	--[a]
Cu	<2.6 E-1	<4.1 E-1	<1.9 E-1	<7.7 E-2	2.1 E-1	--[a]
Fe	1.72	3.48	2.49	2.47	2.22	--[a]
Gd	<7.8 E-1	<1.23	<5.8 E-1	<2.3 E-1	<4.0 E-1	--[a]
In	<5.20	<8.23	<3.87	<1.55	<2.68	--[a]
Mn	<7.8 E-2	<1.2 E-1	6.7 E-2	7.3 E-2	6.5 E-2	--[a]
Mo	<1.3 E-1	<2.1 E-1	1.6 E-1	4.0 E-2	7.9 E-2	--[a]
Nb	<5.2 E-1	<8.2 E-1	<3.9 E-1	<1.5 E-1	<2.7 E-1	--[a]
Ni	<1.6 E-1	<2.5 E-1	<1.2 E-1	2.4 E-1	<8.0 E-2	--[a]
Si	<5.2 E-1[b]	1.92[b]	1.38[b]	6.3 E-1[b]	1.13[b]	--[a]
Sn	<7.8 E-1	<1.23	<5.8 E-1	<2.3 E-1	<4.0 E-1	--[a]
U	6.36 E+1	6.03 E+1	6.21 E+1	6.45 E+1	6.56 E+1	--[a]
Zr	1.20 E+1	1.24 E+1	1.33 E+1	1.39 E+1	1.29 E+1	--[a]

---

a. Data unused owing to loss of sample material.

b. Contamination occurred during analysis.

TABLE E-8. ELEMENTAL CONTENT OF THE CORE DEBRIS SAMPLES FROM THE LOWER VESSEL (BULK PARTICLE 11-1-A)

Element	427[a,b] (31.62 mg)	428[a,b] (45.15 mg)
Ag	<2.8 E-1	<2.0 E-1
Al	--[c]	--[c]
B	1.8 E-1	6.9 E-2
Cd	<4.0 E-2	<2.8 E-2
Cr	5.5 E-1	6.4 E-1
Cu	<2.8 E-1	<2.0 E-1
Fe	2.09	1.66
Gd	<8.5 E-1	<6.0 E-1
In	<5.69	<3.99
Mn	9.1 E-2	8.4 E-2
Mo	2.5 E-1	1.4 E-1
Nb	<5.7 E-1	<4.0 E-1
Ni	<1.7 E-1	<1.2 E-2
Si	2.41[c]	1.12[c]
Sn	<8.5 E-1	<6.0 E-1
U	6.41 E+1	6.94 E+1
Zr	1.20 E+1	1.36 E+1

---

a. Samples 427 and 428 were obtained from loose fragments of Particle 11-1-A during handling.

b. Tellurium analysis performed on these samples.

c. Contamination occurred during analysis.

TABLE E-9. ELEMENTAL CONTENT OF THE CORE DEBRIS SAMPLES FROM THE LOWER VESSEL (BULK PARTICLE 11-5-C)

	Location Number								
Element	1 433[a] (42.90 mg)	2 435[a] (113.59 mg)	3 434[a] (90.27 mg)	4 431[a] (102.87 mg)	5 432[a] (99.60 mg)	6 430[a] (44.86 mg)	7 429[a] (23.74 mg)	8 436[a] (75.46 mg)	9 437 (51.35 mg)
Ag	--[b]	<7.9 E-2	<1.0 E-1	<8.7 E-2	<9.0 E-2	<2.0 E-1	<3.8 E-1	<1.2 E-1	<1.8 E-1
Al	--[b]	--[c]	--[c]	--[c]	--[c]	--[c]	--[c]	--[c]	--[c]
B	--[b]	3.8 E-2	3.3 E-2	1.1 E-1	9.8 E-2	9.2 E-2	8.1 E-2	5.1 E-2	1.1 E-1
Cd	--[b]	<1.1 E-2	<1.4 E-2	<1.2 E-2	<1.3 E-2	<2.8 E-2	5.6 E-1	<1.7 E-2	<2.5 E-2
Cr	--[b]	2.5 E-1	3.4 E-1	3.7 E-1	5.8 E-1	5.9 E-1	8.2 E-1	1.11	1.14
Cu	--[b]	<7.9 E-2	<1.0 E-1	<8.7 E-2	<9.0 E-2	<2.0 E-1	<3.8 E-1	<1.2	<1.8 E-1
Fe	--[b]	8.7 E-1	1.18	1.25	1.83	2.31	2.88	2.89	3.11
Gd	--[b]	<2.4 E-1	<3.0 E-1	<2.6 E-1	<2.7 E-1	<6.0 E-1	<1.14	<3.6 E-1	<5.3 E-1
In	--[b]	<1.58	<1.99	<1.75	<1.81	<4.0	<7.58	<2.39	<3.51
Mn	--[b]	3.9 E-2	5.3 E-2	4.6 E-2	6.3 E-2	7.8 E-2	<1.1 E-1	8.8 E-2	9.1 E-2
Mo	--[b]	6.0 E-2	<5.0 E-2	6.6 E-2	5.2 E-2	<1.0 E-1	2.0 E-1	<6.0 E-2	1.5 E-1
Nb	--[b]	<1.6 E-1	<2.0 E-1	<1.7 E-1	<1.8 E-1	<4.0 E-1	<7.6 E-1	<2.4 E-1	<3.5 E-1
Ni	--[b]	<4.8 E-2	<6.0 E-2	6.6 E-2	1.7 E-1	<1.2 E-1	<2.3 E-1	3.3 E-1	2.4 E-1
Si	--[b]	5.8 E-1	7.4 E-1	7.8 E-1	8.0 E-1	9.9 E-1	2.55	8.0 E-1	2.02
Sn	--[b]	<2.4 E-1	<3.0 E-1	<2.6 E-1	<2.7 E-1	<6.0 E-1	<1.14	<3.6 E-1	<5.3 E-1
U	--[b]	6.66 E+1	6.29 E+1	6.12 E+1	6.45 E+1	6.57 E+1	6.37 E+1	6.71 E+1	6.04 E+1
Zr	--[b]	1.25 E+1	1.15 E+1	1.15 E+1	1.25 E+1	1.21 E+1	1.11 E+1	1.35 E+1	1.31 E+1

---

a. Tellurium analysis performed on these samples.

b. Data unused owing to loss of sample material.

c. Contamination occurred during analysis.

APPENDIX F

RADIOCHEMICAL ANALYSES

APPENDIX F
RADIOCHEMICAL ANALYSES

This appendix presents the results of the radiochemical analyses of the lower vessel debris samples and a discussion of the results. Gamma-emitting radionuclides measured by gamma spectroscopy were Co-60, Ru-106, Sb-125, Cs-134, Cs-137, Ce-144, and Eu-154. Results of the Sr-90 analysis were obtained by radiochemical separation and subsequent beta-emitter analysis. The I-129 and fissile/fertile material results were obtained by neutron activation analysis, with subsequent gamma spectroscopy and delayed neutron analysis, respectively. Results of all analyses are reported in μCi/g sample, except for the fissile/fertile material contents, which are reported in mg U-235 or U-238 per sample. All radionuclide activities are decayed to April 1, 1986.

Evaluation of Radionuclide Analysis Results

Table F-1 lists the average fission product concentrations for each particle cross section that was sampled. It should be noted that two cross sections were sampled and analyzed from Particles 11-1 and 11-4. The analysis results are discussed for each group of radionuclides in the approximate order of volatility from the least to the most volatile, as listed in Table 10 in the main body of this report. This order is used because the results for the low volatile radionuclides provide information that assists in understanding the behavior of the medium and high volatiles.

Low Volatiles

The low volatile isotopes measured were U-235, U-238, and Ce-144; the only measurable fission product in this group. The U-235 and U-238 concentrations are listed in Appendix E; the U-235 enrichments are listed in Table F-2. The enrichment and zone of the core where the prior-molten material originated can significantly affect the quantities of fission products present in the debris. Table F-2, which summarizes the U-235 and U-238 data, indicates a range of enrichments from 1.8 to 3.1. However, the bulk of the data (31 of 35 measurements) is in the range from 2.1 to 2.6.

TABLE F-1. AVERAGE RADIONUCLIDE CONCENTRATIONS

	Particles/Concentrations (μCi/g)[b]								
Radionuclide	7-1-B	11-1-A	11-1-C	11-2-C	11-4-B	11-4-D	11-5-C	11-6-B	11-7-C
^{60}Co	1.05 E+1[a]	4.6 E0	59.0 E0[a]	1.7 E+1	1.9 E+1	1.9 E+1	8.5 E0	4.4 E0[a]	1.6 E+1
^{90}Sr	5.2 E+3	5.2 E+3	5.1 E+3	6.7 E+3	7.2 E+3	6.6 E+2	5.2 E+3	4.9 E+3	5.9 E+3
^{106}Ru	1.8 E+1[a]	1.2 E+1	1.6 E+1	1.4 E+1	2.0 E+1	1.6 E+1	2.0 E+1	--[a]	1.5 E+1
^{129}I	9.0 E-5[a]	2.7 E-5	1.0 E-5[a]	4.9 E-5	2.1 E-4	2.0 E-5[a]	2.0 E-5	4.9 E-5	2.4 E-5
^{125}Sb	1.6 E+1[a]	--[a]	9.0 E0[a]	5.8 E0[a]	1.8 E+1	1.3 E+1	--[a]	--[a]	--[a]
^{134}Cs	4.04 E+1	2.72 E+1	1.27 E+1	1.86 E+1	3.64 E+1	3.18 E+1	1.84 E+1	2.73 E+1	2.85 E+1
^{137}Cs	1.32 E+3	8.87 E+2	4.13 E+2	6.12 E+2	1.21 E+3	1.05 E+3	4.92 E+2	9.05 E+2	9.51 E+2
^{144}Ce	4.55 E+2	4.46 E+2	4.21 E+2	4.00 E+2	4.36 E+2	4.39 E+2	3.99 E+2	3.91 E+2	4.15 E+2
^{154}Eu	3.8 E+1	3.9 E+1	3.8 E+1	3.3 E+1	3.4 E+1	3.6 E+1	4.2 E+1	4.0 E+1	3.6 E+1

---

a. Some values were below the detection limit and were not included in the average.

b. Data are decay corrected to April 1, 1986.

TABLE F-2. U-235 ENRICHMENT OF THE LOWER VESSEL DEBRIS SAMPLES

	Sample Location/^{235}U Enrichment								
Particle	1	2	3	4	5	6	7	8	9
7-1-B	2.2	2.3	2.3	2.4	2.6				
11-1-A	2.0	1.B							
11-1-C	2.3	2.9							
11-2-C	2.4	2.6	2.2	2.2	2.6	2.5			
11-4-B	2.2	2.4	2.3	2.6					
11-4-D	2.6	2.3	2.2						
11-5-C	2.2	2.1	2.3	2.2	2.2	3.1[a]	--	2.2	2.2
11-6-B	2.5	2.3	2.4						
11-7-C	2.6	2.5	2.1						

---

a. Large associated uncertainty.

The measurements near an enrichment of 3.0% have high uncertainties, which suggests that the lower vessel debris samples are mainly a composite of the 1.98- and 2.64%-enriched assemblies. In fact, the average concentration for all measurements is 2.3, which would suggest that the material in the lower plenum is on the average a relatively even mixture of the 1.98 and 2.64% fuel assemblies.

The following observations can be made from inspection of the data in Table F-2: Particles 7-1-B, 11-4-B, 11-4-D, and 11-7-C appear to have enrichment gradients with enrichments ranging from 2.1 or 2.2 to 2.6 at opposing edges of the particles. These data suggest the presence of interaction zones between assemblies where the prior-molten material was not well mixed. Particle 11-1-A appears to be composed of prior-molten material from a 1.98%-enriched assembly (all enrichments at or below 2.0). Particle 11-5-C appears to be a relatively homogeneous mixture of the two enrichments.

The only fission product measured in the lower vessel debris that is in the low volatility group in Table 7 in the main body of this report is Ce-144. The measured concentrations for all samples (Appendix F) range from 314 to 563 μCi/g, with an average of approximately 420 μCi/g, a range of 25 to 35% from the average. The average on a particle basis (Table F-1) is again about 420 μCi/g, but the range is 7 to 8%. These data indicate that the high and low concentrations for all samples, as indicated in Appendix E, are not characteristic of the debris, and that averaging on a particle basis tends to substantially reduce the spread in the data. All data are well within the range that is consistent with variations in enrichment, as discussed above.

Medium Volatiles

The fission products that are expected to have a medium volatility are Sr-90, Eu-154, Sb-125, and Ru-106. Strontium-90 and Eu-154 are expected to be the least volatile and least influenced by the chemical form of the material. On a particle average basis, the concentration of Sr-90 averages 5.8 E+3 μCi/g, with a variation of <25% around the average; Eu-154 has a particle-averaged concentration of 3.7 E+1 μCi/gm, with a variation of <12%. The concentrations for both radionuclides fall in a very narrow range, which suggests that both radionuclides are relatively evenly distributed within the debris. The data for individual analyses tends to have a greater range, but are consistent with the particle averages.

The radionuclides, Sb-125 and Ru-106, are expected to exhibit a greater range of concentrations in the lower vessel debris, as they exhibited a substantial range in the upper vessel debris, suggesting that these radionuclides are significantly affected by the melting process (see page 98). For Sb-125, many of the samples had concentrations below the detection limit (25 of 37 total samples). The average concentration of all measurable concentrations for Sb-125 is 1.36 E+1 μCi/g, with a high concentration of about 26 μCi/g. These data are discussed further in the following section. The average concentrations listed in Table F-1 indicate a significant range of concentrations for individual particles.

Ruthenium-106 was measurable in almost all samples (33 of 37), and the particles have an average concentration of 16.4 μCi/g, with a variation of less than 30% around the average, indicating a relatively consistent concentration for this radionuclide.

High Volatiles

The two high volatile radionuclides measurable were Cs-137 and I-129. The concentration of I-129, where measurable (28 of 37 analyses), had an average concentration of 6.0 E-5 μCi/g; however, the range of concentrations were from 2.4 E-6 to 4.5 E-4, a factor of 1.9 E+2. These data indicate wide variations in the radioiodine concentrations in the debris. As indicated in Table F-1, Particle 11-4-B contains substantially more I-129 (factors of 5 to 10) than any other particle. Note that the upper portion of Particle 11-4-D does not contain similar concentrations.

Cesium-137 was measurable at all sample locations, at an average concentration of approximately 835 μCi/g. The high and low concentrations are widely variable, with a low concentration of 25 μCi/g and a high concentration of 2.12 E+3 μCi/g. This is a range of a factor of 84, which is much wider than the low volatiles, but less than that observed for I-129.

On a particle average basis (Table F-2), the concentrations are more consistent with an average of 871 μCi/g and a range of a factor of 3, indicating that the high and low concentrations are generally not associated with specific particles. Note that the highest average concentrations are associated with Particles 11-4 (like I-129) and 7-1. These data are discussed in greater detail in the following section.

Tables F-3 through F-11 contain the results of the radionuclide analyses (decay corrected to April 1, 1986); Tables F-12 through F-20 contain the radionuclide retentions as compared to the ORIGEN-2 concentrations for the core average.

TABLE F-3. RADIONUCLIDE CONTENT OF DEBRIS SAMPLES FROM THE LOWER VESSEL (BULK PARTICLE 11-1-C)

	Concentration (μCi/g)	
Radionuclide	400 (26.42 mg)	401 (39.51 mg)
^{60}Co	9.0 ± 2.8 E0	<3.0 E0
^{90}Sr	5.13 ± 0.77 E+4	5.02 ± 0.75 E+13
^{106}Ru	2.40 ± 0.33 E+1	8.8 ± 6.2 E0
^{129}I	--[a]	1.01 ± 0.15 E-5
^{125}Sb	9.0 ± 6.7 E0	<4.5 E0
^{134}Cs	1.72 ± 0.19 E+1	8.2 ± 2.1 E0
^{137}Cs	5.63 ± 0.01 E+2	2.64 ± 0.01 E+2
^{144}Ce	4.45 ± 0.04 E+2	3.98 ± 0.02 E+2
^{154}Eu	3.15 ± 0.17 E+1	4.55 ± 0.12 E+1
^{235}U[b]	0.38	0.62[c]
^{238}U[b]	16.8	21.3[c]

---

a. No sample.

b. Reported in mg of fissile (^{235}U equivalent) and fertile (^{238}U equivalent).

c. These data contain relatively large uncertainties.

TABLE F-4. RADIONUCLIDE CONTENT OF DEBRIS SAMPLES FROM THE LOWER VESSEL (BULK PARTICLE 11-4-D)

	Concentration (μCi/g)		
Radionuclide	1 403 (21.43 mg)	2 402 (33.96 mg)	3 404 (41.13 mg)
^{60}Co	1.64 ± 0.18 E+1	1.86 ± 0.18 E+1	2.20 ± 0.14 E+1
^{90}Sr	4.93 ± 0.74 E+3	6.6 ± 1.0 E+3	8.2 ± 1.2 E+3
^{106}Ru	1.51 ± 0.64 E+1	1.63 ± 0.48 E+1	1.51 ± 0.74 E+1
^{129}I	1.12 ± 0.17 E-5	<1.2 E-5	2.78 ± 0.42 E-5
^{125}Sb	<9.0 E0	1.09 ± 0.74 E+1	1.46 ± 0.63 E+1
^{134}Cs	3.19 ± 0.14 E+1	2.40 ± 0.22 E+1	3.96 ± 0.17 E+1
^{137}Cs	1.04 ± 0.01 E+3	7.79 ± 0.01 E+2	1.34 ± 0.01 E+3
^{144}Ce	4.22 ± 0.03 E+2	4.47 ± 0.02 E+2	4.50 ± 0.03 E+2
^{154}Eu	3.58 ± 0.19 E+1	3.74 ± 0.18 E+1	3.49 ± 0.15 E+1
^{235}U[a]	0.34	0.49	0.60
^{238}U[a]	13.25	21.5	27.52

---

a. Reported in mg of fissile (^{235}U equivalent) and fertile (^{238}U equivalent).

TABLE F-5. RADIONUCLIDE CONTENT OF DEBRIS SAMPLES FROM THE LOWER VESSEL (BULK PARTICLE 11-6-B)

	Concentration (μCi/g)		
Radionuclide	1 405 (25.19 mg)	2 406 (29.40 mg)	3 407 (72.36 mg)
^{60}Co	<3.5 E0	4.3 ± 3.20 E0	4.6 ± 2.5 E0
^{90}Sr	4.32 ± 0.65 E+3	5.26 ± 0.75 E+3	5.01 % 0.75 E+3
^{106}Ru	--[a]	--[a]	<9.8 E0
^{129}I	2.66 ± 0.40 E-5	6.57 ± 0.99 E-5	5.6 ± 0.84 E-5
^{125}Sb	<4.2 E0	<5.3 E0	<6.7 E0
^{134}Cs	2.3 ± 1.3 E+1	2.74 ± 0.19 E+1	3.16 ± 0.16 E+1
^{137}Cs	7.43 ± 0.01 E+2	9.22 ± 0.01 E+2	1.05 ± 0.01 E+3
^{144}Ce	3.56 ± 0.03 E+2	4.03 ± 0.03 E+2	4.13 ± 0.02 E+2
^{154}Eu	3.68 ± 0.14 E+1	4.12 ± 0.16 E+1	4.33 ± 0.12 E+1
^{235}U[b]	0.41	0.46	1.12
^{238}U[b]	16.30	19.86	47.08

---

a. Not detected.

b. Reported in mg of fissile (^{235}U equivalent) and fertile (^{238}U equivalent).

TABLE F-6. RADIONUCLIDE CONTENT OF DEBRIS SAMPLES FROM THE LOWER VESSEL (BULK PARTICLE 7-1-B)

	Concentration (μCi/g)				
Radionuclide	1 410 (86.46 mg)	2 409 (28.78 mg)	3 412 (40.87 mg)	4 411 (65.94 mg)	5 408 (16.47 mg)
^{60}Co	2.01 ± 0.29 E+1	1.47 ± 0.20 E+1	4.0 ± 3.2 E0	3.4 ± 3.0 E0	a
^{90}Sr	7.0 ± 1.1 E+3	8.7 ± 1.3 E+3	3.86 ± 0.58 E+3	3.95 ± 0.59 E+3	2.57 ± 0.39 E+3
^{106}Ru	--[a]	4.08 ± 0.31 E+1	1.14 ± 0.68 E+1	9.7 ± 6.5 E0	1.05 ± 0.93 E+1
^{129}I	9.9 ± 1.5 E-5	1.48 ± 0.50 E-4	--[b]	2.30 ± 0.76 E-5	<2.2 E-5
^{125}Sb	1.69 ± 0.91 E+1	1.58 ± 0.65 E+1	<4.9 E0	<4.5 E0	<3.9 E0
^{134}Cs	6.48 ± 0.12 E+1	6.58 ± 0.08 E+1	2.93 ± 0.12 E+1	2.16 ± 0.09 E+1	2.06 ± 0.21 E+1
^{137}Cs	2.12 ± 0.01 E+3	2.18 ± 0.01 E+3	9.50 ± 0.01 E+2	7.02 ± 0.01 E+2	6.77 ± 0.01 E+2
^{144}Ce	5.63 ± 0.04 E+2	4.81 ± 0.03 E+2	4.08 ± 0.03 E+2	4.12 ± 0.02 E+2	4.14 ± 0.04 E+2
^{154}Eu	3.00 ± 0.28 E+1	3.12 ± 0.18 E+1	4.14 ± 0.11 E+1	4.46 ± 0.11 E+1	4.52 ± 0.17 E+1
^{235}U[c]	1.15	0.45	0.64	1.09	0.29
^{238}U[c]	52.11	19.24	27.37	44.97	10.96

---

a. Not detected.

b. No sample.

c. Reported in mg of fissile (^{235}U equivalent) and fertile (^{238}U equivalent).

TABLE F-7. RADIONUCLIDE CONTENT OF DEBRIS SAMPLES FROM THE LOWER VESSEL (BULK PARTICLE 11-4-B)

	Concentration (µCi/g)			
Radionuclide	1 413 (48.01 mg)	2 414 (38.83 mg)	3 415 (78.61 mg)	4 416 (64.60 mg)
^{60}Co	1.27 ± 0.16 E+1	2.05 ± 0.14 E+1	2.43 ± 0.13 E+1	1.86 ± 0.14 E+1
^{90}Sr	5.86 ± 0.88 E+3	6.06 ± 0.91 E+3	9.5 ± 1.5 E+3	7.3 ± 1.1 E+3
^{106}Ru	1.75 ± 0.43 E+1	1.99 ± 0.44 E+1	2.08 ± 0.50 E+1	2.24 ± 0.58 E+1
^{125}Sb	1.62 ± 0.29 E+1	1.57 ± 0.46 E+1	1.24 ± 0.74 E+1	2.62 ± 0.33 E+1
^{129}I	6.15 ± 0.92 E-5	3.25 ± 0.49 E-4	4.50 ± 0.68 E-4	1.97 ± 0.30 E-5
^{134}Cs	2.30 ± 0.20 E+1	4.43 ± 0.15 E+1	3.34 ± 0.22 E+1	4.49 ± 0.14 E+1
^{137}Cs	7.60 ± 0.01 E+2	1.47 ± 0.01 E+3	1.12 ± 0.01 E+3	1.49 ± 0.01 E+3
^{144}Ce	3.72 ± 0.02 E+2	4.41 ± 0.02 E+2	4.99 ± 0.02 E+2	4.33 ± 0.03 E+2
^{154}Eu	3.15 ± 0.14 E+1	3.15 ± 0.14 E+1	3.79 ± 0.18 E+1	3.72 ± 0.13 E+1
^{235}U^{a}	0.69	0.57	1.12	1.02
^{238}U^{a}	30.75	23.92	49.27	39.89

---

a. Reported in mg of fissile (^{235}U equivalent) and fertile (^{238}U equivalent).

TABLE F-8. RADIONUCLIDE CONTENT OF DEBRIS SAMPLES FROM THE LOWER VESSEL (BULK PARTICLE 11-7-C)

	Concentration (μCi/g)		
Radionuclide	1 419 (22.29 mg)	2 418 (27.85 mg)	3 417 (116.36 mg)
^{60}Co	1.33 ± 0.22 E+1	1.46 ± 0.19 E+1	2.09 ± 0.18 E+1
^{90}Sr	5.77 ± 0.87 E+3	6.18 % 0.93 E+3	5.68 ± 0.85 E+3
^{106}Ru	1.39 ± 0.71 E+1	1.40 ± 0.70 E+1	1.80 ± 0.64 E+1
^{125}Sb	<5.4 E0	<5.6 E0	<4.2 E0
^{129}I	4.22 ± 0.63 E-5	1.97 ± 0.30 E-5	1.10 ± 0.17 E-5
^{134}Cs	1.68 ± 0.14 E+1	3.09 ± 0.12 E+1	3.79 ± 0.15 E+1
^{137}Cs	5.64 ± 0.01 E+2	1.02 ± 0.01 E+3	1.27 ± 0.01 E+3
^{144}Ce	3.14 ± 0.03 E+2	4.53 ± 0.02 E+2	4.78 ± 0.03 E+2
^{154}Eu	2.76 ± 0.19 E+1	3.92 ± 0.15 E+1	3.99 ± 0.16 E+1
^{235}U[a]	0.33	0.44	1.6
^{238}U[a]	12.65	17.87	77.41

---

a. Reported in mg of fissile (^{235}U equivalent) and fertile (^{238}U equivalent).

TABLE F-9. RADIONUCLIDE CONTENT OF DEBRIS SAMPLES FROM THE LOWER VESSEL (BULK PARTICLE 11-2-C)

	Concentration (µCi/g)					
Radionuclide	1 422 (34.61 mg)	2 424 (21.88 mg)	3 423 (64.74 mg)	4 421 (116.19 mg)	5 425 (67.15 mg)	6 420 (52.13 mg)
^{60}Co	1.72 ± 0.17 E+1	1.93 ± 0.19 E+1	1.72 ± 0.19 E+1	1.82 ± 0.21 E+1	<1.6 E0	1.36 ± 0.14 E+1
^{90}Sr	6.54 ± 0.93 E+3	9.7 ± 1.5 E+3	7.1 ± 1.1 E+3	6.52 ± 0.98 E+3	5.62 ± 0.84 E+3	4.61 ± 0.69 E+3
^{106}Ru	1.34 ± 0.58 E+1	1.25 ± 0.82 E+1	1.39 ± 0.83 E+1	1.72 ± 0.41 E+1	1.27 ± 0.82 E+1	1.33 ± 0.36 E+1
^{125}Sb	<6.4 E0	<6.8 E0	<6.8 E0	<5.7 E0	<6.8 E0	5.8 ± 5.2 E0
^{129}I	2.28 ± 0.34 E-5	1.48 ± 0.22 E-4	4.68 ± 0.70 E-5	--[a]	1.0 ± 0.15 E-5	1.64 ± 0.25 E-5
^{134}Cs	1.81 ± 0.18 E+1	2.45 ± 0.18 E+1	1.95 ± 0.18 E+1	1.82 ± 0.15 E+1	2.45 ± 0.18 E+1	6.9 ± 2.4 E0
^{137}Cs	5.97 ± 0.01 E+2	8.08 ± 0.01 E+2	6.47 ± 0.01 E+2	5.85 ± 0.01 E+2	8.08 ± 0.01 E+2	2.27 ± 0.01 E+2
^{144}Ce	4.22 ± 0.02 E+2	3.46 ± 0.08 E+2	4.66 ± 0.02 E+2	4.26 ± 0.02 E+2	3.46 ± 0.08 E+2	3.94 ± 0.02 E+2
^{154}Eu	3.80 ± 0.14 E+1	3.75 ± 0.18 E+1	4.14 ± 0.12 E+1	3.61 ± 0.15 E+1	3.75 ± 0.18 E+1	8.8 ± 2.6 E0
^{235}U[b]	0.51	0.34	--[a]	1.59	--[a]	0.79
^{238}U[b]	21.31	12.93	--[a]	73.2	--[a]	31.95

---

a. No sample.

b. Reported in mg of fissile (^{235}U equivalent) and fertile (^{238}U equivalent).

TABLE F-10. RADIONUCLIDE CONTENT OF DEBRIS SAMPLES FROM THE LOWER VESSEL (BULK PARTICLE 11-1-A)

	Concentration (μCi/g)	
Radionuclide	427 (31.62 mg)	428 (45.15 mg)
^{60}Co	4.0 ± 2.7 E0	5.3 ± 3.2 E0
^{90}Sr	4.97 ± 0.75 E+3	5.44 ± 0.82 E+3
^{106}Ru	1.00 ± 0.75 E+1	1.37 ± 0.77 E+1
^{125}Sb	<5.9 E0	<7.6 E0
^{129}I	2.03 ± 0.30 E-5	3.42 ± 0.51 E-5
^{134}Cs	2.32 ± 0.01 E+1	3.12 ± 0.15 E+1
^{137}Cs	7.64 ± 0.02 E+2	1.01 ± 0.01 E+3
^{144}Ce	4.24 ± 0.03 E+2	4.68 ± 0.04 E+2
^{154}Eu	3.98 ± 0.11 E+1	3.76 ± 0.17 E+1
^{235}U[a]	0.48	0.68
^{238}U[a]	23.64	37.66

---

[a] Reported in mg of fissile (^{235}U equivalent) and fertile (^{238}U equivalent).

TABLE F-11. RADIONUCLIDE CONTENT OF DEBRIS FROM THE LOWER VESSEL (Bulk Particle 11-5-C)

	Concentration (µCi/g)								
Radionuclide	1 433 (42.90 mg)	2 435 (113.59 mg)	3 434 (90.27 mg)	4 431 (102.87 mg)	5 432 (99.60 mg)	6 430 (44.86 mg)	7 429 (23.74 mg)	8 436 (75.46 mg)	9 437 (51.35 mg)
^{60}Co	<3.6 E0	4.3 ± 2.0 E0	4.8 ± 1.6 E0	6.8 ± 1.9 E0	9.5 ± 1.4 E0	9.9 ± 1.8 E0	1.09 ± 0.21 E+1	1.58 ± 0.16 E+1	1.45 ± 0.19 E+1
^{90}Sr	1.10 ± 0.17 E+4	2.87 ± 43 E+4	--[a]	3.25 ± 0.49 E+3	1.04 ± 0.16 E+3	4.69 ± 0.70 E+3	5.45 ± 0.82 E+3	7.6 ± 1.1 E+3	5.86 ± 0.89 E+3
^{106}Ru	9.5 ± 6.4 E0	8.6 ± 7.4 E0	1.26 ± 0.27 E+1	3.11 ± 0.14 E+1	1.72 ± 0.25 E+1	1.71 ± 0.74 E+1	2.44 ± 0.42 E+1	2.93 ± 0.52 E+1	2.88 ± 0.38 E+1
^{125}Sb	<2.2 E0	<2.0 E0	<2.4 E0	<3.7 E0	<5.1 E0	<6.2 E0	<7.6 E0	9.9 ± 9.7 E0	1.00 ± 0.68 E+1
^{129}I	<8.2 E-6	<2.0 E-6	2.38 ± 0.36 E-6	7.72 ± 1.2 E-6	--[b]	3.03 ± 0.45 E-5	2.89 ± 0.43 E-5	3.15 ± 0.47 E-5	2.15 ± 0.32 E-5
^{134}Cs	<5.5 E-1	<2.2 E0	3.3 ± 3.1 E0	7.1 ± 1.5 E0	1.29 ± 0.19 E+1	2.21 ± 0.16 E+1	2.52 ± 0.12 E+1	3.06 ± 0.17 E+1	2.75 ± 0.14 E+1
^{137}Cs	2.55 ± 0.19 E+1	6.75 ± 0.21 E+1	1.12 ± 0.01 E+2	2.36 ± 0.02 E+2	4.36 ± 0.02 E+2	7.29 ± 0.02 E+2	8.63 ± 0.02 E+2	1.03 ± 0.01 E+3	9.27 ± 0.01 E+2
^{144}Ce	3.75 ± 0.02 E+2	3.70 ± 0.02 E+2	3.41 ± 0.06 E+2	4.03 ± 0.03 E+2	3.89 ± 0.02 E+2	4.40 ± 0.02 E+2	4.01 ± 0.03 E+2	4.33 ± 0.14 E+2	4.42 ± 0.08 E+2
^{154}Eu	4.81 ± 0.11 E+1	4.59 ± 0.06 E+1	4.38 ± 0.07 E+1	4.35 ± 0.08 E+1	4.09 ± 0.11 E+1	4.16 ± 0.15 E+1	3.88 ± 0.19 E+1	3.73 ± 0.17 E+1	3.51 ± 0.15 E+1
^{235}U[c]	0.63	1.69	1.46	1.57	1.41	0.71[b]	0.35[a]	1.3	0.74
^{238}U[c]	28.25	80.74	63.13	70.64	64.77	23.01[b]	9.22[a]	60.25	33.82

---

a. No data.

b. There is a large (~100%) uncertainty associated with these values.

b. Reported in mg of fissile (^{235}U equivalent) and fertile (^{238}U equivalent).

TABLE F-12. RADIONUCLIDE RETENTION FOR PARTICLE 7-1-B NORMALIZED TO URANIUM CONTENT

	Radionuclide Retention[a] (%)				
Radionuclide	1	2	3	4	5
$^{90}\mathrm{Sr}$	146	164	73	73	49
$^{106}\mathrm{Ru}$	--	16.7	4.7	3.9	4.3
$^{125}\mathrm{Sb}$	10.1	8.5	--	--	--
$^{129}\mathrm{I}$	5.7	7.7	--	1.2	--
$^{137}\mathrm{Cs}$	38.7	35.8	15.6	11.3	11.1
$^{144}\mathrm{Ce}$	161	124	105	104	107
$^{154}\mathrm{Eu}$	74	69	92	97	100

---

a. Retention calculated using whole core average concentration.

TABLE F-13. RADIONUCLIDE RETENTION FOR PARTICLE 11-1-A NORMALIZED TO URANIUM CONTENT

Radionuclide	Radionuclide Retention[a] (%) 1	Radionuclide Retention[a] (%) 2
^{90}Sr	100	101
^{106}Ru	3.7	4.5
^{125}Sb	--	--
^{129}I	1.1	1.4
^{137}Cs	11.3	13.4
^{144}Ce	97.7	96.9
^{154}Eu	49	82

---

a. Retention calculated using whole core average concentration.

TABLE F-14. RADIONUCLIDE RETENTION FOR PARTICLE 11-1-C NORMALIZED TO URANIUM CONTENT

Radionuclide	Radionuclide Retention[a] (%)	
	1	2[b]
^{90}Sr	102	100
^{106}Ru	10.3	3.8
^{125}Sb	5.1	--
^{129}I	--	0.52
^{137}Cs	9.7	4.6
^{144}Ce	12.0	108
^{154}Eu	73	107

---

a. Retention calculated using whole core average concentration.

b. Uses the elemental concentrations from the ICP analysis.

TABLE F-15. RADIONUCLIDE RETENTION FOR PARTICLE 11-2-C NORMALIZED TO URANIUM CONTENT

	Radionuclide Retention[a] (%)					
Radionuclides	1	2	3[a]	4	5[b]	6
^{90}Sr	134	207	147	130	110	95
^{106}Ru	6.0	5.8	6.3	7.5	5.4	4.9
^{125}Sb	--	--	--	--	--	3.4
^{129}I	1.3	8.7	2.7	--	0.54	0.93
^{137}Cs	10.6	15.0	11.7	10.2	13.8	4.1
^{144}Ce	118	100	132	116	92.7	110
^{154}Eu	91	94	101	85	87	--

---

a. Retention calculated using whole core average concentration.

b. Elemental data from Appendix E were used for uranium content.

TABLE F-16. RADIONUCLIDE RETENTION FOR PARTICLE 11-4-B NORMALIZED TO URANIUM CONTENT

Radionuclides	Radionuclide Retention[a] (%) 1	2	3	4
^{90}Sr	116	120	191	143
^{106}Ru	7.5	8.8	9.1	9.5
^{125}Sb	9.1	9.1	8.1	15.2
^{129}I	3.3	18.3	25.0	1.1
^{137}Cs	13	26	20	26
^{144}Ce	100	123	137	120
^{154}Eu	73	76	90	89

---

a. Retention calculated using whole core average concentration.

TABLE F-17. RADIONUCLIDE RETENTION FOR PARTICLE 11-4-D NORMALIZED TO URANIUM CONTENT

Radionuclides	Radionuclide Retention[a] (%) 1	2	3
^{90}Sr	97	127	165
^{106}Ru	6.7	7.0	6.2
^{125}Sb	--	6.2	7.8
^{129}I	0.63	--	1.4
^{137}Cs	18	14	22
^{144}Ce	117	121	116
^{154}Eu	96	97	77

---

a. Retention calculated using whole core average concentration.

TABLE F-18. RADIONUCLIDE RETENTION FOR PARTICLE 11-5-C NORMALIZED TO URANIUM CONTENT

	Radionuclide Retention[a] (%)								
Radionuclides	1	2	3	4	5	6[b]	7[b]	8	9
^{90}Sr	211	51	--	60	20	92	110	120	112
^{106}Ru	3.9	3.3	4.9	12	7.3	7.3	11	12	12
^{125}Sb	--	--	--	--	--	--	--	4.4	5.4
^{129}I	--	--	0.12	0.39	--	1.6	1.6	1.7	1.1
^{137}Cs	0.41	1.0	1.7	3.6	7.0	12	14	14	15
^{144}Ce	98	90	84	101	103	118	111	93	115
^{154}Eu	108	96	93	94	93	96	95	84	79

---

a. Retention calculated using whole core average concentration.

b. Elemental analysis from Appendix E were used to calculate the retentions.

TABLE F-19. RADIONUCLIDE RETENTION FOR PARTICLE 11-6-B NORMALIZED TO URANIUM CONTENT

	Radionuclide Retention[a] (%)		
Radionuclides	1	2	3
^{90}Sr	84	98	97
^{106}Ru	--	--	--
^{125}Sb	--	--	--
^{129}I	1.4	3.4	3.0
^{137}Cs	12	15	18
^{144}Ce	94	102	109
^{154}Eu	84	90	98

---

a. Retention calculated using whole core average concentration.

TABLE F-20. RADIONUCLIDE RETENTION FOR PARTICLE 11-7-C NORMALIZED TO URANIUM CONTENT

	Radionuclide Retention[a] (%)		
Radionuclides	1	2	3
^{90}Sr	128	121	108
^{106}Ru	6.7	6.0	7.4
^{125}Sb	--	--	--
^{129}I	2.6	1.0	0.58
^{137}Cs	11	17	21
^{144}Ce	95	121	124
^{154}Eu	72	90	89

---

a. Retention calculated using whole core average concentration.

APPENDIX G

VOID FRACTIONS

APPENDIX G

VOID FRACTIONS

Area fractions of pores and metallic inclusions were determined from photomicrographs by measuring the number of pores or metallic inclusions for a given size range that are listed in Appendix B. The area fractions (volume fractions) were calculated from the size distributions, and the numerical results (in percent) are listed for different samples and different areas in the samples as referenced by the photograph number. the procedure for these measurements is enumerated below. Pore size and size distributions were obtained on as-polished metallographic sections.

PORE SIZE

The pore size and size distribution were obtained with an Omnicon Alpha™ Image Analyzer using the oversize or cumulative count. With this mode, the number of pores having a maximum horizontal chord larger than a predetermined size was determined. For pores sizes 1 μm and greater, pore sizes were determined directly from the Bausch and Lomb metallograph. For pore sizes less than 1 μm, pores sizes would be determined from scanning electron microscopy (SEM) photographs obtained with at lease 1000X magnification and with the Omnicon Alpha™ Image Analyzer.

PORE SIZE DISTRIBUTION

The pore size distribution was derived from the cumulative distribution by subtracting the pore count of successive size ranges, provided these readings were equidistant. If the size ranges were not equally spaced, the differences in pore count were multiplied by the relative spacing of the size range intervals to correctly shape the distribution. The pore size distribution was fitted to a normal distribution based on Equation (G-1):

$$Y = \frac{V_p I}{s \quad 2\pi} \exp - \frac{x - \bar{x}^2}{s^2} \qquad \text{(G-1)}$$

where

Y = ordinate of the distribution

I = pore size interval

s = standard deviation of the sample

x = Pore size

$\bar{x}$ = Average pore size

V_p = total pore volume.

TOTAL PORE VOLUME

The total pore volume was calculated from the pore size determined from the cumulative distribution. Each pore volume was calculated from the projected area of the spherical pores and the total area examined using Equation (C-2):

$$V_p = \frac{\sum_{i=1}^{N} \frac{\pi d_i^2}{4} N_i}{A} \qquad \text{(G-2)}$$

where

d_i = pore diameter (μm)

N_i = number of pores

A = total area examined (μm^2).

EXTERNAL CALIBRATION

Before the pore size and size distribution were determined, the calibration factor for the image analyzer was verified. Although either a ruler with an accurate scale or the calibration slide with two patterns of circles of accurately known diameters can be used, calibration using area measurement was used since they produce the most accurate results. The area of the reference circle was measured with the image analyzer, and the displayed area was recorded. The calibration factor was calculated from Equation (G-3).

$$K = \frac{\text{actual area}}{\text{displayed area}} \tag{G-3}$$

INTERNAL CALIBRATION

The internal calibration of the image analyzer was also checked prior to making the pore size and distribution measurements, since the internal calibration was designed to maintain accurate relations among the various measurements. A circle on the calibration slide covered about 3/4 of the height of the field of measurement. The projected length and Feret's diameter were measured from the displayed value. These measurements were nearly identical. The area of the test circle was then measured from the display. The measured area agreed within 2% of the area calculated from $\pi L^2/4$ using one of the above measured lengths for L. If the values did not agree, the image analyzer was recalibrated.

PORE FRACTIONS (%)

Particle 11-4-C
7.6
34.9
40.1
11.9
9.2
12.7
9.3
8.0
16.71 Average
13.02 Standard Deviation

Particle 11-6-A
26.4
23.8
27.4
27.7
28.3
16.8
19.6
27.4
22.1
35.3
25.48 Average
5.18 Standard Deviation

Particle 7-1-A
51.3
5.4
27.2
27.4
18.4
45.7
22.0
18.8
20.9
56.5
13.9
28.3
23.8
21.5
27.29 Average
14.35 Standard Deviation

Particle 11-1-B
26.4
2.7
30.3
26.6
29.0
23.00 Average
11.47 Standard Deviation

Particle 11-4-A
0.84
8.6
13.6
9.1
13.6
9.15 Average
5.22 Standard Deviation

Particle 11-7-B
2.1
14.4
8.25 Average
8.70 Standard Deviation

Particle 11-5-A	Particle 11-2-B
6.8	30.3
31.8	
34.7	
34.7	
27.00 Average	
13.54 Standard Deviation	

Metallic Inclusion Fractions (%)

Particle 11-4-C	Particle 11-4-A
0.79	0.13
	0.39

Particle 11-7-B
0.097